JACOPO MARCONI

PARAMETRIC REDUCED ORDER MODELS FOR IMPERFECT STRUCTURES WITH GEOMETRIC NONLINEARITIES

A thesis submitted in partial fulfillment of the requirements for the degree of
Doctor of Philosophy

Candidate: Jacopo Marconi, M.Sc. Mechanical Engineering, Politecnico di Milano

Examination Board
Prof. Francesco Braghin, Politecnico di Milano
Prof. Paolo Tiso, Eidgenössische Technische Hochschule Zürich
Prof. Malte Krack, University of Stuttgart
Prof. Stefano Zucca, Politecnico di Torino

PHD THESIS

Department of Mechanical Engineering
https://www.mecc.polimi.it/nc/us/
2021, October

Giovanni: "Be', noi... Lavoriamo nella meccanica di precisione: tecnologie avanzate al servizio di progettazioni particolari e specifiche. Non so... Hardware e quelle cose, cioè... creiamo dei supporti che poi serviranno per progettare grosse situazioni, non so mecc... Proprio... Strumenti di precisione per una svolta magari futura anche della meccanica... Eh? Non so se mi spiego?"

Aldo: "Sì, insomma... Abbiamo un negozio di ferramenta. Cioè, non è che il negozio di ferramenta è nostro... noi ci lavoriamo come commessi, come... galoppini, insomma"

— Tre uomini e una gamba

Jacopo Marconi: *Parametric Reduced Order Models for imperfect structures with geometric nonlinearities*, PhD Thesis, © 2021, October.

E-MAIL:
jacopo.marconi@polimi.it

The titlepage reproduces the logo of Politecnico di Milano, representing a simplified detail taken from Raffaello's *School of Athens*.

ABSTRACT

In common engineering applications, the design and analysis of complex systems is bounded to undergo a phase of numerical studies, which are fundamental to fill the gap between preliminary results, usually based on simplified analytical models, and reality. Structural dynamics, in particular, is normally studied with the aid of the Finite Element Method (FEM), which consists in accurately reproducing the geometry of a real structure through the union of small *elements*, each one pertaining to a portion of the material of the whole structure. The more the model is complex and the more the model is rich in geometrical details, the more elements are required; this usually leads to models counting hundred of thousands or even millions of unknowns, whose numerical analysis can be extremely expensive in terms of computational resources and times. For these reasons, since the very origin of FEM (and even more then, when computational resources were much more limited than the ones available today), there has always been a struggle to develop strategies to *reduce* the complexity of the problem. First examples are to be found in the so-called modal analysis, where the full solution of the system is sought in terms of a weighted sum of a relatively low number of system eigenvectors (usually in the order of tents); this way, simulation times are greatly reduced. Modal analysis and its derivative methods, however, provide a solution only to problems featuring a dynamics that can be considered to be *linear*.

When a structure undergoes a displacement that is relatively large with respect to its characteristic dimensions, usually the hypothesis of small deformations does not hold anymore: we talk in these cases of *geometric nonlinearities* and one has to resort to nonlinear dynamic analysis. The numerical complexity of the latter, however, is further increased by the fact some quantities (such as elastic internal forces and stiffness matrix) are now displacement-dependent and need to be evaluated at each analysis step/iteration of the adopted numerical scheme. For practical interest applications, this usually exponentially increases the computational times associated with the single analysis, often already demanding in the case of linear dynamics. Moreover, several phenomena that can be found in nonlinear dynamics and that have no counterpart in linear dynamics require specific numerical tools to be studied; the latter, however, usually can handle only a very limited number of unknowns.

For these reasons, the development of NonLinear Reduced Order Models (NL-ROM, or ROM in short), is a research topic which gained ever-increasing momentum over the last decades. Several solutions are already available in the literature, which will be briefly addressed throughout the present dissertation. A theme that almost every method shares, however, is the fact that the construction of the ROM itself is usually an expensive process which, in fact, may hinder the efficiency of the method. A way to amortize these *offline* construction times is thus to have the ROM to be *parametric* (pROM), that is, valid over a set of one or more parameters rather than for a single instance of the structure. This way the pROM can be built once and used multiple times so that the attainable overall speedups can be very high.

In the present dissertation, after introducing some rudiments of nonlinear FEM and of a class of ROMs, some nonlinear pROMs for the analysis of structures affected by the presence of defects are developed and discussed. Indeed, in many engineering applications, it is important to assess the performances of a system not only in the nominal-blueprint case, when the geometry is "perfect", but also in the case in which small imperfections are present. Notable examples are the micro electro-mechanical system (MEMS) industry, where the characteristics of the sensors are directly related to the imperfections of the production process, and

the aerospace field, where the presence of lightweight and slender structures undergoing high-amplitude vibrations usually triggers nonlinear responses strongly affected by the imperfect geometry of the real components.

The present work is organized as follows:

- Chapter 1 reviews the large deformation theory for continua and its implementation in a Finite Element framework;
- in Chapter 2 linear and nonlinear projection-based Reduced Order Models are reviewed, with special focus on the method based on Modal Derivatives (MDs), which is used in the following chapters. A practical use example is also given to show potential real applications of the presented method (Marconi, Bonaccorsi, et al., 2021);
- in Chapter 3, a novel parametric ROM is introduced for the analysis of defected structures (DpROM), based on an approximated strain theory (Marconi, Tiso, and Braghin, 2020);
- the DpROM is revisited and extended in Chapter 4, where it is shown that a more rigorous deformation theory can be adopted to increase the accuracy and the applicability range of the method (Marconi, Tiso, Quadrelli, et al., 2021);
- in Chapter 5, a possible extension of the DpROM to a substructuring setting is presented, where arbitrary (small) defects are allowed thanks to the Finite Element Tearing and Interconnecting (FETI) scheme adopted.
- finally, Chapter 6 concludes the work with possible future works and research directions.

SOMMARIO

Nella comune pratica ingegneristica, la progettazione e lo studio di sistemi complessi passa sempre e inevitabilmente attraverso l'analisi numerica, che sopperisce ai limiti di modelli analitici semplificati, generalmente utilizzati solo in fase preliminare. Lo studio strutturale di sistemi meccanici viene di prassi affrontato con l'ausilio del metodo agli elementi finiti (FEM), il quale permette di costruire modelli che riproducono accuratamente la geometria reale della struttura rappresentandola come unione di *elementi*, ognuno attenente ad una porzione di materiale dell'insieme. Più la complessità del problema cresce e il modello si arricchisce di dettagli geometrici, più elementi sono richiesti per descrivere il problema; nella pratica, ciò spesso porta a modelli che contano centinaia di migliaia o anche milioni di incognite, motivo per il quale l'analisi è spesso dispendiosa sia in termini di risorse computazionali che di tempo. Per questo motivo fin dalle origini del FEM, quando peraltro le risorse computazionali erano molto più limitate di quelle odierne, si sono sempre cercati dei metodi per *ridurre* la complessità del problema. I primi esempi si ritrovano nell'analisi modale, che va a ricostruire la soluzione dell'intero sistema come la somma di un numero molto ridotto di autovettori del sistema (in genere nell'ordine della decina); di conseguenza, i tempi di calcolo vengono estremamente velocizzati. L'analisi modale (e metodi derivati), tuttavia, è uno strumento valido nei casi in cui la dinamica può considerarsi *lineare*.

Quando lo spostamento della struttura diventa relativamente grande rispetto alle sue dimensioni caratteristiche, l'ipotesi di piccoli spostamenti non è più valida: in questo caso si parla di *nonlinearità geometrica*, e si deve ricorrere ad analisi dinamiche nonlineari. La complessità computazionale di queste ultime è ulteriormente aggravata dal fatto che alcune quantità (forze elastiche interne e matrice di rigidezza) dipendono dallo spostamento corrente della struttura, e quindi vanno rivalutate ad ogni step o iterazione del metodo di risoluzione adottato. Per sistemi di interesse pratico, questo porta a far esplodere i tempi richiesti per una singola analisi. Inoltre, molti fenomeni legati alla dinamica nonlineare possono essere studiati soltanto utilizzando strumenti che, attualmente, sono in grado di processare soltanto un limitatissimo numero di incognite.

Per queste ragioni, lo sviluppo di nuovi e diversi modelli ridotti nonlineari (NL-ROM, o solo ROM per brevità) è un tema che ha preso sempre più momento negli ultimi anni e che impegna diversi gruppi di ricerca in tutto il mondo. Già diverse soluzioni sono disponibili, brevemente ricapitolate nel corso di questo lavoro. Un tema che però accomuna quasi tutti i metodi è il fatto che la costruzione del ROM è tipicamente di per sè un processo oneroso in termini di tempo e risorse (anche se, sicuramente, più conveniente che affrontare la simulazione del sistema non ridotto). Un modo per ammortizzare ulteriormente i costi di costruzione del ROM è quello di fare sì che sia *parametrico*, ovvero valido per diversi valori di uno o più parametri. Utilizzando il ROM parametrico (pROM) molteplici volte al posto di analisi complete, si possono comparativamente ottenere fattori di velocizzazione notevoli.

Nel presente lavoro, dopo aver introdotto i rudimenti necessari di FEM nonlineare e di una classe di ROM nonlineari, saranno presentati alcuni pROM nonlineari dedicati allo studio parametrico di strutture nelle quali sono presenti dei difetti che influiscono sulla risposta dinamica delle stesse. Questo tema è infatti di interesse in molti ambiti, come quello dell'industria dei sistemi micro elettro-meccanici (MEMS), dove sono intrensicamente presenti difetti di produzione che vanno ad impattare sulle performance dei prodotti, o nel settore aerospaziale, dove la diffusa presenza di strutture sottili soggette a spostamenti elevati spesso porta a risposte dinamiche nonlineari che sono fortemente influenzate dalla precisone geometrica dei vari com-

ponenti.

Il presente lavoro è organizzato come segue:

- nel Capitolo 1 vengono ripresi gli elementi della teoria di grandi deformazione di corpi continui, e della sua implementazione nel quadro del FEM nonlineare;
- nel capitolo 2 si passano in rassegna diversi ROM lineari e nonlineari basati su approcci di proiezione in sottospazi, con speciale attenzione al metodo basato sulle Derivate Modali (MDs), che costituiranno la base dei metodi presentati nei successivi capitoli. Un esempio pratico di come i ROM presentati possono essere utilizzati per applicazioni reali è infine presentato a conclusione del capitolo (Marconi, Bonaccorsi et al., 2021);
- nel capitolo 3 viene presentato un nuovo ROM parametrico per la rapperesentazione di strutture con difetti di forma (chiamato DpROM), basato su una teoria di deformazione approssimata (Marconi, Tiso e Braghin, 2020);
- il DpROM è rivisitato ed esteso nel capitolo 4, dove si mostra come un modello di deformazione più rigoroso può essere adottato per ottenere una maggiore accuratezza e maggiore campo di validità del modello stesso (Marconi, Tiso, Quadrelli et al., 2021);
- nel capitolo 5 si presenta una possibile estensione del DpROM al campo del Substructuring, dove il metodo del Finite Element Tearing and Interconnecting (FETI) viene utilizzato per gestire indipendentemente i difetti applicati ad ogni sottostruttura.
- Infine, il capitolo 6 conclude il lavoro con possibili sviluppi futuri e linee di ricerca.

ACKNOWLEDGEMENTS

Here we are, the acknowledgments. What can I (what can anyone) say that's not already been said? One would think that it should be only natural to say thanks to the people who helped you on the road, yet I am doubtful that the number of these people and the different ways in which each one of them should be thanked would be fit for the few lines in which it is reasonable to frame this paragraph. Fortunately enough, seldom PhD dissertations are bestsellers: there will be little harm if a handful of readers will find this account incomplete or inaccurate. But first things first, let us start with the people that are likely to read this work.

I would like to thank my supervisors, Prof. Francesco Braghin and Dr. Paolo Tiso. The oblivious cheerfulness with which the first undertakes each project has often been an inspiration for me, at times too skeptical towards certain ideas which, in the end, turned out to be successful. His eclectic curiosity showed me how one can follow his own – one could say – Kafkaesque way through the meanders of engineering with a smile on the face and a glass in the hand. Second only in the alphabet, Paolo has been an invaluable mentor: always available to discuss everything, from the tiniest detail to the most out-reached ideas, he has been a constant source of inspiration and enthusiasm for research. Even when work seemed to be at a dead-end, he was able to keep a positive mind and a cheerful attitude.

I also cannot help to thank again Paolo and Prof. George Haller for hosting me in their group in Zurich: my life would not be the same had it not been for this experience. The uncountable chats, meetings, table soccer matches, and evenings (in or out the office) with Stergios, Shobhit, Mattia, Thomas and Sten will not easily be forgotten.

As for my colleagues in Polimi... having shared what we shared, I know that every word would be belittling. I cannot mention all the support received from half of you half as in full as I should like; and I can express my gratitude to less than half of you half as well as you deserve. I am confident, however, that I need not to spell out in every detail the multiform ways in which each one of you is dear to me. I just hope that the future will give me the chance to make up for the words that failed me today.

J. M.

4th October 2021

CONTENTS

1 NONLINEAR FEM

"perch'elli 'ncontra che più volte piega
l'oppinion corrente in falsa parte,
e poi l'affetto l'intelletto lega."

—Dante Alighieri, Paradiso, Canto XIII 118-120

The aim of this chapter is to review the basics of solid mechanics for large deformations, from which the nonlinear FE model is derived. Being mainly textbook material, it is intended just as a quick introduction/reference for students and non-experts, virtually containing the bare minimum amount of information to understand the topics discussed in the following chapters. For a complete and rigorous dissertation on continuum mechanics and the Finite Element Method instead, many specialist texts are available. The reader who is already familiar with these topics is nonetheless encouraged to skim through the chapter to get acquainted with the notation used throughout the whole work.

1.1 DEFORMATION OF CONTINUA

Let us consider an initially undeformed body of coordinates $\mathbf{x}_0 = \{x_{01}, x_{02}, x_{03}\} = \{x_0, y_0, z_0\}$. When the body undergoes deformation, a material fiber of length $d\mathbf{x}_0$ stretches (contracts) to a fiber of length $d\mathbf{x}$, being $\mathbf{x} = \{x_1, x_2, x_3\} = \{x, y, z\}$ the final coordinates of the deformed body. We call $\mathbf{u}(\mathbf{x}_0) = \mathbf{x} - \mathbf{x}_0 = \{u_1, u_2, u_3\} = \{u, v, w\}$ the *displacement* of one material point from the undeformed to the deformed configurations and $\mathcal{F}$ the *transformation map* $\mathbf{x} = \mathcal{F}(\mathbf{x}_0) = \mathbf{u}(\mathbf{x}_0) + \mathbf{x}_0$. Figure 1 schematically shows this deformation process. The length of the deformed fiber then writes

$$d\mathbf{x} = \frac{\partial \mathbf{x}}{\partial \mathbf{x}_0} d\mathbf{x}_0 = \frac{\partial \mathcal{F}(\mathbf{x}_0)}{\partial \mathbf{x}_0} d\mathbf{x}_0 = \left(\frac{\partial \mathbf{u}}{\partial \mathbf{x}_0} + \frac{\partial \mathbf{x}_0}{\partial \mathbf{x}_0} \right) d\mathbf{x}_0 = \mathbf{F} d\mathbf{x}_0 = (\mathbf{D} + \mathbf{I}) d\mathbf{x}_0, \quad (1.1)$$

where $\mathbf{F} = \nabla \mathcal{F}$ is the deformation gradient, $\mathbf{I}$ is the identity matrix and $\mathbf{D}$ is the displacement derivative matrix, defined as

$$D_{ij} = \frac{\partial u_i}{x_{0j}} = u_{i,j} \quad \text{with} \quad i, j = 1, 2, 3. \quad (1.2)$$

The stretch of the fiber thus writes

$$\mathcal{S} = d\mathbf{x}^T d\mathbf{x} - d\mathbf{x}_0^T d\mathbf{x}_0 = d\mathbf{x}_0^T (\mathbf{F}^T \mathbf{F} - \mathbf{I}) d\mathbf{x}_0 = d\mathbf{x}_0^T (\mathbf{D} + \mathbf{D}^T + \mathbf{D}^T \mathbf{D}) d\mathbf{x}_0. \quad (1.3)$$

The strains are measured through the Green-Lagrange strain tensor $\mathbf{E}$, which is linked to the stretch as $\mathcal{S} = 2 d\mathbf{x}_0^T \mathbf{E} d\mathbf{x}_0$, leading to

$$\mathbf{E} = \frac{1}{2} \left(\mathbf{D} + \mathbf{D}^T + \mathbf{D}^T \mathbf{D} \right). \quad (1.4)$$

In contrast to linear deformation theory, where small strains are assumed, the quadratic term $\mathbf{D}^T \mathbf{D}$ cannot be neglected for large deformations. The tensorial formulation above can be used to define the Hooke law as

$$S_{ij} = C_{4,ijkl} E_{kl} \quad \longleftrightarrow \quad \mathbf{S} = \mathbf{C}_4 : \mathbf{E}, \quad (1.5)$$

where $\mathbf{C}_4$ is the constitutive linear elastic fourth order tensor and $\mathbf{S}$ is the Piola-Kirchhoff stress tensor:

$$\mathbf{S} = \begin{bmatrix} S_{xx} & S_{xy} & S_{xz} \\ S_{yx} & S_{yy} & S_{yz} \\ S_{zx} & S_{zy} & S_{zz} \end{bmatrix},$$

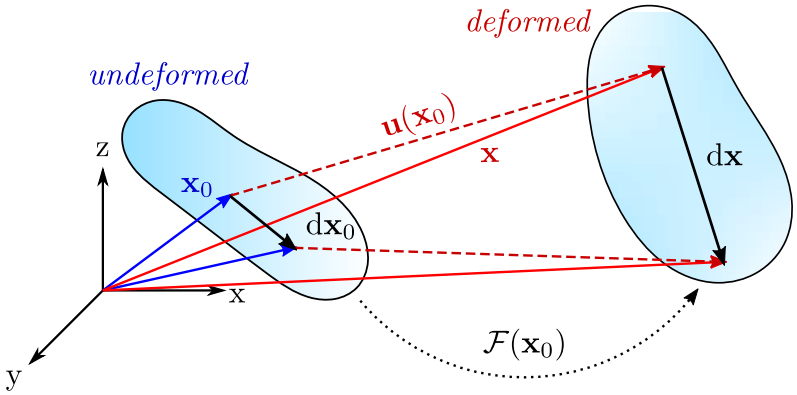

Figure 1: Undeformed and deformed body configurations.

and $\mathbf{C}$ is the linear elastic constitutive relation (fourth order) tensor. Equation 1.5, however, is not easy to handle in computer programs, as it involves tensor operations which are usually unavailable by default and/or are computationally inefficient. The elastic problem is then often conveniently recast in a vectorized form using Voigt notation.

To ease the notation, we use the subscripts x, y, z to denote the partial derivative with respect to the corresponding spatial coordinates x_0, y_0, z_0 (e.g. $u_z = \partial u/\partial z$). The Voigt strain and stress vectors then can be rearranged as:

$$\mathbf{E}_v = \begin{Bmatrix} \epsilon_{xx} \\ \epsilon_{yy} \\ \epsilon_{zz} \\ \gamma_{xy} \\ \gamma_{xz} \\ \gamma_{yz} \end{Bmatrix} = \underbrace{\begin{Bmatrix} u_x \\ v_y \\ w_z \\ u_y + v_x \\ u_z + w_x \\ v_z + w_y \end{Bmatrix}}_{\text{linear}} + \underbrace{\begin{Bmatrix} \frac{1}{2}(u_x^2 + v_x^2 + w_x^2) \\ \frac{1}{2}(u_y^2 + v_y^2 + w_y^2) \\ \frac{1}{2}(u_z^2 + v_z^2 + w_z^2) \\ u_x u_y + v_x v_y + w_x w_y \\ u_x u_z + v_x v_z + w_x w_z \\ u_y u_z + v_y v_z + w_y w_z \end{Bmatrix}}_{\text{quadratic}}, \quad \mathbf{S}_v = \begin{Bmatrix} S_{xx} \\ S_{yy} \\ S_{zz} \\ S_{xy} \\ S_{xz} \\ S_{yz} \end{Bmatrix} \tag{1.6}$$

and the constitutive matrix $\mathbf{C}$ for an isotropic linearly elastic material writes

$$\mathbf{C} = \begin{bmatrix} \lambda + 2\mu & \lambda & \lambda & 0 & 0 & 0 \\ \lambda & \lambda + 2\mu & \lambda & 0 & 0 & 0 \\ \lambda & \lambda & \lambda + 2\mu & 0 & 0 & 0 \\ 0 & 0 & 0 & \mu & 0 & 0 \\ 0 & 0 & 0 & 0 & \mu & 0 \\ 0 & 0 & 0 & 0 & 0 & \mu \end{bmatrix} \tag{1.7}$$

where the Lamé constants $\lambda = \nu E/((1+\nu)(1-2\nu))$ and $\mu = E/(2(1+\nu))$ have been used (being E and ν the Young modulus and the Poisson's ratio, respectively). Hooke's law can now be rewritten as a simple matrix product:

$$\mathbf{S}_v = \mathbf{C}\mathbf{E}_v. \tag{1.8}$$

As FE formulations usually spring from a virtual work expression, we can define it as

$$W = W_{int} - W_{ext} = \int_{V_o} \mathbf{S}_v^T \delta\mathbf{E}_v \, dV_o - W_{ext} = \int_{V_o} \mathbf{S} : \delta\mathbf{E} \, dV_o - W_{ext} \tag{1.9}$$

using either Voigt or tensor formulations, with W_{int} and W_{ext} denoting the work done by internal and external forces, respectively, and $\delta\mathbf{E}$ ($\delta\mathbf{E}_v$) the virtual variation of the strains. The latter can be written as

$$\delta\mathbf{E} = \frac{1}{2}(\delta\mathbf{D} + \delta\mathbf{D}^T + \delta\mathbf{D}^T\mathbf{D} + \mathbf{D}^T\delta\mathbf{D} + \underbrace{\delta\mathbf{D}^T\delta\mathbf{D}}_{\text{negligible}}) \approx \frac{1}{2}(\mathbf{F}^T\delta\mathbf{D} + \delta D^T\mathbf{F}). \tag{1.10}$$

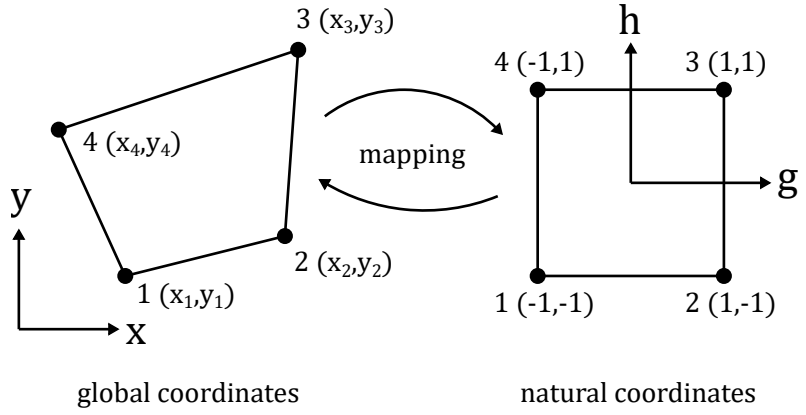

Figure 2: Isoparametric mapping for a plane quadrilateral with 4 nodes.

The expression of the virtual work can then manipulated to write the internal forces and, taking the virtual variation of W, to compute the tangent stiffness matrix. This step will be better developed in the next section, directly in the FE framework. The interest reader can find more details in Crisfield, 1991 (chapter 4).

1.2 ELEMENT FORMULATION

In this section we derive the expressions of the internal elastic forces and of the tangent stiffness matrix for one continuum element (e.g. tetrahedron, hexahedron, wedge) in a *total Lagrangian* setting. Before proceeding, let us quickly recover a few concepts regarding the isoparametric mapping underlying the formulation of this type of elements.

1.2.1 Isoparametric Mapping

The displacement fields along the three directions u_1, u_2, u_3 can be related to the displacement at the nodes $\mathbf{u}^e \in \mathbb{R}^{n_e}$ of the element (n_e number of element's dofs) using interpolating functions. These *shape functions* N_i (with $i = 1, ..., n_n$, being n_n the number of the element's nodes) are defined in a convenient space, called *natural* space (of coordinates $\{g, h, r\}$), which is independent from the real shape/dimension/orientation of the element. The mapping between the global/physical and the natural coordinates, schematically represented in Fig. 2, allows to treat integration over the volume (area) with ease, as the domain of integration is the same for all the elements of the same type and the actual element shape is accounted for through the jacobian of the transformation. The displacement field over the element writes:

$$\mathbf{u} = \begin{Bmatrix} u_1 \\ u_2 \\ u_3 \end{Bmatrix} = \begin{bmatrix} \mathbf{N}(g,h,r)^T & 0 & 0 \\ 0 & \mathbf{N}(g,h,r)^T & 0 \\ 0 & 0 & \mathbf{N}(g,h,r)^T \end{bmatrix} \begin{Bmatrix} \mathbf{u}_1^e \\ \mathbf{u}_2^e \\ \mathbf{u}_3^e \end{Bmatrix} = \mathcal{N}(g,h,r)\mathbf{u}^e, \quad (1.11)$$

where the vector $\mathbf{N} \in \mathbb{R}^{n_n \times 1}$ collects the shape functions and $\mathbf{u}^e \in \mathbb{R}^{n_e \times 1}$ contains the nodal displacements along the three directions[1]. The integral of a generic function f over the physical domain can be carried out in the natural coordinates as follows

$$F = \int_{x_o}^{x_f} \int_{y_o}^{y_f} \int_{z_o}^{z_f} f(x,y,z)\, dxdydz = \int_{g_o}^{g_f} \int_{h_o}^{h_f} \int_{r_o}^{r_f} f(g,h,r)\, \det(\mathbf{J})\, dgdhdr, \quad (1.12)$$

1 Notice that, as we consider a general 3D case, $n_e = 3n_n$.

with $g_o, h_o, r_o = -1$, $g_f, h_f, r_f = +1$ and being $\mathbf{J}$ the jacobian of the map between the natural and physical coordinates, defined as

$$\begin{Bmatrix} \partial_g \\ \partial_h \\ \partial_r \end{Bmatrix} = \begin{bmatrix} \partial_g x & \partial_g y & \partial_g z \\ \partial_h x & \partial_h y & \partial_h z \\ \partial_r x & \partial_r y & \partial_r z \end{bmatrix} \begin{Bmatrix} \partial_x \\ \partial_y \\ \partial_z \end{Bmatrix} = \mathbf{J} \begin{Bmatrix} \partial_x \\ \partial_y \\ \partial_z \end{Bmatrix}, \tag{1.13}$$

where we adopted the shorthand notation $\partial_\star \bullet = \partial \bullet / \partial \star$.

1.2.2 Derivatives

To compute the strains, the derivatives of the displacement field in the *physical space* are required. As the shape functions are defined over the natural space, we have to apply the chain rule. Let us consider the u displacement along x only (the same will hold for v and w as well), we have:

$$\begin{cases} \frac{\partial u}{\partial x} = \frac{\partial (\mathbf{N}(g,h,r)^T \mathbf{u}_1^e)}{\partial x} = \left(\frac{\partial \mathbf{N}^T}{\partial g}\frac{\partial g}{\partial x} + \frac{\partial \mathbf{N}^T}{\partial h}\frac{\partial h}{\partial x} + \frac{\partial \mathbf{N}^T}{\partial g}\frac{\partial g}{\partial x} \right) \mathbf{u}_1^e \\ \frac{\partial u}{\partial y} = \frac{\partial (\mathbf{N}(g,h,r)^T \mathbf{u}_1^e)}{\partial y} = \left(\frac{\partial \mathbf{N}^T}{\partial g}\frac{\partial g}{\partial y} + \frac{\partial \mathbf{N}^T}{\partial h}\frac{\partial h}{\partial y} + \frac{\partial \mathbf{N}^T}{\partial r}\frac{\partial r}{\partial y} \right) \mathbf{u}_1^e \\ \frac{\partial u}{\partial z} = \frac{\partial (\mathbf{N}(g,h,r)^T \mathbf{u}_1^e)}{\partial z} = \left(\frac{\partial \mathbf{N}^T}{\partial g}\frac{\partial g}{\partial z} + \frac{\partial \mathbf{N}^T}{\partial h}\frac{\partial h}{\partial z} + \frac{\partial \mathbf{N}^T}{\partial r}\frac{\partial r}{\partial z} \right) \mathbf{u}_1^e \end{cases}, \tag{1.14}$$

which, reorganized in matrix form, writes

$$\begin{Bmatrix} \partial_x u \\ \partial_y u \\ \partial_z u \end{Bmatrix} = \begin{bmatrix} \partial_x g & \partial_x h & \partial_x r \\ \partial_y g & \partial_y h & \partial_y r \\ \partial_z g & \partial_z h & \partial_z r \end{bmatrix} \begin{Bmatrix} \partial_g \mathbf{N}^T \\ \partial_h \mathbf{N}^T \\ \partial_r \mathbf{N}^T \end{Bmatrix} \mathbf{u}_1^e = \mathbf{J}^{-1} \mathcal{G}_{nat} \mathbf{u}_1^e = \mathcal{G} \mathbf{u}_1^e. \tag{1.15}$$

The matrix $\mathcal{G}_{nat} \in \mathbb{R}^{3 \times n_n}$ thus collects the derivatives of the shape functions in with respect to the natural coordinates, while the inverse of the jacobian, $\mathbf{J}^{-1}$, takes into account the mapping to the physical space, yielding $\mathcal{G}$. In the following, we use the vectorized form of the displacement derivative matrix $\mathbf{D}$, defined as:

$$\theta = \begin{Bmatrix} u_x \\ u_y \\ u_z \\ v_x \\ v_y \\ v_z \\ w_x \\ w_y \\ w_z \end{Bmatrix} = \begin{bmatrix} \mathcal{G} & \mathbf{0} & \mathbf{0} \\ \mathbf{0} & \mathcal{G} & \mathbf{0} \\ \mathbf{0} & \mathbf{0} & \mathcal{G} \end{bmatrix} \begin{Bmatrix} \mathbf{u}_1^e \\ \mathbf{u}_2^2 \\ \mathbf{u}_3^e \end{Bmatrix} = \mathbf{G}\mathbf{u}^e, \tag{1.16}$$

where we call $\mathbf{G} \in \mathbb{R}^{9 \times n_e}$ *shape derivative matrix*, which will be repeatedly used in this and the following chapters.

How to: Jacobian

The jacobian components can be written as, for instance

$$J_{12} = \frac{\partial y}{\partial g} = \frac{\partial \mathbf{N}(g,h,r)^T}{\partial g} \mathbf{y}^e, \tag{1.17}$$

where $\mathbf{x}^e, \mathbf{y}^e, \mathbf{z}^e \in \mathbb{R}^{n_n \times 1}$ are the nodal coordinates of the element along the three directions. The Jacobian can thus be numerically computed as:

$$\mathbf{J} = \mathcal{G}_{nat} \begin{bmatrix} \mathbf{x}^e, & \mathbf{y}^e, & \mathbf{z}^e \end{bmatrix}. \tag{1.18}$$

1.2.3 Internal forces and tangent stiffness matrix

Now that an expression for the displacement derivatives is available through the shape functions and the nodal displacements, we can finally write the strains for the finite element and compute the virtual work. Equation (1.6) can be recast as

$$\mathbf{E}_v = \left[\mathbf{H} + \frac{1}{2}\mathbf{A}(\theta)\right]\theta, \tag{1.19}$$

where $\mathbf{H}$ is a constant matrix, defined as:

$$\mathbf{H} = \begin{bmatrix} 1 & 0 & 0 & 0 & 0 & 0 & 0 & 0 & 0 \\ 0 & 0 & 0 & 0 & 1 & 0 & 0 & 0 & 0 \\ 0 & 0 & 0 & 0 & 0 & 0 & 0 & 0 & 1 \\ 0 & 1 & 0 & 1 & 0 & 0 & 0 & 0 & 0 \\ 0 & 0 & 1 & 0 & 0 & 0 & 1 & 0 & 0 \\ 0 & 0 & 0 & 0 & 0 & 1 & 0 & 1 & 0 \end{bmatrix}, \tag{1.20}$$

and where $\mathbf{A}$ is a matrix whose elements are the entries of θ, defined as:

$$\mathbf{A}(\theta) = \begin{bmatrix} u_x & 0 & 0 & v_x & 0 & 0 & w_x & 0 & 0 \\ 0 & u_y & 0 & 0 & v_y & 0 & 0 & w_y & 0 \\ 0 & 0 & u_z & 0 & 0 & v_z & 0 & 0 & w_z \\ u_y & u_x & 0 & v_y & v_x & 0 & w_y & w_x & 0 \\ u_z & 0 & u_x & v_z & 0 & v_x & w_z & 0 & w_x \\ 0 & u_z & u_y & 0 & v_z & v_y & 0 & w_z & w_y \end{bmatrix}. \tag{1.21}$$

The strain variation thus writes

$$\delta\mathbf{E}_v = \mathbf{H}\delta\theta + \frac{1}{2}\mathbf{A}(\theta)\delta\theta + \frac{1}{2}\delta\mathbf{A}(\theta)\theta + O(\delta\theta^2), \tag{1.22}$$

and, exploiting the fact that $\delta\mathbf{A}(\theta)\theta = \mathbf{A}(\delta\theta)\theta = \mathbf{A}(\theta)\delta\theta$ (which can be easily verified), we can write:

$$\delta\mathbf{E}_v = [\mathbf{H} + \mathbf{A}(\theta)]\,\delta\theta + O(\delta\theta^2) \approx [\mathbf{H} + \mathbf{A}(\theta)]\,\mathbf{G}\delta\mathbf{u}^e = \mathbf{B}(\mathbf{u}^e)\delta\mathbf{u}^e, \tag{1.23}$$

where $\mathbf{B}$ is the strain–displacement matrix and where higher order terms were neglected under the hypothesis of small virtual displacements. The expression of the virtual work for the element then reads

$$W^e_{int} = (\delta\mathbf{u}^e)^T \left(\int_{V^e_0} \mathbf{B}^T\mathbf{S}_v \, dV^e_0\right) = (\delta\mathbf{u}^e)^T\mathbf{f}^e_{int}, \tag{1.24}$$

$$\mathbf{f}^e_{int} = \int_{V^e_0} \mathbf{B}^T\mathbf{S}_v \, dV^e_0, \tag{1.25}$$

where V^e_0 is the volume of the undeformed element and $\mathbf{f}^e_{int}$ is the vector of the element internal elastic forces.

The element tangent stiffness matrix can be obtained from the virtual variation of the elastic forces, that is:

$$\begin{aligned} \delta\mathbf{f}^e_{int} &= \int_{V^e_0} \mathbf{B}^T(\mathbf{u}^e)\delta\mathbf{S}_v + \delta\mathbf{B}^T(\mathbf{u})\mathbf{S}_v \, dV^e_0 \\ &= \int_{V^e_0} \mathbf{B}^T(\mathbf{u}^e)\mathbf{C}\delta\mathbf{E}_v + \delta\mathbf{B}^T(\mathbf{u})\mathbf{S}_v \, dV^e_0 \\ &= \int_{V^e_0} \mathbf{B}^T(\mathbf{u}^e)\mathbf{C}\mathbf{B}(\mathbf{u}^e)\delta\mathbf{u}^e + \delta\mathbf{B}^T(\mathbf{u})\mathbf{S}_v \, dV^e_0. \end{aligned} \tag{1.26}$$

The latter term must be rearranged to make explicit the dependency on $\mathbf{u}^e$. It can be shown that

$$\delta\mathbf{B}^T(\mathbf{u})\mathbf{S}_v = \mathbf{G}^T\mathbf{A}(\delta\theta)^T\mathbf{S}_v = \mathbf{G}^T\hat{\mathbf{S}}\delta\theta = \mathbf{G}^T\hat{\mathbf{S}}\mathbf{G}\delta\mathbf{u}^e, \tag{1.27}$$

where

$$\hat{\mathbf{S}} = \begin{bmatrix} \mathbf{S} & \mathbf{o} & \mathbf{o} \\ \mathbf{o} & \mathbf{S} & \mathbf{o} \\ \mathbf{o} & \mathbf{o} & \mathbf{S} \end{bmatrix}, \qquad \mathbf{S} = \begin{bmatrix} S_{xx} & S_{xy} & S_{xz} \\ S_{yx} & S_{yy} & S_{yz} \\ S_{zx} & S_{zy} & S_{zz} \end{bmatrix}. \tag{1.28}$$

Using the formulation above, Eq. (1.26) rewrites

$$\delta \mathbf{f}^e_{int} = \left(\int_{V^e_o} \left[\mathbf{B}(\mathbf{u}^e)^T(\mathbf{u}^e) \mathbf{C} \mathbf{B}(\mathbf{u}^e) + \mathbf{G}^T \hat{\mathbf{S}} \mathbf{G} \right] \, dV^e_o \right) \delta \mathbf{u}^e \tag{1.29}$$

from which we can derive the two components of the tangent stiffness matrix:

$$\mathbf{K}^e_{t1} = \int_{V^e_o} \mathbf{B}(\mathbf{u}^e)^T(\mathbf{u}^e) \mathbf{C}_v \mathbf{B}(\mathbf{u}^e) \, dV^e_o \tag{1.30}$$

$$\mathbf{K}^e_{t\sigma} = \int_{V^e_o} \mathbf{G}^T \hat{\mathbf{S}} \mathbf{G} \, dV^e_o \tag{1.31}$$

and

$$\mathbf{K}^e_t = \mathbf{K}^e_{t1} + \mathbf{K}^e_{t\sigma}. \tag{1.32}$$

The obtained expression for $\mathbf{K}^e_t$ features a term which depends directly on the displacements and a term directly proportional to the stresses (and thus indirectly on the displacements). Again, for more details the reader is referred to Crisfield, 1991 (chapter 5).

In a *standard FE procedure*, $\mathbf{K}^e_t$ and $\mathbf{f}^e_{int}$ are computed through *Gauss quadrature*, first computing the shape function derivatives ($\mathcal{G}_{nat}, \mathbf{J}$ and $\mathcal{G}$), then computing strains and stresses ($\boldsymbol{\theta}, \mathbf{E}_v$ and $\mathbf{S}_v$). Then, once the stresses are available, internal forces and stiffness matrices are computed. As it will detailed later, this procedure has a deep impact on the performances of most projection-based reduction techniques.

How to: Gauss quadrature

Generally, in FE procedures integrals are carried out through some quadrature rule, which basically approximates the integral as a weighted sum of the function to integrate evaluated at specific points. Gauss quadrature is a popular method that falls into this category, and provides a set of evaluation points and weights to carry out the sum. In the general case of the integration of a function f over the element volume, we can then compute the integral as

$$\begin{aligned} F &= \int_{-1}^{1} \int_{-1}^{1} \int_{-1}^{1} f(g,h,r) \det(\mathbf{J}(g,h,r)) \, dg dh dr \\ &\approx \sum_{i=1}^{n_g} \sum_{j=1}^{n_g} \sum_{k=1}^{n_g} \alpha_i \alpha_j \alpha_k f(g_i, h_j, r_k) \det(\mathbf{J}(g_i, h_j, r_k)), \end{aligned} \tag{1.33}$$

where n_g is the number of quadrature points along one dimension, $\alpha_{i,j,k}$ and g_i, h_j, r_k are the weights and evaluation points given by the corresponding quadrature rule, respectively. More details can be found in many FE books, for instance see Belytschko et al., 2014 (Appendix 3).

1.3 TENSORIAL APPROACH

Although model order reduction has not been introduced yet, it is now convenient to discuss an alternative representation of the nonlinear internal elastic forces (and of the tangent stiffness matrix), still at full order model level. As anticipated in the previous section, in a standard FE procedure one needs to compute strain and stresses to compute and assemble the internal force vector $\mathbf{f}_{int}$ and the tangent stiffness matrix $\mathbf{K}_t$. Considering for example a transient analysis of a structure in time and assuming to use a standard solution algorithm (e.g. Newark scheme), one has to repeat this assembly operation for *each time step*, and multiple times within the time step itself for *each iteration* of the solution of the nonlinear system of equation (e.g. through Newton's algorithm). Needless to say, the whole process is very expensive, particularly for large FE models.

Looking back at Eqs. (1.25), (1.30), (1.31), however, one can see that these expressions can be written as explicit functions of the displacement $\mathbf{u}^e$ only, through Hooke's law. In other words, it is possible to precompute all the stiffness coefficients which multiply $\mathbf{u}^e$ and write a polynomial expression for both $\mathbf{f}_{int}$ and $\mathbf{K}_t$. For instance, using the constitutive relation in Eq. (1.25), we can write

$$\begin{aligned}\mathbf{f}^e_{int} &= \int_{V^e_0} \mathbf{B}^T \mathbf{C} \mathbf{E}_\nu \, dV^e_0, \\ &= \int_{V^e_0} \mathbf{G}^T (\mathbf{H} + \mathbf{A}(\mathbf{G}\mathbf{u}^e))^T \mathbf{C} \left(\mathbf{H} + \frac{1}{2}\mathbf{A}(\mathbf{G}\mathbf{u}^e) \right) \mathbf{G}\mathbf{u}^e \, dV^e_0,\end{aligned} \tag{1.34}$$

from which it is clear how for continuum elements with total Lagrangian formulation and linear elastic material f_{int} can be expressed as *third order polynomials* in $\mathbf{u}^e$. As a consequence, we expect to be able to write a second order stiffness tensor ${}_2\mathbf{K}^e \in \mathbb{R}^{n_e \times n_e}$ for the linear terms, a third order tensor ${}_3\mathbf{K}^e \in \mathbb{R}^{n_e \times n_e \times n_e}$ for the quadratic terms and a fourth order tensor ${}_4\mathbf{K}^e \in \mathbb{R}^{n_e \times n_e \times n_e \times n_e}$ for the cubic ones. Equation (1.34) will then rewrite as

$$\mathbf{f}^e_{int} = {}_2\mathbf{K}^e \mathbf{u}^e + ({}_3\mathbf{K}^e \cdot \mathbf{u}^e) \cdot \mathbf{u}^e + (({}_4\mathbf{K}^e \cdot \mathbf{u}^e) \cdot \mathbf{u}^e) \cdot \mathbf{u}^e. \tag{1.35}$$

Let us illustrate how to retrieve the expressions of these tensors, at element level, using *Einstein notation*. First, let us introduce the localization matrix $\mathbf{L}$, such that

$$\mathbf{A}(\theta) = \mathbf{L} \cdot \theta \longleftrightarrow A_{IJ} = L_{IJi}\theta_i = L_{IJi}G_{ij}u^e_j, \tag{1.36}$$

so that we "extract" $\mathbf{u}^e$ from the matrix $\mathbf{A}$. The entries of $\mathbf{L}$ are given in Table 1. Equalling the terms of the same order in $\mathbf{u}^e$ in Eqs. (1.34) and (1.35), we find

$$\int_{V^e_0} G_{iI} H_{ji} C_{jk} H_{kl} G_{lm} \cancel{u^e_m} \, dV^e_0 = {}_2K^e_{Im} \cancel{u^e_m} \xrightarrow[\text{rename}]{m \to J} {}_2K^e_{IJ}, \tag{1.37}$$

$$\begin{aligned}\int_{V^e_0} G_{iI} \left(\frac{1}{2} H_{ji} C_{jk} L_{kla} G_{am} \cancel{u^e_m} + L_{jia} G_{am} \cancel{u^e_m} C_{jk} H_{kl} \right) G_{ln} \cancel{u^e_n} \, dV^e_0 \\ = {}_3K^e_{Imn} \cancel{u^e_m} \cancel{u^e_n} \xrightarrow[\text{rename}]{m,n \to J,K} {}_3K^e_{IJK},\end{aligned} \tag{1.38}$$

$$\begin{aligned}\int_{V^e_0} G_{iI} L_{jia} G_{am} \cancel{u^e_m} C_{jk} L_{klb} G_{bn} \cancel{u^e_n} G_{lp} \cancel{u^e_p} \, dV^e_0 \\ = {}_4K^e_{Imnp} \cancel{u^e_m} \cancel{u^e_n} \cancel{u^e_p} \xrightarrow[\text{rename}]{m,n,p \to J,K,L} {}_4K^e_{IJKL},\end{aligned} \tag{1.39}$$

where displacements were explicitly cancelled out to illustrate the procedure[2].

2 Notice that the change of subscripts is not necessary, as once displacements are simplified the indexes are not repeated anymore and thus need not to be summed over. However, we prefer to change the subscripts to capital letters when there is no summation involved, consistently with the adopted notation.

Table 1: Elements L_{IJK} of the sparse $6 \times 9 \times 9$ matrices $\mathbf{L}$ in the 3D case.

$L^{(1)}_{111} = 1,$	$L^{(1)}_{421} = 1,$	$L^{(1)}_{531} = 1,$	$L^{(1)}_{412} = 1,$	$L^{(1)}_{222} = 1,$	$L^{(1)}_{632} = 1,$	$L^{(1)}_{513} = 1,$	$L^{(1)}_{623} = 1,$	$L^{(1)}_{333} = 1,$
$L^{(1)}_{144} = 1,$	$L^{(1)}_{454} = 1,$	$L^{(1)}_{564} = 1,$	$L^{(1)}_{445} = 1,$	$L^{(1)}_{255} = 1,$	$L^{(1)}_{665} = 1,$	$L^{(1)}_{546} = 1,$	$L^{(1)}_{656} = 1,$	$L^{(1)}_{366} = 1,$
$L^{(1)}_{177} = 1,$	$L^{(1)}_{487} = 1,$	$L^{(1)}_{597} = 1,$	$L^{(1)}_{478} = 1,$	$L^{(1)}_{288} = 1,$	$L^{(1)}_{698} = 1,$	$L^{(1)}_{579} = 1,$	$L^{(1)}_{689} = 1,$	$L^{(1)}_{399} = 1.$

In Einstein notation, internal forces write

$$f^e_{int,I} = {}_2K^e_{Ii} u^e_i + {}_3K^e_{Iij} u^e_i u^e_j + {}_4K^e_{Iijk} u^e_i u^e_j u^e_k, \tag{1.40}$$

from which the tangent stiffness matrix can be computed as

$$K^e_{t,IJ} = \frac{\partial f^e_{int,I}}{\partial u^e_J} = {}_2K^e_{IJ} + ({}_3K^e_{IJj} + {}_3K^e_{IjJ}) u^e_j + ({}_4K^e_{IJij} + {}_4K^e_{IiJj} + {}_4K^e_{IijJ}) u^e_i u^e_j. \tag{1.41}$$

Using Eqs. (1.40) and (1.41) it is possible to compute the tensors for each element and then assemble the global tensors:

$${}_\alpha\mathbf{K}^F = \bigcup_{e=1}^{N_e} {}_\alpha\mathbf{K}^e \quad with \quad \alpha = 2, 3, 4, \tag{1.42}$$

where N_e is the total number of element in the global (full order[3]) model and where we used the symbol $\cup$ to denote the assembling procedure. These global tensors can be precomputed *offline* once and for all, before the analysis starts. Then $\mathbf{f}_{int}$ and $\mathbf{K}_t$ can be evaluated *online* during the analysis, contracting the tensors on the global displacement field $\mathbf{u}^F$, with no need for assembly.

WHY ARE TENSORS NOT USED? The tensorial approach, avoiding the computational costs associated to the repeated assembly of vectors and matrices during the analysis, promises relevant savings in terms of computational times. It is then legit to wonder why such a strategy is not implemented in any (commercial) FE software.

There are three main reasons. First of all, the precomputation of the tensors is expensive. To have a rough idea, if T_{c2} is the time to compute the (standard) second order tensor of one element, the time to compute the three tensors for the same element is $T_c \approx T_{c2}(1 + n_e + n_e^2)$. One would have then first to evaluate if the cost associated to the construction of the tensors is greater than the cost of a standard analysis or not. The second issue is due to online costs being also very high, as the contraction of $\mathbf{u}^F \in \mathbb{R}^n$ over the tensors grows with n^2, being n number of dofs of the global (full order) FE model. The real bottleneck, however, it the fact that the tensors *cannot be stored* in the volatile memory of most calculators due to their size. Even for relatively small models ($n \sim 10^3$) and even exploiting sparsity, one would simply run out of memory.

As it will explained in the context of model order reduction, however, the tensorial formulation becomes very efficient when dealing with systems with a low number of dofs, which is the reason why the approach has been introduced here.

1.3.1 Sample code

In this last section, some useful bits of MATLAB® code are reported, as the standard FE user might not be familiar with operations featuring tensors of order higher than two. We use the tensor toolbox by Sandia National Laboratories (Bader and Kolda, 2006; Bader, Kolda, et al., 2015).

3 We use the superscript "F" for the global model, later referred to as Full Order Model (FOM).

Element–tensor construction (3D–version):

```
function [K3, K4] = compute_tensors(C, H, L, nodes, ne)
  % This function computes third and fourth order stiffness tensors for
  % a continuum element. It uses the tensor_toolbox developed by Sandia
  % National Laboratories.

  [X, W] = get_quadrature_rule(); % your quadrature points and weights

  K3h = tenzeros([ne,ne,ne]); % initialization (ne: element's dofs)
  K4  = tenzeros([ne,ne,ne,ne]);
  for i = 1 : length(W)
    g = X(1, i); % quadrature points
    h = X(2, i);
    r = X(3, i);
    we = W(i); % quadrature weights
    [G,detJ] = shape_function_derivatives(nodes,g,h,r);

    % construct core part of the tensors for each gauss point
    GHC = tensor((C*H*G)');
    TC = tensor(C);  % create tensor object, rename it to distinguish
    TG = tensor(G);  % create tensor object out of matrix
    LGG = ttt(ttt(L, TG, 3, 1), TG, 2, 1);
    K3h_int = ttt(GHC, LGG, 2, 1);
    K3h = K3h + K3h_int*detJ*we; % sum over contributions

    K4_int = ttt(ttt(permute(LGG,[2 1 3]),TC,2,1),LGG,3,1);
    K4 = K4 + K4_int*detJ*we;
  end

  K3 = K3h./2 + permute(K3h, [3 2 1]); % build third order tensors using K3h
  K4 = K4./2;
end
```

The localization matrix:

```
function L = localization(dimension)
  if dimension == 2 % 2D-problem
    L = tenzeros([3,4,4]);
    L(1,1,1) = 1; L(3,2,1) = 1; L(3,1,2) = 1; L(2,2,2) = 1;
    L(1,3,3) = 1; L(3,4,3) = 1; L(3,3,4) = 1; L(2,4,4) = 1;
  elseif dimension==3 % 3D-problem
    L = tenzeros([6,9,9]);
    L(1,1,1)=1; L(4,2,1)=1; L(5,3,1)=1; L(4,1,2)=1; L(2,2,2)=1; L(6,3,2)=1;
    L(5,1,3)=1; L(6,2,3)=1; L(3,3,3)=1; L(1,4,4)=1; L(4,5,4)=1; L(5,6,4)=1;
    L(4,4,5)=1; L(2,5,5)=1; L(6,6,5)=1; L(5,4,6)=1; L(6,5,6)=1; L(3,6,6)=1;
    L(1,7,7)=1; L(4,8,7)=1; L(5,9,7)=1; L(4,7,8)=1; L(2,8,8)=1; L(6,9,8)=1;
    L(5,7,9)=1; L(6,8,9)=1; L(3,9,9)=1;
  end
end
```

where we reported also the 2D-problem version of the matrix $\mathbf{L}$, such that:

$$\mathbf{A}(\boldsymbol{\theta}) = \mathbf{L}\cdot\boldsymbol{\theta}, \;\; \textit{with} \;\; \boldsymbol{\theta} = \begin{Bmatrix} u_x \\ u_y \\ v_x \\ v_y \end{Bmatrix} \;\; \textit{and} \;\; \mathbf{A}(\boldsymbol{\theta}) = \begin{bmatrix} u_x & 0 & v_x & 0 \\ 0 & u_y & 0 & v_y \\ u_y & u_x & v_y & v_x \end{bmatrix}. \tag{1.43}$$

Finally, element internal forces and tangent stiffness matrix can be computed according to Eqs. (1.40)–(1.41) as:

```
% precompute (for the tangent stiffness matrix)
K3et = K3e + permute(K3e, [1 3 2]);
K4et = K4e + permute(K4e, [1 3 2 4]) + permute(K4e, [1 4 2 3]);

function [Ket, fe] = tensors_KF(K2e, K3e, K4e, K3et, K4et, ue)
    fe  = K2e*ue + ttsv(K3e,  ue, -1) + ttsv(K4e,  ue, -1);
    Ket = K2e    + ttsv(K3et, ue, -2) + ttsv(K4et, ue, -2);
end
```

2 MODEL ORDER REDUCTION FOR GEOMETRIC NONLINEARITIES

Throw the lumber over, man! Let your boat of life be light, packed with only what you need

—Jerome K. Jerome, Three Men in a Boat

In engineering applications often analysts have to construct large FE models in the order of hundreds of thousands or even millions of unknowns. The struggle to reduce the computational burden for these analyses is thus as old as the FEM itself, branching in the development of better solvers and algorithms, in the formulation of simplified kinematic elements (e.g. Euler-Bernoulli beam elements) and in the usage of *reduced order models* (ROMs), which try to reproduce the response of the *full order model* (FOM). In this chapter an overview of reduction methods for structural dynamics is given, with focus on the ones that will be used and developed in the following chapters.

2.1 REDUCTION IN LINEAR DYNAMICS

It is first convenient to tackle reduction methods for linear dynamic problems. The equations of motion in this context write

$$\mathbf{M}^F\ddot{\mathbf{u}}^F + \mathbf{C}^F\dot{\mathbf{u}}^F + \mathbf{K}^F\mathbf{u}^F = \mathbf{f}_{ext}(t), \tag{2.1}$$

where $\mathbf{M}^F$, $\mathbf{C}^F$, $\mathbf{K}^F \in \mathbb{R}^{n\times n}$ are the full order mass, damping and stiffness matrices, respectively, being n the number of dofs of the FOM. Equation (2.1) implies a linearization about an equilibrium condition, usually $\mathbf{u}^F = 0$.

A well-established reduction process is the so-called “modal analysis". Considering the unforced, undamped system version of Eq. (2.1):

$$\mathbf{M}^F\ddot{\mathbf{u}}^F + \mathbf{K}^F\mathbf{u}^F = 0, \tag{2.2}$$

and assuming a harmonic solution of the type

$$\mathbf{u}^F(t) = \boldsymbol{\phi}_j e^{i\omega_j t}, \tag{2.3}$$

we obtain the eigenvalue problem

$$(\mathbf{K}^F - \omega_j^2\mathbf{M}^F)\boldsymbol{\phi}_j = 0, \tag{2.4}$$

which admits $j = 1, ..., n$ eigenfrequencies ω_j and eigenvectors $\boldsymbol{\phi}_j$. The latter are usually referred to as *Vibration Modes* (VMs) or natural modes, whereas ω_j are called *resonance frequencies* or natural frequencies. VMs physically represent how a structure freely vibrates at a given frequency, are linearly independent from each other and *M- and K-orthogonal*, i.e.

$$\boldsymbol{\phi}_i^T\mathbf{M}^F\boldsymbol{\phi}_j = \delta_{ij}, \tag{2.5a}$$

$$\boldsymbol{\phi}_i^T\mathbf{K}^F\boldsymbol{\phi}_j = \delta_{ij}\omega_i\omega_j \ \textit{(this is not Einstein summation)}, \tag{2.5b}$$

with δ_{ij} is the Kronecker delta[1].

1 VMs are defined up to a constant, here we considered a *mass-normalization*, i.e. $\boldsymbol{\Phi}_i = \boldsymbol{\Phi}'_i / \sqrt{\boldsymbol{\Phi}_i'^T\mathbf{M}^F\boldsymbol{\Phi}'_i}$ where $\boldsymbol{\Phi}'_i$ is a generic, not-normalized mode.

Since a set of n linearly independent vectors is again a suitable basis for the space $\mathbf{R}^n$, the full response of the system can be described with a coordinate change and using *mode superposition* as

$$\mathbf{u}^F(t) = \sum_{k=1}^{n} \boldsymbol{\phi}_k \eta_k(t) = \boldsymbol{\Phi}\boldsymbol{\eta}(t). \tag{2.6}$$

where $\boldsymbol{\eta} = [\eta_1, ..., \eta_n]^T \in \mathbb{R}^n$ are the new *modal* coordinates and $\boldsymbol{\Phi} = [\boldsymbol{\phi}_1, ..., \boldsymbol{\phi}_n] \in \mathbb{R}^{n\times n}$ collects the VMs by columns.

Plugging Eq. (2.6) into (2.1) and pre-multiplying by $\boldsymbol{\Phi}^T$ one obtains

$$\boldsymbol{\Phi}^T\mathbf{M}^F\boldsymbol{\Phi}\ddot{\boldsymbol{\eta}} + \boldsymbol{\Phi}^T\mathbf{C}^F\boldsymbol{\Phi}\dot{\boldsymbol{\eta}} + \boldsymbol{\Phi}^T\mathbf{K}^F\boldsymbol{\Phi}\boldsymbol{\eta} = \boldsymbol{\Phi}^T\mathbf{f}_{ext}(t), \tag{2.7}$$

or, compactly,

$$\mathbf{M}^F_\phi\ddot{\boldsymbol{\eta}} + \mathbf{C}^F_\phi\dot{\boldsymbol{\eta}} + \mathbf{K}^F_\phi\boldsymbol{\eta} = \mathbf{f}_{ext,\phi}(t). \tag{2.8}$$

Stemming from the aforementioned orthogonality properties of the VMs, we have that the mass and stiffness matrices are diagonal and (if the eigenmodes are mass-normalized) write

$$\mathbf{M}^F_\phi = \mathrm{diag}(1, \ \dots \ , 1), \tag{2.9a}$$
$$\mathbf{K}^F_\phi = \mathrm{diag}(\omega_1^2, \dots, \omega_n^2), \tag{2.9b}$$

If no damping is present or if Rayleigh damping is considered (where we have $\mathbf{C}^F = \alpha\mathbf{M}^F + \beta\mathbf{K}^F$), then the n equations of the system are *fully decoupled*:

$$\ddot{\eta}_j + 2\xi_j\omega_j\dot{\eta}_j + \omega_j^2\eta_j = f_{ext,j}(t). \tag{2.10}$$

where the dimensionless damping coefficient is $\xi_j = (\alpha\omega_j + \beta/\omega_j)/2$ if Rayleigh damping is considered, and where $f_{ext,j}(t) = \boldsymbol{\phi}_j^T\mathbf{f}_{ext}(t)$.

Equation (2.8) is however still of dimension n, so the only gain in this case would be the diagonalization of the system. Incidentally, we notice that, although theoretically possible, on the one hand the computation of the full set of eigenfrequencies and eigenvectors of a high-dimensional system could be very expensive, on the other hand suffers from numerical issues which lead to very inaccurate or even wrong results.

2.1.1 Modal Displacement Method

The most common approach to construct a ROM out of Eqs. (2.7)-(2.8) is to select only a subset of VMs in $\boldsymbol{\Phi}$. This approach goes under the name of Modal Displacement Method (MDM), which basically consists in including only the VMs which are expected to effectively participate in the response. Consider an external load given by the summation of different contributions as

$$\mathbf{f}_{ext}(f) = \mathbf{P}_1 g_1(t) + \mathbf{P}_2 g_2(t) + ... + \mathbf{P}_P g_P(t) = \mathbf{P}\mathbf{g}(t), \tag{2.11}$$

where $\mathbf{P}_p$ (with $p \in [1, P]$) are the spatial distributions of the loads and $g_p(t)$ are the associated time-varying functions describing the evolution of the loads. The idea is then to assume that the response $\mathbf{u}(t)$ can be well-represented by

$$\mathbf{u}(t) \approx \sum_{k\in\mathcal{I}} \Phi_k\boldsymbol{\eta}_k(t) = \boldsymbol{\Phi}_\mathcal{I}\boldsymbol{\eta}_\mathcal{I}(t), \tag{2.12}$$

where $\mathcal{I}$ is a set of indexes of m_ϕ selected VMs (e.g. $\mathcal{I} = [1, 2, 7]$, so that $\boldsymbol{\Phi}_\mathcal{I} = [\boldsymbol{\Phi}_1, \boldsymbol{\Phi}_2, \boldsymbol{\Phi}_7]$ and $\boldsymbol{\eta}_\mathcal{I} = [\eta_1, \eta_2, \eta_7]$) whose eigenfrequencies fall into (or reasonably close to) the frequency range given by $\mathbf{g}(t)$'s spectra and which reconstruct the

spatial distribution of the load $\mathbf{P}$ (see Dickens et al., 1997 for more details on the residual error associated to this issue).

The reduced system then writes

$$\boldsymbol{\Phi}_J^T \mathbf{M}^F \boldsymbol{\Phi}_J \ddot{\boldsymbol{\eta}}_J + \boldsymbol{\Phi}_J^T \mathbf{C}^F \boldsymbol{\Phi}_J \dot{\boldsymbol{\eta}}_J + \boldsymbol{\Phi}_J^T \mathbf{K}^F \boldsymbol{\Phi}_J \boldsymbol{\eta}_J = \boldsymbol{\Phi}_J^T \mathbf{f}_{ext}(t), \tag{2.13a}$$

$$\mathbf{M}_{\phi_J} \ddot{\boldsymbol{\eta}}_J + \mathbf{C}_{\phi_J} \dot{\boldsymbol{\eta}}_J + \mathbf{K}_{\phi_J} \boldsymbol{\eta}_J = \mathbf{f}_{ext,\phi_J}(t), \tag{2.13b}$$

and, being of dimension $m_\phi \ll n$, is extremely fast to solve. In the MOR framework, the rectangular matrix $\boldsymbol{\Phi}_J$ is called *Reduced Order Basis* (ROB) and $\boldsymbol{\eta}_J$ is the *reduced coordinates* vector.

2.1.2 Mode Acceleration Correction

The MDM assumes that the reduced space spanned by the ROB $\boldsymbol{\Phi}_J$ is able to reproduce the whole frequency content of the load. Typically, however, the truncation given in Eq. (2.12) becomes simply

$$\mathbf{u}(t) \approx \sum_{k=1}^{m_\phi} \Phi_k \eta_k(t) = \boldsymbol{\Phi}_m \boldsymbol{\eta}_m(t), \tag{2.14}$$

so that all the modes which are left out would contribute to the quasi-static response. To take this into account, the Mode Acceleration Correction (MAC) can be used.

Let us rewrite the equations of motion as

$$\mathbf{u}^F = (\mathbf{K}^F)^{-1}(\mathbf{f}_{ext} - \mathbf{M}^F \ddot{\mathbf{u}}^F), \tag{2.15}$$

and, under the assumption that *accelerations* are well represented by the modal truncation (as higher frequency modes are assumed to behave quasi-statically),

$$\mathbf{u}^F = (\mathbf{K}^F)^{-1} \left(\mathbf{f}_{ext} - \sum_{k=1}^{m_\phi} \mathbf{M}^F \boldsymbol{\Phi}_k \ddot{\eta}_k \right), \tag{2.16}$$

where, from Eq. (2.10) and considering damping negligible,

$$\ddot{\eta}_k = f_{ext,k} - \omega_k^2 \eta_k = \boldsymbol{\Phi}_k^T \mathbf{f}_{ext} - \omega_k^2 \eta_k. \tag{2.17}$$

Finally, we obtain[2]

$$\mathbf{u}^F = \sum_{k=1}^{m_\phi} \boldsymbol{\Phi}_k \eta_k + \underbrace{\left((\mathbf{K}^F)^{-1} - \sum_{k=1}^{m_\phi} \frac{\boldsymbol{\Phi}_k \boldsymbol{\Phi}_k^T}{\omega_k^2} \right) \mathbf{f}_{ext}}_{\text{corrective term}}. \tag{2.18}$$

The last term is thus correcting *a posteriori* the modal solution with the static contribution that is not already accounted for by the first m_ϕ modes. More details on the derivation can be found in Géradin and Rixen, 2014 (see Chapters 2.4 and 2.8.2).

2.1.3 Example: cantilever beam

MDM and MAC are just two methods out of many others that can be found in literature, which account for the static contributions in different ways and/or take into account even other effects (e.g. rigid body modes, when these are allowed). Another possible and effortless way to take into account the static contribution is to append to the ROB of VMs also the actual static deformation, computed as

$$\mathbf{u}_s = \mathbf{K}^{-1} \mathbf{f}_{ext}, \tag{2.19}$$

so that the basis $\mathbf{V}$ becomes

$$\mathbf{V} = [\mathbf{u}_s, \boldsymbol{\Phi}_1, ..., \boldsymbol{\Phi}_m]. \tag{2.20}$$

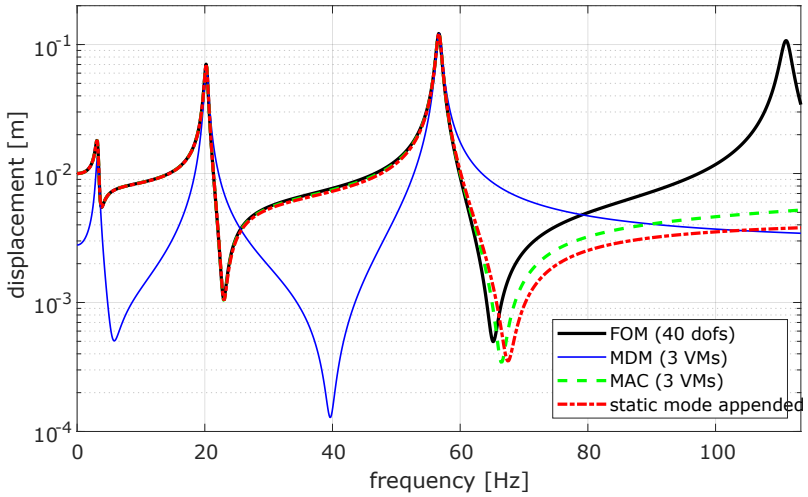

Figure 3: Frequency Response of the tip of a cantilever beam with enforced vertical base motion.

In figure 3 the full and reduced frequency responses for a cantilever beam excited enforcing the vertical motion of the base are shown. The beam is meshed with 20 Euler-Bernoulli beam elements (each of length $l_e = 0.2$ m), with elastic modulus $E = 70$ GPa, density $\rho = 2800\,\mathrm{kg/m^3}$, and square section of side $a = 10$ mm.

As it can be observed, the MDM accurately captures the response in the neighbourhood of the resonances of the modes included in the basis, but fails to retrieve the correct solution elsewhere. The MAC and the static-mode augmented basis instead yield almost the same results, which are able to reconstruct the correct solution also in between the considered modes. As expected, all the methods fail to predict the fourth resonance, whose VM was not included in the ROB.

Finally, notice that the static-mode augmented basis adds a reduced coordinate to the system, whereas MAC adds the static contribution a posteriori without increasing the number of unknowns. However, the former method might be useful in the context of nonlinear MOR, where a correction based on mode superposition might not hold anymore.

2.2 GEOMETRICALLY NONLINEAR SYSTEMS

For large displacement around the equlibrium, Eq. (2.1) does not hold anymore. Instead, linear elastic forces must be replaced by a nonlinear function of the displacement as

$$\mathbf{M}^F\ddot{\mathbf{u}}^F + \mathbf{C}^F\dot{\mathbf{u}}^F + \mathbf{f}_{int}(\mathbf{u}^F) = \mathbf{f}_{ext}(t), \tag{2.21}$$

where $\mathbf{f} : \mathbb{R}^n \to \mathbb{R}^n$ is the vector of internal nodal forces. Depending on the constitutive law of the material and the kinematic assumptions, $\mathbf{f}$ can assume different shapes. For instance, for linear elastic constitutive law and Green-Lagrange strain tensor, the nonlinear elastic forces are polynomials up to the third order, as shown in Chapter 1. The same is true for linear elastic materials and von-Karman kinematic models of beams and plates, which are valid for bending displacements in the order of the thickness. Other elements and kinematic descriptions may however lead to more complex formulations, e.g. for co-rotational elements, featuring trigonometric functions. Notice once more that the term $\mathbf{f}_{int}(\mathbf{u}^F)$ needs to be computed at *each* iteration of a numerical solution scheme (along with its jacobian matrix), whereas in

2 notice, again, that mass-normalized VMs are hereby considered.

linear analysis only $\mathbf{K}^F$ must be computed once and for all. As a consequence, it is already clear why reduction of nonlinear systems is highly desirable. On top of this, as it will be shown in the results of Chapter 4, many numerical tools to compute the frequency response of nonlinear systems can handle only a very low number of dofs (in the order of tens), and would fail otherwise. In such circumstances, resorting to a ROM is mandatory.

2.2.1 Galerkin projection

As for linear system, a possible way to approach reduction of nonlinear systems is to assume that its full response can be well approximated by the linear combination of a set of vectors (often generically called *modes*), that is

$$\mathbf{u}^F(t) \approx \mathbf{V}\boldsymbol{\eta}(t), \tag{2.22}$$

where $\mathbf{V} \in \mathbb{R}^{n\times m}$ is the ROB (containing, for the time being, unspecified modes) and where $\boldsymbol{\eta} \in \mathbb{R}^m$ is now the generic vector of reduced coordinates. Substituting this approximation in Eq. (2.21), we get

$$\mathbf{M}^F\mathbf{V}\ddot{\boldsymbol{\eta}}(t) + \mathbf{C}^F\mathbf{V}\dot{\boldsymbol{\eta}}(t) + \mathbf{f}_{int}(\mathbf{V}\boldsymbol{\eta}(t)) - \mathbf{f}_{ext}(t) = \mathbf{r}(t), \tag{2.23}$$

where $\mathbf{r}$ is the (unknown) residual arising from the approximation. The equation above can be premultiplied by a matrix $\mathbf{W}^T \in \mathbb{R}^{n\times m}$, so that a square system is obtained. This procedure goes by the name of Petrov-Galerkin projection. The *Galerkin projection* correspondes to the special case in which $\mathbf{W} = \mathbf{V}$, which entails

$$\mathbf{V}^T\mathbf{r} = 0, \tag{2.24}$$

as the residual lies in a subspace orthogonal to $\mathtt{colsp}(\mathbf{V})$.[3]

The equations of motion then write

$$\mathbf{M}_r\ddot{\boldsymbol{\eta}} + \mathbf{C}_r\dot{\boldsymbol{\eta}} + \mathbf{f}_{int,r} = \mathbf{f}_{ext,r}, \tag{2.25}$$

where

$$\mathbf{M}_r = \mathbf{V}^T\mathbf{M}\mathbf{V}, \quad \mathbf{C}_r = \mathbf{V}^T\mathbf{C}\mathbf{V}, \quad \mathbf{f}_{ext,r} = \mathbf{V}^T\mathbf{f}_{ext}, \tag{2.26}$$

and

$$\mathbf{f}_{int,r} = \mathbf{V}^T\mathbf{f}_{int}(\mathbf{V}\boldsymbol{\eta}). \tag{2.27}$$

The latter equation, although representing the reduced nonlinear elastic forces, needs to be evaluated over the full order model (as well as its jacobian matrix). For this reason, the simple Galerkin projection by itself cannot provide high speedups (in the author's experience, one can obtain at most a speedup factor of 2).

2.2.2 Projection-based NL-ROM requirements

The efficient construction of a Nonlinear (NL) ROM requires:

1. **a good choice of the reduction basis $\mathbf{V}$**, which
   - *spans the FOM solution subspace*, usually on the basis of the expected spectrum of the response with respect to the imposed excitation. While almost trivial in linear analysis thanks to the superposition principle, in nonlinear dynamics sub- and/or super-harmonics may arise, posing additional difficulties in the choice of the basis.

3 The space spanned by the columns of $\mathbf{V}$.

  - *(optional) can be efficiently computed.* In other words, it should be possible to compute the basis *a priori* and in a lower time than that required for a full order solution. This point may seem trivial, but many reduction strategies (e.g. the Proper Orthogonal Decomposition (POD) -based ones) rely upon the knowledge of the full solution. This is justified by the fact that the ROM obtained this way is very accurate and can be used for a multy-query analysis or to construct *parametric* reduced order models. Throughout the present work, the focus will be on the so called *model-driven* strategies, i.e. the ones which rely on some properties of the model (e.g. VMs) to construct the basis, which can be constructed without the need for a FOM solution.
  - *(desirable) is valid for different loading cases*, which is a given in linear modal analysis, but which is not granted for some nonlinear MOR methods (e.g. the ones based on the computation of static loads).

2. **an efficient way to compute the reduced internal forces $\mathbf{f}_{\mathtt{int},\mathtt{r}}$** (Eq. (2.27)). As mentioned earlier, if no measure is undertaken, the only way to evaluate $\mathbf{f}_\mathtt{r}$ would be by expanding the reduced coordinates $\boldsymbol{\eta}$ using the basis $\mathbf{V}$ to compute the FOM displacements $\mathbf{u}^\mathtt{F}$, then compute $\mathbf{f}(\mathbf{u}^\mathtt{F})$ at FOM-level, and finally project the result on the reduced space. This process is extremely expensive and almost extinguishes any gain provided by the Galerkin projection, reason why alternative strategies are sought.

3. (desirable) **a reliable error indicator**. Although an error of some kind can always be computed with or without the need of the FOM solution (e.g. the norm of the residual produced by the FOM *evaluated* at the ROM solution), to the best of the author knowledge there is no report in literature of non-POD based ROMs equipped with an *a priori and quantitative* error estimate. Worth of notice is the error analysis described in Nicolaidou et al., 2021 to predict the presence of internal resonances.

In the following an overview of some selected solutions to cope with items 1 and 2 is provided, whereas error indicators will be discussed separately in the following chapters along with the associated numerical studies.

2.2.3 Tentative ROM classification

Reduced order models are used in many fields of science and engineering. For this reason, ROM literature seldom features an uniform nomenclature and classification, much depending on the authors' background. In this section we spend just a few words to highlight what are the main characteristics and properties one should pay attention to when considering a ROM for nonlinear structural mechanics.

A first distinction can be done on the basis of how the ROM is obtained, between:

- *intrusive methods*, which need low-level manipulation of the code used to compute the solution, either for the construction of the basis and/or for the evaluation of the reduced forces. These methods often need access to the element-level formulation and/or the modification of the solvers and, for these reason, cannot be directly used in commercial software;

- *non-intrusive methods*, which can be applied directly using the outputs normally provided by commercial software.

Secondly, depending on how the ROM itself is constructed, we can distinguish between:

- *data-driven methods*, that is the ones which rely upon the presence of pre-existing data for the construction of the ROM. We include in this category

all the methods which use either experimental data or FOM-solutions (e.g. POD-based methods, see next).

- *model-driven (data-free) methods*, which, loosely speaking, are based on the knowledge of the model and its inherent characteristics (e.g. eigenmodes).

Notice that this distinction is sometimes blurred (one method could use both data and model information). In the present work, the focus is on methods that can be used by the structural analyst in a *design phase*, when no experimental data is available and where the cost associated to FOM solutions is usually not acceptable. That is, on model-driven methods.

Finally, it is important to underline that *projection-based methods*, which have been introduced in the previous sections and which are the object of the present dissertation, constitute only a subset of model order reduction methods, see for instance Cyril Touzé et al., 2021 for a review of nonlinear mapping methods.

2.2.4 Evaluation of nonlinear terms

Reduced order stiffness tensors

As already introduced in section 1.3, depending on the kinematic assumptions and on the material constitutive law, the (full order) internal elastic force vector can be expressed as polynomials[4] as

$$\mathbf{f}_{int}(\mathbf{u}^F) = {}_2\mathbf{K}^F\mathbf{u}^F + ({}_3\mathbf{K}^F \cdot \mathbf{u}^F)\cdot\mathbf{u}^F + (({}_4\mathbf{K}^F \cdot \mathbf{u}^F)\cdot\mathbf{u}^F)\cdot\mathbf{u}^F. \tag{2.28}$$

where ${}_2\mathbf{K}^F \in \mathbb{R}^{n\times n}$, ${}_3\mathbf{K}^F \in \mathbb{R}^{n\times n\times n}$ and ${}_4\mathbf{K}^F \in \mathbb{R}^{n\times n\times n\times n}$ are the second, third and fourth order FOM stiffness tensors, respectively. As already discussed, these tensors cannot be computed at FOM level for their excessive memory requirements. Using Galerkin projection, however, it is possible to directly compute the reduced order version of these stiffness tensors using element-level projection and assembly. Indeed, internal reduced forces in Eq. (2.27) can be computed as

$$\mathbf{f}_{int,r} = \sum_{e=1}^{N_e} (\mathbf{V}^e)^T \mathbf{f}^e_{int}(\mathbf{V}^e\boldsymbol{\eta}), \tag{2.29}$$

being $\mathbf{V} \in \mathbb{R}^{n\times m}$ the reduced basis, $\mathbf{V}^e \in \mathbb{R}^{n_e\times m}$ its restriction to the rows corresponding to the e-th nodal dofs and $\mathbf{f}^e_{int}$ the element internal elastic forces. The latter can be also expressed using tensors and applying Galerkin projection to Eq. (1.35) as

$$\begin{aligned}\mathbf{f}^e_{int,r} = {}&(\mathbf{V}^e)^T\,{}_2\mathbf{K}^e\mathbf{V}^e\boldsymbol{\eta} + (\mathbf{V}^e)^T({}_3\mathbf{K}^e\cdot(\mathbf{V}^e\boldsymbol{\eta}))\cdot(\mathbf{V}^e\boldsymbol{\eta})\\ &+ (\mathbf{V}^e)^T(({}_4\mathbf{K}^e\cdot(\mathbf{V}^e\boldsymbol{\eta}))\cdot(\mathbf{V}^e\boldsymbol{\eta}))\cdot(\mathbf{V}^e\boldsymbol{\eta}).\end{aligned} \tag{2.30}$$

which can conveniently expressed using Einstein summation as

$$\begin{aligned}(f^e_{int,r})_I = {}&V^e_{iI\,2}K^e_{ij}V^e_{jk}\eta_k + V^e_{iI\,3}K^e_{ijk}V^e_{jl}V^e_{km}\eta_l\eta_m\\ &+ V^e_{iI\,4}K^e_{ijkl}V^e_{jm}V^e_{kn}V^e_{lp}\eta_l\eta_m\eta_p,\end{aligned} \tag{2.31}$$

so that, following the same procedure described in section 1.3, we can write the element reduced stiffness tensors as

$${}_2Q^e_{IJ} = V^e_{iI\,2}K^e_{ij}V^e_{jk}, \tag{2.32a}$$

$${}_3Q^e_{IJK} = V^e_{iI\,3}K^e_{ijk}V^e_{jJ}V^e_{kK}, \tag{2.32b}$$

$${}_4Q^e_{IJKL} = V^e_{iI\,4}K^e_{ijkl}V^e_{jJ}V^e_{kK}V^e_{lL}, \tag{2.32c}$$

4 in section 1.3 the expressions for continuum total Lagrangian elements with linear elastic constitutive law were given.

where ${}_2\mathbf{Q}^e \in \mathbb{R}^{m\times m}$, ${}_3\mathbf{Q}^e \in \mathbb{R}^{m\times m\times m}$ and ${}_4\mathbf{Q}^e \in \mathbb{R}^{m\times m\times m\times m}$ are the element reduced order second, third and fourth order stiffness tensors, respectively. Then, as done in Eq. (2.29), the assembly procedure for the reduced model can be carried out just as a simple summation of the elemental contribution, i.e.

$$ {}_\star\mathbf{Q} = \sum_{e=1}^{N_e} {}_\star\mathbf{Q}^e, \tag{2.33} $$

with $\star = 2,3,4$. Following this procedure, one needs not to assemble the FOM tensors. Finally, the reduced internal forces write

$$ \mathbf{f}_{int,r}(\boldsymbol{\eta}) = {}_2\mathbf{Q}\boldsymbol{\eta} + ({}_3\mathbf{Q}\cdot\boldsymbol{\eta})\cdot\boldsymbol{\eta} + (({}_4\mathbf{Q}\cdot\boldsymbol{\eta})\cdot\boldsymbol{\eta})\cdot\boldsymbol{\eta}. \tag{2.34} $$

Using this representation, $\mathbf{f}_{int,r}(\boldsymbol{\eta})$ is expressed directly in the reduced space as a function of the reduced coordinates $\boldsymbol{\eta}$, and one can precompute *once and for all* the reduced stiffness tensor and perform simulations without switching back and forth from the reduced to the full space and back again, without the need for assembling procedures. Usually, the *online* speedups achieved through the tensorial approach are very high (usually > 100). However, the *offline* costs associated to the precomputation of the tensors cannot be neglected and lower the effective speedup provided by the ROM (see Ch. 3-4 for more details).

Notice that Eq. (2.34) is an *exact* representation of Eqs. (2.27)-(2.29) when the nonlinearity is a third order polynomial[5], stemming from the kinematic and material assumptions. In all the other cases, however, this is just an approximation which may come, for instance, from a Talyor expansion of a generic nonlinear function.

Sample code

Sample code to compute reduced order tensors (in MATLAB® , using again SNL tenors toolbox):

```
function compute_reduced_tensors(nodes, elements, connectivity, V)
    ne = size(elements, 2);
    Q3 = 0; % initialize
    Q4 = 0; % initialize
    for e = 1 : ne
        element_nodes = elements(ne, :);    % el-node IDs
        element_dofs = connectivity(e, :);  % el-dofs IDs
        xyz = nodes(element_nodes, :);      % el-coordinates
        [K3e, K4e] = compute_tensors(C, H, L, xyz, ne);
        % get the basis partition pertaining the eth-element
        Ve = tensor(V(element_dofs, :));
        Vt = permute(Ve,[2 1]);
        % project tensors
        Q3e = ttt(ttt(ttt(Vt, K3e, 2, 1), Ve, 3, 1), Ve, 2, 1);
        Q4e = ttt(ttt(ttt(ttt(Vt, K4e, 2, 1), Ve, 4, 1), Ve, 3, 1), Ve, 2, 1);
        Q3 = Q3 + Q3e;  % sum over element contributions
        Q4 = Q4 + Q4e;
    end
end
```

Hyper-reduction

Another possible approach to efficiently compute Eq. (2.27) is to *approximate* the reduced internal forces by evaluating them only at a few specific locations of the FOM mesh. The aim is to make so that the cost associated to the assembling solution

5 If the nonlinearity is given as a polynomial with order higher than 3, a tensorial representation can still be derived using tensors of order higher than 4.

scales with m rather than with n. For the sake of completeness, we report here in brief two popular methods, upon which many others were built. For a more comprehensive dissertation, the interested reader is referred to Jain, 2015.

The first method is the *Energy Conserving Sampling and Weighting* (ECSW), where the nonlinear terms are approximated by

$$\mathbf{f}_{int,r} = \sum_{e=1}^{N_e} (\mathbf{V}^e)^T \mathbf{f}^e_{int}(\mathbf{V}^e \boldsymbol{\eta}) \approx \sum_{e \in E} \xi_e (\mathbf{V}^e)^T \mathbf{f}^e_{int}(\mathbf{V}^e \boldsymbol{\eta}), \tag{2.35}$$

where $E \subset \{1, \dots, N_e\}$ lists a subset of elements, and where $\xi_i \in \mathbb{R}^+$ are positive weights. Equation (2.35) closely resembles a quadrature rule for the evaluation of integrals: internal forces are evaluated only on a (possibly small) set of elements and then opportunely weighted and summed. Both the set E and the weights ξ_e are determined matching the work done by the projected internal forces *on a training set coming from a FOM (time) simulation* through a minimization problem.

The second approach is the *Discrete Empirical Interpolation Method*, which aims at approximating the internal forces as the superposition of some force-modes as

$$\mathbf{f}_{int,r} \approx \mathbf{U}\mathbf{c}, \tag{2.36}$$

where $\mathbf{c} \in \mathbb{R}^{m \times m}$ are unknown factors and $\mathbf{U} \in \mathbb{R}^{n \times m}$ is a basis of force modes, obtained with a Singular Value Decomposition (SVD) of a *FOM-training set of forces in time* as

$$\mathbf{U}\boldsymbol{\Sigma}\mathbf{W}^T = \Big[\mathbf{f}_{int}(t_0),\, \mathbf{f}_{int}(t_0 + \Delta t),\, \dots,\, \mathbf{f}_{int}(t_0 + N_t \Delta t)\Big], \tag{2.37}$$

where Δt and N_t are the time step and the number of time steps in the training set, respectively. To find $\mathbf{c}$, a boolean matrix $\mathbf{P} \in \mathbb{R}^{n \times m}$ is introduced, with the function of "picking" rows out of $\mathbf{f}_{int}$, so that:

$$\mathbf{P}^T \mathbf{f}_{int} = \mathbf{P}^T \mathbf{U}\mathbf{c}, \tag{2.38}$$

and

$$\mathbf{c} = (\mathbf{P}^T\mathbf{U})^{-1} (\mathbf{P}^T \mathbf{f}_{int}). \tag{2.39}$$

The matrix $\mathbf{P}$ can be determined with a Greedy algorighm, see Chaturantabut and Sorensen, 2010 for more details. The reduced internal forces thus write

$$\mathbf{f}_{int,r} = \mathbf{V}^T\mathbf{U}(\mathbf{P}^T\mathbf{U})^{-1} \underbrace{(\mathbf{P}^T \mathbf{f}_{int})}_{\text{dofs subset}}. \tag{2.40}$$

Notice that the term highlighted in the above equation represent a subset of *degrees of freedom* of the FOM. Since to compute the single-dof force contribution requires the evaluation of $\mathbf{f}_{int}$ at all the elements sharing the node containing the selected dof, DEIM may ultimately lead to the selection of a larger set of elements than ECSW.

Both the presented strategies however rely upon a FOM simulation, which naturally imposes severe limitations to the applicability of the method both in terms of efficiency and versatility (i.e., the reduction is valid only for the trained set). Still, these methods find applicability in the context of linear and nonlinear parametric ROMs, first because they offer a way to approximate non-affine parameter dependencies to affine ones (Quarteroni et al., 2016), and secondly because the cost associated to the evaluation of the training sets over sampled points of the parameter space can be amortized by the repeated evaluations of the parametric ROM (Rafiq and Bazaz, 2020).

However, several alternative versions of DEIM and ECSW have been proposed in literature to overcome these limitations, see for instance Jain and Tiso, 2018 where a surrogate training set is proposed to replace the FOM solution and Ryckelynck, 2005, where an adaptive procedure is described.

2.3 REDUCTION BASIS

A crucial element for a projection-based ROM is, of course, the Reduced Order Basis (ROB) $\mathbf{V}$, which defines the reduced subspace where the approximated solution is sought. As anticipated, in the selection of a good basis is not trivial. Indeed, in nonlinear structural dynamics the basis should include vectors/modes

- which take into account effects arising due to the presence of large displacement (e.g. stretching-bending coupling in thin walled plates and beams);
- which can describe nonlinear dynamics phenomena (e.g. sub-/super-harmonics, internal resonances, isolated responses).

An extensive account of existing options available in literature is given in the next chapters, whereas the present section is devoted to a detailed review of Modal Derivatives (MDs), which will also be used in the developments of the following chapters.

2.3.1 Vibration Modes

Before introducing MDs, however, it might be helpful take a step back to VMs. Consider again the equations of motion (2.21) and asstume to select as ROM $\mathbf{V}$ the *full* set $\mathbf{\Phi} \in \mathbb{R}^{n\times n}$ of eigenmodes of the linear system, we obtain

$$\mathbf{\Phi}^T\mathbf{M}^F\mathbf{\Phi}\ddot{\boldsymbol{\eta}}(t) + \mathbf{\Phi}^T\mathbf{C}^F\mathbf{\Phi}\dot{\boldsymbol{\eta}}(t) + \mathbf{\Phi}^T\mathbf{f}_{int}(\mathbf{\Phi}\boldsymbol{\eta}(t)) - \mathbf{\Phi}^T\mathbf{f}_{ext}(t) = \mathbf{r}(t), \tag{2.41}$$

which is completely equivalent to the original system, since the columns of the basis $\mathbf{V}$ span the same space as the Euclidean basis[6]. Upon this consideration, one can think to select a reduced basis out of $\mathbf{\Phi}$, selecting only the modes which participate the most. Many methods in literature indeed are devoted to providing instruction, recipes and algorithms to select suitable VMs to construct the ROB. The selection however is generally challenging and often the proposed solutions are ad hoc and/or applicable to selected cases. In C. Touzé et al., 2014, for instance, the reduction of a plate system is considered and VMs are selected upon inspection, by making a distinction between membrane and bending dominated modes. An additional difficulty to be addressed is the fact that numerically computed high-frequency eigenmodes are not accurate, so that in practise the full set of eigenmodes is never available. In any case, even if $\mathbf{\Phi}$ were given, the inspection of n modes for system typically featuring hundreds of thousands dofs might be challenging. In the review paper Mignolet et al., 2013 some other solutions are reported, such as the adoption of the so-called *dual modes* (Ricardo Perez et al., 2014), obtained through nonliner static solves imposing VM-like loads, with the aim to capture the nonlinear transverse-membrane coupling of some dominant modes.

2.3.2 Modal Derivatives

Another solution to form the basis is to resort to *Modal Derivatives* (MDs), which, loosely speaking, are basis vectors automatically capturing the nonlinear complement contribution not provided by VMs. Historically, MDs were first proposed in Idelsohn and Cardona, 1985 as an extension of modal analysis. For this reason, the MD-approach features more or less the same advantages and disadvantages of linear VM-based reduction, as well as the spectrum-based construction criteria.

Let us start from the illustrative example of a beam clamped at both ends. The first 3 vibration modes about the rest configuration are reported in Fig. 4, where both axial and transverse displacements u and w, respectively, are shown on the

6 I.e. an identity matrix $\mathbf{I}_n \in \mathbb{R}^{n\times n}$.

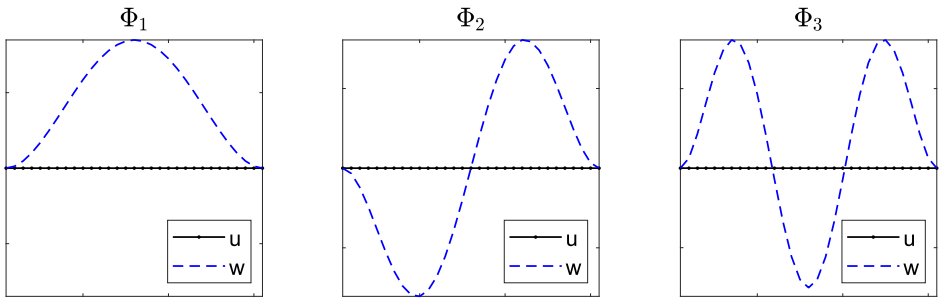

Figure 4: First three VMs of a clamp-clamp beam, with axial displacement u (represented on the vertical axis) in black and vertical displacement w dashed in blue. The horizontal axis is the x spatial coordinate. 30 von Karman beam elements were used.

vertical axis. As it can be noticed, these are pure bending modes and no displacement is present along the axial direction. If a ROM was constructed using only these VMs, for large displacement the system would be "uncapable" to stretch in the axial direction (as a pulled string would do): this would act as an additional constrain on the model, as if all the nodes were constrained with rollers in the x-direction. Such constrain would then activate for large displacements and increase the stiffness of the system, leading an extreme (and non-physical) hardening behaviour.

Figure 5 shows all the (static) MDs associated to the first 3 VMs, which are all *pure membrane modes*. In this toy example, with 87 dofs, it is possible to compute all the VMs and it turns out that the first 3 axial VMs are the 10th, 16th and 20th. These (but probably *not only* these) VMs modes should be included in the basis to represent the sought stretching behaviour.

In Fig. 6 a comparison of the frequency responses of the ROM obtained using the first 3 VMs only, the one with the addition of the first 12 membrane dominated modes, and the ROM with 6 static MDs appended. As it can be seen, the first two wrongly predict a much steeper hardening behaviour than that provided by the MD-approach, which accurately approximate the response of the FOM. From this example, it is apparent how the simple selection of axial modes to append to the basis is not as straightforward as one would think, hence the necessity of all the methods and criteria earlier discussed. In addition, the response for a ROM with 1 VM and the associated MD is reported, showing just a small loss of accuracy with respect to the one using 3 VMs.

MDs computation

One way to compute MDs is to differentiate the eigenvalue problem (2.4), obtaining

$$\left(\mathbf{K}^F\big|_0 - \omega_i^2\big|_0 \mathbf{M}^F\right) \frac{\partial \boldsymbol{\phi}_i}{\partial \eta_j}\bigg|_0 + \left(\frac{\partial \mathbf{K}^F}{\partial \eta_j}\bigg|_0 - \frac{\partial \omega_i^2}{\partial \eta_j}\bigg|_0 \mathbf{M}^F - \frac{\partial \mathbf{M}^F}{\partial \eta_j}\bigg|_0 \omega_i^2\big|_0\right) \boldsymbol{\phi}_i\big|_0 = 0, \quad (2.42)$$

where $(\star)\big|_0$ means "evaluated at equilibrium" (omitted hence on, to ease the notation, although we indicate the linear stiffness matrix as $\mathbf{K}_0^F = \mathbf{K}^F\big|_0$) and where

$$\theta_{ij} \triangleq \frac{\partial \boldsymbol{\phi}_i}{\partial \eta_j}, \quad (2.43)$$

is the Modal Derivative of the i-th VM $\boldsymbol{\phi}_i$ with respect to the modal amplitude of the j-th VM η_j. Intuitively, MDs thus represent a *sensitivity* of VMs with respect to modal amplitudes, and account for mild-large departures from the equilibrium position with respect to which they are computed.

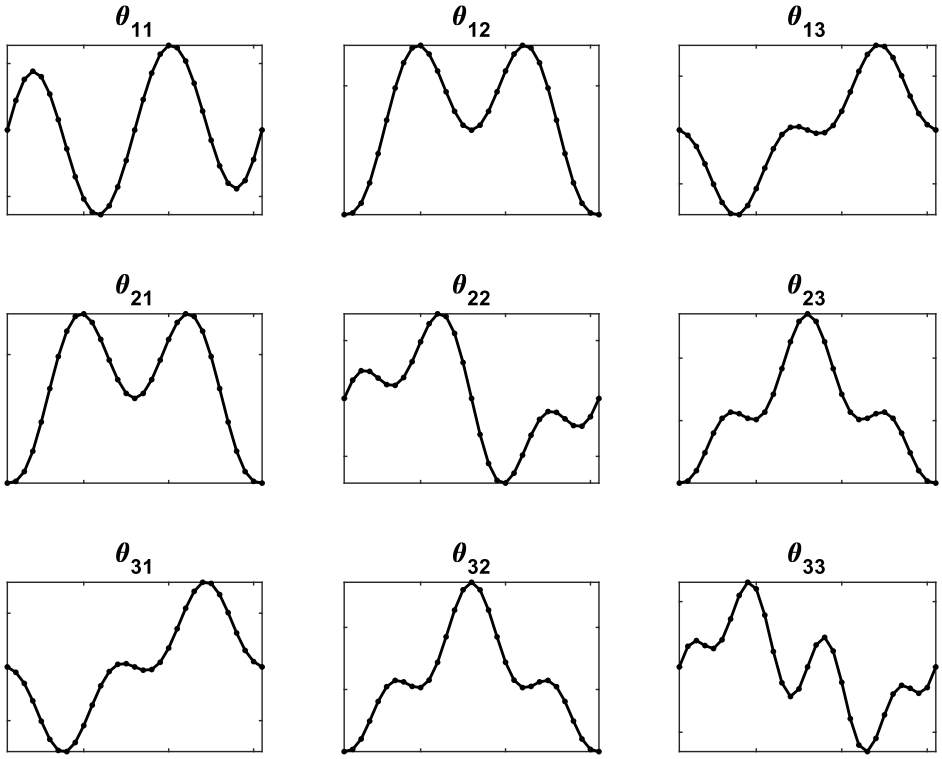

Figure 5: (Static) MDs of the clamp-clamp beam relative to the first 3 VMs (only the *axial* displacement u is reported on the vertical axis, in black). The horizontal axis is the x spatial coordinate. 30 von Karman beam elements were used.

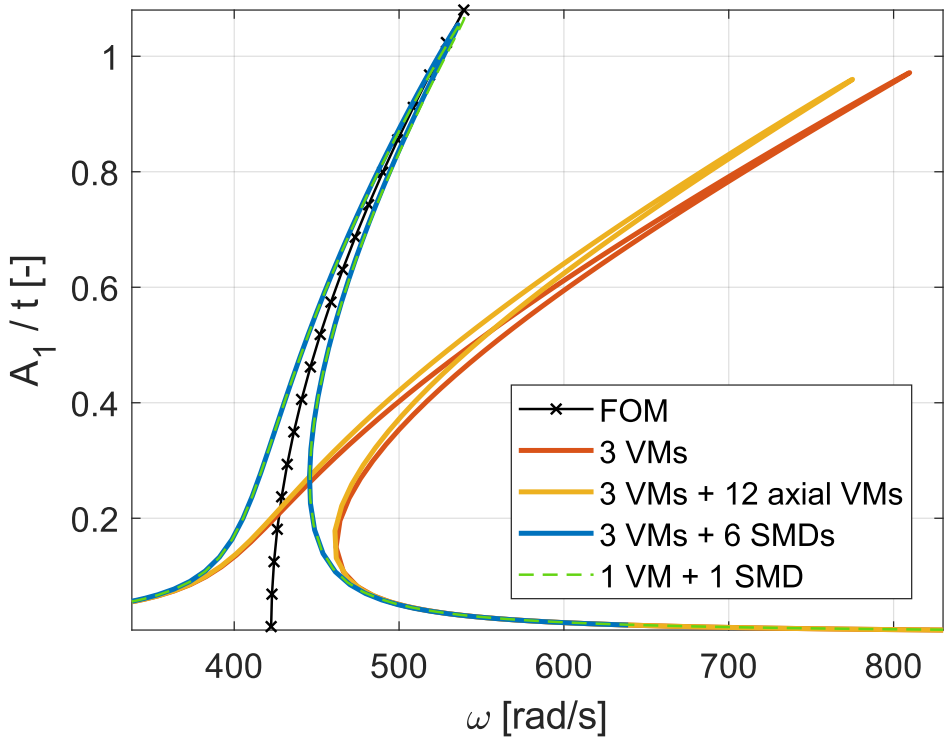

Figure 6: Frequency Responses (FR) for a clamped-clamped beam (the model used here is the one presented in Ch. 4.7, for $\xi = 0$). The FR are obtained using the Harmonic Balance method with 7 harmonics [Krack and Gross, 2019]. On the vertical axis, the amplitude of the first harmonic A_1 normalized over the beam thickness t is reported. For the FOM, only the backbone curve is shown.

The system in Eq. (2.42) is singular, with both θ_{ij} and $\partial\omega_i^2/\partial\eta_j$ unknown. As shown in Jain, Tiso, Rutzmoser, et al., 2017, the system can be made full rank by adding a normalization condition on the eigenmodes, that is

$$\boldsymbol{\phi}_i^T \mathbf{M}^F \boldsymbol{\phi}_j = 1, \tag{2.44}$$

differentiating which one obtains

$$\boldsymbol{\phi}_i^T \mathbf{M}^F \frac{\partial \boldsymbol{\phi}_i}{\partial \eta_j} = 0, \tag{2.45}$$

where the $\mathbf{M}^F$ is assumed to be a constant matrix. This way, Eq. (2.42) rewrites in matrix form as

$$\begin{bmatrix} (\mathbf{K}_0^F - \omega_i^2 \mathbf{M}^F) & -\mathbf{M}^F \boldsymbol{\phi}_i \\ -(\mathbf{M}^F \boldsymbol{\phi}_i)^T & 0 \end{bmatrix} \begin{Bmatrix} \frac{\partial \boldsymbol{\phi}_i}{\partial \eta_j} \\ \frac{\partial \omega_i^2}{\partial \eta_j} \end{Bmatrix} = \begin{Bmatrix} -\frac{\partial \mathbf{K}^F}{\partial \eta_j} \boldsymbol{\phi}_i \\ 0 \end{Bmatrix}, \tag{2.46}$$

Another solution is to compute the so called Static Modal Derivatives (SMDs) by neglecting all the inertial terms in Eq. (2.42) to obtain

$$\theta_{ij} = -(\mathbf{K}_0^F)^{-1} \frac{\partial \mathbf{K}^F}{\partial \eta_j} \boldsymbol{\phi}_i. \tag{2.47}$$

Apart from the fact that SMDs are cheaper to compute than MDs, they also feature the symmetry property by which $\theta_{ij} = \theta_{ji}$ (see also Fig. 5). The practical implication is that if one retains m_ϕ VMs in the basis, the associated MDs are $m_{MD} = m_\phi^2$, while SMD are only $m_{SMD} = m_\phi(m_\phi + 1)/2$. Worth of notice is the fact that the expression for SMD is also independently obtained by Weeger et al., 2016 expanding with a Taylor series a nonlinear static problem.

How to: stiffness matrix derivative

To compute the stiffness matrix derivative, one has first to switch from the linear stiffness matrix to the *tangent* stiffness matrix (which is configuration dependent) and evaluate it in the modal space, that is

$$\mathbf{K}_0^F \rightarrow \mathbf{K}^F(\mathbf{u} = \boldsymbol{\Phi}\boldsymbol{\eta}),$$

so that the derivative with respect to a modal coordinate η_j can be computed as

$$\frac{\partial \mathbf{K}^F(\mathbf{u})}{\partial \eta_j} = \frac{\partial \mathbf{K}^F(\boldsymbol{\Phi}\boldsymbol{\eta})}{\partial \eta_j} = \frac{\partial \mathbf{K}^F(\boldsymbol{\Phi}_j \eta_j)}{\partial \eta_j}. \tag{2.48}$$

As already discussed in Ch. 1, the tangent stiffness matrix is usually expressed as in Eqs. (1.30)-(1.31) as function of strains and stresses. In the case of continuum elements, we saw in Section 1.3 that we can write the expression of the internal forces directly as a function of the displacement only as (Eq. (1.34)):

$$\mathbf{f}_{int}^e = \int_{V_0^e} \mathbf{G}^T (\mathbf{H} + \mathbf{A}(\mathbf{G}\mathbf{u}^e))^T \mathbf{C} \left(\mathbf{H} + \frac{1}{2}\mathbf{A}(\mathbf{G}\mathbf{u}^e) \right) \mathbf{G}\mathbf{u}^e \, dV_0^e.$$

From this expression, the tangent stiffness matrix can be derived taking the virtual variation of the internal forces, which writes

$$\begin{aligned} \delta\mathbf{f}_{int}^e = &\int_{V_0^e} \mathbf{G}^T (\mathbf{H} + \mathbf{A})^T \mathbf{C} \left(\mathbf{H} + \frac{1}{2}\mathbf{A} \right) \mathbf{G}\delta\mathbf{u}^e \, dV_0^e \\ &+ \int_{V_0^e} \mathbf{G}^T \left(\frac{1}{2}\mathbf{H}^T \mathbf{C}\delta\mathbf{A} + \delta\mathbf{A}^T \mathbf{C}\mathbf{H} + \mathbf{A}^T \mathbf{C}\delta\mathbf{A} + \delta\mathbf{A}^T \mathbf{C}\mathbf{A} \right) \mathbf{G}\mathbf{u}^e \, dV_0^e, \end{aligned} \tag{2.49}$$

where the shorthand notation $\mathbf{A} = \mathbf{A}(\mathbf{G}\mathbf{u}^e)$ and $\delta\mathbf{A} = \mathbf{A}(\mathbf{G}\delta\mathbf{u}^e)$ was used. Since $\mathbf{A}(\mathbf{G}\mathbf{u}^e)\delta\mathbf{u}^e = \mathbf{A}(\mathbf{G}\delta\mathbf{u}^e)\mathbf{u}^e$, we can also rewrite the former equation as

$$\delta\mathbf{f}^e_{int} = \int_{V^e_o} \mathbf{G}^T \left[(\mathbf{H}+\mathbf{A})^T\mathbf{C}\left(\mathbf{H}+\frac{1}{2}\mathbf{A}\right) + \frac{1}{2}\mathbf{H}^T\mathbf{C}\mathbf{A} + \mathbf{A}^T\mathbf{C}\mathbf{A} \right] \mathbf{G}\delta\mathbf{u}^e \, dV^e_o + \int_{V^e_o} \mathbf{G}^T\delta\mathbf{A}^T\mathbf{C}\,(\mathbf{H}+\mathbf{A})\,\mathbf{G}\mathbf{u}^e \, dV^e_o = \mathbf{K}'\delta\mathbf{u}^e + \mathbf{K}''\delta\mathbf{u}^e. \quad (2.50)$$

From the latter equation one can find the tangent stiffness matrix cancelling out the displacement virtual variation, however first we have to find a more convenient form for $\mathbf{K}''$ due to the fact that $\delta\mathbf{u}^e$ is "inside" $\delta\mathbf{A}^T$. Let us switch to Einstein notation and, recalling Eq. (1.36), we can write

$$(\delta f^e_{int,2})_I = K''_{Ii}\delta u^e_i = G_{iI}L_{jik}G_{kl}\delta u^e_l C_{jm}(H_{mn}+A_{mn})G_{np}p_p, \quad (2.51)$$

so that the second contribution to the tangent stiffness matrix is

$$K''_{IJ} = G_{iI}L_{jik}G_{kJ}C_{jm}(H_{mn}+A_{mn})G_{np}p_p. \quad (2.52)$$

In matrix notation, the final tangent stiffness matrix writes:

$$\mathbf{K}^e(\mathbf{u}^e) = \int_{V^e_o} \mathbf{G}^T \left[\mathbf{H}^T\mathbf{C}\mathbf{H} + \mathbf{H}^T\mathbf{C}\mathbf{A} + \mathbf{A}^T\mathbf{C}\mathbf{H} + 2\mathbf{A}^T\mathbf{C}\mathbf{A} \right] \mathbf{G} \, dV^e_o + \int_{V^e_o} \mathbf{G}^T \left[(\mathbf{L}\cdot\mathbf{G}) \cdot_{11} (\mathbf{C}(\mathbf{H}+\mathbf{A})\mathbf{G}\mathbf{u}^e) \right] dV^e_o. \quad (2.53)$$

Once an expression of the tangent stiffness matrix as a function of the displacements is obtained, one should change to modal coordinates and then take the derivative. However, before substituting $\mathbf{u}^e = \mathbf{\Phi}^e\boldsymbol{\eta}$ in Eq. (2.53), it can be observed that

$$\frac{\partial(\mathbf{\Phi}\boldsymbol{\eta})}{\partial\eta_j} = \boldsymbol{\phi}_j,$$

and that the derivatives we are interested in are to be evaluated *at equilibrium*, that is for $\boldsymbol{\eta} = \mathbf{0}$. Upon these considerations, we can directly use instead $\mathbf{u}^e = \boldsymbol{\phi}^e_j\eta_j$, leading to

$$\mathbf{K}^e(\mathbf{u}^e) = \int_{V^e_o} \mathbf{G}^T \left[\mathbf{H}^T\mathbf{C}\mathbf{H} + \mathbf{H}^T\mathbf{C}\mathbf{A}_j\eta_j + \mathbf{A}_j^T\mathbf{C}\mathbf{H}\eta_j + 2\mathbf{A}_j^T\mathbf{C}\mathbf{A}_j\eta_j^2 \right] \mathbf{G} \, dV^e_o + \int_{V^e_o} \mathbf{G}^T \left[(\mathbf{L}\cdot\mathbf{G}) \cdot_{11} (\mathbf{C}(\mathbf{H}+\mathbf{A}_j\eta_j)\mathbf{G}\boldsymbol{\phi}^e_j\eta_j) \right] dV^e_o. \quad (2.54)$$

Finally, taking the derivative with respect to η_j and evaluating the result at equilibrium, we get to

$$\left.\frac{\partial\mathbf{K}^e}{\partial\eta_j}\right|_0 = \int_{V^e_o} \mathbf{G}^T \left\{ \left[\mathbf{H}^T\mathbf{C}\mathbf{A}_j + \mathbf{A}_j^T\mathbf{C}\mathbf{H} \right] \mathbf{G} + \left[(\mathbf{L}\cdot\mathbf{G}) \cdot_{11} (\mathbf{C}\mathbf{H}\mathbf{G}\boldsymbol{\phi}^e_j) \right] \right\} dV^e_o, \quad (2.55)$$

and the global stiffness derivative matrix can then be assembled from the element expression with the usual procedures. Finally, notice that the stiffness matrix derivative can also be computed in a *non-intrusive* way by using finite differences as

$$\frac{\partial\mathbf{K}^e}{\partial\eta_j} \approx \frac{\mathbf{K}^e(\boldsymbol{\phi}_j\Delta\eta_j) - \mathbf{K}^e_0}{\Delta\eta_j}, \quad (2.56)$$

which, however, suffers from the issue of how selecting $\Delta\eta_j$, that is small enough to have an accurate derivative but not too small in order not to incur into numerical artifacts.

Quadratic Manifold

Before concluding this section, we just give a quick overview of an alternative use of MDs. As mentioned earlier, Reduced Basis approaches are not the only possibility to construct a ROM and many other strategies relying upon nonlinear mappings are available in literature. The *Quadratic Manifold* (QM) is one of such techniques, where the solution is assumed to evolve on a low-dimension manifold rather than a low dimension subspace, that is

$$\mathbf{u}(t) \approx \boldsymbol{\Gamma}(\boldsymbol{\eta}(t)) \triangleq \boldsymbol{\Phi}\boldsymbol{\eta} + \frac{1}{2}\boldsymbol{\Omega} : (\boldsymbol{\eta} \otimes \boldsymbol{\eta}), \tag{2.57}$$

where $\boldsymbol{\Gamma} : \mathbb{R}^m \to \mathbb{R}^n$ is a nonlinear function of the reduced coordinates $\boldsymbol{\eta}$, which in this case are just the modal amplitudes of the VMs included in $\boldsymbol{\Phi}$. The MDs are included, by columns, in $\boldsymbol{\Omega} \in \mathbb{R}^{n\times m\times m}$ (i.e. $\theta_{ij} = \boldsymbol{\Omega}_{:,i,j}$) and are "enslaved" by the VMs modal amplitudes. This way, the number of unknowns is reduced to m, whereas in the classic *Linear Manifold* approach (where MDs are just appended to the basis, with independent reduced coordinates) the unknowns are m^2 (or $m(m+1)/2$ for SMDs). In the following, we will not use this approach; the interest reader is referred to Jain, 2015; Jain, Tiso, Rutzmoser, et al., 2017 and to Cyril Touzé et al., 2021 for a review.

2.4 AN APPLICATION: A MEMS GYROSCOPE

In this last section, we report the practical case of a nonlinear MEMS gyroscope whose analysis and design were carried out thanks to a ROM using MDs. In particular, it was possible to design the sensitivity of the sensor computing the nonlinear frequency response (magnitude and phase) and to design the control loop to drive the system. The work here presented can be found in Marconi, Bonaccorsi, et al., 2021.

ABSTRACT We describe how mechanical nonlinearities can be exploited to obtain a frequency-matched MEMS gyroscope. Exploiting the hardening behavior of the oscillator, we show how it is possible to match drive and sense frequency by changing the drive displacement amplitude. This way, both the resonance amplitudes of the drive and sense axes are exploited, boosting the sensitivity of the device. Moreover, the near-flat drive frequency response increases both the robustness and bandwidth. A prototype of a yaw gyroscope was also manufactured to test the feasibility of the proposed approach.

2.4.1 Introduction

MEMS gyroscopes have countless applications and can be found, for example, in a wide range of consumer products, military devices, automotive subsystems, and Internet of Things (IoT) gadgets. Focusing on consumer-grade MEMS gyroscopes typically found in everyday products, and given their constantly growing market, it is of extreme importance to produce them efficiently and in large numbers. However, batch fabrication often leads to manufacturing imperfections. Due to this technological spread, MEMS devices show performances that may be considerably different from the nominal design case. This can usually be observed, among other effects, in a considerable spread level of the drive and sense frequencies of the devices.

To cope with this issue, several strategies have been put into place; the most commonly adopted solution is the so-called split-mode operation Acar and Shkel, 2008, where drive and sense frequencies, f_d and f_s respectively, are designed to be separated by a certain mismatched defined as $\Delta f = f_s - f_d$ in order to operate in a frequency range where the sensitivity and the bandwidth of the sensor is reasonably constant. This solution, however, does not fully exploit the sense resonance peak, which would boost the sensitivity to an external angular rate input. Even though in frequency-matched Prikhodko et al., 2016 gyroscope $f_d = f_s$ is imposed and the sensitivity is maximized, this solution is less popular as (on top of bandwidth restriction) it requires more power and electronics in order to keep the frequencies matched by constantly adjusting the rotor voltage. On top of this, these systems are highly sensitive to temperature and environmental changes, as well as to stress and ageing effects Tatar et al., 2013.

In this work we propose an alternative approach that uses a mode-matched strategy in which the natural frequency of the drive axis is progressively changed by sweeping amplitude along the hardening backbone curve of the nonlinear frequency response. This is new with respect to the classical approach that relies on sense mode electrostatic softening. A similar approach was proposed in Schwarzelbach et al., 2001, albeit with some limitations. In that case, it was suggested to tune the frequencies by simply changing the drive voltage, which poses some concerns on the robustness of the approach. In the present work, the mode-matched control is obtained by means of a Phase-Locked Loop (PLL) and Amplitude Gain Control (AGC) Acar and Shkel, 2008; Chang et al., 2007 that guarantees the inertial device is constantly kept at resonance on the backbone curve. The sense frequency, which can be measured by means of quadrature and phase shift between the sense and drive axes, is then used to adjust the reference voltage for the AGC. This way the

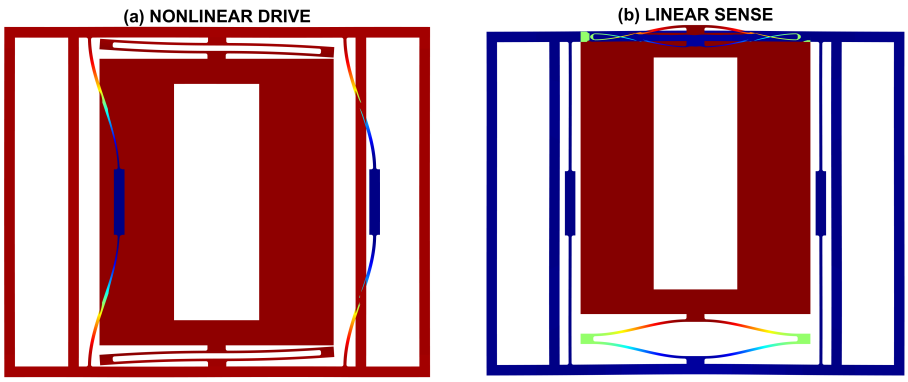

Figure 7: (a) Drive mode, (b) Sense mode. The FE model is meshed with 237,636 tetrahedral elements with quadratic shape functions (TET10), for a total of 1,216,029 DOFs. This is the same model used to construct the ROM.

drive and sense frequencies can be matched and, setting an acceptable sensitivity range for the sensor, one can derive the operative range of the device.

Finally, a non-linear MEMS gyroscope prototype was designed in collaboration with STMicroelectronics and tested to experimentally demonstrate the feasibility of our drive-based mode matching approach.

2.4.2 Nonlinear mechanical model

The vibration of tuning-fork MEMS gyroscopes oscillators Acar and Shkel, 2008 is typically obtained through a pair of driving electrodes to which is applied a sinusoidal or square signal Kempe, 2011 whose frequency matches the drive-mode resonance. This allows to precisely control the motion along the x-axis with little effort. Although MEMS gyroscopes are typically designed to work in a linear regime, geometric nonlinearities need to be taken into account as the oscillation amplitude gets larger. A common solution to release stresses and mitigate nonlinear effects is simply to avoid double-clamped beams and use folded beams. As in this case we want the drive axis to show a pronounced hardening effect, the drive frame was suspended using four double-clamped beams and the sense mass, inside the drive frame, by two folded beams. A Duffing oscillator model can be used to describe the drive axis, while the sense axis can be considered to behave linearly:

$$\begin{cases} m_d \ddot{x}_d + c_d \dot{x} + k_d x_d + k_{d,3} x_d^3 = F_d \\ m_s \ddot{x}_s + c_s \dot{x}_s + k_s x_s = F_{cor}(\Omega) \end{cases} \tag{2.58}$$

where for the sake of simplicity we omitted negligible gyroscopic terms and cross-coupling between axes. It is a known result Nayfeh and Mook, 1985 that the drive frequency depends on the oscillation amplitude as

$$\omega_d(x_d) = \sqrt{\omega_{0,d}^2 + \frac{3}{4}\frac{k_{d,3}}{m_d} x_d^2} \tag{2.59}$$

where $\omega_{0,d} = \sqrt{k_d/m_d}$ is the eigenfrequency associated with the linear system underlying the nonlinear model. Equation (2.59) describes the hardening effect we desire in order to tune and match the drive and sense frequencies.

The model given by Eqs. (2.58) can be difficult to tune, as there are no available expressions for the nonlinear coefficients of the beams. One solution is to resort to Finite Element (FE) simulation, performing a number of nonlinear-static traction tests on the drive axis in order to derive a force-displacement curve. From the latter,

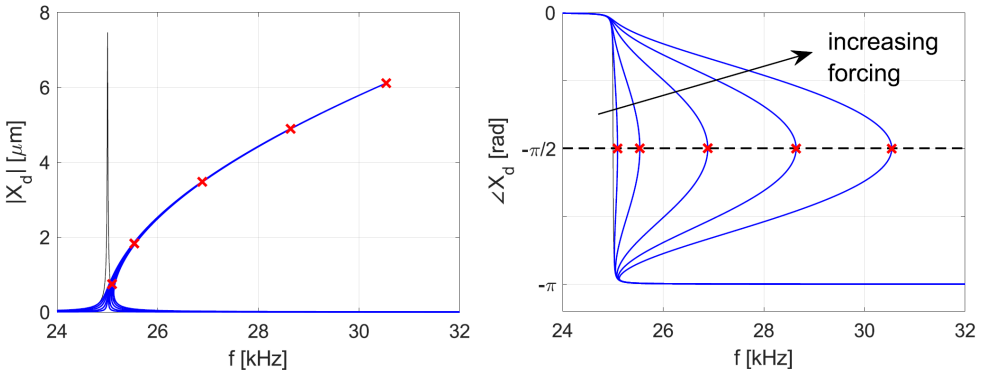

Figure 8: Drive amplitude response (top) and drive phase (bottom) for different forcing amplitudes (up to 12 dBm), computed using the Harmonic Balance method (with H=5 harmonics). The linear response is shown in black for comparison (12 dBm). The operation points are marked by red crosses, at the top of the amplitude responses and on the $-\pi/2$ line in the phase plot. A quality factor of 2200 has been considered.

the stiffness linear, quadratic and cubic coefficients can be computed. This approach can provide a quick and inexpensive way to obtain the model, but it is often too coarse to correctly capture the nonlinear dynamic response of the system. On top of that, the two-degree-of-freedom (DOFs) model in Eq. (2.58) cannot describe more complex nonlinear behaviours such as superharmonics, subharmonics and internal resonances, which may occur due to the interaction with higher frequency modes.

For this reasons, we resorted to a ROM with MDs and a tensorial approach for the fast evaluation of the internal reduced elastic forces. A reduction basis $\mathbf{V}$ composed of Vibration Modes (VMs, $\boldsymbol{\phi}_i$) and Modal Derivatives (MDs, θ_{ij}) was thus selected, the latter with the role of taking into account geometric nonlinearities. In particular, we retained only the first and second VMs (drive and sense, shown in Fig. 7) and their associated MDs, so that $\mathbf{V} = [\boldsymbol{\phi}_1, \boldsymbol{\phi}_2, \theta_{11}, \theta_{12}, \theta_{22}]$.

2.4.3 Frequency-matched nonlinear gyroscope

Frequency response

The founding principle of the operational mode we propose is that, along the backbone curve of the system, the phase of the response with respect to the forcing stays constant and equal to $-\pi/2$. Fig. 8 shows the forced response obtained using the ROM described in the former section and the NLvib MATLAB® package Krack and Gross, 2019; Marconi, Tiso, Quadrelli, et al., 2021 to perform Harmonic Balance.

As it can be observed, increasing the driving force makes the drive mode move towards higher frequencies but, regardless of the amplitude, the system will stay at resonance, with a constant phase. The red crosses correspond to these points. It is clear now that, using a standard controller equipped with PLL and AGC, it is possible to track the nonlinear response changing the drive amplitude. Also, it is worthwhile noticing that the slope of the frequency response increases almost linearly with frequency in the range $\Delta f = 27.5 - 30.5\,\text{kHz}$. In this interval, the drive amplitude changes from 4 µm to 6 µm, meaning that in a range of approximately 3000 Hz the drive amplitude changes by only 2 µm.

Control scheme

As already discussed, using a PLL+AGC controller allows us to change the drive amplitude and frequency. This can be achieved just by setting a different reference voltage V_{ref} for the AGC. However, we need to build an outer control loop to

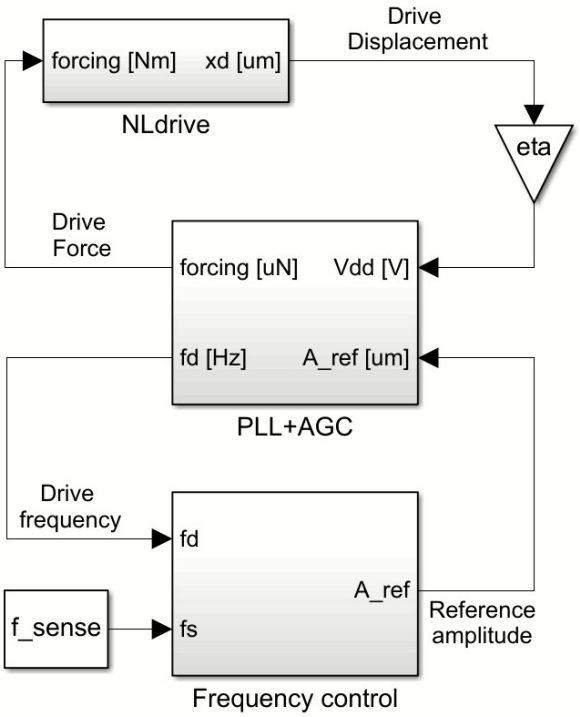

Figure 9: Control scheme, featuring the nonlinear drive system, the PLL+AGC controller and a frequency controller. The sense axis natural frequency is assumed to be known.

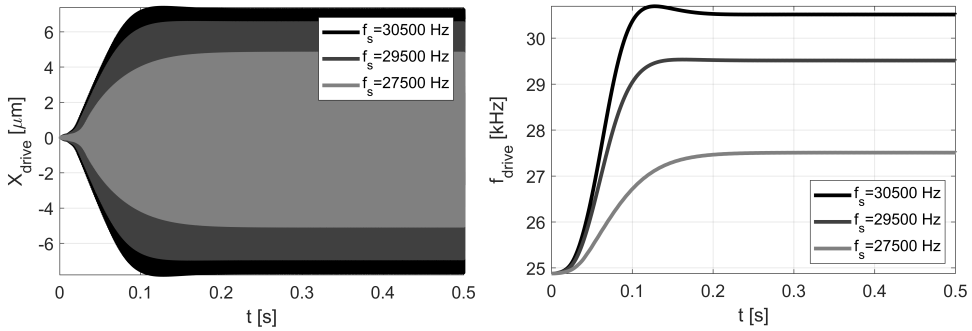

Figure 10: Responses for the controlled system assuming different sense frequencies. Top: drive amplitude. Bottom: drive frequency.

change V_{ref} so that the drive amplitude, starting from zero at ω_{0d}, increases following the backbone up to the sense frequency ω_s, ensuring thus frequency matching. As mentioned earlier in the introduction, a way to accomplish this is to extract ω_s reading the quadrature signal, but other strategies Sung et al., 2009 could be also adopted (e.g. using a phase detector for the sense signal).

For the purposes of this work, we simulated the controlled system in MATLAB® Simulink assuming the sense frequency as known. The control scheme is shown in Fig. 9. Starting from zero amplitude, the frequency controller changes the amplitude reference for the AGC+PLL block, which starts driving the system at the linear resonance. The amplitude reference is then progressively increased and so are the drive frequency and displacement. The results for $f_s = 27.5, 29.5, 30.5$ kHz are shown in Fig. 10, where the frequency controller is shown to behave correctly in this frequency range, although a finer tuning of the gains could improve performances.

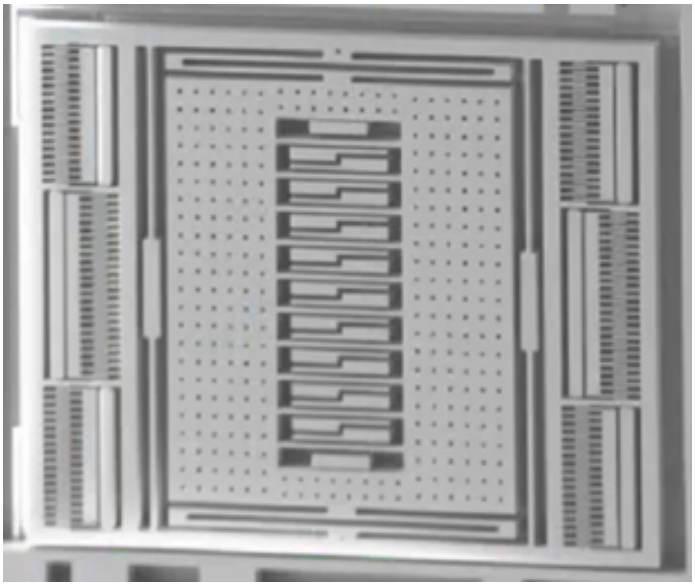

Figure 11: Scanning Electron Microscope (SEM) magnification of the non-linear MEMS gyroscope prototype (courtesy of STMicroelectronics).

2.4.4 Experimental results

Fig. 11 shows the SEM photo of the prototype, manufactured by STMicroelectronics. For the experimental validations, we performed both open-loop and closed-loop tests. In the open-loop configuration, the system has been forced with a forward frequency sweep (24–32 kHz, RBW=100 Hz, from -15 to 12 dBm) provided by an Agilent 4395A spectrum analyzer, which is also used for acquisition. Using the same setup, we measured the sense frequency $f_s = 27453$ Hz. The closed-loop tests have been carried out instead using an electronic board equipped with PLL and AGC, and measuring the drive actuation and drive detection voltages and frequency with a Tektronix TDS 2014 oscilloscope. The reference for the AGC has been manually increased from the power supply unit.

Fig. 12 shows the experimental results for the two tests, in terms of drive amplitude and frequency. As it can be observed, the maxima of the open-loop frequency responses (gray lines) occur approximately on the backbone (red line), described by the points obtained with the closed-loop tests. For the sake of completeness, in Fig. 13 the comparison between experimental and numerical data is shown.

2.4.5 Conclusions

We presented a new MEMS gyroscope concept, sense and drive frequencies are matched by sweeping the drive frequency along the backbone of the nonlinear system. The drive frequency, indeed, depends on the drive amplitude, which can be adjusted setting a different reference for the AGC. The forcing of the drive is always kept 90-degree phased with respect to the position of the drive itself, thanks to a PLL. Finally, an outer frequency controller changes the AGC reference, based on the error $\Delta f = f_s - f_d$. The device has been manufactured and some preliminary experimental tests have been showed, which so far have confirmed the numerical models. Several questions are still open and will need further studies, such as frequency stability with temperature, the effect of noise, the robustness against external disturbances, and the possible locking due to internal resonances.

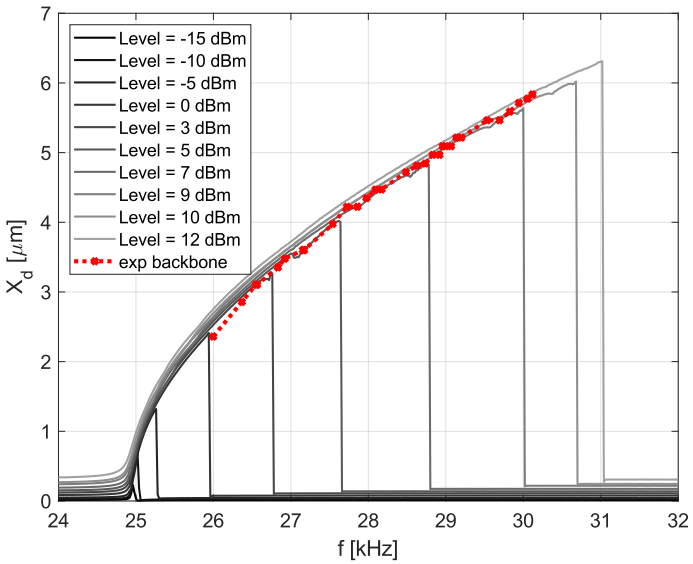

Figure 12: Experimental results: open-loop drive responses (gray, solid) for different excitation levels and closed-loop responses for different AGC reference voltages (red, dotted).

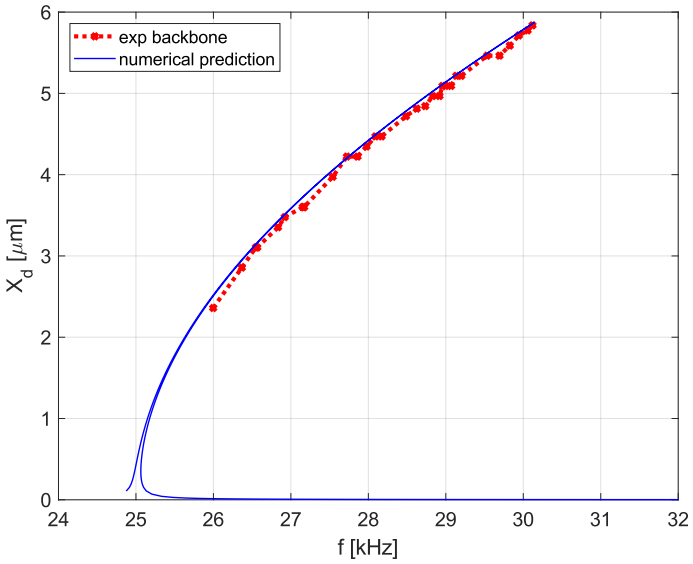

Figure 13: Comparison between experimental results (red) and numerical prediction (blue).

Acknowledgment

This research was carried out with the financial support of STMicroelectronics. The authors would also like to thank the AMS R&D team of STMicroelectronics for the support and Leonardo Gaffuri Pagani for designing the electronic control board.

3 A NL–PROM FOR SHAPE DEFECTS

The content of this chapter can be found in Marconi, Tiso, and Braghin, 2020; as such, it is a self-contained work which will briefly touch some of the contents already discussed (more in deep) in the previous chapters: we apologize for possible repetitions.

ABSTRACT We propose a formulation to derive a reduced order model for geometric nonlinearities which is shown to be valid for a set of parametrized defects. The latter are imposed in terms of the superposition of precomputed perturbations of the nominal structure's 3D-mesh, and parametrized by their amplitudes. A reduced order model is then built *once and for all* using these defect shapes and the *nominal model* information only. A suitable reduced order basis is introduced as well in order to effectively represent the influence of the defects on the dynamics of the structure. In contrast to many nonlinear parametric reduced order models, the one we propose does not need any previous training of the model in the parameter space. In this way, prohibitively expensive full order simulations can be avoided and offline times are greatly reduced. Numerical tests are performed on a MEMS resonator and a silicon micro-beam to study the effect of shape imperfections on the dynamic response of the system.

3.1 INTRODUCTION

The Finite Elements Method (FEM) is arguably one of the most popular analysis tool in a wide range of scientific and engineering fields. Nowadays many commercial software offer increasingly elaborate simulation packages which may even include multi-physics. Such programs usually come along with powerful Computer-Aided Design (CAD) environments which allow the representation of very complex systems, a crucial requirement in many disciplines. In mechanical engineering, very large FE models, counting several hundred thousands or even millions of degrees of freedom (dofs), are not rare. This fact leads to the necessity of Reduced Order Models (ROM) as a mean to alleviate computational burden and times.

Reduced Basis methods represent perhaps the most well-know and widespread way to come up with such ROMs. Loosely speaking, these approaches consist in selecting a suitable and reasonably small collection of vectors (the reduced basis) to approximate the full solution of the problem, of dimension N, with a M-dimensional reduced solution, where M is the number of basis vectors and $M \ll N$. From this point onward, to compute a ROM one could follow a number of techniques, which largely depend on the availability of data (e.g. results coming from previous simulations), on the accessibility to the (FE) model and solvers, on the specific problem under study and on the physics involved (e.g. mechanics, fluid dynamics, thermal analysis).

Historically, in structural mechanics, *modal analysis* Bathe, 2014 has always been the most popular reduction method for linear dynamic simulations, where Galerkin projection is used to reduce the high dimensional space of the full structural model (often referred to as High Fidelity Model, HFM) to a low-dimensional space spanned by the Vibration Modes (VMs, i.e. the eigenvectors of the linear system, also known as natural modes) included in the projection basis. Substructuring techniques are also widely exploited, where the model is divided in multiple subsystem which can

be independently reduced to be later assembled back together Allen et al., 2020; Craig and Bampton, 1968; Klerk et al., 2008; Rubin, 1975.

In the context of nonlinear dynamics, the problem of running large FE models is way more severe than in a linear environment. However, even if resorting to model order reduction is almost mandatory, rigorous tools to do so are still object of research today. For this reason, in last years a huge effort has been made to develop nonlinear ROMs for a number of applications, ranging from contacts Balajewicz et al., 2015; Géradin and Rixen, 2016, gears Blockmans et al., 2015, bolted junctions Pichler et al., 2017 and flexible multi-body dynamics Wu and Tiso, 2016; Wu, Tiso, Tatsis, et al., 2019 to geometric nonlinearities Kuether et al., 2015. The latter topic will be the focus of this work. In spite of the fact that no unique or widely accepted technique has been established over the others, literature is mature enough to offer the analyst an ample range of choices to cope with the main challenges of model order reduction, namely, the selection of a Reduced Order Basis (ROB) and of an efficient way to compute reduced nonlinear generalized forces. With reference to the latter problem, three main options are available. A first way to proceed is to directly compute all the (modal) coupling stiffness coefficients (quadratic and cubic terms), task that can be accomplished through *non-intrusive* methods (i.e. not relying on low-level FE formulations, e.g. ICE - *Implicit Condensation and Expansion* method, where coefficients are identified from a set of static analyzes Hollkamp and Gordon, 2008) or through *intrusive* methods (i.e. where FE formulation must be available for manipulation C. Touzé et al., 2014). Either ways, internal forces assume a polynomial form and can be directly evaluated, so that assembly of internal forces and tangent stiffness matrix is no longer required. A second option would be to resort to the so called *hyper-reduction* techniques, where the full internal force vector is obtained by computing forces on an extremely small set of elements only. This usually comes to the expense of relevant offline times, as the full solution is required to obtain the *training vectors* needed to identify the aforementioned set of elements. In a recent work Jain and Tiso, 2018, a method has been proposed to alleviate this problem by substituting this full nonlinear solution with a linear one, while in Ryckelynck, 2005 an adaptive *a priori* approach is described. Last but not least, in the case of linear elastic material constitutive law, one may recognize that explicitly writing internal forces in terms of displacements leads to a third order polynomial, whose coefficients can be pre-computed and stored in second, third and fourth order tensors. This (intrusive) *tensorial approach* is the one we will adopt in this work, and it is crucial for our method. As for the problem of the ROB selection, again, many choices are possible. An extension of the popular Rayleigh-Ritz approach is given in Noor and Peterst, 1980, while an extensive review of basis vectors can be found in Mignolet et al., 2013, where *dual modes*, a careful selection of VMs and Proper Orthogonal Decomposition (POD) are discussed. In Amabili, 2013, an ad hoc recipe is given to find a suitable VM basis in the case of a circular cylincrical shells, even in presence of moderate imperfections. Here, however, we will make use *Modal Derivatives* (MDs) Idelsohn and Cardona, 1985; Sombroek et al., 2018, since they feature a set of advantages which make them better fit to our purposes, as it will be detailed later in Section 3.4.

All of the methods discussed above usually refer to a model of a structure whose geometry is well defined without uncertainty, model that in the remainder we will address to as the *nominal model*. In some circumstances however, it may be relevant to assess how a structure behaves in presence of *shape defects*. This is the case for instance of MEMS devices, whose dynamic response is usually strongly affected by the presence of manufacturing defects Acar and Shkel, 2008; Farokhi et al., 2013. Stochastic analysis is therefore often required to assess performances, and a Monte Carlo approach, where simulations are repeated for each and every set of randomly generated parameters, is usually the way to go. In terms of FE, a shape defect can be modeled by changing the nominal geometry and remeshing, or directly applying a transformation to the nodal coordinates of the nominal mesh. After the new mesh

is obtained, matrices can be built and simulations performed. This procedure, with its variants, is already expensive for linear FE analysis, and for nonlinear analysis is simply inconceivable.

Two possible strategies can be used to address this problem. The first would be to resort to the family of the so called *reanalysis techniques*, which basically consist in exploiting a full, known response of a nominal structure to compute an approximate solution for the same structure with some kind of modification in geometry, mechanical properties or applied loads. Combined Approximations (CA) and Virtual Distortion Method (VDM) are two popular methods out of many available in literature Kołakowski et al., 2008. To the authors' knowledge however, though these methods usually address *material nonlinearity* both for statics and dynamics Kirsch et al., 2006, when it comes to *geometric nonlinearities* they address static problems only Kirsch, 2003; Zeoli et al., 2005, usually by alleviating the computational effort during Newton-Raphson equilibrium iterations.

The second option is to resort to to *parametric ROMs* (PROM). Again, as for ROMs, theory is well developed for linear analysis. Moment-matching is a popular strategy, where basically the (n-th) derivatives of the system equations with respect to the parameters (n-th moments) between the full and reduced models are required to match Daniel et al., 2004; Fröhlich et al., 2018; van Ophem et al., 2019. An extensive survey of existing (projection-based) methods for parametric reduced order models is given in Benner et al., 2015, covering the issues of a proper selection of the ROB (e.g. mode-matching, POD), of the very construction of the model (e.g. global and local bases, basis/subspace/model interpolation) and of a correct sampling of the parameter space.

Parametric model order reduction for nonlinear problems is instead a field still in constant evolution, but which already displays a wide number of solutions. Most of these methods are again ROB based. However, while in many circumstances one can construct a ROB for nonlinear non-parametric ROMs and/or linear parametric ROMs just by exploiting information about the model, nonlinear PROMs usually rely upon a number of HFM simulations (or experimental data, if available) for the construction of the reduced model itself Balajewicz et al., 2015; Benner et al., 2015. Due to the way they are obtained, these two groups of ROMs are sometimes referred to as "model-driven" (or "data-free") and "data-driven", respectively. Hybrid solution are also possible, of course. Then, nonlinear PROMs are (mostly) data-driven methods. The first step usually consists in sampling the parameter space at some locations (selected randomly, via greedy search algorithm, Latin Hypercube, Smolyak sparse grid, to name a few). The HFM solutions corresponding to these set of parameters are computed in a second phase. Following, a ROB is obtained performing a POD. This latter indeed features some nice properties, such as optimality of the (spatial) reduction basis and error bound. One can then use the basis obtained in this way directly Balajewicz et al., 2015 or use interpolation approaches between the available (trained) full solutions and/or bases in the parameter space to compute a new response for a new (untrained) parameter. Interpolation approaches are also used to approximate the nonlinear reduced terms Hesthaven and Ubbiali, 2018; Xiao, Fang, Buchan, et al., 2015; Xiao, Fang, Pain, et al., 2017. Interpolation on Grassman manifold via tangent spaces is another popular option Oulghelou and Allery, 2018; Zimmermann, 2019, and data-regression techniques are also available. In Le Guennec et al., 2018 for instance, the CUR method was expanded to handle parametric dependence by building multidimensional interpolation functions for car crash simulations. At multiple stages, however, this method requires the expert's judgment and a good knowledge of the system under study (this is however justified, if not even desirable, in an industrial context).

While in X. Q. Wang, O'Hara, et al., 2018; X. Q. Wang, Phlipot, et al., 2018 ROM were sought to describe *localized* defects, the present work aim is to develop a nonlinear ROM to represent *shape defects* "parametrically", though this word assumes here a slightly different meaning than in the context depicted above. Rather than

having a parameter describing a property or a physical dimension of the structure (e.g. density, length, width), here the parameter will define the amplitude of a shape representing the defect. More precisely, the defect will be given by the *linear superposition of precomputed shapes*, whose amplitudes are regulated by a parameter vector. Such defect shapes can be of any kind, as long as compatible with the boundary conditions of the nominal geometry. The final ROM, in tensorial form, will then be a function of the parameter vector, and will be able to describe any (small enough) variation of the system from the nominal geometry. Thus, to study a different defected configuration, remeshing will not be required anymore, as the defects will be embedded in the ROM formulation itself. To obtain such a model, an alternative expression for strains is required. This formulation was used by Budianksy to investigate post-buckling behavior of imperfect structures in Koiter analysis Budiansky, 1967; Koiter, 1981. Basically, it relies on the treatment of defects as additional fictitious displacements. The technique proved successful in a number of other works, as for instance in deriving the natural frequencies of imperfect beams and shells Jansen, 2008; Wedel-Heinen, 1991 or to develop a ROM for buckling in presence of imperfections Tiso, 2006.

To summarize, the model-driven method we propose aims to provide a fast and versatile tool to aid the design phase of structures subject to known shape defects. Even if many domain mappings are available in literature to parametrize a geometry (see for instance Lassila and Rozza, 2010, where free form deformations (FFD) are used), these shape defects are introduced in the strain formulation in order to be able to treat them as they were displacements. With respect to most methods already available in literature, which rely upon the sampling of the parameter space through multiple and highly expensive full simulations, this PROM requires only the nominal geometry of the structure and a set of user-defined shapes representing the defects. Without the need for training, offline costs to compute the model are therefore heavily cut down, while online computations are extremely fast thanks to the explicit (tensorial) expression of the nonlinear internal forces. Moreover, in contrast to data-based methods that usually are valid only for a particular loading case (unless the load itself is included as a parameter to train), the obtained ROM can be run for an arbitrary number of different load cases (within the frequency validity range). Of course, the aforementioned benefits come at the expenses of *intrusiveness* and with the restrictions of small defects and of geometrical nonlinearities, whereas data-driven solutions have wider applicability. Moreover, it should also be mentioned that the presented model does not exhaustively address all the problems that may arise in connection to the presence of defects. In particular, residual or locked-in stresses are not taken into account in the present formulation.

The work is organized as follows: *Section* 3.2 will describe the procedure by which the defects are introduced in the nominal model as *fictitious* displacements, leading to a new form of the internal forces, without the need of reconstructing the full model for the structure afflicted by the imperfections. In *Section* 3.3 the new internal forces are explicitly written in a tensorial fashion (and directly in reduced form), featuring additional terms which depend on the selected set of defect-shapes. *Section* 3.4 will discuss suitable ROBs for the model at hand and will introduce a new kind of reduction shapes, representing defect-sensitivities, to enrich the projection basis. Nomenclature and procedures for the following numerical studies are introduced in *Section* 3.5. In *Section* 3.6 the model is validated on a test structure, representing a MEMS resonator, over a range of selected relevant defects, while in *Section* 3.7 a shallow arch is presented as a second example. Finally, in *Section* 3.8 conclusions are drawn.

3.2 MODIFIED STRAIN FORMULATION

As already introduced in the previous section, the method we present here relies on the same procedure adopted by Budiansky in Budiansky, 1967. Its core assumption is to think of the defects as fictitious displacements to impose to the *nominal structure* (i.e. without defects). Strains associated to these defects produce non-physical stresses that need to be removed. We will make use of Budiansky's notation to better illustrate the concept.

Suppose that, under loading, a structure displaces by $\mathbf{u}$. Introducing the linear and quadratic functionals L_1 and L_2, the strain can be written as

$$\varepsilon(\mathbf{u}) = L_1(\mathbf{u}) + \frac{1}{2}L_2(\mathbf{u}). \tag{3.1}$$

By considering a fictitious displacement $\mathbf{u}_d$ representing the defect, the total strain, as described earlier, is given by

$$\begin{aligned} \varepsilon_{total} \approx \ \varepsilon' &= \varepsilon(\mathbf{u}+\mathbf{u}_d) - \varepsilon(\mathbf{u}_d) \\ &= L_1(\mathbf{u}+\mathbf{u}_d) + \frac{1}{2}L_2(\mathbf{u}+\mathbf{u}_d) - L_1(\mathbf{u}_d) - \frac{1}{2}L_2(\mathbf{u}_d) \\ &= L_1(\mathbf{u}) + \frac{1}{2}L_2(\mathbf{u}) + L_{11}(\mathbf{u},\mathbf{u}_d), \end{aligned} \tag{3.2}$$

where L_{11} is a bilinear functional operator defined as

$$L_2(\mathbf{u}+\mathbf{u}_d) = L_2(\mathbf{u}) + 2L_{11}(\mathbf{u},\mathbf{u}_d) + L_2(\mathbf{u}_d),$$

and where $\varepsilon(\mathbf{u}_d)$ is the strain due to defects only. From Eq. (3.2) it can be seen how an additional bilinear term in the strain expression appeared, depending on the defect. Corresponding internal forces will arise as well, allowing the parametrization of the model, as it will be later shown in Section 3.3.

In the following, these arguments - until now reported only in general terms, are applied to the case of tri-dimensional continuum mechanics and finite element discretization.

3.2.1 Continuum formulation

Let us consider a material point of final coordinates $\mathbf{x} = \{x, y, z\}$ after deformation, defined as

$$\mathbf{x} = \mathbf{x}_0 + \mathbf{u} + \mathbf{u}_d, \tag{3.3}$$

being $\mathbf{x}_0 = \{x_0, y_0, z_0\}$ the initial coordinates, $\mathbf{u} = \{u, v, w\}$ the "real" displacement vector and $\mathbf{u}_d = \{u_d, v_d, w_d\}$ the vector of small fictitious displacements corresponding to the defect along the three directions.

According to continuum mechanics [Crisfield, 1991], we can define a strain measure considering the stretching of a line element undergoing the displacement $\mathbf{u}+\mathbf{u}_d$. Differentiating Eq. (3.3) we obtain

$$\mathbf{x} = \frac{\partial \mathbf{x}}{\partial \mathbf{x}_0}d\mathbf{x}_0 = \frac{\partial(\mathbf{x}_0+\mathbf{u}+\mathbf{u}_d)}{\partial \mathbf{x}_0}d\mathbf{x}_0 = (\mathbf{I}+\mathbf{D}+\mathbf{D}_d)d\mathbf{x}_0 = (\mathbf{F}+\mathbf{D}_d)d\mathbf{x}_0, \tag{3.4}$$

where $\mathbf{I}, \mathbf{D}, \mathbf{D}_d, \mathbf{F} \in \mathbb{R}^{3\times 3}$ are the identity matrix, the (real) displacement-derivative matrix, the fictitious displacement-derivative matrix and the deformation gradient respectively. The stretch then is given by

$$d\mathcal{S} = d\mathbf{x}^T d\mathbf{x} - d\mathbf{x}_0^T d\mathbf{x}_0. \tag{3.5}$$

In our case however, we have first to remove the stretch associated to the defect only. Defining

$$\mathbf{x}_d = \mathbf{x}_0 + \mathbf{u}_d\,, \tag{3.6}$$

and differentiating

$$d\mathbf{x}_d = \frac{\partial \mathbf{x}_d}{\partial \mathbf{x}_0} d\mathbf{x}_0 = \frac{\partial(\mathbf{x}_0 + \mathbf{u}_d)}{\partial \mathbf{x}_0} d\mathbf{x}_0 = (\mathbf{I} + \mathbf{D}_d) d\mathbf{x}_0, \tag{3.7}$$

we can define the stretch due to the defects only as

$$d\mathcal{S}_d = d\mathbf{x}_d^T d\mathbf{x}_d - d\mathbf{x}_0^T d\mathbf{x}_0, \tag{3.8}$$

so that the total stretch is obtained subtracting Eq. (3.8) from Eq. (3.5) as

$$\begin{aligned} d\mathcal{S}' &= d\mathbf{x}^T d\mathbf{x} - d\mathbf{x}_d^T d\mathbf{x}_d \\ &= \underbrace{d\mathbf{x}_0^T (\mathbf{F}^T \mathbf{F} - \mathbf{I}) d\mathbf{x}_0}_{\text{nominal structure}} + \underbrace{d\mathbf{x}_0^T (\mathbf{D}_d^T \mathbf{D} + \mathbf{D}^T \mathbf{D}_d) d\mathbf{x}_0}_{\text{mixed terms due to defects}} = 2(d\mathbf{x}_0^T \mathbf{E}_2 d\mathbf{x}_0), \end{aligned} \tag{3.9}$$

where the contributions coming from the nominal structure and from the defects have been highlighted and where $\mathbf{E}$ is a modified version of the Green-Lagrange strain (second order) tensor. In particular, we can write

$$\mathbf{E}_2 = \underbrace{\frac{1}{2}(\mathbf{D}^T + \mathbf{D})}_{\mathbf{E}_2^l} + \underbrace{\frac{1}{2}\mathbf{D}^T \mathbf{D}}_{\mathbf{E}_2^q} + \underbrace{\frac{1}{2}\mathbf{D}_d^T \mathbf{D} + \frac{1}{2}\mathbf{D}^T \mathbf{D}_d}_{\mathbf{E}_2^d}, \tag{3.10}$$

being $\mathbf{E}_2^{l,q,d}$ the linear, quadratic and (bilinear) defect-related strain tensors respectively. Notice how Eq. (3.10) has the same structure predicted by Eq. (3.2). Using Voigt notation[1], the strain components can be written as

$$\begin{aligned} \mathbf{E}_v = \mathbf{E}_v^l + \mathbf{E}_v^q + \mathbf{E}_v^d = \begin{Bmatrix} \varepsilon_{xx} \\ \varepsilon_{yy} \\ \varepsilon_{zz} \\ \gamma_{xy} \\ \gamma_{xz} \\ \gamma_{yz} \end{Bmatrix} = \begin{Bmatrix} u_x \\ v_y \\ w_z \\ u_y + v_x \\ u_z + w_x \\ v_z + w_y \end{Bmatrix} + \begin{Bmatrix} \frac{1}{2}(u_x^2 + v_x^2 + w_x^2) \\ \frac{1}{2}(u_y^2 + v_y^2 + w_y^2) \\ \frac{1}{2}(u_z^2 + v_z^2 + w_z^2) \\ u_x u_y + v_x v_y + w_x w_y \\ u_x u_z + v_x v_z + w_x w_z \\ u_y u_z + v_y v_z + w_y w_z \end{Bmatrix} \\ + \begin{Bmatrix} u_x u_{d,x} + v_x v_{d,x} + w_x w_{d,x} \\ u_y u_{d,y} + v_y v_{d,y} + w_y w_{d,y} \\ u_z u_{d,z} + v_z v_{d,z} + w_z w_{d,z} \\ u_{d,x} u_y + u_x u_{d,y} + v_{d,x} v_y + v_x v_{d,y} + w_{d,x} w_y + w_x w_{d,y} \\ u_{d,x} u_z + u_x u_{d,z} + v_{d,x} v_z + v_x v_{d,z} + w_{d,x} w_z + w_x w_{d,z} \\ u_{d,y} u_z + u_y u_{d,z} + v_{d,y} v_z + v_y v_{d,z} + w_{d,y} w_z + w_y w_{d,z} \end{Bmatrix}, \end{aligned} \tag{3.11}$$

where $u_\star = \partial u / \partial \star_0$ and $u_{d,\star} = \partial u_d / \partial \star_0$ (with $\star = x, y, z$) are the displacement derivatives *with respect to the nominal initial configuration* (similar definitions for $v_\star$ $v_{d,\star}$ and $w_\star$ $w_{d,\star}$ hold).

The virtual work of internal forces can be written as

$$W_{int} = \int_{V_o} \mathbf{S}_v^T \delta \mathbf{E}_v dV_o = \int_{V_o} \mathbf{S} : \delta \mathbf{E}_2 dV_o, \tag{3.12}$$

being $\mathbf{S}_v^T = \{\sigma_{xx}, \sigma_{yy}, \sigma_{zz}, \tau_{xy}, \tau_{xy}, \tau_{yz}\}$ the Piola-Kirchhoff stress vector and $\mathbf{S}$ the corresponding tensor, the symbol ":" denoting double contraction. The integration volume is denoted by V_o. The virtual strain change is:

$$\delta \mathbf{E}_2 = \frac{1}{2}\mathbf{F}^T \delta \mathbf{D} + \frac{1}{2}\delta \mathbf{D}^T \mathbf{F} + \underbrace{\frac{1}{2}\delta \mathbf{D}^T \delta \mathbf{D}}_{\text{h.o.t.}} + \frac{1}{2}\mathbf{D}_d^T \delta \mathbf{D} + \frac{1}{2}\delta \mathbf{D}^T \mathbf{D}_d, \tag{3.13}$$

where higher order terms can be neglected for infinitesimal virtual displacements and where $\delta \mathbf{D}_d = \mathbf{0}$, being the defect given.

1 We will use subscript v to denote Voigt notation

In principle, since we are operating in a Lagrangian environment and we are defining all quantities with respect to the *nominal* configuration, the external work should be modified through push-forward/pull-back operations, depending if one defined the forces in the nominal or in the deformed configurations respectively. This way, the changes induced by the defects on locations, areas and/or volumes onto which the external forces are applied would be correctly addressed. In the present work though, assuming that the change between the two configurations is small, these aspects are neglected.

3.2.2 Finite Element Formulation

Let us consider now a structure discretized using 3D-continuum elements and having n_n nodes per element. We define the *displacement derivative vector* and the defect derivative vector $\theta, \theta_d \in \mathbb{R}^9$ as

$$\theta = \{u_x \ u_y \ u_z \ v_x \ v_y \ v_z \ w_x \ w_y \ w_z\}^T = \mathbf{G}\mathbf{u}^e, \tag{3.14}$$

$$\theta_d = \{u_{d,x} \ u_{d,y} \ u_{d,z} \ v_{d,x} \ v_{d,y} \ v_{d,z} \ w_{d,x} \ w_{d,y} \ w_{d,z}\}^T = \mathbf{G}\mathbf{u}_d^e, \tag{3.15}$$

respectively, where $\mathbf{u}^e \in \mathbb{R}^{3n_n}$ is the nodal displacement vector of one element, $\mathbf{u}_d^e \in \mathbb{R}^{3n_n}$ is the nodal defect-displacement vector, and $\mathbf{G}$ is a matrix collecting the shape function derivatives with respect to physical coordinates. Recalling Eq. (3.11), we can define the strain vector as

$$\begin{aligned} \mathbf{E}_v = \mathbf{E}_v^l + \mathbf{E}_v^q + \mathbf{E}_v^d &= \mathbf{H}\theta + \frac{1}{2}\mathbf{A}(\theta)\theta + \mathbf{A}(\theta)\theta_d \\ &= \left(\mathbf{H} + \frac{1}{2}\mathbf{A}(\theta) + \mathbf{A}(\theta_d)\right)\theta, \end{aligned} \tag{3.16}$$

where $\mathbf{H}$ and $\mathbf{A}(\theta)$ were defined in Chapter 1. Notice that in Eq. (3.16) the property $\mathbf{A}(\theta)\theta_d = \mathbf{A}(\theta_d)\theta$ was exploited. For more details, the reader is referred to literature [Crisfield, 1991].

From Eq. (3.16), virtual strain variation writes

$$\delta\mathbf{E}_v = (\mathbf{H} + \mathbf{A}(\theta) + \mathbf{A}(\theta_d))\mathbf{G}\delta\mathbf{u}^e = \mathbf{B}\delta\mathbf{u}^e, \tag{3.17}$$

where $\mathbf{B}$ is the strain-displacement matrix and, again, $\delta\theta_d = 0$. Recalling Eq. (3.12), the internal virtual work over the element's volume V_o^e writes

$$W_{int} = (\delta\mathbf{u}^e)^T \int_{V_o^e} \mathbf{B}^T\mathbf{S}_v dV_o^e = \delta\mathbf{p}^T\mathbf{f}_{int} \tag{3.18}$$

while the internal force vector is given by

$$\mathbf{f}_{int} = \int_{V_o^e} \mathbf{B}^T\mathbf{S}_v dV_o^e = \int_{V_o^e} \mathbf{B}^T\mathbf{C}\mathbf{E}_v dV_o^e, \tag{3.19}$$

where Hook's law $\mathbf{S}_v = \mathbf{C}\mathbf{E}_v$ has been introduced, being $\mathbf{C}$ the elastic constitutive matrix. From here on, one can take again the variation of internal forces and write an expression for the tangent stiffness matrix, which will include some additional terms generated by the defect.

3.3 TENSORIAL APPROACH

In this section we derive the (element-level) tensors required to explicitly write the internal forces (and consequently the tangent stiffness matrix). Following Eq. (3.19), writing each term explicitly yields

$$\mathbf{f}_{int} = \int_{V_o^e} \mathbf{G}^T \left(\mathbf{H} + \mathbf{A} + \mathbf{A}_d\right)^T \mathbf{C} \left(\mathbf{H} + \frac{1}{2}\mathbf{A} + \mathbf{A}_d\right) \mathbf{u}^e \, dV_o^e, \tag{3.20}$$

where $\mathbf{A}_d = \mathbf{A}(\theta_d)$. Equation (3.20) can be split into the following contributions

$$\mathbf{f}^{(n,1)} = \mathbf{G}^T(\mathbf{H}^T\mathbf{C}\mathbf{H})\mathbf{G}\mathbf{u}^e = {}_2\mathbf{K}\mathbf{u}^e, \tag{3.21a}$$

$$\mathbf{f}^{(n,2)} = \mathbf{G}^T\left(\frac{1}{2}\mathbf{H}^T\mathbf{C}\mathbf{A} + \mathbf{A}^T\mathbf{C}\mathbf{H}\right)\mathbf{G}\mathbf{u}^e, \tag{3.21b}$$

$$\mathbf{f}^{(n,3)} = \frac{1}{2}\mathbf{G}^T(\mathbf{A}^T\mathbf{C}\mathbf{A})\mathbf{G}\mathbf{u}^e, \tag{3.21c}$$

$$\mathbf{f}^{(d,2)} = \mathbf{G}^T(\mathbf{H}^T\mathbf{C}\mathbf{A}_d + \mathbf{A}_d^T\mathbf{C}\mathbf{H})\mathbf{G}\mathbf{u}^e, \tag{3.21d}$$

$$\mathbf{f}^{(d,3)} = \mathbf{G}^T\left(\mathbf{A}^T\mathbf{C}\mathbf{A}_d + \frac{1}{2}\mathbf{A}_d^T\mathbf{C}\mathbf{A}\right)\mathbf{G}\mathbf{u}^e + \mathbf{G}^T(\mathbf{A}_d^T\mathbf{C}\mathbf{A}_d)\mathbf{G}\mathbf{u}^e, \tag{3.21e}$$

where, for convenience, integration over volume is implicitly assumed and where the superscript $^{(\star,i)}$ denotes terms associated to the nominal structure only ($\star = n$) or to the structure with defects ($\star = d$) of order i in $\mathbf{u}^e$ and/or $\mathbf{u}_d^e$. The linear stiffness term is trivially given by ${}_2\mathbf{K}$.

It is at this point convenient to re-express matrix $\mathbf{A}$ ($\mathbf{A}_d$) as

$$\mathbf{A} = \mathbf{L}\cdot\theta = \mathbf{L}\cdot(\mathbf{G}\mathbf{u}^e), \tag{3.22}$$

being $\mathbf{L} \in \mathbb{R}^{6\times9\times9}$ a constant localization matrix, whose expression is given in Chapter 1.

Remark 1 (*notation*). In the following, we'll adopt the notation described in Jain, 2015, which is compatible with the MATLAB® *Tensor Toolbox* Bader, Kolda, et al., 2015 used in this work. In short, the notation $\mathbf{A}\cdot\mathbf{B}$ will always denote the contraction of the last dimension of $\mathbf{A}$ over the first dimension of $\mathbf{B}$. Where this is not the case, it will be explicitly indicated as $\mathbf{A}\cdot_{ij}\mathbf{B}$, meaning contraction of $\mathbf{A}$'s i^{th} dimension over $\mathbf{B}$'s j^{th} dimension. For matrices with more than two dimensions, transpose operation will be explicitly denoted as well. For instance, $\mathbf{A}^{T(i\leftrightarrow j)}$ means that dimension i is switched with dimension j. When Einstein's notation is used, we assume summation over the (repeated) *lowercase* indexes, while *uppercase* indexes are not to be summed over (e.g. $C_{IJ} = A_{Ii}B_{iJ}$).

3.3.1 Quadratic terms

Being the expression of the linear terms of equation (3.20) trivial, we start here by directly considering the quadratic ones. Upon a closer inspection of Equations (3.21)b-d, an underlying common structure can be recognized. For this reason, it will be sufficient to study the term

$$\mathbf{G}^T(\mathbf{H}^T\mathbf{C}\mathbf{A})\mathbf{G}\mathbf{u}^e \quad \rightarrow \quad (G^TH^TC)_{Ii}(L_{ijk}G_{kl}u_l^e)G_{jm}u_m^e = f_I, \tag{3.23}$$

By defining the element third-order tensor ${}_3\hat{\mathbf{K}}$ as[2]

$${}_3\hat{K}_{Ilm}u_l^e u_m^e = f_I, \tag{3.24}$$

we get to

$${}_3\hat{K}_{IJK} = (G^TH^TC)_{Ii}(L_{ijk}G_{kJ})G_{jK}, \tag{3.25a}$$

$${}_3\hat{\mathbf{K}} = (\mathbf{G}^T\mathbf{H}^T\mathbf{C})\cdot(\mathbf{L}\cdot\mathbf{G})\cdot_{21}\mathbf{G}. \tag{3.25b}$$

Notice that ${}_3\hat{K}_{ijk} = {}_3\hat{K}_{ikj}$. Finally, using ${}_3\hat{\mathbf{K}}$, we can define

$${}_3\mathbf{K} = \frac{1}{2}{}_3\hat{\mathbf{K}} + {}_3\hat{\mathbf{K}}^{T(1\leftrightarrow3)}, \tag{3.26}$$

$${}_{3d}\mathbf{K} = {}_3\hat{\mathbf{K}} + {}_3\hat{\mathbf{K}}^{T(1\leftrightarrow3)}. \tag{3.27}$$

2 To avoid confusion with indexes, subscripts denoting tensors' names will be put on the left side. Moreover, as full order tensors will never be used, we drop the superscript e for the tensors.

Recalling Eqs (3.21)b-d, it can be easily shown that the following expression hold

$$\mathbf{f}^{(n,2)} = ({}_3\mathbf{K}\cdot\mathbf{u}^e)\mathbf{u}^e, \tag{3.28a}$$

$$\mathbf{f}^{(d,2)} = ({}_{3d}\mathbf{K}\cdot\mathbf{u}^e)\mathbf{u}^e_d. \tag{3.28b}$$

Notice that all the computations here have been done only considering the terms in $\mathbf{u}^e$, but we would have obtained the same results even by using $\mathbf{A}_d$ instead of $\mathbf{A}$ in Eq. (3.23).

3.3.2 Cubic terms

As previously done for quadratic terms, even for cubic forces a core term can be isolated:

$$\begin{aligned} f_I &= {}_4\hat{K}_{Ilqr}u^{e,I}_l u^{e,II}_q u^e_r \\ &= G^T_{Ii}(L_{ijk}G_{kl}u^{e,I}_l)^{T(1\leftrightarrow 2)}C_{jm}(L_{mnp}G_{pq}u^{e,II}_q)G_{nr}u^e_r, \end{aligned} \tag{3.29}$$

which defines:

$${}_4\hat{K}_{IJKL} = G^T_{Ii}(L_{ijk}G_{kJ})^{T(1\leftrightarrow 2)}C_{jm}(L_{mnp}G_{pK})G_{nL}, \tag{3.30a}$$

$${}_4\hat{\mathbf{K}} = \mathbf{G}^T(\mathbf{L}\cdot\mathbf{G})^{T(1\leftrightarrow 2)}\cdot_{21}\mathbf{C}\cdot(\mathbf{L}\cdot\mathbf{G})\cdot_{21}\mathbf{G}. \tag{3.30b}$$

Notice that, according to this definition, internal forces are obtained following the sequence of products $(({}_4\hat{\mathbf{K}}\cdot\mathbf{p})\cdot\mathbf{u}^{e,II})\mathbf{u}^{e,I}$. Recalling Eqs. (3.21)c-e, opportunely choosing $\mathbf{u}^{e,I/II}$ as $\mathbf{u}^e$ or $\mathbf{u}^e_d$ as required and using ${}_4\hat{\mathbf{K}}$, the following fourth-order tensors are defined:

$${}_4\mathbf{K} = \frac{1}{2}{}_4\hat{\mathbf{K}}, \tag{3.31}$$

$${}_{4d}\mathbf{K} = {}_4\hat{\mathbf{K}}^{T(2\leftrightarrow 3)} + \frac{1}{2}{}_4\hat{\mathbf{K}}, \tag{3.32}$$

$${}_{4dd}\mathbf{K} = {}_4\hat{\mathbf{K}}. \tag{3.33}$$

Thus, as it can be easily verified, internal forces write

$$\mathbf{f}^{(n,3)} = (({}_4\mathbf{K}\cdot\mathbf{u}^e)\cdot\mathbf{u}^e)\mathbf{u}^e, \tag{3.34}$$

$$\mathbf{f}^{(d,3)} = (({}_{4d}\mathbf{K}\cdot\mathbf{u}^e)\cdot\mathbf{u}^e)\mathbf{u}^e_d + (({}_{4dd}\mathbf{K}\cdot\mathbf{u}^e)\cdot\mathbf{u}^e_d)\mathbf{u}^e_d. \tag{3.35}$$

Finally, notice again that the tensors obtained in this and in previous section are defined for a *single element*. In theory, these could be assembled as usual into the global stiffness tensors. However, this is impossible in practice due to memory limitations. For this reason, Galerkin projection is applied at element level during the assembly procedure so that the global reduced tensors are directly obtained.

3.3.3 Tensor reduction

As shown previously, the quadratic and cubic terms of the internal forces write

$$\begin{aligned} \mathbf{f}^{(2)} &= \mathbf{f}^{(n,2)} + \mathbf{f}^{(d,2)} \\ &= ({}_3\mathbf{K}\cdot\mathbf{u}^e)\mathbf{u}^e + ({}_{3d}\mathbf{K}\cdot\mathbf{u}^e)\mathbf{u}^e_d, \end{aligned} \tag{3.36a}$$

$$\begin{aligned} \mathbf{f}^{(3)} &= \mathbf{f}^{(n,3)} + \mathbf{f}^{(d,3)} \\ &= (({}_4\mathbf{K}\cdot\mathbf{u}^e)\cdot\mathbf{u}^e)\mathbf{u}^e + (({}_{4d}\mathbf{K}\cdot\mathbf{u}^e)\cdot\mathbf{u}^e)\mathbf{u}^e_d + (({}_{4dd}\mathbf{K}\cdot\mathbf{u}^e)\cdot\mathbf{u}^e_d)\mathbf{u}^e_d. \end{aligned} \tag{3.36b}$$

Assume now to have a suitable reduction basis $\mathbf{V}^e$ for $\mathbf{u}^e$ and assume $\mathbf{u}^e_d$ to be a linear combination of a number of predefined defect shapes, collected by columns in matrix $\mathbf{U}^e$. Then, we can write

$$\mathbf{u}^e \approx \mathbf{V}^e\boldsymbol{\eta}, \tag{3.37a}$$

$$\mathbf{u}^e_d = \mathbf{U}^e\boldsymbol{\xi}, \tag{3.37b}$$

where $\mathbf{V}^e \in \mathbb{R}^{n_e \times m}$, $\mathbf{U}^e \in \mathbb{R}^{n_e \times m_d}$, $\boldsymbol{\eta} \in \mathbb{R}^m$ is the reduced coordinates vector, and $\boldsymbol{\xi} \in \mathbb{R}^{m_d}$ is the vector of defect-shape amplitudes, being n_e, m, m_d the number of one element dofs, modes in the basis, and defect-shapes, respectively. Substituting equations (3.37) into (3.36), we can write the following reduced tensors, here written in tensor and Einstein notations:

$$
\begin{aligned}
{}_3\mathbf{Q} &= (((\mathbf{V}^e)^T \cdot {}_3\mathbf{K}) \cdot \mathbf{V}^e) \cdot_{21} \mathbf{V}^e \\
{}_{3d}\mathbf{Q} &= (((\mathbf{V}^e)^T \cdot {}_{3d}\mathbf{K}) \cdot \mathbf{V}^e) \cdot_{21} \mathbf{U}^e \\
{}_4\mathbf{Q} &= ((((\mathbf{V}^e)^T \cdot {}_4\mathbf{K}) \cdot \mathbf{V}^e) \cdot_{31} \mathbf{V}^e) \cdot_{21} \mathbf{V}^e \\
{}_{4d}\mathbf{Q} &= ((((\mathbf{V}^e)^T \cdot {}_{4d}\mathbf{K}) \cdot \mathbf{V}^e) \cdot_{31} \mathbf{V}^e) \cdot_{21} \mathbf{U}^e \\
{}_{4dd}\mathbf{Q} &= ((((\mathbf{V}^e)^T \cdot {}_{4dd}\mathbf{K}) \cdot \mathbf{V}^e) \cdot_{31} \mathbf{U}^e) \cdot_{21} \mathbf{U}^e
\end{aligned}
\tag{3.38}
$$

or

$$
\begin{aligned}
{}_3Q_{IJK} &= (V^e_{iI})\,{}_3K_{ijk}(V^e_{kJ}V^e_{jK}) \\
{}_{3d}Q_{IJK} &= (V^e_{iI})\,{}_{3d}K_{ijk}(V^e_{kJ}U^e_{jK}) \\
{}_4Q_{IJKL} &= (V^e_{iI})\,{}_4K_{ijkl}(V^e_{lJ}V^e_{kK}V^e_{jL}) \\
{}_{4d}Q_{IJKL} &= (V^e_{iI})\,{}_{4d}K_{ijkl}(V^e_{lJ}V^e_{kK}U^e_{jL}) \\
{}_{4dd}Q_{IJKL} &= (V^e_{iI})\,{}_{4dd}K_{ijkl}(V^e_{lJ}U^e_{kK}U^e_{jL})
\end{aligned}
$$

where ${}_3\mathbf{Q} \in \mathbb{R}^{m\times m\times m}$, ${}_{3d}\mathbf{Q} \in \mathbb{R}^{m\times m\times m_d}$, ${}_4\mathbf{Q} \in \mathbb{R}^{m\times m\times m\times m}$, ${}_{4d}\mathbf{Q} \in \mathbb{R}^{m\times m\times m\times m_d}$ and ${}_{4dd}\mathbf{Q} \in \mathbb{R}^{m\times m\times m_d\times m_d}$. The reduced internal force vectors for quadratic and cubic terms write

$$
\tilde{\mathbf{f}}^{(2)} = ({}_3\mathbf{Q}\cdot\boldsymbol{\eta})\boldsymbol{\eta} + ({}_{3d}\mathbf{Q}\cdot\boldsymbol{\xi})\boldsymbol{\eta}, \tag{3.39a}
$$

$$
\tilde{\mathbf{f}}^{(3)} = (({}_4\mathbf{Q}\cdot\boldsymbol{\eta})\cdot\boldsymbol{\eta})\boldsymbol{\eta} + (({}_{4d}\mathbf{Q}\cdot\boldsymbol{\xi})\cdot\boldsymbol{\eta})\boldsymbol{\eta} + (({}_{4dd}\mathbf{Q}\cdot\boldsymbol{\xi})\cdot\boldsymbol{\xi})\boldsymbol{\eta}. \tag{3.39b}
$$

Finally, notice that

i. once $\mathbf{V}$ and $\mathbf{U}$ are selected and tensors from Eqs. (3.38) are computed, defects can be toggled on/off and leveraged just by changing $\boldsymbol{\xi}$, the parameter-vector of defect shapes amplitudes

ii. the terms $({}_{3d}\mathbf{Q}\cdot\boldsymbol{\xi})$, $(({}_{4dd}\mathbf{Q}\cdot\boldsymbol{\xi})\cdot\boldsymbol{\xi})$ and $({}_{4d}\mathbf{Q}\cdot\boldsymbol{\xi})$ can be precomputed before each analysis and added to ${}_2\mathbf{Q}$ and ${}_3\mathbf{Q}$, respectively; thus, online computations will involve only three tensors rather than five.

iii. generally speaking, the formulae derived in this paragraph are valid either referred to the global structure or to the single element. As mentioned earlier though, projection should be carried out at element level ($\mathbf{V}^e$ is the element-partition of $\mathbf{V} \in \mathbb{R}^n$).

iv. the tensorial formulation arises from linear elastic constitutive law and Total Lagrangian formulation. Should other kinematic models (e.g. corotational) be adopted, the polynomial formulation should be retrieved (e.g. using Taylor expansion) before applying the presented method.

3.4 ENHANCED BASIS FOR DEFECTS

To compute the reduced tensors, one needs to specify first (a) the defect-shapes in $\mathbf{U}$ and (b) the reduced order basis (ROB) $\mathbf{V}$. The choice of the latter is critical, since the most expensive step of the present method corresponds to the offline computation of the tensors which, as already highlighted, can only be obtained directly in reduced form. An *a priori* selection of the ROB is then crucial, as most

(if not all) of the advantages provided by the present approach would be lost if one had to choose a new basis and compute the reduced tensors for every and each different choice of the parameter-vector $\boldsymbol{\xi}$.

As already mentioned in the introduction, the choice of a projection basis for a parametric model can be done as proposed by a number of different parametric model order reduction techniques (e.g. moment-matching, POD). However, the particular form of the internal forces (which follows from the strain formulation, Eq. (3.11)) allows for another option, that will be now discussed.

We first tested a ROB with vibration modes (VMs) and modal derivatives (MDs) in their static form Jain, Tiso, Rutzmoser, et al., 2017, computed on the *nominal structure*. We here briefly recall how to compute MDs with reference to continuum elements. MDs are defined as

$$\theta_{ij} \triangleq \frac{\partial \boldsymbol{\phi}_i}{\partial \eta_j} = -\mathbf{K}|_{eq}^{-1} \frac{\partial \mathbf{K}(\boldsymbol{\phi}_j \eta_j)}{\partial \eta_j}\bigg|_{eq} \boldsymbol{\phi}_i, \tag{3.40}$$

where $\boldsymbol{\phi}_j$ is the j-th vibration mode, η_j its modal amplitude and $\mathbf{K}$ is the tangent stiffness matrix. The tangent stiffness matrix evaluated for a displacement $\mathbf{u}^F = \boldsymbol{\phi}_j \eta_j$ writes (at element level):

$$\mathbf{K}^e = \frac{\partial \mathbf{f}^e}{\partial \mathbf{u}^e} = \int_{V_0} \mathbf{G}^T \left[\mathbf{H}^T \mathbf{C} \mathbf{H} + \mathbf{H}^T \mathbf{C} \mathbf{A}_\eta + 2\mathbf{A}_\eta^T \mathbf{C} \mathbf{H} + 3\mathbf{A}_\eta^T \mathbf{C} \mathbf{A}_\eta\right] \mathbf{G} \, dV_0, \tag{3.41}$$

where $\mathbf{A}_\eta = \mathbf{A}(\mathbf{G}\boldsymbol{\phi}_j^e \eta_j)$. Taking the derivative with respect to the modal coordinate η_j and evaluating the resulting expression at equilibrium (i.e. for $\eta_j = 0$) leads to

$$\frac{\partial \mathbf{K}^e(\boldsymbol{\phi}_j^e \eta_j)}{\partial \eta_j}\bigg|_{eq} = \int_{V_0} \mathbf{G}^T \left[\mathbf{H}^T \mathbf{C} \mathbf{A}_\phi + 2\mathbf{A}_\phi^T \mathbf{C} \mathbf{H}\right] \mathbf{G} \, dV_0, \tag{3.42}$$

where $\mathbf{A}_\phi = \mathbf{A}(\mathbf{G}\boldsymbol{\phi}_j^e)$. This last equation defines the derivative of the tangent stiffness matrix with respect to the j-th modal coordinate *at element level*, and can be assembled for the whole system following the usual FE procedures; then Eq. (3.40) can be evaluated.

With VMs and MDs only, however, the basis proves to be sufficient to represent a subclass of defects only. In particular it yields accurate results only when the defect-base $\mathbf{U}$ corresponds to a subset of VMs. The reason why this happens is likely to reside in the fact that MDs are included in the ROB, and MDs represent *de facto* modal sensitivities.

On the stream of these considerations, the idea is then to enrich the ROB adding *defect sensitivities* (DSs). A similar approach was used in Hay et al., 2010, where POD-modes sensitivities were added to the ROB to model the flow past a square cylinder, with the incidence angle as a geometric parameter. The method showed better accuracy with respect to other traditional POD-based approaches. DSs are obtained following the same procedure to compute MDs. Consider the eigenvalue problem evaluated at equilibrium (i.e. for $\mathbf{u}^F = \mathbf{0}$):

$$\left(\mathbf{K}|_{eq} - \omega_i^2 \mathbf{M}\right) \boldsymbol{\phi}_i = 0, \tag{3.43}$$

being ω_i and $\boldsymbol{\phi}_i \in \mathbb{R}^n$ the i-th eigenfrequency and eigenvector respectively. Moreover, recalling Eqs. (3.20), (3.21) and (3.36) the tangent stiffness matrix is a function of both displacements and defects. Taking the derivative of the eigenvalue problem with respect to the j-th amplitude parameter ξ_j and assuming $\xi_i = 0$ for $i \neq j$ (so that $\mathbf{u}_d = \mathbf{U}_j \xi_j$), we write

$$\left(\mathbf{K}|_{eq} - \omega_i^2|_{eq} \mathbf{M}\right) \frac{\partial \boldsymbol{\phi}_i}{\partial \xi_j}\bigg|_{eq} + \left(\frac{\partial \mathbf{K}}{\partial \xi_j}\bigg|_{eq} - \frac{\partial \omega_i^2}{\partial \xi_j}\bigg|_{eq} \mathbf{M}\right) \boldsymbol{\phi}_i|_{eq} = \mathbf{0}. \tag{3.44}$$

Notice that $\mathbf{M}$ is the mass matrix referred to the *nominal system*, and it is assumed not to vary significantly in presence of defects (its derivatives w.r.t. ξ_j are therefore

zero). Equation (3.44) cannot directly be solved for $\partial\boldsymbol{\phi}_i/\partial\xi_j$ since the coefficient matrix is singular by definition. Though workarounds can be found in literature, here we prefer to neglect mass terms as it's done for static MDs, allowing us to define DSs as

$$\boldsymbol{\Xi}_{ij} \triangleq \left.\frac{\partial\boldsymbol{\phi}_i}{\partial\xi_j}\right|_{eq} = -\mathbf{K}|_{eq}^{-1}\left.\frac{\partial\mathbf{K}}{\partial\xi_j}\right|_{eq}\boldsymbol{\phi}_i, \tag{3.45}$$

which represent the sensitivity of mode i with respect to defect j. In Eq. (3.45), $\mathbf{K} = \mathbf{K}(\mathbf{u}^F, \mathbf{u}_d^F)$ must be evaluated for $\mathbf{u}^F = \mathbf{0}$ (equilibrium) and $\mathbf{u}_d^F = \mathbf{U}_j\xi_j$, as well as its derivative $\partial\mathbf{K}/\partial\xi_j$. Strictly speaking, however, we have that the latter depends on ξ_j. This is not desirable, as it would make the ROB $\mathbf{V}$ depend on the parameter amplitude. We can make then the further assumption to take the stiffness matrix derivative around the nominal configuration, that is for $\xi_j = 0$. This way we have, for the single element,

$$\begin{aligned}\left.\frac{\partial\mathbf{K}^e}{\partial\xi_j}\right|_{eq} &= \frac{\partial\mathbf{K}^e(\mathbf{u}^e = \mathbf{0}, \mathbf{u}_d^e = \mathbf{U}_j^e\xi_j)}{\partial\xi_j} \\ &= \mathbf{G}^T\left(\mathbf{H}^T\mathbf{C}\mathbf{A}_d + \mathbf{A}_d^T\mathbf{C}\mathbf{H} + 2\xi_j\mathbf{A}_d^T\mathbf{C}\mathbf{A}_d\right)\mathbf{G} \\ &= \mathbf{G}^T\left(\mathbf{H}^T\mathbf{C}\mathbf{A}_d + \mathbf{A}_d^T\mathbf{C}\mathbf{H}\right)\mathbf{G},\end{aligned} \tag{3.46}$$

where $\mathbf{U}_j^e$ is the element subset of the j-th column of $\mathbf{U}$ and where, in this case, $\mathbf{A}_d = \mathbf{A}(\mathbf{G}\mathbf{U}_j^e)$. Finally, $(\partial\mathbf{K}/\partial\xi_j)|_{eq}$ is formed through standard finite element assembly.

In conclusion, the ROB will be composed of a set of m_Φ VMs $\boldsymbol{\phi}_i$, collected in matrix $\boldsymbol{\Phi}$, a set of $m_\Phi(m_\Phi+1)/2$ (S)MDs θ_{ij}, collected in matrix $\boldsymbol{\Theta}$, and a set of $m_d m_\Phi$ DSs $\boldsymbol{\Xi}_{ij}$, collected in matrix $\boldsymbol{\Upsilon}$, so that

$$\mathbf{V} = [\boldsymbol{\Phi}, \boldsymbol{\Theta}, \boldsymbol{\Upsilon}], \tag{3.47}$$

for a total of $(3/2 + m_\Phi/2 + m_d)m_\Phi$ basis vectors. As already mentioned, in the particular case in which defects are chosen from the set of VMs, and these VMs with associated MDs are included in the basis, then one could avoid to compute their respective DSs, reducing the size of the ROB. However, since rigorously $\theta_{ij} \neq \boldsymbol{\Xi}_{ij}$, this would be just an approximation. Refer to 3.9 for more details.

Remark 2 (*on basis selection*). Generally speaking, not all the MDs and DSs in the projection basis will be strictly required to obtain an accurate ROM. Techniques to select a subset of MDs are already available in literature Jain, Tiso, Rutzmoser, et al., 2017; Tiso, 2011 and one could think of applying similar strategies even to DSs. Though an interesting topic, as $\mathbf{V}$'s dimension strongly affects both offline and online computational times, this is out of the scope of the present work. Therefore, it will not be treated here.

3.5 METHOD

3.5.1 Model types

We test the proposed method on a FE model of a realistic system. For each selected combination of defects, simulations are performed for four different models. First, the solution is computed for the high fidelity model including defects (HFM-d) and its "classic" reduced counterpart (ROM-d), that is without the new strain definition and without parametrization. By this we mean that the reduced order basis $\mathbf{V}$ is obtained form the mesh that directly incorporates defects. As such, DDs are not

Table 2: Acronyms for the different models considered in the numerical study.

MODEL	Description
HFM-n	high fidelity model of the *nominal* structure (i.e. without defects)
HFM-d	high fidelity model of the structure *with defects*
ROM-n	"classic" reduced order model (with VMs and MDs) in tensorial form, computed from the HFM-n
ROM-d	"classic" reduced order model (with VMs and MDs) in tensorial form, computed from the HFM-d
DP-ROM	*defect-parametric* ROM (with VMs, MDs and DSs) in tensorial form, computed from HFM-n and a given set of defects

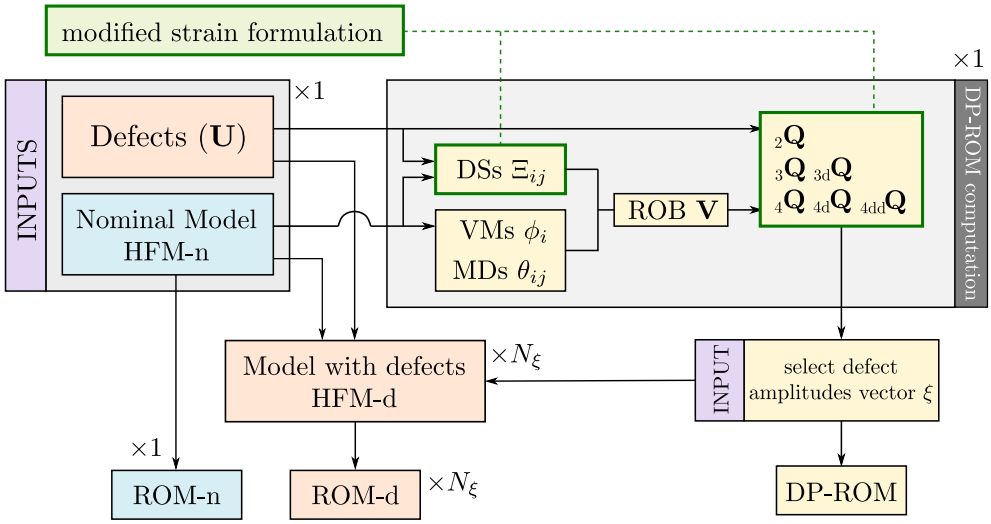

Figure 14: Work-flow map. From the inputs (HFM-n, **U** and ξ), ROM-n, HFM-d, ROM-d and DP-ROM are computed. Close to each box, it is shown how many times each block must be evaluated (N_ξ is the number of defect combinations). It is also shown (in green) where the modified strain formulation comes into play.

needed. Secondly, the Defect-Parametric Reduced Order Model (DP-ROM) will be run. This refers to the ROM discussed in this work. Finally, the "classic" ROM-n computed from the high fidelity *nominal* model (HFM-n) is simulated to highlight the fact that defects are significantly changing the response from the nominal case. A summary of the model types is given in Table 2.

3.5.2 Procedure

Figure 14 synthesizes the sequence of operations followed for the numerical simulations and, at the same time, attempts to put in evidence the contribution of each of the elements individually discussed in the previous sections (as, for instance, the strain formulation and the defects). As common inputs, the user must first specify the nominal geometry and a set of (admissible) displacement fields to model defects (namely, **U**). ROM-n can be directly computed from HFM-n only. Once the amplitude of the defects (ξ) is defined, HFM-d is instead obtained by shifting HFM-n's node positions by a displacement defined by $\mathbf{u}_d^F = \mathbf{U}\xi$. ROM-d follows. Finally, to construct DP-ROM, we compute VMs and MDs using HFM-n (as done for ROM-n) and DSs are obtained using available information about defects. Tensors are then

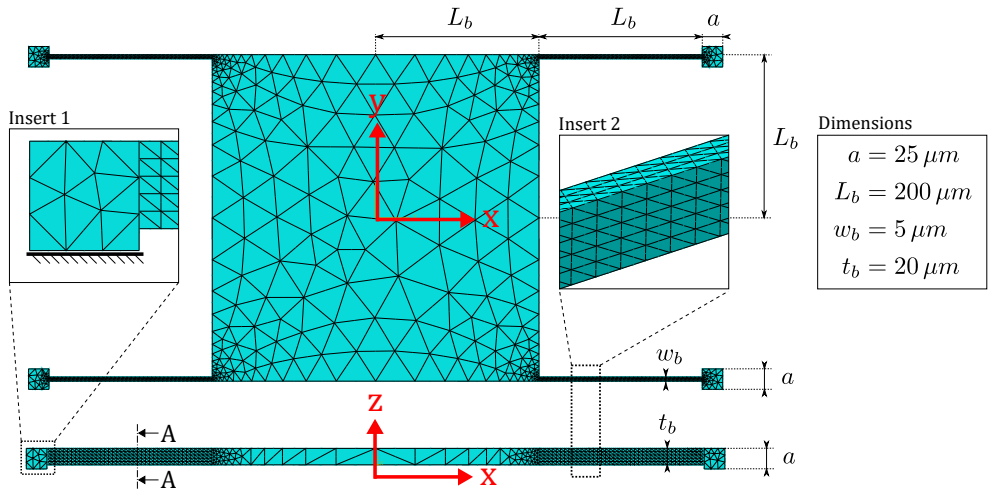

Figure 15: MEMS resonator model and mesh, xy-plane view (top) and xz-plane view (bottom). Insert 1 shows an anchor encastered to the ground, while insert 2 is a close-up on the beam's mesh. The structure is meshed in ABAQUS using free quadratic tetrahedra (TET10), counting 17,158 elements, 30,616 nodes and 91,212 dofs.

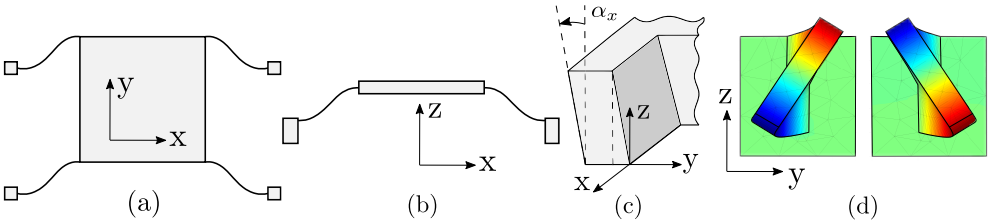

Figure 16: Schematic representation of (a) first vibration mode ϕ_1, (b) second vibration mode ϕ_2, (c) wall angle defect, (d) section A-A of the left beams ($x < 0$, see Fig. 15) at half length for modal derivative θ_{13} (symmetric about y-axis), where the color-map shows y-displacement. For θ_{13} mass does not move, thus is not shown here.

computed exploiting the modified strain formulation. At this point one can select ξ, and optionally precompute the quadratic and cubic tensor deviations due to defects (see Section 3.3.3). Notice that HFM-d and ROM-d have to be computed *for each combination of defects*, while ROM-n (obviously) and DP-ROM are computed *once and for all*, the latter needing just the aforementioned (inexpensive) precomputation. Once the models are ready, time integration is performed in Matlab using Newmark's scheme with full Newton-Raphson iterations. Rayleigh damping is introduced selecting a Q factor of 10,000 in correspondence of the first and second eigenfrequencies. Errors between HFM-d and DP-ROM are then evaluated.

3.6 NUMERICAL TESTS – I

3.6.1 Micromechanical resonator FE-model

DESCRIPTION DP-ROM is tested on a simple MEMS resonator, shown in Fig. 15 (*nominal* structure). Despite not representing any particular real device, such a system is a common element in many MEMS sensors (e.g. accelerometers, gyroscopes), whose dynamic behavior is strongly influenced by the presence of manufacturing defects Izadi et al., 2018; Weinberg and Kourepenis, 2006. The system is composed

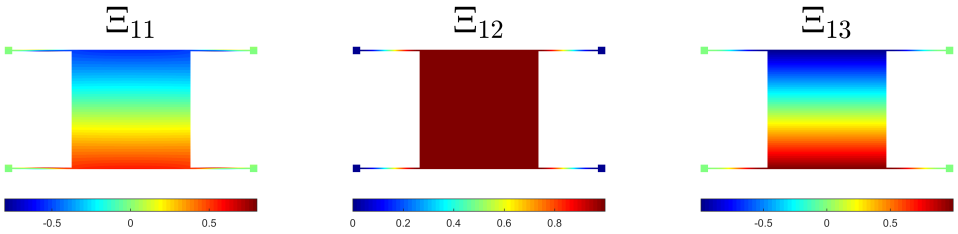

Figure 17: Defect Sensitivities for the first VM $\boldsymbol{\phi}_1$ with respect to defect $\mathbf{U}_1$, $\mathbf{U}_2$ and $\mathbf{U}_3$. Colormap shows the out-of-plane displacement. Notice that although Ξ_{11} looks very similar to Ξ_{13} if considering the mass only, in the first case the beams undergo torsion, while in the latter pure bending.

by a $400 \times 400 \times 20\,\mu m$ mass suspended by four $200 \times 5 \times 20\,\mu m$ slender beams, which are connected to the mass at one end and to an anchor at the other end. Anchors are $25 \times 25 \times 25\,\mu m$ parallelepipeds, encastered at the base, keeping the mass suspended over the ground and free to oscillate. Mesh details are given in Fig. 15 as well. The material is silicon ($E = 148$ GPa, $\rho = 2330\ \frac{kg}{m^3}$).

DEFECTS Out of the many possible defects that could be imposed to the structure, we selected three defect shapes that produce, even when small (see below), appreciable differences on the dynamic response with respect to the nominal device. The first shape-defect ($\mathbf{U}_1$) is the second eigenmode $\boldsymbol{\phi}_2$, which corresponds to a mass motion along z-axis; the second one ($\mathbf{U}_2$) is given by an inclination of the walls of the structure parallel to the xz-plane by a *wall angle* α_x, that is

$$v_d = \tan(\alpha_x) z, \tag{3.48}$$

being z the elevation of the nodes from ground, and where $u_d = w_d = 0$; the third one ($\mathbf{U}_3$) is the static MD θ_{13}, which basically consists in a counter-torsion of the four beams while the mass stays still. The defect-shapes are shown in Fig. 16. The defect-basis is then

$$\mathbf{U} = [\mathbf{U}_1\ ,\ \mathbf{U}_2\ ,\ \mathbf{U}_3] = [\boldsymbol{\phi}_2\ ,\ \mathbf{U}_{\alpha_x}\ ,\ \theta_{13}]\,, \tag{3.49}$$

and the corresponding amplitude vector is

$$\boldsymbol{\xi} = [\xi_1\ ,\ \xi_2\ ,\ \xi_3]^T. \tag{3.50}$$

The vectors in $\mathbf{U}$ are normalized such that a value $\xi_i = 1$ corresponds to a maximum displacement of $1\,\mu m$ for $\mathbf{U}_1$ and $\mathbf{U}_3$, and to an angle $\alpha_x = 1°$ for $\mathbf{U}_2$. As it will be shown later, all these defects introduce a coupling between (in-plane) drive and out-of-plane directions.

LOAD CASE A nodal mono-harmonic load is placed in the middle of the lateral face of the mass, aligned with y-axis, with frequency equal to the first resonance ω_1 *of the HFM-d*. This is the typical operative condition of a MEMS resonator, which are kept at resonance with a Phase Locked Loop (PLL) and Amplitude Gain Control (AGC). Notice that, for each simulation, the natural frequencies of the system may slightly change depending on the imposed defects: for each set of defects then, the HFM-d's first eigenfrequency is used for HFM-d, ROM-d and DP-ROM (but not for ROM-n, which is always driven at the nominal natural frequency ω_{1n}). Figure 16a schematically shows the actuation mode $\boldsymbol{\phi}_1$ (*drive mode*).

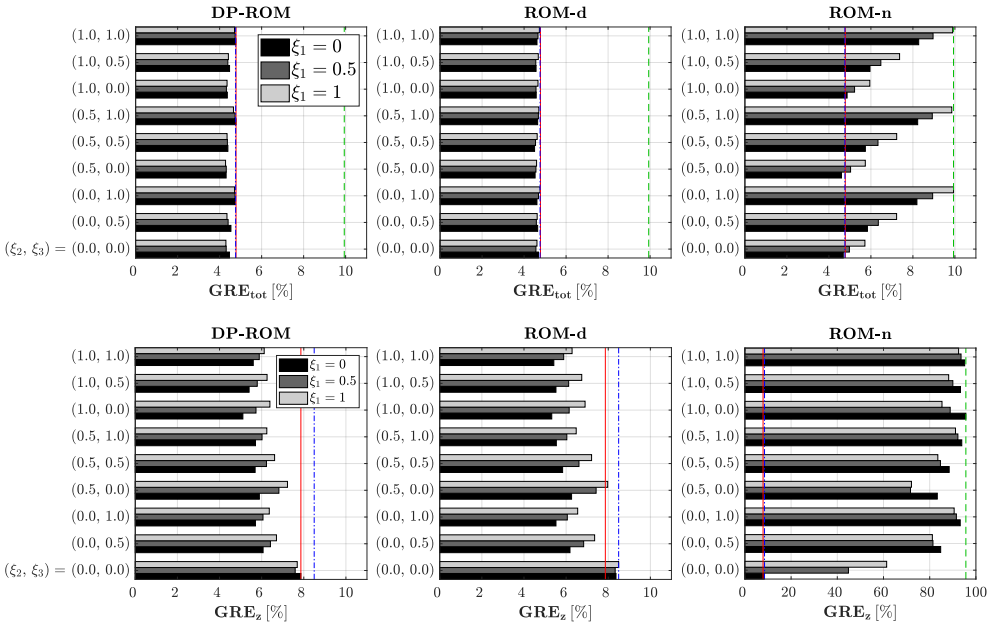

Figure 18: Global Relative Errors (GRE) for the three ROMs. On the vertical axis the pair (ξ_2, ξ_3) is shown. For each pair, the three bars indicate a different value for ξ_1. The vertical lines mark the maximum errors for the DP-ROM (solid, red), ROM-d (dash-dotted, blue) and ROM-n (dashed, green).

REDUCTION BASIS For every reduced model, the ROB is composed by the first (24.2 kHz)[3], second (79.6 kHz) and third vibration modes (139.5 kHz) with their respective MDs (for a total of 9 vectors). In the case of the DP-ROM, also defect sensitivities are included, for a total of 9 DSs (derivatives of the 3 VMs with respect to each defect-shape). Notice that for the present study we include in the basis even those DSs relative to defects coinciding with VMs (namely, $\mathbf{U}_1$). This is done in order to avoid a special treatment for this case, keeping the analysis as general as possible. Again, hints on how neglecting VM-related DSs would change the analysis are given in 3.9. Figure 17 shows the DSs related to the drive mode $\boldsymbol{\phi}_1$.

3.6.2 Error evaluation

To assess the accuracy of the method, we adopt the global relative error (GRE) as an error indicator Jain, Tiso, Rutzmoser, et al., 2017, defined as

$$\mathrm{GRE}_t = \frac{\sqrt{\sum_{i=1}^{N_t} (\mathbf{u}_i^F - \hat{\mathbf{u}}_i^F)^T (\mathbf{u}_i^F - \hat{\mathbf{u}}_i^F)}}{\sqrt{\sum_{i=1}^{N_t} (\mathbf{u}_i^F)^T \mathbf{u}_i^F}} \times 100, \tag{3.51}$$

where $\mathbf{u}_i^F = \mathbf{u}^F(t_i)$ is the displacement vector for the i-th time step of the reference solution (HFM-d) and where $\hat{\mathbf{u}}_i^F$ is the corresponding approximated solution.

Equation (3.51) considers the totality of displacements, disregarding the fact that the order of magnitude of the response along the three directions is different. It is then useful to define the GRE separately for the out-of-plane direction as:

$$\mathrm{GRE}_z = \frac{\sqrt{\sum_{i=1}^{N_t} (\mathbf{w}_i - \hat{\mathbf{w}}_i)^T (\mathbf{w}_i - \hat{\mathbf{w}}_i)}}{\sqrt{\sum_{i=1}^{N_t} \mathbf{w}_i^T \mathbf{w}_i}} \times 100, \tag{3.52}$$

where $\mathbf{w}$ is the z-displacement vector. In many MEMS applications, displacements due to unwanted coupling between axes (as it is here the case between drive and z-

3 Values referred to HFM-n

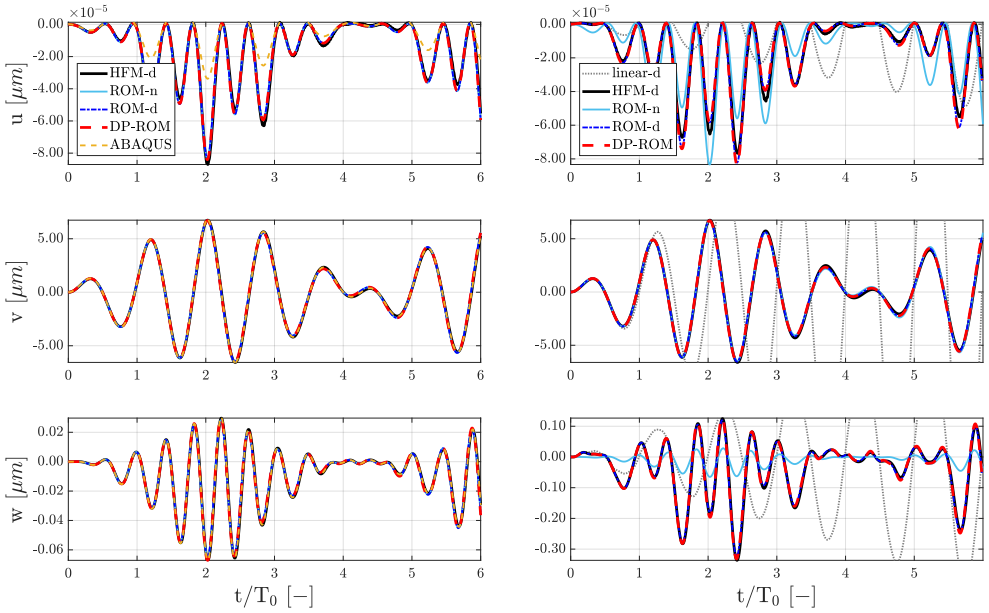

Figure 19: Time domain response at the force application node along the three directions. Left: results for the nominal configuration ($\xi_1 = \xi_2 = \xi_3 = 0$) for all the models plus a full model run on ABAQUS. Right: results for the $\xi_1 = \xi_2 = \xi_3 = 1$ case. T_0 is the period of the harmonic driving force.

direction) superimpose to a desired measurement signal. Their correct estimation is therefore critical. Figure 18 shows the errors considering all the displacements (top) and only **w** (bottom). In both cases, we can see that the ROM-d and DP-ROM yield approximately the same errors. Instead, looking at the performances of ROM-n, it can be easily seen that along the out-of-plane direction errors become immediately unacceptable, as the defects lead to a coupling between drive and z-direction which is not present in the nominal case. It should also be noted that the displacements in z are much smaller than the ones along y (drive direction), therefore y-errors tend to "hide" z-errors in GRE_t. Figure 19 shows the time response at the force application node in the three directions in the nominal case and in the $\xi_1 = \xi_2 = \xi_3 = 1$ case. To validate our in-house Matlab code, results were compared with ABAQUS ones for the nominal case, showing agreement. Small discrepancies in the x-response are attributed to possible differences between our Matlab code and ABAQUS in the FE formulation, integration procedures, solvers and convergence tolerances (notice that due to the symmetry of the nominal problem the displacement u, which is in the order of 10^{-5}, should be rigorously zero at the forcing location; therefore u can be imputed to numerical reasons and mesh asymmetries only). Notice that, while the response along z changes significantly from case to case, the x and y responses are barely affected by the presence of the defects.

Role of the reduction basis

We briefly want to stress the importance of using the correct reduction basis. Given the assumption of small defects, one may be driven to think that it might actually be enough to use the *nominal* reduction basis $\mathbf{V}_{nom}$ (i.e. the basis comprising VMs and MDs only, computed on the nominal geometry) not only for ROM-n, but also for ROM-d and DP-ROM. To dispel this doubt and further support the arguments already discussed in Section 3.4, we ran a numerical test for the MEMS resonator model ($\xi_1 = \xi_2 = \xi_3 = 1$ case) when using the same *nominal* ROB used for ROM-n, that is $\mathbf{V}_{nom} = [\mathbf{\Phi}, \mathbf{\Theta}]$. Again, 3 VMs and their corresponding 6 MDs are included in the basis. Eigenfrequencies, time responses and GREs are shown in Fig. 20. As it

(a)

	f_{01} [Hz]
HFM-n	24,205
HFM-d	24,265
ROM-n	24,205
ROM-d*	52,641
DP-ROM*	52,705

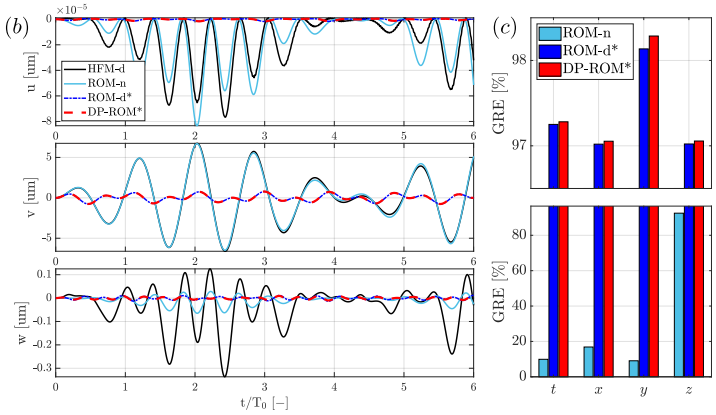

Figure 20: Simulations for ROM-d and DP-ROM when using the same (nominal) reduction basis as ROM-n. The two model are marked by a * to denote the differences with respect to the definitions given in Table 2. The testing conditions are the same used for Fig. 19 (right). In particular, we have again $\xi_1 = \xi_2 = \xi_3 = 1$. (a) First eigenfrequencies for the different models, (b) time domain responses, (c) errors in terms of GRE (total and for individual axes). Plot is split to increase visibility.

can be easily observed, the two ROMs yield now completely different results, with a drastic overestimation of the first eigenfrequency. It is thus evident how information about the defects must be present both in the model to be reduced *and* in the reduction basis itself.

Remark 3 (*ROM-d vs DP-ROM*). Looking at Fig. 20, one can also see that even when using the *same* reduction basis, ROM-d and DP-ROM lead to slightly different results (regardless of how wrong they might be with respect to HFM-d). This follows from the fact that ROM-d is computed from HFM-d whereas DP-ROM from HFM-n, with the modified strain formulation to take defects into account. As such, the latter is just an approximation of the former. Small discrepancies are therefore expected. The only case in which ROM-d and DP-ROM would coincide would be the one where $\boldsymbol{\xi} = \mathbf{0}$ *and* $\mathbf{V}_{\mathrm{ROM-d}} = \mathbf{V}_{\mathrm{DP-ROM}}$. The first condition would make VMs (and MDs) of the nominal and of the defected models coincide, while the second would also imply that DSs are either added to $\mathbf{V}_{\mathrm{ROM-d}}$ or removed from $\mathbf{V}_{\mathrm{DP-ROM}}$.

3.6.3 Computational times

In order to assess the computational savings provided by the proposed method, we define three speed-up coefficients as

$$\mathrm{SP1} = \frac{t_{full}}{t_{online}}, \tag{3.53a}$$

$$\mathrm{SP2} = \frac{t_{full}}{t_{online} + t_{offline}}, \tag{3.53b}$$

$$\mathrm{SP3} = \frac{t_{full} N_{on}}{t_{online} N_{on} + t_{offline} N_{off}}, \tag{3.53c}$$

where t_{full} is the (online) computational time for the full analysis of HFM-d, t_{online} and $t_{offline}$ are the ROMs' online and offline times respectively, N_{on} is the number of online runs and N_{off} is the number of times a ROM has been computed. Notice that $t_{offline}$ accounts for both the times for the ROB and tensors computation.

Table 3: Computational times (in seconds) and speed-ups (average values). Speed-ups are computed using ABAQUS' online time (average value over 10 cluster runs) as reference. All the simulations (both on ABAQUS and Matlab) were run on ETH Zürich Euler cluster with 27 CPUs (4GB RAM each). The times marked by * are the ones that are affected by parallel computing. The small difference in ROM-d and DP-ROM online times is due to the number of reduced coordinates (9 and 18, respectively).

	offline (basis)	*offline (tensors)*	*online*	N_{off}	N_{on}	*total time (27 cases)*	*total time (hh:mm:ss)*	*SP1 (online)*	*SP2 (on+off, 1 case)*	*SP3 (on+off, 27 cases)*
HFM-n (Abaqus)	-	-	2,399.7*	0	27	64,792	17:59:52	-	-	-
ROM-d	18.2	112.1*	5.2	27	27	3,659	1:00:58	461.5	17.7	17.7
DP-ROM	35.9	174.5*	5.8	1	27	367	0:06:07	413.7	11.1	176.5

All the simulations have been carried out on the Euler cluster of ETH Zürich (with 27 CPUs) in Matlab R2017b, using in-house developed codes. This was done mainly in order to make a fair assessment of the approximation errors discussed in the previous section by avoiding unwanted/unforeseen error sources. However, it would be unfair to compute speed-ups referring to the full simulation carried out in this environment, for it would be much slower with respect to a state-of-art commercial software. For this reason, speed-ups reported in Table 3 are computed with reference to a full (nominal) simulation in ABAQUS/CAE 6.14-1 (same model HFM-n, load and fixed time steps). All computational times are shown in Table 3 as well.

As it can be easily observed, online speed-ups (SP1) are very high, as it is usually the case for all tensorial approaches and other reduction techniques. To make a more comprehensive performance assessment, it is better to look at SP2, which includes the offline costs. It is however to stress the fact that, if the simulation time-span is large enough, $t_{offline}$ may become negligible compared to t_{online} so that SP2 $\rightarrow$ SP1 for $t_{online} \rightarrow +\infty$. This holds true for SP3 as well. However, if the same ROM can be exploited more than once, be it for different load cases or for different parameter sets - as in the case of the DP-ROM, we have that SP3 $\rightarrow$ SP1 even for $N_{on} \rightarrow +\infty$. In the present case, for a moderatly short time-span and relatively low number of simulations, we have SP3 $= 175.5$, almost half of the theoretical maximum limit SP1 $= 413.7$. Following these considerations, we can confidently say that the DP-ROM, if fully exploited as in the intention of the authors, will have SP3 $\approx$ SP1. As already stated in the introduction, a Monte-Carlo analysis would make the perfect fit with this method, and one could think to couple it even with uncertainty quantification methods Pivovarov D, 2019.

3.6.4 About Scalability

Before concluding this section, we would like to make a few comments on how computational times are expected to change with the size of the full model and on the tensors computation.

On the one hand, considering *online* times, it is known that HFM times grow more than linearly with the number of dofs of the structure. In contrast, the original size of the model is irrelevant for ROMs, and online speed is determined by the size of the ROB. Even in this case however, computational times grow more than linearly with the basis size. On the other hand, ROM *offline* costs grow almost *linearly* with the number of elements thanks to element-level projection assembly. Moreover, the number of *dofs of the element* (30 for the 10-nodes tetrahedra TET10 in our test case) greatly affects performances.

Additionally, to give a rough idea of the influence of the basis dimension and of parallel computing, the tensor computational speed (in terms of elements per second) is shown in Fig. 21. These results were obtained in Matlab R2017a on a local machine equipped with 2 Intel(R) Xeon(R) CPUs (E5-268W 0) @ 3.10 GHz and

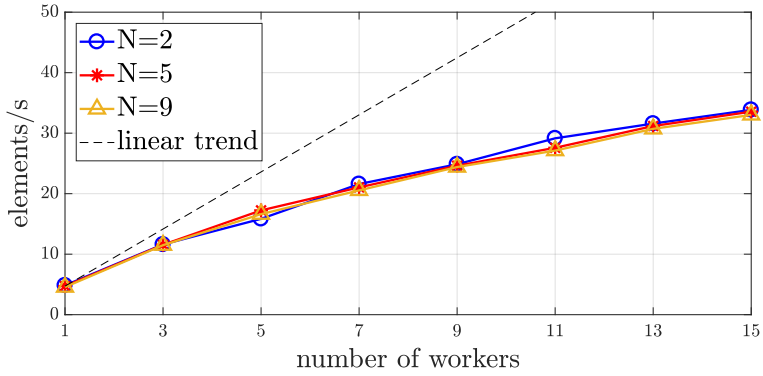

Figure 21: Tensor computational speed as a function of the number of parallel Matlab workers. N is the number of vectors in the reduced order basis. Data are referred to the MEMS model described in this work, notice however that these values remain almost unchanged when coarser or finer meshes were considered.

64 GB RAM. As it is often the case with parallel computing, speed grows less than linearly with the number of workers. The impact of ROB's size is not negligible, but very weak if compared to other parameters' one. Finally, notice once more that Matlab was used to compute tensors. Thus, a Fortran or C++ dedicated routine could greatly improve performances, reducing offline times and making the method even more attractive.

3.7 NUMERICAL TESTS – II

In the previous section, a structure subject to multiple defects was studied with the aim to assess the accuracy and the speed of the proposed method. In that setup the focus was on correctly describing cross-coupling effects. These, however, would likely manifest in a linear setting as well (even if, of course, in a different manner). In this example, instead, we consider the simple case of a beam, clamped at both ends, where the defect will deform the nominal structure into a shallow arch, with the purpose to study a case in which the presence of the defect drastically changes the nonlinear dynamics of the structure. The silicon beam has the same dimension of the suspension beams of the previous test case, with length L_b along x, width w_b along y and thickness t_b along z (see Fig. 15). We used a mesh with 320 hexahedral quadratic elements (HEX20), for a total of 2117 nodes and 6129 dofs. The defect shape is given by

$$v_d(x, \xi) = \xi \cos\left(\frac{\pi}{L_b} x\right), \quad x \in [-L_b/2\,,\, L_b/2], \tag{3.54}$$

where ξ is the amplitude parameter ($u_d = w_d = 0$). The load, $f_{ext} = \mathrm{step}(t)$, is placed at half length on one edge of the beam and is aligned with the positive y-axis. For ROM-n and ROM-d, the reduction basis contains the first 5 VMs and 15 MDs, while for DP-ROM it includes even 5 DSs. Figure 22 shows the errors in the forcing direction and the time responses at the excitation node in the two worst cases. As it can be seen, the GRE is almost always less than 10% and the hardening/softening behavior of the shallow arch is nicely captured by the DP-ROM, even for very large defects ($\xi = \pm 100\%\, w_b$). Higher order harmonics in the full solution, of course, cannot be captured by the tested ROMs due to truncation of the basis. In analogy with what we have done in the previous test case, we reported even the responses and the errors we would obtain if using the nominal model with no defects. Notice that the kink in ROM-n's GRE_y is purely coincidental (for those

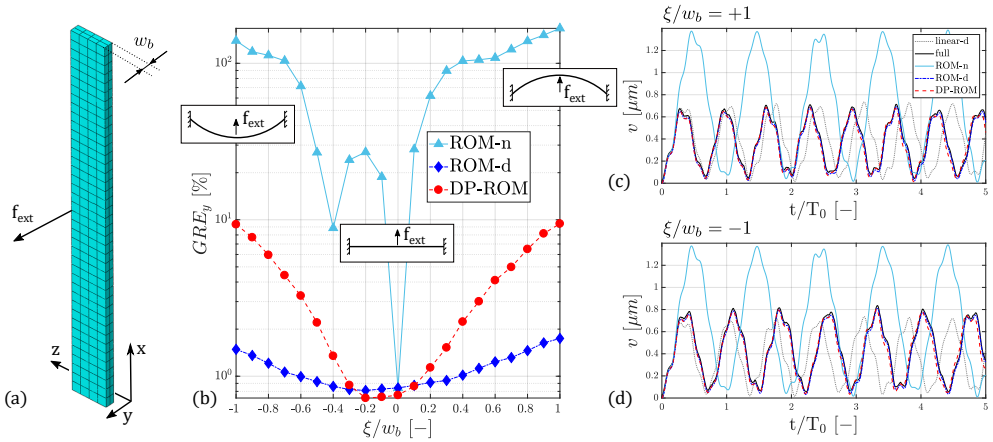

Figure 22: Shallow-arch defect. (a) Model mesh, (b) error along y-axis (GRE_y, in logarithmic scale), for $\xi \in [-5, +5]$, step-load time domain responses in y-direction in the *worst cases* for positive (c) and negative (d) values of ξ. T_0 is the period corresponding to the first eigenfrequency of the nominal structure; $w_b = 5\,\mu m$ is the beam thickness in y-direction. HFM-d linear responses (gray dotted lines) are shown in (c) and (d) to put in evidence the hardening/softening behaviors.

particular defect amplitudes and load level, the softening behavior of the structure brings the nominal response close to the HFM-d's one).

3.8 CONCLUSIONS

In this work we proposed a parametric ROM to describe shape defects, defined in terms of a shifted nodal position of a tri-dimensional mesh with respect to the nominal geometry. These "defect shapes" are embedded in the strain formulation, which allows for the parametrization of the model. Indeed, using tensorial reduction, we showed how these defect shapes can be directly included in a ROM which can be computed once and for all and which yields accurate results in a neighbourhood of the nominal configuration *for any defect shape*. We also discussed the need to enhance the projection basis with defect sensitivities (DSs), which can be computed using the modified strain formulation. Incidentally, DSs could be of interest even in the context of shape optimization, since they can be analytically derived and do not need remeshing. In contrast to many strategies employed in nonlinear parametric model order reduction, no training of the model is needed, so that the offline costs reduce to the computation of the reduced order tensors only. Two numerical examples were given. First, a MEMS resonator was studied under operative conditions, where the presence of defect shapes introduced a not negligible coupling between axes. Error and computational time analyses showed that consistent speed-ups can be achieved with minimal loss of accuracy. Finally, a shallow-arch micro-beam was studied for different heights of the arch under step loading excitation, showing that the hardening/softening behavior of the structure can be accurately represented. All in all, we think that the proposed method provides a very efficient tool to aid the design phase of structures subject to shape defects, as in the case of MEMS industry.

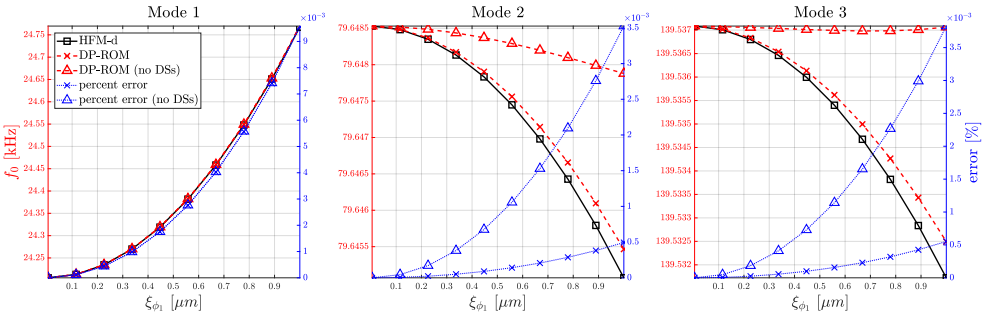

Figure 23: First three natural frequencies for increasing defect amplitudes. Eigenfrequencies for HFM-d (solid black line), for DP-ROM with and without DSs (red dashed lines) are shown on the left vertical axis. Percent errors (blue, dotted lines) are shown on the right vertical axis. $\boldsymbol{\phi}_1$ is the imposed defect.

3.9 APPENDIX: ON MDS AND DSS FOR VM–DEFECTS

As it has already been pointed out in Section 3.4, MD θ_{ij} can also be interpreted as the sensitivity of the structure with respect to a defect coinciding with vibration mode $\boldsymbol{\phi}_i$. To our purposes, this would suggest that if we were to choose a defect-shape from a set of VMs, no further DS would be needed to enhance the reduction basis, as MDs would replace DSs. However, comparing Eq. (3.46) and Eq. (3.42), it turns out that the two expressions are not equivalent.

Selecting a defect $\mathbf{U} = \boldsymbol{\phi}_j$, we have that $\mathbf{A}_d = \mathbf{A}(\mathbf{G}\mathbf{U}^{el}) = \mathbf{A}(\mathbf{G}\boldsymbol{\phi}_j^{el}) = \mathbf{A}_\phi$. By comparing the two expressions:

$$\left.\frac{\partial \mathbf{K}^e(\boldsymbol{\phi}_j^e \xi_j)}{\partial \xi_j}\right|_{eq} = \mathbf{G}^T\left(\mathbf{H}^T\mathbf{C}\mathbf{A}_d + \mathbf{A}_d^T\mathbf{C}\mathbf{H}\right)\mathbf{G} \neq \mathbf{G}^T\left[\mathbf{H}^T\mathbf{C}\mathbf{A}_\phi + \mathbf{A}_\phi^T\mathbf{C}\mathbf{H}\right]\mathbf{G}$$
$$+ \mathbf{G}^T\left[(\mathbf{L}\cdot\mathbf{G})\cdot_{11}(\mathbf{C}\mathbf{H}\mathbf{G}\boldsymbol{\Phi}_i)\right] = \left.\frac{\partial \mathbf{K}^e(\boldsymbol{\phi}_j^e \eta_j)}{\partial \eta_j}\right|_{eq}, \quad (3.55)$$

we notice an additional term in the MDs (integration over volume, again, is implicitly assumed).

An inexpensive way to assess the impact of this discrepancy is to look at the evolution of the eigenfrequencies of the reduced system when including only MDs and when including also DSs. Figure 23 shows the eigenfrequencies trends for the model described in Section 3.5 when the first VM $\boldsymbol{\phi}_1$ is imposed as a defect. As it can be easily observed, for the second and third modes frequencies tend to diverge if DSs are not included. For the present system and the selected defect amplitudes however the percent error is very small, and one could then think to use only MDs in the basis. Finally, notice that each defect-shape might have a different impact on the accuracy on the DP-ROM: for instance, imposing the second VM as a defect to our nominal model, we could show that errors are more pronounced on the first eigenfrequency if DSs are not included. For this reason, we recommend to critically choose whether to exclude or not DSs case by case.

4 A HIGHER ORDER NL–PROM USING NEUMANN EXPANSION

The method presented in the previous chapter is based on a strain approximation, whose validity and limitations cannot be evaluated in advance. This poses some questions in terms of applicability of the method and degree of accuracy that can be expected. In this chapter, the method is further refined and different approximation levels are identified, tested and compared. The content of this chapter can be found in Marconi, Tiso, Quadrelli, et al., 2021; as such, we apologize for content to some extent already presented previously.

ABSTRACT We present an enhanced version of the parametric nonlinear reduced order model for shape imperfections in structural dynamics we studied in the previous chapter. In this model, the total displacement is split between the one due to the presence of a shape defect and the one due to the motion of the structure. This allows to expand the two fields independently using different bases. The defected geometry is described by some user-defined displacement fields which can be embedded in the strain formulation. This way, a *polynomial function* of both the defect field and actual displacement field provide the nonlinear internal elastic forces. The latter can be thus expressed using tensors and, owning the reduction in size of the model given by a Galerkin projection, high simulation speed-ups can be achieved. We show that the adopted deformation framework, exploiting *Neumann expansion* in the definition of the strains, leads to better accuracy as compared to the previous work. Two numerical examples of a clamped beam and a MEMS gyroscope finally demonstrate the benefits of the method in terms of speed and increased accuracy.

4.1 INTRODUCTION

The Finite Element (FE) method has long been a fundamental analysis and design tool in many areas of science and engineering. In structural mechanics it is almost mandatory to use FE models to investigate the behavior of complex systems, which often have many geometric details that would be difficult to handle with alternative approaches, such as lumped parameter or analytical models Belytschko et al., 2014. However, large FE simulations would often require considerable computational resources and time, so in some cases designers may prefer to perform real experiments rather than numerical ones. On the one hand, this need for fast and affordable FE simulations has given rise to numerical techniques to improve computational efficiency: domain decomposition and substructuring Klerk et al., 2008; Toselli and Widlund, 2005 and FE Tearing and Interconnecting (FETI, Farhat and Roux, 1991) are just a few examples. On the other hand, model order reduction methods have emerged, consisting in the construction of a Reduced Order Model (ROM), whose number of degrees of freedom (dofs) is much smaller than that of the reference Full Order Model (FOM). The use of linear ROMs also in industrial contexts is nowadays well established as the theory underlying them. Guyan reduction Guyan, 1965 and *modal analysis* He and Fu, 2001 are two well-known examples in mechanical statics and dynamics, respectively, where FOM's static deformations and Vibration Modes (VMs, also known as eigenmodes or natural modes of the linear system) are used to construct a Reduced Basis (RB) that projects the governing equations onto a lower dimension subspace. Linear ROMs were also successfully coupled with substructuring techniques in the Craig-Bampton and Rubin methods

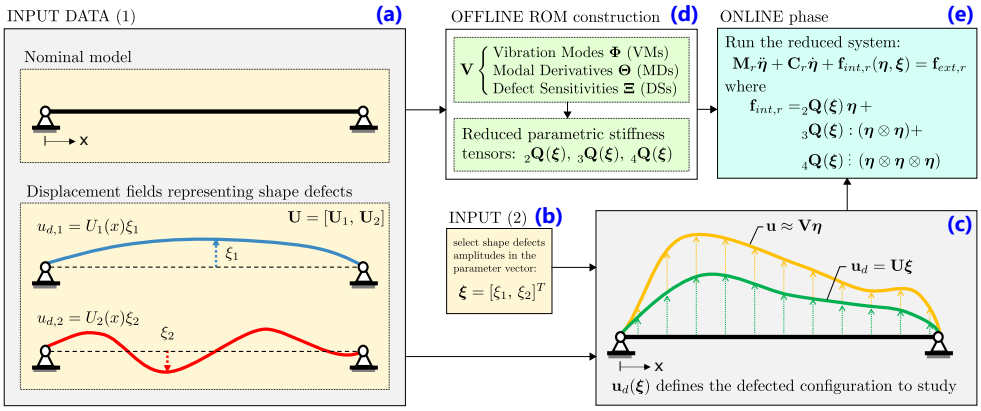

Figure 24: Overview of the proposed method, schematically illustrated for a pinned beam.

Craig and Bampton, 1968; Rubin, 1975, which are available in many commercial software.

For nonlinear FE studies many solutions have been proposed over the last decades, but none of them seems to have prevailed over the others, as each of them offers certain advantages, requires certain costs and/or targets specific problems. Overall, however, the literature is mature enough to provide the analyst with many different options in several practical applications, ranging from bolted joints Pichler et al., 2017, gears Blockmans et al., 2015, contacts Balajewicz et al., 2015; Géradin and Rixen, 2016, friction Mehrdad Pourkiaee and Zucca, 2019 and viscoplasticity Ghavamian et al., 2017 to flexible multi-body dynamics with geometric nonlinearities Wu, Tiso, Tatsis, et al., 2019 and substructuring Wu, Tiso, and van Keulen, 2018.

Nonlinear ROMs can be classified according to (i) whether they are RB-projection based or not, (ii) whether they are data- or model-driven and (iii) their (non-) intrusiveness. In the following we consider mostly projection approaches, as the one adopted in this work; alternatively, one could resort to different strategies, such as normal form theory or Spectral Submanifolds. The most recent contributions in this sense include Vizzaccaro et al., 2020 and Jain and Haller, 2021; Jain, Tiso, and Haller, 2018; Ponsioen et al., 2020. In (ii), for data-driven ROMs we usually refer to ROMs constructed using previous FOM simulation data (or experimental data, R. Perez et al., 2017), as opposed to model-driven methods that rely on some intrinsic properties of the model itself for ROM construction, such as modal approaches Amabili, 2013; Hollkamp and Gordon, 2008; Kuether et al., 2015; C. Touzé et al., 2014. As for intrusiveness, we usually denote a ROM as non-intrusive Mignolet et al., 2013 if it can be used with routines and solvers of commercial FE software and, conversely, as intrusive a method requiring dedicated routines. Specifically, intrusive methods require access and manipulation to element-level quantities, as for instance nonlinear generalized forces and jacobians. Other distinctions can be made in terms of the types of nonlinearities that a given model can handle and the way nonlinear functions are evaluated Jain, 2015. All these differences ultimately affect the two phases that all ROMs have in common: the *offline* phase, in which the ROM is constructed, and the *online* phase, in which the simulation responses are retrieved. As the main goal of ROMs is to reduce computational effort and time, a key aspect to keep in mind when choosing a method is the overhead cost to pay in the offline phase; in the case of data-driven methods, this cost can be as high as the cost associated to the solution of the FOM Balajewicz et al., 2015. Generally speaking then, data-driven methods (usually based on Proper Orthogonal Decomposition, or POD, strategies Lu et al., 2019) are used in scenarios where the high cost associated to the data generation can be amortized: typically, this is the case of multi-query analysis. In this sense, although not as versatile and generally applicable as data-driven POD-based approaches, model-driven strategies in structural

dynamics are desirable, for no FOM simulation is required a priori. Rayleigh-Ritz procedures Noor and Peterst, 1980, dual modes Mignolet et al., 2013 and Modal Derivatives (MDs) Idelsohn and Cardona, 1985; Jain, Tiso, Rutzmoser, et al., 2017; Sombroek et al., 2018 are some popular examples.

One way to mitigate the offline overhead costs of all the aforementioned methods, but especially the data-driven ones, is to resort to (nonlinear) parametric ROMs, (NL-)pROMs. Also in this context, the literature on linear systems is quite well developed and consolidated. An extensive survey and comparison of these methods can be found in Baur et al., 2017. The reduction of nonlinear parametric Partial Differential Equations (PDEs) is instead still an active research topic, which has attracted increasing interest in various disciplines over the years. Interestingly, the vast majority of nonlinear parametric model order reduction methods is data-driven, POD-based. Some recent examples include non-intrusive interpolation methods for evaluating nonlinear functions with hypersurfaces Xiao, Fang, Buchan, et al., 2015; Xiao, Fang, Pain, et al., 2017 and use of Gaussian Processes and machine learning for error evaluation and refinement of the pROM Xiao, 2019 or interpolation on the Grassman manifold via tangent spaces Zimmermann, 2019. Alternatively, many of these methods approximate the nonlinear function using *hyper-reduction* methods as the Discrete Empirical Interpolation Method (DEIM) Barrault et al., 2004; Chaturantabut and Sorensen, 2010 to speed up the evaluation, and in this sense online basis selection and adaptive algorithms were studied Cho et al., 2020; Phalippou et al., 2020. However, as mentioned above, POD (and DEIM) needs a number of FOM simulations to construct the ROM. For this reason, Kast et al., 2020 implemented a Multi-Fidelity strategy in which the parametric dependence was reconstructed using a large number of low-fidelity models and a minimal number of high-fidelity evaluations. Other approaches exploit machine learning to construct an input-output relationship, with convolutional neural networks Hesthaven and Ubbiali, 2018 and autoencoders Maulik et al., 2020, which require the training of a network, again, using preexisting data. Note that most of the above methods lead to pROMs that are only *evaluated* in the online phase, i.e. no simulation is actually performed[1], but the solutions at the known parameter locations are “interpolated" to obtain the result.

Although model-driven NL-pROMs seem to be less popular, they offer the undeniable advantage of being simulation-free, thus considerably cutting down the offline costs. Interesting recent examples are loosely based on the extension of methods for linear systems, such as the Non-Linear Moment Matching (NLMM) scheme Astolfi, 2008, 2010; Ionescu and Astolfi, 2016. In Ref. Rafiq and Bazaz, 2020, a non-parametric ROM is constructed with NLMM and DEIM for each parameter instance sampled from the parameter space. These models are then “adjusted" onto a common subspace where they are interpolated to produce the pROM. This strategy, however, requires the solution of a set of nonlinear algebraic equations on the FOM at different time instances, for different signal generators, and at each point on the parameter grid. For large systems, the computational effort could still be significant, although lower than that of POD methods.

In this paper we propose a NL-pROM for *geometric nonlinearities* and parametrized *shape defects* to study the behavior of imperfect structures. This is motivated by the fact that, as it is observed in many engineering applications, even small imperfections can significantly change characteristics and performances of a system, as for instance in the case of MEMS devices Acar and Shkel, 2008; Izadi et al., 2018 and mistuning of gas turbine blades Mehrdad Pourkiaee and Zucca, 2019. Other ROMs have already been developed in this sense X. Q. Wang, O'Hara, et al., 2018; X. Q. Wang, Phlipot, et al., 2018, but limited to *localized* defects. Regarding geometric nonlinearities, we recall that in the case of continuum finite elements with linear

1 By *simulation* we refer to the solution of a set of equations describing a system in any kind of analysis setting (e.g. in time or frequency domain).

elastic constitutive law and Total Lagrangian formulation, as in our study, the nonlinear elastic forces are a polynomials which can be represented using tensors, so that qualitatively[2] the FOM governing equations write[3]

$$\mathbf{M}\ddot{\mathbf{u}}^F + \mathbf{C}_d\dot{\mathbf{u}}^F + {}_2\mathbf{K}^F\mathbf{u}^F + {}_3\mathbf{K}^F : (\mathbf{u}^F \otimes \mathbf{u}^F) + {}_4\mathbf{K}^F \vdots (\mathbf{u}^F \otimes \mathbf{u}^F \otimes \mathbf{u}^F) = \mathbf{f}_{ext}(t) \quad (4.1)$$

where $\mathbf{M}$, $\mathbf{C}_d \in \mathbb{R}^{n\times n}$ are the mass and damping matrices, $\mathbf{u}^F$, $\dot{\mathbf{u}}^F$, $\ddot{\mathbf{u}}^F \in \mathbb{R}^n$ the displacement, velocity and acceleration vectors, and $\mathbf{f}_{ext}(t) \in \mathbb{R}^n$ an external forcing, being n the FOM number of dofs. ${}_2\mathbf{K}^F \in \mathbb{R}^{n\times n}$, ${}_3\mathbf{K}^F \in \mathbb{R}^{n\times n\times n}$ and ${}_4\mathbf{K}^F \in \mathbb{R}^{n\times n\times n\times n}$ are the stiffness tensors for the linear, quadratic and cubic elastic internal forces.

Conceptually, the method retrace the one we presented in Marconi, Tiso, and Braghin, 2020, but it is based on a different deformation scheme (of which our earlier work resulted to be a sub-case). An overview of the individual steps of the method is shown in Fig. 24. The user defines as input data the nominal structure (in terms of geometry, material properties and FE mesh) and a number m of displacement fields representing the *shape defects*, which are intended as small deviations from the nominal geometry (Fig. 24a). These can be known analytically, from experimental measurements or previous simulations, and finally they can be discretized with displacement field vectors $\mathbf{U}_i$ and collected in a matrix $\mathbf{U} = [\mathbf{U}_1, ..., \mathbf{U}_m]$. Each defect can then be leveraged in amplitude by the parameter vector $\boldsymbol{\xi} = [\xi_1, ..., \xi_m]^T$ (Fig. 24b) so that the final defected geometry represented by the model is given by the global defect displacement field $\mathbf{u}_d = \mathbf{U}\boldsymbol{\xi}$, i.e. a linear superposition of the selected defects (Fig. 24c). With this information about the nominal structure and shape defects, we assemble the RB using a modal approach with VMs, MDs and Defect Sensitivities (DSs). We then construct the reduced stiffness tensors, *once and for all*, projecting the element-level tensors with the selected RB (Fig. 24d). In this way, linear, quadratic and cubic elastic forces can be evaluated directly with respect to the reduced coordinates *and* shape defect magnitudes without switching between the full and reduced order space when evaluating the nonlinear function. Our strategy can then be classified as model-driven (simulation-free). Finally, in the online phase, the simulation is performed with the reduced governing equations (Fig. 24e). Notice that the model is used to *run* a simulation, not to *evaluate* a solution as in interpolation-like techniques: as such, different forcing terms and also different analysis types (e.g. transient, frequency response) are possible. All of this is possible thanks to the modified definition of the Green-Lagrange strain tensor we use. Specifically, our strain tensor embeds two subsequent transformations: (i) the one from nominal to defected geometry (which, at the end, will be parametrized), and (ii) the one from the defected configuration to the deformed/final one. The deformation produced by the latter is the one we measure, so no strain/stresses are introduced by the presence of the defect in (i); however, the deformation of (ii) will depend on (i). The formulation we obtain however contains rational terms which cannot be used for a tensorial representation (which can describe polynomials only). Given the assumed small entity of the shape defects, we advocate the use of a Neumann expansion to approximate the Green-Lagrange tensor, obtaining again a polynomial form. Applying standard FE procedures, we finally get to the expression of the reduced elastic internal forces, which will parametrically depend on the defect amplitudes $\boldsymbol{\xi}$. In this framework, we show that the model in Marconi, Tiso, and Braghin, 2020 (whose deformation formulation was based on Budiansky, 1967) corresponds to a lower order Neumann expansion with integrals evaluated on the nominal volume, and that the higher order approximation we propose here leads to better accuracy and to a larger applicability range.

2 Due to memory limitations, third and fourth order stiffness tensors cannot be computed for the FOM, but they can be constructed in reduced form directly operating at element level Jain, 2015.

3 $\otimes$ denotes the outer product, : and $\vdots$ the double and triple contraction operations. Using Einstein notation, we have that $\mathbf{X} = \mathbf{x}\otimes\mathbf{x}\otimes\mathbf{x}$ (being $\mathbf{x}$ a vector) corresponds to $X_{IJK} = x_I x_J x_K$, $\mathbf{a} = \mathbf{B} : \mathbf{C}$ (being $\mathbf{B}$ and $\mathbf{C}$ a 3- and a 2-dimensional matrix, respectively) to $a_I = B_{Iij}C_{ij}$ and, similarly, $\mathbf{a} = \mathbf{B}\vdots\mathbf{C}$ to $a_I = B_{Iijk}C_{ijk}$ (where $\mathbf{B}$ and $\mathbf{C}$ are now 4- and 3- dimensional, respectively).

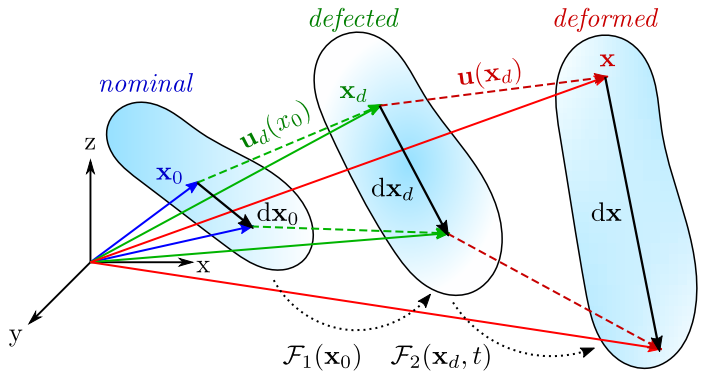

Figure 25: Scheme for the considered deformation setting. A nominal structure, of coordinates $\mathbf{x}_0$, undergoes a deformation described by the transformation map $\mathcal{F}_1$. The structure is now in the deformed configuration (coordinates $\mathbf{x}_d$). A second transformation $\mathcal{F}_2$ and the displacement $\mathbf{u}$ describe the deformation from the defected configuration to the final one.

The work is organized as follows: the modified strain formulation is given in Section 4.2 and approximated using Neumann expansion in Section 4.3. In Section 4.4 the FE discretization is developed and then used in Section 4.5 to construct the reduced order stiffness tensors. The choice and computation of the RB is described in Section 4.6. Finally, numerical studies in Sections 4.7 and 4.8 demonstrate the effectiveness of the proposed approach on a 2D FE clamped beam and on a MEMS gyroscope and computational times are discussed.

4.2 STRAIN FORMULATION: A TWO-STEPS DEFORMATION APPROACH

Strategies to represent the motion of imperfect structures by splitting the total displacement into a constant part, representing a geometrical imperfection, and a variable part, representing the actual displacement, are not new, and have been successfully used in many analytical studies with applications to beams and plates Amabili, 2006; Budiansky, 1967; Camier et al., 2009. In Ref. Amabili, 2006 a shallow shell model is obtained from the von Karman plate model by introducing an additional out-of-plane displacement field directly in the definition of the strains and neglecting higher order terms; in Budiansky, 1967 a similar strategy was used for imperfect beams, where the cancellation of h.o.t. was justified by removing the contribution of the deformations artificially produced by the introduction of the defect. In both cases, the imperfection was taken as a natural mode of the system. In Ref. Camier et al., 2009 such limitation was removed and plates were studied expanding the defect using an arbitrary number of natural modes. Using a different approach, the authors introduce the imperfection directly in the governing equations, adding external forces to restore static equilibrium and, finally, enforcing stresses to zero (as the defected configuration is stress-free). In this work we follow an alternative approach, based on a two steps deformation scheme, which applies to solid mechanics in general.

Let us consider the scheme depicted in Fig. 25. A *nominal* body of coordinates $\mathbf{x}_0 = \{x_0, y_0, z_0\}$ undergoes a first deformation described by the map $\mathcal{F}_1$, which brings the body in a new configuration with coordinates $\mathbf{x}_d = \{x_d, y_d, z_d\} = \mathcal{F}_1(\mathbf{x}_0)$. The displacement corresponding to this operation is $\mathbf{u}_d = \{u_d, v_d, w_d\} = \mathbf{x}_d - \mathbf{x}_0$. We will refer to this second configuration as the *defected configuration*. As it will be detailed later, in our method $\mathbf{u}_d$ will be a user-defined displacement field representing a small shape defect which, superimposed to the nominal geometry,

defines the configuration with respect to which we measure deformation. There is no a priori restriction for the choice of the shape of the field $\mathbf{u}_d$ (which can also change the location of the boundaries)[4], as long as no topological changes are introduced (e.g. holes). Let us now consider a second deformation, described by the map $\mathcal{F}_2$, from the defected configuration to the final one, with coordinates $\mathbf{x}(t) = \{x(t), y(t), z(t)\} = \mathcal{F}_2(\mathbf{x}_d, t)$. We will refer to the latter as to the *deformed or final configuration*, whose displacement is given by $\mathbf{u} = \{u, v, w\} = \mathbf{x} - \mathbf{x}_d$.

Considering the infinitesimal line segment $d\mathbf{x}_0$ in the nominal geometry, we can define the line segments $d\mathbf{x}_d$ and $d\mathbf{x}$ in the defected and deformed configurations as

$$d\mathbf{x}_d = \mathbf{F}_1 d\mathbf{x}_0, \tag{4.2a}$$
$$d\mathbf{x} = \mathbf{F}_2 d\mathbf{x}_d = \mathbf{F}_2\mathbf{F}_1 d\mathbf{x}_0, \tag{4.2b}$$

where the deformation gradients $\mathbf{F}_1$ and $\mathbf{F}_2$ are given by

$$\mathbf{F}_1 = \nabla_0 \mathbf{x}_d = \frac{\partial \mathbf{x}_d}{\partial \mathbf{x}_0} = \mathbf{I} + \frac{\partial \mathbf{u}_d}{\partial \mathbf{x}_0} = \mathbf{I} + \mathbf{D}_d, \tag{4.3a}$$
$$\mathbf{F}_2 = \nabla_d \mathbf{x} = \frac{\partial \mathbf{x}}{\partial \mathbf{x}_d} = \mathbf{I} + \frac{\partial \mathbf{u}}{\partial \mathbf{x}_d} = \mathbf{I} + \mathbf{D}_2. \tag{4.3b}$$

and where $\mathbf{D}_d$ and $\mathbf{D}_2$ are the displacement derivative matrices of the first and second transformations, respectively. Using the chain rule, we can also define

$$\mathbf{D} = \frac{\partial \mathbf{u}}{\partial \mathbf{x}_0} = \frac{\partial \mathbf{u}}{\partial \mathbf{x}_d}\frac{\partial \mathbf{x}_d}{\partial \mathbf{x}_0} = \mathbf{D}_2\mathbf{F}_1, \tag{4.4}$$

so that $\mathbf{D}_2 = \mathbf{D}\mathbf{F}_1^{-1}$ can be referred to the nominal coordinates.

Using Eqs. (4.2)–(4.4), the *stretch* between deformed and defected configurations writes

$$\begin{aligned} \mathcal{S} &= d\mathbf{x}^T d\mathbf{x} - d\mathbf{x}_d^T d\mathbf{x}_d \\ &= d\mathbf{x}_0^T \mathbf{F}_1^T (\mathbf{F}_2^T\mathbf{F}_2 - \mathbf{I})\mathbf{F}_1 d\mathbf{x}_0 \\ &= d\mathbf{x}_0^T (\mathbf{D} + \mathbf{D}^T + \mathbf{D}^T\mathbf{D} + \mathbf{D}_d^T\mathbf{D} + \mathbf{D}^T\mathbf{D}_d) d\mathbf{x}_0. \end{aligned} \tag{4.5}$$

Measuring the deformation with respect to the *defected* configuration, the second order strain tensor $\mathbf{E}_2$ is defined as

$$\mathcal{S} = 2d\mathbf{x}_d^T \mathbf{E}_2 d\mathbf{x}_d = 2d\mathbf{x}_0^T \mathbf{F}_1^T \mathbf{E}_2 \mathbf{F}_1 d\mathbf{x}_0, \tag{4.6}$$

which, rearranged, leads to

$$\mathbf{E}_2 = \frac{1}{2}\left(\mathbf{F}_2^T\mathbf{F}_2 - \mathbf{I}\right) = \frac{1}{2}\mathbf{F}_1^{-T}(\mathbf{D} + \mathbf{D}^T + \mathbf{D}^T\mathbf{D} + \mathbf{D}_d^T\mathbf{D} + \mathbf{D}^T\mathbf{D}_d)\mathbf{F}_1^{-1}. \tag{4.7}$$

Looking at Eqs. (4.5) and (4.7), it can be easily verified that $\mathbf{E}_2$ correctly satisfies the minimum requirements for a strain measure to vanish under a rigid body translation ($\mathbf{F}_2 = \mathbf{I}$) and/or rotation ($\mathbf{F}_2^T\mathbf{F}_2 = \mathbf{R}^T\mathbf{R} = \mathbf{I}$, $\mathbf{R}$ being an orthonormal rotation matrix), *for any* $\mathbf{F}_1$. Eq. (4.7) is indeed an exact expression for the strains from defected to final configuration. Notice however that in this form all the quantities are computed with respect to the nominal coordinates $\mathbf{x}_0$.

4.3 STRAIN APPROXIMATIONS

The introduced strain measure, being referred to the nominal geometry only, paves the way for the pre-computation of the stiffness tensors, as it will be shown in the

4 $\mathcal{F}_1(\mathbf{x}_0)$ can be thought as a transformation corresponding to a static analysis with imposed forces and/or boundary displacements.

following sections. However, as mentioned in the introduction, a tensorial formulation can be applied only when the internal forces display a polynomial dependence on the displacements, which in the present case include both $\mathbf{u}_d$ and $\mathbf{u}$. The inverse of the deformation gradient $\mathbf{F}_1$ in Eq. (4.7) entails a rational dependence on $\mathbf{u}_d$, and therefore needs some attention. Let us consider the following known result:

Neumann expansion

If $\mathbf{P}$ is a square matrix and the Neumann series $\sum_{n=0}^{+\infty} \mathbf{P}^n$ is convergent, we have that

$$(\mathbf{I}-\mathbf{P})^{-1} = \sum_{n=0}^{+\infty} \mathbf{P}^n \tag{4.8}$$

A spectral norm[a] $\varepsilon = \|\mathbf{P}\|_2 < 1$ is a *sufficient* condition for the convergence of the Neumann series. Moreover, it can be shown X. Wang et al., 2013 that truncating the sum to order N the norm error δ_N is bounded as

$$\delta_N = \left\| (\mathbf{I}-\mathbf{P})^{-1} - \sum_{n=0}^{N} \mathbf{P}^n \right\|_2 \leqslant \frac{\varepsilon^{N+1}}{1-\varepsilon} = \delta_{lim}. \tag{4.9}$$

a The spectral norm of a matrix $\mathbf{A}$ is defined as the square root of the largest singular value of $\mathbf{A}^*\mathbf{A}$, being $\mathbf{A}^*$ the conjugate transpose of $\mathbf{A}$, that is: $\|\mathbf{A}\|_2 = \sqrt{\lambda_{max}(\mathbf{A}^*\mathbf{A})}$

Letting $\mathbf{P} = -\mathbf{D}_d$, we can expand $\mathbf{F}_1^{-1}$ using the Neumann series as

$$\mathbf{F}_1^{-1} = (\mathbf{I}+\mathbf{D}_d)^{-1} \approx \sum_{n=0}^{N} (-\mathbf{D}_d)^n. \tag{4.10}$$

The series, under the assumption of small defects (i.e. $\|\mathbf{D}_d\|_2 \ll 1$), is guaranteed to converge. Moreover, we can truncate the sum in Eq. (4.10) to $N = 1$, obtaining:

$$\mathbf{E}_{2,N} = \frac{1}{2}(\mathbf{I}-\mathbf{D}_d)^T(\mathbf{D}+\mathbf{D}^T+\mathbf{D}^T\mathbf{D}+\mathbf{D}_d^T\mathbf{D}+\mathbf{D}^T\mathbf{D}_d)(\mathbf{I}-\mathbf{D}_d), \tag{4.11}$$

which, solving the product, can be rewritten as:

$$\begin{aligned}\mathbf{E}_{2,N} = \frac{1}{2}\Big(&\mathbf{D}+\mathbf{D}^T+\mathbf{D}^T\mathbf{D}+\cancel{\mathbf{D}_d^T\mathbf{D}}+\cancel{\mathbf{D}^T\mathbf{D}_d}\\
&-\cancel{\mathbf{D}_d^T\mathbf{D}}-\mathbf{D}_d^T\mathbf{D}^T-\mathbf{D}_d^T\mathbf{D}^T\mathbf{D}-\mathbf{D}_d^T\mathbf{D}_d^T\mathbf{D}-\cancel{\mathbf{D}_d^T\mathbf{D}^T\mathbf{D}_d}\\
&-\mathbf{D}\mathbf{D}_d-\cancel{\mathbf{D}^T\mathbf{D}_d}-\mathbf{D}^T\mathbf{D}\mathbf{D}_d-\cancel{\mathbf{D}_d^T\mathbf{D}\mathbf{D}_d}-\mathbf{D}^T\mathbf{D}_d\mathbf{D}_d\\
&+\cancel{\mathbf{D}_d^T\mathbf{D}\mathbf{D}_d}+\cancel{\mathbf{D}_d^T\mathbf{D}^T\mathbf{D}_d}+\mathbf{D}_d^T\mathbf{D}^T\mathbf{D}\mathbf{D}_d+\mathbf{D}_d^T\mathbf{D}_d^T\mathbf{D}\mathbf{D}_d+\mathbf{D}_d^T\mathbf{D}^T\mathbf{D}_d\mathbf{D}_d\Big).\end{aligned} \tag{4.12}$$

where we stroke out terms that cancel each other. Finally, neglecting the terms $\mathcal{O}(\mathbf{D}_d^2)$, i.e. assuming that the first transformation $\mathcal{F}_1$ is linear, Eq. (4.12) reduces to:

$$\mathbf{E}_{2,N1} = \frac{1}{2}\left(\mathbf{D}+\mathbf{D}^T+\mathbf{D}^T\mathbf{D}-\mathbf{D}_d^T\mathbf{D}^T-\mathbf{D}\mathbf{D}_d-\mathbf{D}_d^T\mathbf{D}^T\mathbf{D}-\mathbf{D}^T\mathbf{D}\mathbf{D}_d\right) \tag{4.13}$$

The modified Green-Lagrange strain tensor $\mathbf{E}_{2,N1}$ is a polynomial function of the derivatives of the displacement fields $\mathbf{u}$ and $\mathbf{u}_d$, and can be thus used to compute a ROM using tensors. Notice that defect-induced strains are not present when there is no deformation, that is $\mathbf{E}_{2,N1} = \mathbf{0}$ (being proportional to $\mathbf{D}$) when $\mathbf{u} = \mathbf{0}$.

Remark 1 *(on Budiansky approximation).* The strain formulation in Budiansky, 1967, used by Budiansky to study buckling in presence of defects, was obtained by subtracting the strain that a defect would produce on the nominal structure from the

strain of the deformed structure measured with respect to the nominal configuration. It can be shown that truncating the Neummann series to the zero-th order (i.e. setting $N = 0$, so that $\mathbf{F}_1^{-1} = \mathbf{I}$) and using Eq. (4.7) and (4.10), the strain writes:

$$\mathbf{E}_{2,N0} = \frac{1}{2}\left(\mathbf{D} + \mathbf{D}^T + \mathbf{D}^T\mathbf{D} + \mathbf{D}_d^T\mathbf{D} + \mathbf{D}^T\mathbf{D}_d\right), \tag{4.14}$$

which is the same strain tensor we adopted in Marconi, Tiso, and Braghin, 2020 following Budiansky's approximation.

4.4 FINITE ELEMENT FORMULATION

In this and the next Section we derive in detail the FE formulation leading to the parametrized reduced internal elastic forces (Eqs. (4.27) and (4.28)), which are used in the following numerical tests. We start deriving the elastic internal forces (at element-level) for the FE discretization of the *full order* model based on the strain as defined in Eq. (4.13). We remark that this full model represents just an approximation of the *reference* full order model FOM_d (where the defect is embedded directly in the mesh by shifting the position of the nodes). Although not offering any direct advantage over FOM_d, this full model will allow us to compute the parametric ROM, as it will be explained in Section 4.5.

First, it is convenient to switch to Voigt notation, exploiting the symmetry of $\mathbf{E}_{2,N1}$. Let $\theta = \{u_{,x}\, u_{,y}\, u_{,z}\, v_{,x}\, v_{,y}\, v_{,z}\, w_{,x}\, w_{,y}\, w_{,z}\}^T$ be the vectorized form of $\mathbf{D}$ and, similarly, θ_d the vectorized form of $\mathbf{D}_d$.[5] Calling $\mathbf{u}^e \in \mathbb{R}^{n_e}$ and $\mathbf{u}_d^e \in \mathbb{R}^{n_e}$ the nodal displacement and defect vectors, respectively, of a continuum finite element with n_e dofs and $\mathbf{G} \in \mathbb{R}^{9\times n_e}$ the shape function derivatives matrix, the displacement derivative vectors can be written as functions of the displacements:

$$\theta = \mathbf{G}\mathbf{u}^e, \quad \text{and} \quad \theta_d = \mathbf{G}\mathbf{u}_d^e.$$

Equation (4.13) rewrites:

$$\mathbf{E}_{v,N1} = \left(\mathbf{H} + \frac{1}{2}\mathbf{A}(\theta) + \mathbf{A}_2(\theta_d) + \mathbf{A}_3(\theta_d)\mathbf{A}(\theta)\right)\theta = \mathcal{B}(\mathbf{u}^e, \mathbf{u}_d^e)\mathbf{u}^e, \tag{4.15}$$

where $(\bullet)_v$ denotes Voigt notation, $\mathbf{H}$ and $\mathbf{A}$ were defined in chapter 1 and

$$\mathbf{A}_2 = -1 \tag{4.16a}$$

$$\times \begin{bmatrix} u_{d,x} & v_{d,x} & w_{d,x} & 0 & 0 & 0 & 0 & 0 & 0 \\ 0 & 0 & 0 & u_{d,y} & v_{d,y} & w_{d,y} & 0 & 0 & 0 \\ 0 & 0 & 0 & 0 & 0 & 0 & u_{d,z} & v_{d,z} & w_{d,z} \\ u_{d,y} & v_{d,y} & w_{d,y} & u_{d,x} & v_{d,x} & w_{d,x} & 0 & 0 & 0 \\ u_{d,z} & v_{d,z} & w_{d,z} & 0 & 0 & 0 & u_{d,x} & v_{d,x} & w_{d,x} \\ 0 & 0 & 0 & u_{d,z} & v_{d,z} & w_{d,z} & u_{d,y} & v_{d,y} & w_{d,y} \end{bmatrix},$$

$$\mathbf{A}_3 = -1/2 \tag{4.16b}$$

$$\times \begin{bmatrix} 2u_{d,x} & 0 & 0 & v_{d,x} & w_{d,x} & 0 \\ 0 & 2v_{d,y} & 0 & u_{d,y} & 0 & w_{d,y} \\ 0 & 0 & 2w_{d,z} & 0 & u_{d,z} & v_{d,z} \\ 2u_{d,y} & 2v_{d,x} & 0 & u_{d,x}+v_{d,y} & w_{d,y} & w_{d,x} \\ 2u_{d,z} & 0 & 2w_{d,x} & v_{d,z} & u_{d,x}+w_{d,z} & v_{d,x} \\ 0 & 2v_{d,z} & 2w_{d,y} & u_{d,z} & u_{d,y} & v_{d,y}+w_{d,z} \end{bmatrix}$$

such that

$$\begin{aligned} \mathbf{D} + \mathbf{D}^T + \mathbf{D}^T\mathbf{D} &\longleftrightarrow (2\mathbf{H} + \mathbf{A}(\theta))\theta, \\ -\mathbf{D}_d^T\mathbf{D}^T - \mathbf{D}\mathbf{D}_d &\longleftrightarrow 2\mathbf{A}_2(\theta_d)\theta, \\ -\mathbf{D}_d^T\mathbf{D}^T\mathbf{D} - \mathbf{D}^T\mathbf{D}\mathbf{D}_d &\longleftrightarrow 2\mathbf{A}_3(\theta_d)\mathbf{A}(\theta)\theta. \end{aligned}$$

5 For the derivatives of the displacement components, we use the notation $u_{,x} = \frac{\partial u}{\partial x_0}$ and $u_{d,x} = \frac{\partial u_d}{\partial x_0}$ (similar definition for v, w and the other spatial coordinates).

Exploiting the property by which $\mathbf{A}(\theta)\delta\theta = \mathbf{A}(\delta\theta)\theta$, the virtual variation of the strain in Eq. (4.15) writes

$$\begin{aligned}\delta\mathbf{E}_{v,N1} &= (\mathbf{H} + \mathbf{A} + \mathbf{A}_2 + 2\mathbf{A}_3\mathbf{A})\,\mathbf{G}\delta\mathbf{u}^e \\ &= \mathbf{B}(\mathbf{u}, \mathbf{u}_d)\delta\mathbf{u}^e,\end{aligned} \tag{4.17}$$

where $\mathbf{B}$ is the strain-displacements matrix and where we dropped the explicit dependencies on θ_d and θ to ease the notation. The virtual work of internal forces on one element is given by

$$\begin{aligned}W^e_{int} &= \int_{V^e_d} \delta\mathbf{E}^T_{v,N1}\mathbf{S}_v \, dV^e_d \\ &= (\delta\mathbf{u}^e)^T \int_{V^e_d} \mathbf{B}^T\mathbf{S}_v \, dV^e_d,\end{aligned} \tag{4.18}$$

where $\mathbf{S}_v = \mathbf{C}\mathbf{E}_v$ is the Piola-Kirchhoff stress in Voigt notation, being $\mathbf{C}$ the linear elastic constitutive matrix, and where V^e_d is the volume of the element in the defected configuration. The expression for the element internal forces $\mathbf{f}^e_{int}$ follows from the virtual work:

$$\begin{aligned}\mathbf{f}^e_{int} &= \int_{V^e_d} \mathbf{B}^T\mathbf{C}\mathbf{E}_{v,N1} \, dV^e_d\,, \\ &= \int_{V^e_d} \mathbf{B}(\mathbf{u}^e, \mathbf{u}^e_d)^T\,\mathbf{C}\,\mathcal{B}(\mathbf{u}^e, \mathbf{u}^e_d)\mathbf{u}^e \, dV^e_d.\end{aligned} \tag{4.19}$$

The global internal force vector $\mathbf{f}_{int}$ can be then obtained assembling the element-level $\mathbf{f}^e_{int}$ using standard FE procedures. Finally, the tangent stiffness matrix can be computed as usual taking the virtual variation of the internal forces (see Appendix 4.11). Equations (4.15) and (4.19) can be used to perform tests and/or simulations of the full model and to compare the results to the corresponding FOM-d in order to assess the quality of the approximation *before* the reduction of the model. In the next section, the DpROM derived from this formulation is presented.

4.4.1 Element–level tensors

Equation (4.19) in full can be written as

$$\mathbf{f}^e_{int} = \int_{V^e_d} \mathbf{G}^T\,(\mathbf{H} + \mathbf{A} + \mathbf{A}_2 + 2\mathbf{A}_3\mathbf{A})^T\,\mathbf{C}\left(\mathbf{H} + \frac{1}{2}\mathbf{A} + \mathbf{A}_2 + \mathbf{A}_3\mathbf{A}\right)\mathbf{G}\mathbf{u}^e \; dV^e_d. \tag{4.20}$$

In the present form, the displacement vectors $\mathbf{u}^e$ and $\mathbf{u}^e_d$ are encapsulated in the expressions of $\mathbf{A}$, $\mathbf{A}_2$ and $\mathbf{A}_3$. As our aim is to compute the stiffness coefficients of the elastic forces, we need to make them explicit in Eq. (4.20). We can write:

$$\mathbf{A} = \mathbf{L}_1 \cdot \theta = \mathbf{L}_1 \cdot (\mathbf{G}\mathbf{u}^e), \tag{4.21a}$$
$$\mathbf{A}_2 = \mathbf{L}_2 \cdot \theta_d = \mathbf{L}_2 \cdot (\mathbf{G}\mathbf{u}^e_d), \tag{4.21b}$$
$$\mathbf{A}_3\mathbf{A} = (\mathbf{L}_3 \cdot \theta_d) \cdot \theta = (\mathbf{L}_3 \cdot (\mathbf{G}\mathbf{u}^e_d)) \cdot (\mathbf{G}\mathbf{u}^e), \tag{4.21c}$$

where $\mathbf{L}_1, \mathbf{L}_2 \in \mathbb{R}^{6\times 9\times 9}$ and $\mathbf{L}_3 \in \mathbb{R}^{6\times 9\times 9\times 9}$ are constant sparse matrices (see Appendix 4.10)[6].

6 $\mathbf{L}_1$ coincides with $\mathbf{L}$ defined in chapter 1

We can separate the contributions in Eq. (4.20) as

$$\begin{aligned}\mathbf{f}_1^e &= \int_{V_d^e} \mathbf{G}^T \Big(\mathbf{H}^T\mathbf{C}\mathbf{H} + \mathbf{H}^T\mathbf{C}\mathbf{A}_2 \\ &\quad + \mathbf{A}_2^T\mathbf{C}\mathbf{H} + \mathbf{A}_2^T\mathbf{C}\mathbf{A}_2 \Big) \mathbf{G}\mathbf{u}^e \, dV_d^e, \end{aligned} \tag{4.22a}$$

$$\begin{aligned}\mathbf{f}_2^e &= \int_{V_d^e} \mathbf{G}^T \Big(\frac{1}{2}\mathbf{H}^T\mathbf{C}\mathbf{A} + \mathbf{A}^T\mathbf{C}\mathbf{H} + \frac{1}{2}\mathbf{A}_2^T\mathbf{C}\mathbf{A} \\ &\quad + \mathbf{A}^T\mathbf{C}\mathbf{A}_2 + 2\mathbf{A}^T\mathbf{A}_3^T\mathbf{C}\mathbf{H} + \mathbf{H}^T\mathbf{C}\mathbf{A}_3\mathbf{A} \\ &\quad + 2\mathbf{A}^T\mathbf{A}_3^T\mathbf{C}\mathbf{A}_2 + \mathbf{A}_2^T\mathbf{C}\mathbf{A}_3\mathbf{A} \Big) \mathbf{G}\mathbf{u}^e \, dV_d^e, \end{aligned} \tag{4.22b}$$

$$\begin{aligned}\mathbf{f}_3^e &= \int_{V_d^e} \mathbf{G}^T \Big(\frac{1}{2}\mathbf{A}^T\mathbf{C}\mathbf{A} + 2\mathbf{A}^T\mathbf{A}_3^T\mathbf{C}\mathbf{A}_3\mathbf{A} \\ &\quad + \mathbf{A}^T\mathbf{A}_3^T\mathbf{C}\mathbf{A} + \mathbf{A}^T\mathbf{C}\mathbf{A}_3\mathbf{A} \Big) \mathbf{G}\mathbf{u}^e \, dV_d^e, \end{aligned} \tag{4.22c}$$

where $\mathbf{f}_1^e$, $\mathbf{f}_2^e$ and $\mathbf{f}_3^e$ are the linear, quadratic and cubic terms in the displacement $\mathbf{u}^e$, respectively. These can be recasted in tensorial form as

$$\mathbf{f}_1^e = {}_2\mathbf{K}(\mathbf{u}_d^e) \cdot \mathbf{u}^e, \tag{4.23a}$$

$$\mathbf{f}_2^e = {}_3\mathbf{K}(\mathbf{u}_d^e) : (\mathbf{u}^e \otimes \mathbf{u}^e), \tag{4.23b}$$

$$\mathbf{f}_3^e = {}_4\mathbf{K}(\mathbf{u}_d^e) \vdots (\mathbf{u}^e \otimes \mathbf{u}^e \otimes \mathbf{u}^e), \tag{4.23c}$$

where

$${}_2\mathbf{K}(\mathbf{u}_d^e) = {}_{2n}\mathbf{K} + {}_{3d}\mathbf{K} \cdot \mathbf{u}_d^e + {}_{4dd}\mathbf{K} : (\mathbf{u}_d^e \otimes \mathbf{u}_d^e), \tag{4.24a}$$

$${}_3\mathbf{K}(\mathbf{u}_d^e) = {}_{3n}\mathbf{K} + {}_{4d}\mathbf{K} \cdot \mathbf{u}_d^e + {}_{5dd}\mathbf{K} : (\mathbf{u}_d^e \otimes \mathbf{u}_d^e), \tag{4.24b}$$

$${}_4\mathbf{K}(\mathbf{u}_d^e) = {}_{4n}\mathbf{K} + {}_{5d}\mathbf{K} \cdot \mathbf{u}_d^e + {}_{6dd}\mathbf{K} : (\mathbf{u}_d^e \otimes \mathbf{u}_d^e). \tag{4.24c}$$

The element-level tensors in Eqs. (4.24) are named using the left-subscript to denote their dimension with a number and with a letter to specify if the tensor does not multiply the defect vector $\mathbf{u}_d$ (letter "n"), if it multiplies $\mathbf{u}_d$ once (letter "d") or twice (letters "dd"). In particular, a tensor denoted by the letter "n" corresponds to the tensor computed for the *nominal* geometry. For instance, ${}_{3d}\mathbf{K} \in \mathbb{R}^{n_e \times n_e \times n_e}$ is the 3rd-order tensor multiplying $\mathbf{u}_d$ once and ${}_{2n}\mathbf{K} \in \mathbb{R}^{n_e \times n_e}$ is the nominal 2nd-order tensor. Finally, we remark once more that these are *element-level* tensors that, in theory, could be assembled to form the FOM tensors. In practise, however, FOM tensors would require a prohibitive amount of memory and are never computed.

4.5 DPROM FORMULATION

4.5.1 Reduced tensors and internal forces

We now derive the reduced internal forces and tensors via Galerkin projection. Let $\mathbf{V} \in \mathbb{R}^{n \times m}$ be the RB for $\mathbf{u}^F \in \mathbb{R}^n$, with $m \ll n$ vectors (or *modes*), and let $\mathbf{U} \in \mathbb{R}^{n \times m_d}$ be a basis of m_d user-defined defect shapes, collected column-wise, for $\mathbf{u}_d^F \in \mathbb{R}^n$. The selection for the modes in $\mathbf{V}$ will be discussed in Section 4.6. We have then that $\mathbf{u}^F \approx \mathbf{V}\boldsymbol{\eta}$, $\mathbf{u}_d^F = \mathbf{U}\boldsymbol{\xi}$, and, referring to element level quantities, we can reduce $\mathbf{u}^e$ and $\mathbf{u}_d^e$ as:

$$\mathbf{u}^e \approx \mathbf{V}^e\boldsymbol{\eta}, \text{ with } \mathbf{V}^e \in \mathbb{R}^{n_e \times m}, \boldsymbol{\eta} \in \mathbb{R}^m, \tag{4.25a}$$

$$\mathbf{u}_d^e = \mathbf{U}^e\boldsymbol{\xi}, \text{ with } \mathbf{U}^e \in \mathbb{R}^{n_e \times m_d}, \boldsymbol{\xi} \in \mathbb{R}^{m_d} \tag{4.25b}$$

being $\mathbf{V}^e$ and $\mathbf{U}^e$ the partitions of $\mathbf{V}$ and $\mathbf{U}$ pertaining to the element, $\boldsymbol{\eta}$ and $\boldsymbol{\xi}$ the reduced coordinates.

Plugging Eqs. (4.21) and (4.25) into Eqs. (4.22), we can directly identify the reduced order tensor coefficients for $\boldsymbol{\eta}$ and $\boldsymbol{\xi}$ (and their combinations). Defining the

projections of shape function derivative matrix $\mathbf{G}$ over the two basis as $\mathbf{\Gamma} = \mathbf{G}\mathbf{V}^e$ and $\mathbf{\Upsilon} = \mathbf{G}\mathbf{U}^e$, using Einstein's notation we obtain:

$$ {}_{2n}Q^e_{IJ} = \int_{V^e_d} \Gamma_{iI} H_{ji} C_{jk} H_{kl} \Gamma_{kJ} \, dV^e_d, \tag{4.26a} $$

$$ {}_{3d}Q^e_{IJ\underline{K}} = \int_{V^e_d} \Gamma_{iI} \left(H_{ji} C_{jk} L_{2kla} \Upsilon_{aK} + L_{2jia} \Upsilon_{aK} C_{jk} H_{kl} \right) \Gamma_{lJ} \, dV^e_d, \tag{4.26b} $$

$$ {}_{4dd}Q^e_{IJ\underline{KL}} = \int_{V^e_d} \Gamma_{iI} L_{2jia} \Upsilon_{aK} C_{jk} L_{2klb} \Upsilon_{bL} \Gamma_{lJ} \, dV^e_d, \tag{4.26c} $$

$$ {}_{3n}Q^e_{IJK} = \int_{V^e_d} \Gamma_{iI} \Big(\frac{1}{2} H_{ji} C_{jk} L_{1kla} \Gamma_{aK} + L_{1jia} \Gamma_{aK} C_{jk} H_{kl} \Big) \Gamma_{lJ} \, dV^e_d, \tag{4.26d} $$

$$ \begin{aligned} {}_{4d}Q^e_{IJK\underline{L}} = \int_{V^e_d} \Gamma_{iI} \Big(& \frac{1}{2} L_{2jia} \Upsilon_{aL} C_{jk} L_{1klb} \Gamma_{bK} + L_{1jia} \Gamma_{aK} C_{jk} L_{2klb} \Upsilon_{bL} \\ & + 2 L_{3jiab} \Upsilon_{bL} \Gamma_{aK} C_{jk} H_{kl} + H_{ji} C_{jk} L_{3klab} \Upsilon_{bL} \Gamma_{aK} \Big) \Gamma_{lJ} \, dV^e_d, \end{aligned} \tag{4.26e} $$

$$ \begin{aligned} {}_{5dd}Q^e_{IJK\underline{LM}} = \int_{V^e_d} \Gamma_{iI} \Big(& 2 L_{3jiab} \Upsilon_{bL} \Gamma_{aK} C_{jk} L_{2klc} \Upsilon_{cM} \\ & + L_{2jia} \Upsilon_{aL} C_{jk} L_{3klbc} \Upsilon_{cM} \Gamma_{bK} \Big) \Gamma_{lJ} \, dV^e_d, \end{aligned} \tag{4.26f} $$

$$ {}_{4n}Q^e_{IJKL} = \frac{1}{2} \int_{V^e_d} \Gamma_{iI} L_{1jia} \Gamma_{aK} C_{jk} L_{1klb} \Gamma_{bL} \Gamma_{lJ} \, dV^e_d, \tag{4.26g} $$

$$ \begin{aligned} {}_{5d}Q^e_{IJKL\underline{M}} = \int_{V^e_d} \Gamma_{iI} \Big(& L_{1jia} \Gamma_{aK} C_{jk} L_{3klbc} \Upsilon_{cM} \Gamma_{bL} \\ & + L_{3jiab} \Upsilon_{bM} \Gamma_{aK} C_{jk} L_{1klc} \Gamma_{lL} \Big) \Gamma_{lJ} \, dV^e_d, \end{aligned} \tag{4.26h} $$

$$ {}_{6dd}Q^e_{IJKL\underline{MN}} = 2 \int_{V^e_d} \Gamma_{iI} L_{3jiab} \Upsilon_{bM} \Gamma_{aL} C_{jk} L_{3klcd} \Upsilon_{dN} \Gamma_{cK} \Gamma_{lJ} \, dV^e_d, \tag{4.26i} $$

where, for convenience, tensor dimensions of size m are denoted by capital letter subscripts, dimensions of size m_d by underlined capital letter ones. So, for example, ${}_{4dd}\mathbf{Q}^e \in \mathbb{R}^{m \times m \times m_d \times m_d}$.

The global reduced tensors of the full structure can then be computed directly summing up the element contributions as

$$ {}_{\star}\mathbf{Q} = \sum_{e=1}^{N_{el}} {}_{\star}\mathbf{Q}^e $$

where ${}_{\star}\mathbf{Q}^e$ is one of the element-level tensors in Eqs. (4.26), ${}_{\star}\mathbf{Q}$ the assembled tensor for the FOM and N_{el} is the total number of elements. Notice that this procedure is highly parallelizable, as ${}_{\star}\mathbf{Q}^e$ can be computed separately and summed up in the end. Reduced (global) internal forces $\mathbf{f}_{int,r}$ can therefore be defined as

$$ \mathbf{f}_{int,r} = {}_2\mathbf{Q}(\boldsymbol{\xi}) \cdot \boldsymbol{\eta} + {}_3\mathbf{Q}(\boldsymbol{\xi}) : (\boldsymbol{\eta} \otimes \boldsymbol{\eta}) + {}_4\mathbf{Q}(\boldsymbol{\xi}) \vdots (\boldsymbol{\eta} \otimes \boldsymbol{\eta} \otimes \boldsymbol{\eta}), \tag{4.27} $$

where

$$ {}_2\mathbf{Q}(\boldsymbol{\xi}) = \left[{}_{2n}\mathbf{Q} + {}_{3d}\mathbf{Q} \cdot \boldsymbol{\xi} + {}_{4dd}\mathbf{Q} : (\boldsymbol{\xi} \otimes \boldsymbol{\xi}) \right], \tag{4.28a} $$

$$ {}_3\mathbf{Q}(\boldsymbol{\xi}) = \left[{}_{3n}\mathbf{Q} + {}_{4d}\mathbf{Q} \cdot \boldsymbol{\xi} + {}_{5dd}\mathbf{Q} : (\boldsymbol{\xi} \otimes \boldsymbol{\xi}) \right], \tag{4.28b} $$

$$ {}_4\mathbf{Q}(\boldsymbol{\xi}) = \left[{}_{4n}\mathbf{Q} + {}_{5d}\mathbf{Q} \cdot \boldsymbol{\xi} + {}_{6dd}\mathbf{Q} : (\boldsymbol{\xi} \otimes \boldsymbol{\xi}) \right], \tag{4.28c} $$

while the reduced tangent stiffness matrix ${}_t\mathbf{Q}$ can be written simply as

$$ {}_tQ_{IJ} = {}_2Q_{IJ} + ({}_3Q_{IJj} + {}_3Q_{IjJ})\eta_j + ({}_4Q_{IJij} + {}_4Q_{IiJj} + {}_4Q_{IijJ})\eta_i\eta_j. \tag{4.29} $$

Upon inspection of Eq. (4.27), it can be seen that elastic internal forces are cubic in $\boldsymbol{\eta}$ and quadratic in $\boldsymbol{\xi}$, thus producing quintic terms in $(\boldsymbol{\eta}, \boldsymbol{\xi})$.

Remark 2 *(on tensor computation).* Equations (4.26) give directly the stiffness tensors in reduced form, and this is in general highly desirable as their integration over the element volume takes multiple evaluations (e.g. through Gauss quadrature). Since the computational complexity highly depends on the number of dofs of the tensor, it is preferable to integrate directly the reduced ones as long as the number of reduced coordinates m is lower than the number of element's dofs n_e (e.g. $n_e = 60$ for a serendipity hexahedron with quadratic shape functions). In case $m > n_e$, it is computationally more efficient to compute the element tensors first (using Eqs (4.26) and replacing both $\boldsymbol{\Gamma}$ and $\boldsymbol{\Upsilon}$ with $\mathbf{G}$) for Gauss integration, then project the element tensors using $\mathbf{V}$ and $\mathbf{U}$ accordingly. A similar reasoning can be done for m_d, but under the very likely hypothesis that $m_d \ll n_e$ it results almost always convenient to adopt the reduced form.

4.5.2 Volume integration

The tensors in Eqs. (4.27)-(4.28) must be computed over the defected volume V_d. As such, the model cannot be profitably used, as for each new instance of the parameter vector $\boldsymbol{\xi}$ the volume V_d would change and a new integration would be required. This way, one would need to compute a new ROM for each parameter realization, which is in direct contrast to the very idea of pROM. To circumvent this problem, one can adopt the following approximation.

Let ${}_\star\mathbf{Q}^e_\int$ be the generic expression of an element tensor *to be integrated* over the volume V^e_d. We can compute the global reduced tensor ${}_\star\mathbf{Q}$ as:

$$\begin{aligned} {}_\star\mathbf{Q} &= \sum_{e=1}^{N_{el}} \int_{V_d} {}_\star\mathbf{Q}^e_\int \, dV_d \\ &= \sum_{e=1}^{N_{el}} \int_{V_o} {}_\star\mathbf{Q}^e_\int \det(\mathbf{F}_1) \, dV_o. \end{aligned} \tag{4.30}$$

where N_{el} is the total number of elements. The determinant of $\mathbf{F}_1$ can now be approximated retaining only first order terms. To the purpose of illustration, let us consider the following 2D example where the global defect is given by the linear superposition of two shape defects, that is:

$$\mathbf{u}_d(\mathbf{x}_0, \boldsymbol{\xi}) = \begin{Bmatrix} u_d \\ v_d \end{Bmatrix} = \begin{bmatrix} f_u^{(1)}(\mathbf{x}_0) & f_u^{(2)}(\mathbf{x}_0) \\ f_v^{(1)}(\mathbf{x}_0) & f_v^{(2)}(\mathbf{x}_0) \end{bmatrix} \begin{Bmatrix} \xi_1 \\ \xi_2 \end{Bmatrix} = \left[\mathbf{f}^{(1)}, \mathbf{f}^{(2)} \right] \boldsymbol{\xi}, \tag{4.31}$$

where we denote with $\mathbf{f}^{(i)} = [f_u^{(i)}, f_v^{(i)}]^T$ the vector of the functions describing the i-th shape-defect for the x-displacement u_d and the y-displacement v_d, respectively. We can approximate the determinant of $\mathbf{F}_1$ as

$$\det(\mathbf{F}_1) = 1 + u_{d,x} + v_{d,y} + u_{d,x} v_{d,y} - u_{d,y} v_{d,x},$$

$$\begin{aligned} \det(\mathbf{F}_1) = \; & 1 + \xi_1 \left(f^{(1)}_{u,x} + f^{(1)}_{v,y} \right) + \xi_2 \left(f^{(2)}_{u,x} + f^{(2)}_{v,y} \right) \\ & + \xi_1^2 \left(f^{(1)}_{u,x} f^{(1)}_{v,y} - f^{(1)}_{u,y} f^{(1)}_{v,x} \right) + \xi_2^2 \left(f^{(2)}_{u,x} f^{(2)}_{v,y} - f^{(2)}_{u,y} f^{(2)}_{v,x} \right) \\ & + \xi_1 \xi_2 \left(f^{(1)}_{u,x} f^{(2)}_{v,y} + f^{(2)}_{u,x} f^{(1)}_{v,y} - f^{(1)}_{u,y} f^{(2)}_{v,x} - f^{(2)}_{u,y} f^{(1)}_{v,x} \right), \end{aligned}$$

$$\det(\mathbf{F}_1) \approx 1 + \xi_1 \left(f^{(1)}_{u,x} + f^{(1)}_{v,y} \right) + \xi_2 \left(f^{(2)}_{u,x} + f^{(2)}_{v,y} \right),$$

where we neglected higher order terms, consistently with the assumption of small defects (already introduced for the Neumann expansion of the strains). Generalizing this result for m_d defects, we can write

$$\det(\mathbf{F}_1) \approx 1 + \sum_{i=1}^{m_d} \xi_i \left(\operatorname{div} \mathbf{f}^{(i)} \right), \tag{4.32}$$

so that Eq. (4.30) can be approximated as:

$$ {}_\star\mathbf{Q} \approx {}_\star\mathbf{Q}' + \sum_{i=1}^{m_d} \xi_i \left({}_\star\mathbf{Q}''_i \right), \tag{4.33} $$

where

$$ {}_\star\mathbf{Q}' = \sum_{e=1}^{N_{el}} \int_{V_0} {}_\star\mathbf{Q}^e_\int \, dV_0, \tag{4.34a} $$

$$ {}_\star\mathbf{Q}''_i = \sum_{e=1}^{N_{el}} \int_{V_0} {}_\star\mathbf{Q}^e_\int \left(\operatorname{div} \mathbf{f}^{(i)} \right) \, dV_0. \tag{4.34b} $$

${}_\star\mathbf{Q}'$ is the tensor evaluated on the nominal volume and ${}_\star\mathbf{Q}''_i$ is the contribution of the i-th defect, which can be computed again *once and for all* offline, referring to the nominal volume. The additional computational burden to compute ${}_\star\mathbf{Q}''_i$ grows less than linearly with the number of defects, since in a quadrature integration scheme we can use the ${}_\star\mathbf{Q}^e_\int$ evaluated at integration points for both Eqs. (4.34). The additional computations therefore involve only scalar by tensor multiplications and tensor sums, so that most of the added computational time is merely due to memory access management. Notice that one could also compute all the additional tensors needed to describe $\det(\mathbf{F}_1)$ with no approximation (even tough this is in most cases unnecessary, for h.o.t. do not improve accuracy significantly). However, the first order approximation we presented has the advantage to introduce only one new term for every additional defect.

Remark 3 *(on computational efficiency).* The corrective terms $\mathbf{Q}''_i$ in Eq. (4.33) are null for an isochoric transformation between nominal and defected domain ($\det(\mathbf{F}_1)$=1). In practice, one can set up a procedure to avoid the computation of these terms to speed up the construction of the reduced tensors.

Remark 4 *(on Budiansky approximation).* According to the framework presented in Budiansky, 1967 and used in Marconi, Tiso, and Braghin, 2020, integration can only be carried out on the nominal volume V_0. This constitutes an additional approximation on top of the lower-order expansion discussed in Remark 1. As it will be later shown in Section 3.8, when the imposed defect does not represent an (almost) isochoric transformation and/or is not sufficiently small, integration over V_0 is a too coarse approximation and yields large errors.

4.5.3 Equations of motion

Finally, the equations of motion for the parametric reduced order system write:

$$ \mathbf{M}_r \ddot{\boldsymbol{\eta}}(t) + \mathbf{C}_r \dot{\boldsymbol{\eta}}(t) + \mathbf{f}_{int,r}(\boldsymbol{\eta}(t), \boldsymbol{\xi}) = \mathbf{f}_{ext,r}(t), \tag{4.35} $$

where $\mathbf{M}_r = \mathbf{V}^T \mathbf{M}_d \mathbf{V}$ and $\mathbf{C}_r = \mathbf{V}^T \mathbf{C}_d \mathbf{V}$ are the reduced mass and damping matrices, $\mathbf{f}_{ext,r}(t) = \mathbf{V}^T \mathbf{f}_{ext}(t)$ the reduced external forces acting on the system. Notice that since mass and damping matrices must be integrated over V_d, new matrices must be computed for each new parameter realization. However, being these matrices constant during the analysis, this additional cost is negligible.

4.5.4 Truncated version

Before concluding this section, we present a lighter version of the proposed model, with the aim to alleviate the offline computational burden. Considering Eq. (4.13),

Table 4: Acronyms for the different models considered in the numerical studies.

Model	Description
FOM$_\mathrm{d}$	Full Order Model with defect included by shifting the mesh nodes from the nominal configuration (no approximation). It is the reference model.
ROM$_\mathrm{d}$	Reduced Order Model computed from FOM-d. Its reduction basis comprises VMs and MDs.
DpROM-o$_\star$	Defect parametric Reduced Order Model, based on the o-th order Neumann expansion (see Eq. (4.14)). Its reduction basis comprises VMs, MDs and DSs. Tensors are up to the 4-th order (see chapter 3).
DpROM-1$_\star$	Defect parametric Reduced Order Model, based on the 1-st order Neumann expansion (see Eq. (4.13)). Its reduction basis comprises VMs, MDs and DSs. Tensors are up to the 6-th order (see Eqs. (4.26)).
DpROM-1t$_\star$	Truncated version of DpROM-1$_\star$ (see Section 4.5.4). Tensors are up to the 4-th order.
$\star = \mathbf{d}$	indicates that the model is computed integrating over the *defected* volume V_d (see Section 4.5.2).
$\star = \mathbf{n}$	indicates that the model is computed integrating over the *nominal* volume V_0. This is allowed for isochoric transformations and is otherwise an approximation (see Section 4.5.2).

we can make the further assumption that $\mathcal{O}(\mathbf{D}_\mathrm{d}\mathbf{D}^2)$ terms can be neglected, obtaining

$$\mathbf{E}_{2,\mathrm{N1t}} = \frac{1}{2}\left(\mathbf{D} + \mathbf{D}^\mathsf{T} + \mathbf{D}^\mathsf{T}\mathbf{D} - \mathbf{D}_\mathrm{d}^\mathsf{T}\mathbf{D}^\mathsf{T} - \mathbf{D}\mathbf{D}_\mathrm{d}\right). \tag{4.36}$$

All the subsequent equations are consequently modified by putting $\mathbf{A}_3 = \mathbf{o}$ and $\mathbf{L}_3 = \mathbf{o}$, resulting in the fact that the tensors in Eqs. (4.26) can be simplified. In particular, the last two terms in ${}_{4\mathrm{d}}\mathbf{Q}$ (Eq. (4.26e)) and the entire ${}_{5\mathrm{d}}\mathbf{Q}$, ${}_{5\mathrm{dd}}\mathbf{Q}$ and ${}_{6\mathrm{dd}}\mathbf{Q}$ tensors are null. In this sense, the reduced elastic internal forces in Eq. (4.27) are "truncated". As 5-th and 6-th order tensors are the most expensive to construct, neglecting them greatly reduces offline costs. As it will be shown in Section 3.8, this further approximation, although empirical, does not appreciably deteriorate the quality of the results.

4.5.5 Models and nomenclature

In Sections 3.7 and 3.8 we study two numerical examples using different levels of approximation for our Defect-parametric ROM, DpROM. Specifically, we use the 0-th order Neumann expansion for the strains (Eq. (4.14)), the 1-st order one (Eq. (4.13)) and its truncated version, discussed in the previous section. The three variations will also be tested in the case of integration over V_d and over V_0 (which is a further approximation). The acronyms to denote each model are shown in Table 4, where, for convenience, information about the RB of each model (discussed in the next section) is also reported. Finally, notice that the model we presented in Marconi, Tiso, and Braghin, 2020 (chapter 3) corresponds to DpROM-o$_\mathrm{n}$.

4.6 REDUCTION BASIS

To construct the system described so far it is necessary to select the bases $\mathbf{V}$ and $\mathbf{U}$. The latter is simply a collection of *user-defined* displacement vectors, each representing one specific defect, so that the final defected shape is given by a linear superposition (see Eq. (4.25b)). The (properly said) RB is $\mathbf{V}$, whose choice may not be trivial, as it must correctly represent the system response over a range of parameters without the possibility to be changed (since a change would require to recompute the stiffness tensors). As previously done in Marconi, Tiso, and Braghin, 2020, our choice is to use a modal-based approach including VMs, MDs and Defect-

Sensitivities (DSs) Hay et al., 2010 in the RB, as this solution offers a way to construct a basis in a direct way, that is without convoluted basis selection strategies, the need of computing all (or an excessively high number of) eigenvectors or the need for previously computed simulations. We remark however that, in principle, one could use also other RBs, as long as they are valid over the parameter space.

Let us consider the following eigenvalue problem

$$\left(\mathbf{K}_t - \omega_i^2 \mathbf{M}\right) \boldsymbol{\Phi}_i = \mathbf{o} \tag{4.37}$$

where $\mathbf{K}_t = \mathbf{K}_t(\mathbf{u}, \mathbf{u}_d)$ is the tangent stiffness matrix, $\mathbf{M}$ the mass matrix, ω_i the i-th eigenfrequency and $\boldsymbol{\Phi}_i$ the corresponding eigenvector. Static Modal Derivatives θ_{ij} (MDs) are computed neglecting the mass term, by taking the derivative of Eq. (4.37) with respect to η_j and evaluating the resulting expression at equilibrium (i.e. $\eta_j = 0$) and for $\boldsymbol{\xi} = \mathbf{o}$:

$$\theta_{ij} = \left.\frac{\partial \boldsymbol{\Phi}_i}{\partial \eta_j}\right|_0 = -\mathbf{K}_0^{-1} \left.\frac{\partial \mathbf{K}_t(\boldsymbol{\Phi}_j \eta_j, \mathbf{o})}{\partial \eta_j}\right|_0 \boldsymbol{\Phi}_i \,, \tag{4.38}$$

being $\mathbf{K}_0 = \mathbf{K}_t(\mathbf{o}, \mathbf{o})$. Retaining m_Φ VMs in the basis $\mathbf{V}$, $m_\Phi(m_\Phi + 1)/2$ MDs can be computed.

Defect Sensitivities (DSs) $\Xi_{i,j}$ can be obtained following a similar procedure, differentiating each VM $\boldsymbol{\Phi}_i$ with respect to each defect amplitude ξ_j:

$$\Xi_{i,j} = \left.\frac{\partial \boldsymbol{\Phi}_i}{\partial \xi_j}\right|_0 = -\mathbf{K}_0^{-1} \left.\frac{\partial \mathbf{K}_t(\mathbf{o}, \mathbf{U}_j \xi_j)}{\partial \xi_j}\right|_0 \boldsymbol{\Phi}_i. \tag{4.39}$$

A total of $m_d m_\Phi$ DSs can be computed this way, being m_d the number of defects in $\mathbf{U}$. Expressions for the tangent stiffness derivatives are given in Appendix 4.11.

Remark 5 *(on higher derivatives).* Given the increased accuracy of the model, larger defect magnitudes can be considered as compared to Marconi, Tiso, and Braghin, 2020. To fully exploit the increased applicability range, a richer RB might be necessary, reason why we here introduce second Defect-Sensitivities (DS2s) and MDs-Sensitivities (MDSs). Let us take the derivative of Eq. (4.38) with respect to the k-th defect amplitude ξ_k. We define the MDS $\theta_{ij,k}$ as:

$$\theta_{ij,k} = \left.\frac{\partial \theta_{ij}}{\partial \xi_k}\right|_0 = -\mathbf{K}_0^{-1} \left(\left.\frac{\partial \mathbf{K}_t}{\partial \xi_k}\right|_0 \theta_{ij} + \left.\frac{\partial^2 \mathbf{K}_t}{\partial \eta_j \partial \xi_k}\right|_0 \boldsymbol{\Phi}_i + \left.\frac{\partial \mathbf{K}_t}{\partial \eta_j}\right|_0 \Xi_{i,k} \right). \tag{4.40}$$

Notice that $\theta_{ij,k} \neq \theta_{ji,k}$. In the same manner, the second Defect Sensitivities (DS2s) with respect to ξ_k write:

$$\Xi_{i,jk} = \left.\frac{\partial \Xi_{i,j}}{\partial \xi_k}\right|_0 = -\mathbf{K}_0^{-1} \left(\left.\frac{\partial \mathbf{K}_t}{\partial \xi_k}\right|_0 \Xi_{i,j} + \left.\frac{\partial^2 \mathbf{K}_t}{\partial \xi_j \partial \xi_k}\right|_0 \boldsymbol{\Phi}_i + \left.\frac{\partial \mathbf{K}_t}{\partial \xi_j}\right|_0 \Xi_{i,k} \right). \tag{4.41}$$

It is evident that the blind inclusion of DS2s and/or MDSs in the RB would add an unacceptable number of unknowns, especially when considering MDSs. Depending on the type of the analysis (linear/nonlinear), on the kind of the defect (i.e. affecting the linear or the nonlinear dynamics) and on the entity of the defect itself (large/small), one can decide whether to include some vectors or not. Preselection strategies to reduce the basis size, as the one presented in Tiso, 2011 and Jain, Tiso, Rutzmoser, et al., 2017, are beyond the scopes of this work and are not treated hereafter.

4.7 NUMERICAL TESTS – I

We consider now a FE model of an aluminum beam, of length $l_x = 2\,\mathrm{m}$, thickness $t_y = 50\,\mathrm{mm}$ and width $w_z = 0.2\,\mathrm{m}$, clamped at both ends. We use a 2D plain strain

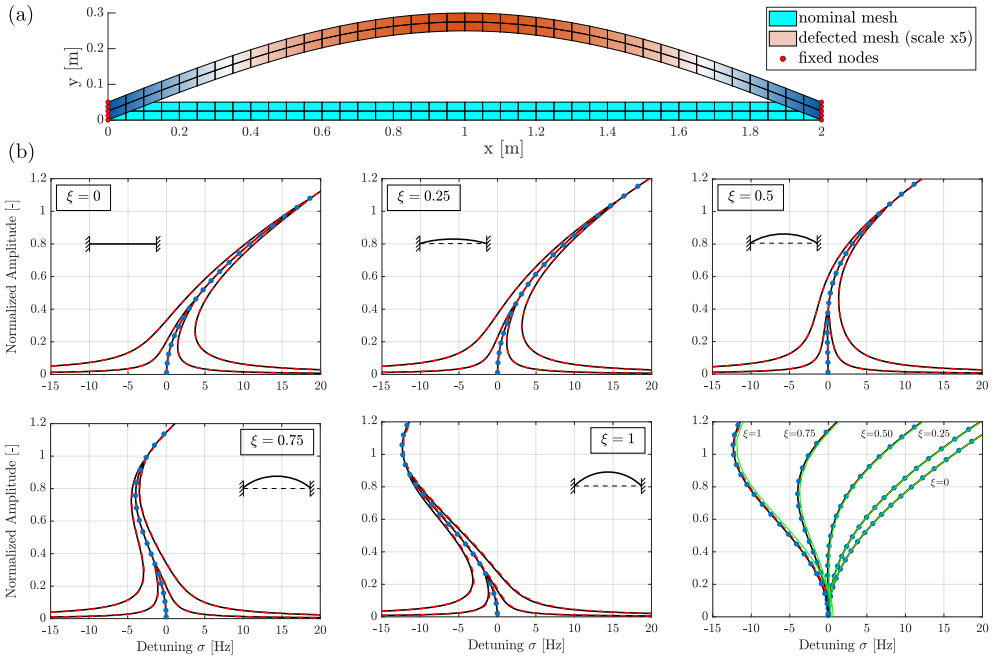

Figure 26: (a) Model-I: Nominal mesh and defected mesh with $\xi = 1$ (and a x5 scale factor). (b) Frequency Responses and backbone curves for different defect amplitudes ξ using the Harmonic Balance method (7 harmonics) for: ROM_d (——), DpROM-1_n (- - -), DpROM-o_n (——, only backbones). Backbones have been computed also for the FOM_d (●●●) using the *shooting method* for validation. The vertical displacement of the mid-span of the beam is shown (first harmonic coefficient of the Fourier series, normalized over the beam thickness t_y). For each plot, the detuning parameter is $\sigma = f - f_{01,d}$, being f [Hz] the forcing frequency and $f_{01,d}$ [Hz] the first eigenfrequency of the FOM_d (corresponding to the selected ξ). The bottom-right figure collects the backbone curves for comparison.

model, with a mesh of 80 quadrilateral elements with quadratic shape functions (630 dofs). A Rayleigh damping matrix $\mathbf{C}_d = \alpha\mathbf{M}_d + \beta\mathbf{K}_0$ is introduced by imposing a quality factor $Q_1 = Q_2 = 100$ on the first and second modes of the linear system ($\alpha = 3.1$, $\beta = 6.3 \cdot 10^{-6}$). A nodal load F is applied to the mid-span of the beam (with $F = 1$ kN and $F = 4$ kN for the forced responses). A single shape defect defined as the vertical translation of the nodes $v_d(x, \xi) = \xi t_y \sin(\pi/l_x x)$ is imposed, deforming the nominal geometry of the straight beam into a shallow arch. Notice that this kind of defect represents an isochoric transformation, therefore integration over the nominal volume V_0 is used for this example (see Section 4.5.2).

Again, refer to Table 4 for the acronyms used for the models of this and the next numerical study. For $\xi = \{0, 0.25, 0.5, 0.75, 1\}$, backbones and Frequency Responses (FR) are computed for ROM_d, DpROM-1_n and DpROM-o_n, constructed using 5 VMs, 15 MDs, and 5 DSs (only for DpROMs), i.e.

$$\mathbf{V} = [\boldsymbol{\Phi}_1, \dots, \boldsymbol{\Phi}_5, \theta_{11}, \theta_{12}, \dots, \theta_{45}, \theta_{55}, \boldsymbol{\Xi}_{1,1}, \dots, \boldsymbol{\Xi}_{5,1}], \tag{4.42}$$

for a total of 25 RB modes (i.e. $m_\Phi = 5$ VMs, $m_\Phi(m_\Phi + 1)/2 = 15$ MDs and $m_d m_\Phi = 5$ DSs, being $\mathbf{U} \in \mathbb{R}^{n \times m_d}$ and $m_d = 1$).

Remark 6 *(on basis choice).* Reduction with MDs was historically introduced as an extension of time-domain linear modal analysis to the field of (mild) geometric non-linearities Idelsohn and Cardona, 1985. As such, the selection criterion is frequency-based, meaning that modes are chosen accordingly to the spectral content of the forcing. Usually, vibration modes are retained up to 3-5 times the highest frequency of interest, as a rule of thumb. All the MDs related to the retained VMs are then included (as well as all the DSs for the DpROMs). Also notice that MDs, loosely

Table 5: Average computational times. The data of the two DpROMs, being very similar, are clustered togeter. For the FR, the times refer to the higher forcing (F = 4 kN). ROM_d, DpROM-1/o_n and FOM_d have 20, 25 (due to the 5 additional DSs) and 630 dofs, respectively. Notice that, being the size of the FOM_d very small, no significant conclusions in terms of speedups can be drawn from this data (refer to the next section for a detailed discussion).

Model–I		**ROM_d**	**DpROM-1/o_d**	**FOM_d**
Harmonic Balance (HB)	*Freq. Response*	649 s	673 s	–
	Backbone	237 s	273 s	–
Shooting	*Backbone*	31 min	35 min	83 h 18 min
ROM construction		0.97 s	6.5 s / 2 s	–

speaking, represent the second order Taylor expansion of the solution Idelsohn and Cardona, 1985; Jain, Tiso, Rutzmoser, et al., 2017 and results are thus expected to deteriorate for high amplitudes of the response. In the present case, being our analysis restricted to the first mode, we include all the vibration modes up to the 5th, being $\omega_{05}/\omega_{01} \approx 9$. This is a rather conservative choice which allows us to study the parametric variations of the model with relative comfort and up to relatively large levels of vibrations. Indeed, it could be shown that retaining VMs up to the 3rd ($\omega_{03}/\omega_{01} \approx 3.7$) is already sufficient to retrieve a good accuracy, showing slight departure at larger amplitudes (with reference to the results in Fig. 3, FOM and ROM backbones start departing for normalized amplitudes greater than 0.8, ultimately leading to a 1Hz-difference at an amplitude of 1.2). Interestingly, the aforementioned empiric rules used to select VMs find theoretical confirmation in Shen et al., 2021; Vizzaccaro et al., 2020, where it is argued that a slow-fast decomposition assumption have to be made for the MD-based *quadratic manifold* approach to work, indicating a threshold ratio of 4 between the linear eigenfrequencies (i.e. $\omega_p/\omega_s \geqslant 4$, $p \neq s$). However, to the best of the authors' knowledge, there is no guarantee that this limit remains valid also in the MD-based *linear manifold* approach used in this work (i.e., where MDs are appended to the RB and additional independent reduced coordinates are introduced).

The Harmonic Balance (HB) method was used (with 7 harmonics) using the NLvib Matlab tool Krack and Gross, 2019 (slightly modified to adapt the direct use of tensors) and our in-house Matlab FE code. To validate the results of the ROMs, the Shooting Method is used to find the backbones of the corresponding FOM-d. Results are shown in Fig. 26. Computations were carried out in Matlab 2020a on a local machine equipped with an Intel(R) Xeon(R) Silver 4214 CPU @2.20 GHz and 256 GB RAM @2666 MHz. Tensors were built in a Julia sub-routine, called by the main Matlab code, which uses the TensorOperations package Jutho et al., 2019 for the tensor contraction. At present, the tensor construction is implemented serially, therefore leaving space for possible future speed-ups exploiting parallel computing, as mentioned earlier. We remark once more that tensors in Eqs. (4.28) are evaluated *offline* before performing HB/shooting: online evaluations use only the 2-nd, 3-rd and 4-th order reduced stiffness tensors for both ROM_d and the DpROMs.

As it can be observed, the shift from hardening to softening behavior is well captured by all the models, with a minor loss of accuracy of the DpROMs as ξ increases. In particular, DpROM-o_n shows a significant frequency offset of the first linear eigenfrequency which remains constant throughout the backbone curve (the same happens for the FRs, but we omitted to plot them for the sake of figures clarity). The main goal of the present test was to assess the accuracy of the method verifying the results against the FOM and over a range of frequencies. However, computational times are collected in Table 5 for completeness. Run times for the shooting method with the (Dp)ROMs are included for comparison. These figures, however, must be taken just as an indication, first because of the difference between

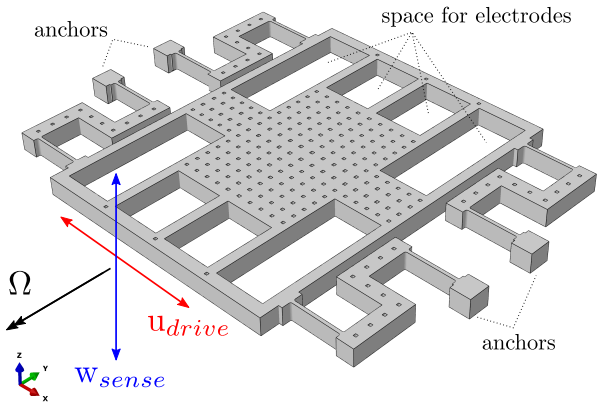

(a) Gyroscope model.

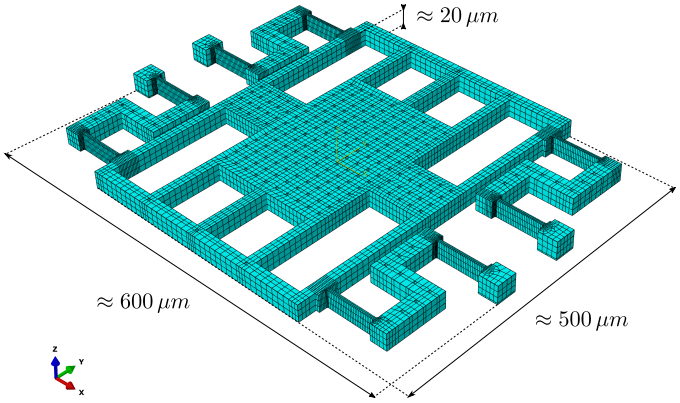

(b) Mesh.

Figure 27: (a) Model–II, a MEMS gyroscope. Drive and sense direction are indicated by arrows. (b) Meshed model, with 14,920 quadratic hexahedra, for a total of 87,767 nodes and 261,495 dofs. Approximate dimension are given.

FOM and ROMs in terms of convergence during continuation (ROMs are less likely to incur into numerical artifacts) and, secondly, because speed and convergence of this kind of analysis is highly sensitive to several parameters and finding the best combination by trial-and-error usually leads to sub-optimal performances. Last but not least, the size of the FOM in this case is too low to really appreciate the savings in terms of ROM construction.

4.8 NUMERICAL TESTS – II

4.8.1 MEMS gyroscope

The last example we present is a prototype MEMS mono-axial gyroscope, shown in Fig. 27a. The device consists in a mass suspended by four S-shaped springs, connected to the ground on the bottom of the anchors. It is a monolithic piece, produced via Deep Reactive Ion Etching (DRIE), a process which removes material from a plane silicon wafer to obtain the final geometry. The etching procedure is the main cause of production shape defects of MEMS devices, as it will be detailed later. In operative conditions, the mass is kept in motion by comb finger electrodes at the natural frequency of the drive mode (i.e. a mode featuring motion mainly in

the x-direction), so that in presence of an external angular rate Ω (along the y-axis) a vertical displacement w_{sense} arises due to Coriolis effect along the z-axis (sense). The latter is then converted into an electrical signal through the parallel plate electrode placed on the ground below the mass, providing the measure for the angular rate. In general, a defect or a combination of them may create a coupling between the x- and z-axes so that the drive motion generates an additional out-of-plane displacement which superimposes to the Coriolis displacement to be measured. This is usually referred to as *quadrature error* since, being proportional to the drive displacement, it is in phase quadrature with the Coriolis signal, proportional to the drive velocity. Though it is possible to tell apart the two contributions, this is highly undesirable as it requires dedicated, over-sized electronics to accommodate the larger displacements. Ultimately, this results in higher power consumption.

4.8.2 FE model, defects and simulation details

The FE model is shown in Fig. 27b and describes in detail the geometry and mesh of the device, counting 14,920 quadratic hexahedral elements for a total of 261,495 dofs. For the present study we selected two typical defects occurring in the production of MEMS devices, namely the *wall angle* (shown in Fig. 28a) and a restriction of the cross section of the beams (Fig. 28b). The first is generated by the fact that the plasma beam of the DRIE process might be not perfectly perpendicular to the working plane, while the second one typically comes from an overexposure to the chemical attacks (*over-etching*). In the spirit of our method, we can describe the global defects as the superposition of these two displacement fields (see Eq. (4.25b)), letting $\mathbf{U} = [\mathbf{U}_1, \mathbf{U}_2]$ with the associated amplitude parameter vector $\boldsymbol{\xi} = [\xi_1, \xi_2]^T$. The wall angle shape defect $\mathbf{U}_1 = [\mathbf{u}_{d1}, \mathbf{v}_{d1}, \mathbf{w}_{d1}]^T$ is given by

$$u_{d1}(\xi_1, z) = \xi_1 \tan(\alpha_y) z, \tag{4.43}$$

and $v_{d1} = w_{d1} = 0$. The tapering of the beams $\mathbf{U}_2 = [\mathbf{u}_{d2}, \mathbf{v}_{d2}, \mathbf{w}_{d2}]^T$ is defined as

$$v_{d2}(\xi_2, x, y) = \frac{2\xi_2}{W_b} \sin\left(\frac{\pi}{L_b}\tilde{x}\right) \tilde{y}, \tag{4.44}$$

where

$$\tilde{x} = x - x_{off}, \quad 0 \leqslant \tilde{x} \leqslant L_b,$$
$$\tilde{y} = y - y_{mid}, \quad 0 \leqslant \tilde{y} \leqslant W_b/2,$$

and $u_{d2} = w_{d2} = 0$. L_b and W_b are the length and the width of the beam, x_{off} an offset depending on the location of each beam and y_{mid} is the y-coordinate corresponding to the middle line of each beam. To ease the interpretation of the amplitude parameters, in the following ξ_1 is reported in degrees to represent the physical wall angle coming from the product $\xi_1 \tan(\alpha_y)$ in Eq. (4.43), while ξ_2 is reported as a percentage of the beam thickness.

We compute the FR of the MEMS gyroscope using the NLvib Matlab tool and our in-house Matlab FE code. We used a reduction basis with 3 VMs, the corresponding 6 MDs and 3 DSs per defect (only for the DpROMs). More details about the RB are given in Appendix 4.12. $H = 5$ harmonics were selected for the HB method (with $N_s = 3H + 1$ time samples per period, the minimum number of samples by which no sampling error is introduced in the harmonics up the the H-th order when considering polynomial nonlinearities up to the third order Woiwode et al., 2020, as in our case). Given the size of the model, we take as reference the results of ROM_d, as it would be prohibitively time and memory consuming to compute the frequency response for FOM_d. Apart from the practical issues, we justify this choice considering on the one side the good results obtained for lower dimensional models (as the one presented in the previous section), and on the other side considering that,

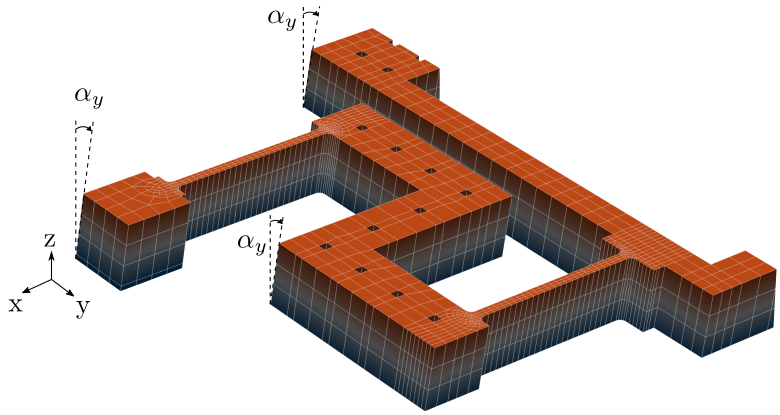

(a) Defect 1, wall angle.

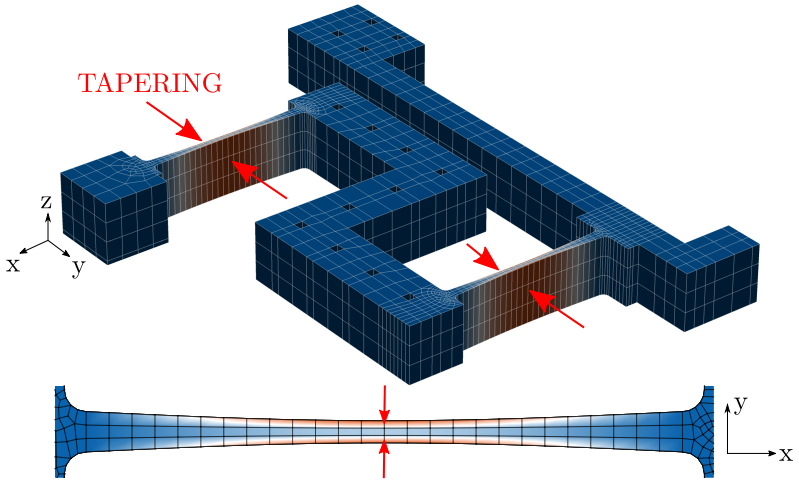

(b) Defect 2, tapering.

Figure 28: (a) First defect shape, $\mathbf{U}_1$: constant wall angle α_y (only one beam is shown). The colormap indicates x-displacement. (b) Second defect shape, $\mathbf{U}_2$: tapering of the suspension beams, 3D and top views (only one beam is shown). The colormap indicates y-displacement (absolute value).

ultimately, our DpROMs will be at best as good as ROM-d, which is not parametric and not approximated in its formulation.

The frequency response was obtained forcing the system in the center of the suspended mass with a nodal load directed along the x-direction, with amplitude $F = 0.4\,\mu N$, and using a Rayleigh damping matrix with $\alpha = 105$ and $\beta = 0$. Figure 29 reports the FRs around the first eigenfrequency of the system for the x-displacement u (drive direction) and the z-displacement w (sense direction) for all the combinations of $\xi_1 = \{0°, 0.5°, 1°\}$ and $\xi_2 = \{0\%, 0.5\%, 1\%, 1.5\%, 2\%\}$. For the present study, all the DpROM versions reported in Table 4 are tested and compared.

4.8.3 Results

With reference fo Fig. 29, considering first the effect of the wall angle defect only, it is apparent how DpROM-o_n performances quickly degrade as soon as the parameter ξ_1 is increased. This can be seen both in the error on the linear eigenfrequency and especially in the overestimated w-response, approximately one order of magnitude higher than the reference. This may be due to the fact that the S-shaped beams are specifically designed to minimize the cross-coupling between the drive (x-) and sense (z-) axes created by the wall angle, so that the w-response is so small (2 orders

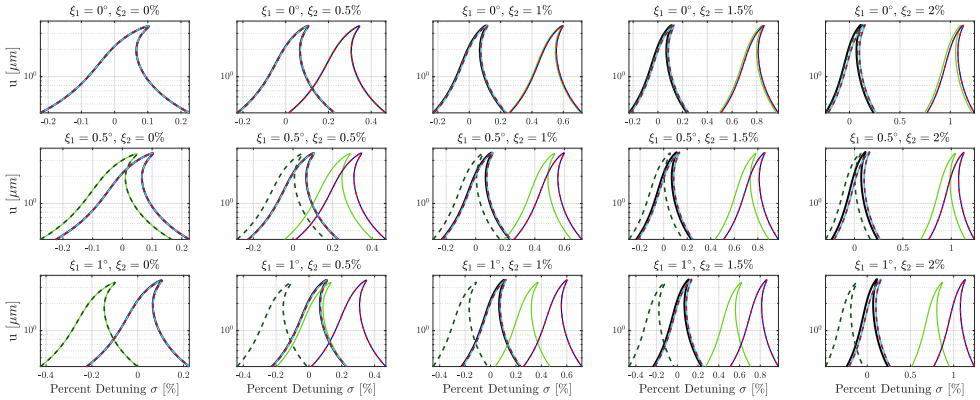

(a) u Frequency Response.

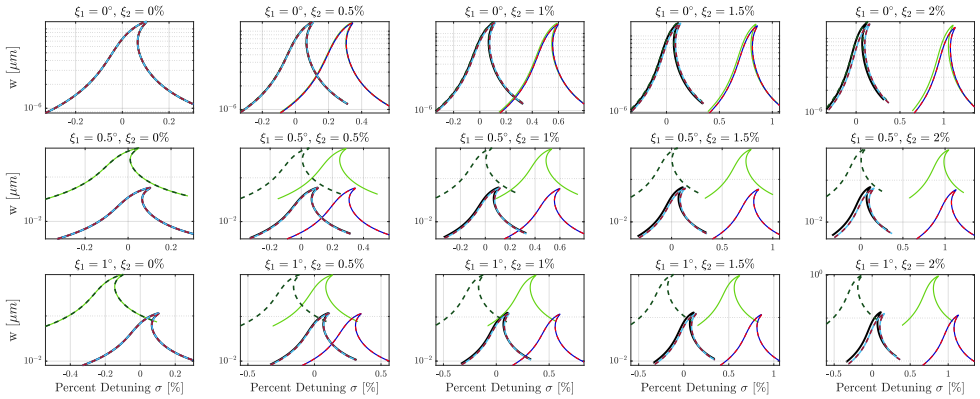

(b) w Frequency Response.

Figure 29: Frequency Responses for different defect amplitudes ξ_1 (shown in degrees) and ξ_2 (reported as percentage of the beam width) using the Harmonic Balance method (5 harmonics) for: ROM_d (—), DpROM-o_n (—), DpROM-1t_n (—), DpROM-1_n (- - -), DpROM-o_d (▪ ▪ ▪), DpROM-1t_d (—) and DpROM-1_d (▪ ▪ ▪). The displacements u and w of the center of the mass is shown (first harmonic coefficient of the Fourier series). For each plot, the percent detuning parameter $\sigma = (f - f_{01,d})/f_{01,d} \times 100$ is referred to the corresponding FOM_d first eigenfrequency $f_{01,d}$.

of magnitude lower than the u-response) that it cannot be accurately captured by DpROM-o_n. The same observations can be made for DpROM-o_d, as the wall angle defect by itself represent an isochoric transformation. The responses of all the other tested DpROMs show instead a perfect match with the reference when $\xi_2 = 0\%$.

If the tapering defect only is considered (i.e. with $\xi_1 = 0°$), we observe that DpROM-(o/1t/1)_n have similar responses, with an error on the eigenfrequency that translates the whole response by an approximately constant Δf. This error is expected, as the tapering is a volume-changing defect and integration over V_0 is thus a too coarse approximation. Moreover, the volume changed by this defect affects the suspension beams dimensions, to which the eigenfrequencies of the system are very sensitive. If on the one hand DpROM-o_d still presents relevant errors, on the other hand DpROM-1t_d and DpROM-1_d show very accurate results in the full range of the tested ξ_2.

For the remaining cases, the trends observed for the parameters ξ_1 and ξ_2 individually mix. Notice that looking at some results (e.g. u-response for $\xi_1 = 1°$, $\xi_2 = 0.5\%$), it may seem that DpROM-o_n gives better results than DpROM-1_n. This is however just a coincidence, as for DpROM-o_n the first defect shifts the first eigenfrequency to lower frequencies while the second defect to higher frequencies, so that the two errors in this case cancel out. Indeed, when the volume correction is

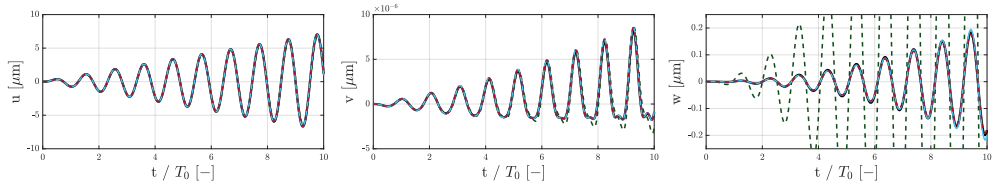

Figure 30: Transient response of the center of the suspended mass of the gyroscope for: ROM_d (▬), DpROM-0_d (▪ ▪ ▪), DpROM-$1t_d$ (▬) and DpROM-1_d (▪ ▪ ▪). The forcing is harmonic with period T_0. Case with $\xi_1 = 1°$, $\xi_2 = 2\%$.

used in DpROM-0_d, only the first effect is observed, and the frequencies are shifted to the left.

In Fig. 30 we also show the transient response of the forced node for ROM_d and DpROMs$_d$ (case with $\xi_1 = 1°$, $\xi_2 = 0.5\%$). Each model is forced at its own first resonance frequency f_0 (as it is usually the case for MEMS gyroscopes) with a harmonic forcing, taking 100 samples per period and for a time span equal to 10 times $T_0 = 1/f_0$, with $F = 50\mu N$. The integration was carried out in Matlab with our in-house code, using a Newmark integration scheme. Looking at the responses along the three axes, we observe that the three DpROMs yield correct results but for DpROM-0_d along the sense z-direction (w component). Also, considering the z-response, we can see that DpROM-1_n is slightly better DpROM-$1t_n$, fact that was not very visible in the FRs.

4.8.4 Computational times

Table 6 reports the average time for the FR analyses and for the construction of the different models. To compare in terms of time ROM_d and the DpROMs, it is convenient to consider the *variable costs* (T_{var}), i.e. the ones that have to be sustained for each new parameter realization, and the *overhead costs* (T_{oh}), i.e. the ones sustained once and for all independently from the number of realizations. In the case of ROM_d we have that $T_{var} = T_{constr} + T_{sim}$, being T_{constr} the time to construct the model (i.e. RB and tensors computation) and T_{sim} the time for one simulation, while $T_{oh} = 0$. For ROM_d indeed, there are no common overhead costs, but a new model must be constructed for each new realization of the parameters. In the case of DpROMs instead, we have that $T^p_{var} = T^p_{sim}$ and $T^p_{oh} = T^p_{constr}$ (we use the superscript "p" to distinguish the parametric models from ROM_d). For the parametric models we have in fact to pay upfront the cost of model construction, which is generally more expensive than the one for ROM_d, but thereafter only the simulation cost must be sustained for each new case. The first trivial conclusion is then that there exist a number $\bar{N}$ of parameter realization above which DpROMs become convenient, that is:

$$N \geqslant \bar{N} = \left\lceil \frac{T^p_{oh}}{T_{var} - T^p_{var}} \right\rceil. \tag{4.45}$$

For $\bar{N}$ to be positive and finite, it follows that

$$T_{var} > T^p_{var} \iff T_{constr} + T_{sim} > T^p_{sim}. \tag{4.46}$$

From Eq. (4.46) it can be seen how the convenience of the parametric model over the non-parametric one depends on the relative weight between the simulation and construction times of the latter and the simulation time of the former, as it can be observed in Table 6 looking at the different speedups[7] for the FR and transient analyses.

That said, it is clearly difficult to draw general and definitive conclusions on the benefits of the two solutions, ROM_d and DpROMs, time-wise. In the experience

7 Speedups are computed considering the variable costs only, with respect to ROM_d.

Table 6: Average computational times for the FR with the HB method and for the construction of each ROM (comprising the time to compute VMs, MDs, DSs and the tensors). ROM_d counts 9 dofs, while DpROMs 15 dofs. Apart from the construction costs, items for the DpROMs are clustered and averaged. Notice that the construction time for ROM_d is sustained for each new parameter realization and contributes to the *variable* costs. DpROM names are reported by their respective suffix.

Model–II	$\textbf{ROM}_\text{d}$	$\textbf{-0}_\text{n}$	$\textbf{-1t}_\text{n}$	$\textbf{-1}_\text{n}$	$\textbf{-0}_\text{d}$	$\textbf{-1t}_\text{d}$	$\textbf{-1}_\text{d}$
ROM construction	209 s	335 s	333 s	816 s	353 s	357 s	1,063 s
HB FR	21.7 s	49.2 s					
Transient analysis	0.43 s	0.51 s					
Overhead cost	–	335 s	333 s	816 s	353 s	357 s	1,063 s
Variable cost (FR)	230.7 s	49.2 s					
Variable cost (transient)	209.4 s	0.51 s					
Speedup (FR)	–	4.7×					
Speedup (transient)	–	410.6×					

of the authors, transient analysis offer the best gains, as simulation speed is very high, grows almost linearly with the simulation time span, and is less sensitive to the number of dofs than other kind of analysis, as the ones requiring continuation methods. When continuation is required, one could potentially find greater benefits in using a model with a low number of dofs, so that ROM_d could actually become the best choice. We remark however that for ROM_d we have to take into account also the construction cost as a variable cost, and that for large FE models the sole computation of structural eigenmodes can already take several minutes, making this cost very high.

4.9 CONCLUSIONS

We presented a ROM for geometric nonlinearities that can parametrically describe a shape imperfection with respect to the nominal (blueprint) design, named for brevity DpROM. The imperfection is given by the superposition of user-defined defect shapes, whose amplitudes are parameters of the model and can be changed without reconstructing the model itself. This result has been made possible thanks to a polynomial representation of the internal forces resulting from a two-step deformation process (which brings the nominal geometry into the defected one and then into the deformed one) and from the approximation of the strains obtained by a Neumann expansion. The latter allowed to eliminate rational expressions under the hypothesis of small defects, so that the elastic internal forces are written as simple polynomials both with respect to the displacement field representing the defect and with respect to the actual displacement field. Using a Galerkin projection and a modal-based approach for selecting the RB, the reduced internal forces have been recast in tensorial form, where the linear, quadratic and cubic stiffness tensors are found to be functions of a parameter vector collecting the amplitudes of the defects imposed on the structure. Within this framework we tested different versions of the DpROM for different degrees of approximation. In particular, we have shown that the model we had previously developed using Budiansky's approach corresponds to the 0th-order expansion of our model, integrated over the nominal volume V_0 (i.e. DpROM-0_n). Finally, in the numerical studies we showed that the higher order approximation DpROM-1_n effectively leads to more accurate results and that for volume-changing defects a large improvement can be achieved by approximating the tensor integral over the real volume of the defective geometry (DpROM-$(0/1)_\text{d}$). The truncated version DpROM-$1t_{\text{n}/\text{d}}$ was also presented, which has almost the same accuracy as its complete counterpart, but without the

need to construct tensors with dimensionality higher than four. The computational costs were then critically discussed, taking into account different types of analysis. In particular, we showed that in transient studies we can usually expect very high speedups from the parametric models. In the case of FR analysis, which we used to assess the quality of the solutions over a range of frequencies as an alternative to multiple time analyses, the gains will be more contained. In this context, to reduce the dofs of both the parametric and non-parametric ROMs and make FR analysis faster and thus closer to transient analysis in terms of time and speedups, we think that an a priori selection of the RB vectors and hyperreduction strategies would actually be very beneficial, and they can constitute the spur for future investigation.

4.10 APPENDIX A — LOCALIZATION MATRICES

We report in Tables 7 and 8 the expressions for the matrices $\mathbf{L}_1$, $\mathbf{L}_2$ and $\mathbf{L}_3$ defined in Eqs. 4.21, for the plane-strain/stress continuum problem (2D case) and the three-dimensional continuum problem (3D case). In the tables, name subscripts are moved to superscripts to avoid confusion with the indexes (e.g. $L^{(1)}_{ijk}$ is a component of $\mathbf{L}_1$).

Table 7: Elements $L^{(1)}_{ijk}$, $L^{(2)}_{ijk}$ and $L^{(3)}_{ijkl}$ of the sparse $3\times4\times4$ matrices $\mathbf{L}_1$, $\mathbf{L}_2$ and of the sparse $3\times4\times4\times4$ matrix $\mathbf{L}_3$, respectively, in the 2D case.

$L^{(1)}_{111}=1$,	$L^{(1)}_{321}=1$,	$L^{(1)}_{312}=1$,	$L^{(1)}_{222}=1$,	$L^{(1)}_{123}=1$,	$L^{(1)}_{343}=1$,	$L^{(1)}_{324}=1$,	$L^{(1)}_{244}=1$.
$L^{(2)}_{111}=1$,	$L^{(2)}_{331}=1$,	$L^{(2)}_{312}=1$,	$L^{(2)}_{232}=1$,	$L^{(2)}_{123}=1$,	$L^{(2)}_{343}=1$,	$L^{(2)}_{324}=1$,	$L^{(2)}_{244}=1$.
$L^{(3)}_{1111}=1$,	$L^{(3)}_{3211}=\frac{1}{2}$,	$L^{(3)}_{3121}=\frac{1}{2}$,	$L^{(3)}_{1331}=1$,	$L^{(3)}_{3431}=\frac{1}{2}$,	$L^{(3)}_{3341}=\frac{1}{2}$,	$L^{(3)}_{3112}=1$,	$L^{(3)}_{2212}=\frac{1}{2}$,
$L^{(3)}_{2122}=\frac{1}{2}$,	$L^{(3)}_{3332}=1$,	$L^{(3)}_{2432}=\frac{1}{2}$,	$L^{(3)}_{2342}=\frac{1}{2}$,	$L^{(3)}_{1213}=\frac{1}{2}$,	$L^{(3)}_{1123}=\frac{1}{2}$,	$L^{(3)}_{3223}=1$,	$L^{(3)}_{1433}=\frac{1}{2}$,
$L^{(3)}_{1343}=\frac{1}{2}$,	$L^{(3)}_{3443}=1$,	$L^{(3)}_{3214}=\frac{1}{2}$,	$L^{(3)}_{3124}=\frac{1}{2}$,	$L^{(3)}_{2224}=1$,	$L^{(3)}_{3434}=\frac{1}{2}$,	$L^{(3)}_{3344}=\frac{1}{2}$,	$L^{(3)}_{2444}=1$.

Table 8: Elements $L^{(1)}_{ijk}$, $L^{(2)}_{ijk}$ and $L^{(3)}_{ijkl}$ of the sparse $6\times9\times9$ matrices $\mathbf{L}_1$, $\mathbf{L}_2$ and of the sparse $6\times9\times9\times9$ matrix $\mathbf{L}_3$, respectively, in the 3D case.

$L^{(1)}_{111}=1$,	$L^{(1)}_{421}=1$,	$L^{(1)}_{531}=1$,	$L^{(1)}_{412}=1$,	$L^{(1)}_{222}=1$,	$L^{(1)}_{632}=1$,	$L^{(1)}_{513}=1$,	$L^{(1)}_{623}=1$,	$L^{(1)}_{333}=1$,
$L^{(1)}_{144}=1$,	$L^{(1)}_{454}=1$,	$L^{(1)}_{564}=1$,	$L^{(1)}_{445}=1$,	$L^{(1)}_{255}=1$,	$L^{(1)}_{665}=1$,	$L^{(1)}_{546}=1$,	$L^{(1)}_{656}=1$,	$L^{(1)}_{366}=1$,
$L^{(1)}_{177}=1$,	$L^{(1)}_{487}=1$,	$L^{(1)}_{597}=1$,	$L^{(1)}_{478}=1$,	$L^{(1)}_{288}=1$,	$L^{(1)}_{698}=1$,	$L^{(1)}_{579}=1$,	$L^{(1)}_{689}=1$,	$L^{(1)}_{399}=1$.
$L^{(2)}_{111}=1$,	$L^{(2)}_{441}=1$,	$L^{(2)}_{571}=1$,	$L^{(2)}_{412}=1$,	$L^{(2)}_{242}=1$,	$L^{(2)}_{672}=1$,	$L^{(2)}_{513}=1$,	$L^{(2)}_{643}=1$,	$L^{(2)}_{373}=1$,
$L^{(2)}_{124}=1$,	$L^{(2)}_{454}=1$,	$L^{(2)}_{584}=1$,	$L^{(2)}_{425}=1$,	$L^{(2)}_{255}=1$,	$L^{(2)}_{685}=1$,	$L^{(2)}_{526}=1$,	$L^{(2)}_{656}=1$,	$L^{(2)}_{386}=1$,
$L^{(2)}_{137}=1$,	$L^{(2)}_{467}=1$,	$L^{(2)}_{597}=1$,	$L^{(2)}_{438}=1$,	$L^{(2)}_{268}=1$,	$L^{(2)}_{698}=1$,	$L^{(2)}_{539}=1$,	$L^{(2)}_{669}=1$,	$L^{(2)}_{399}=1$.
$L^{(3)}_{1111}=1$,	$L^{(3)}_{4211}=\frac{1}{2}$,	$L^{(3)}_{5311}=\frac{1}{2}$,	$L^{(3)}_{4121}=\frac{1}{2}$,	$L^{(3)}_{5131}=\frac{1}{2}$,	$L^{(3)}_{1441}=1$,	$L^{(3)}_{4541}=\frac{1}{2}$,	$L^{(3)}_{5641}=\frac{1}{2}$,	$L^{(3)}_{4451}=\frac{1}{2}$,
$L^{(3)}_{5461}=\frac{1}{2}$,	$L^{(3)}_{1771}=1$,	$L^{(3)}_{4871}=\frac{1}{2}$,	$L^{(3)}_{5971}=\frac{1}{2}$,	$L^{(3)}_{4781}=\frac{1}{2}$,	$L^{(3)}_{5791}=\frac{1}{2}$,	$L^{(3)}_{4112}=1$,	$L^{(3)}_{2212}=\frac{1}{2}$,	$L^{(3)}_{6312}=\frac{1}{2}$,
$L^{(3)}_{2122}=\frac{1}{2}$,	$L^{(3)}_{6132}=\frac{1}{2}$,	$L^{(3)}_{4442}=1$,	$L^{(3)}_{2542}=\frac{1}{2}$,	$L^{(3)}_{6642}=\frac{1}{2}$,	$L^{(3)}_{2452}=\frac{1}{2}$,	$L^{(3)}_{6462}=\frac{1}{2}$,	$L^{(3)}_{4772}=1$,	$L^{(3)}_{2872}=\frac{1}{2}$,
$L^{(3)}_{6972}=\frac{1}{2}$,	$L^{(3)}_{2782}=\frac{1}{2}$,	$L^{(3)}_{6792}=\frac{1}{2}$,	$L^{(3)}_{5113}=1$,	$L^{(3)}_{6213}=\frac{1}{2}$,	$L^{(3)}_{3313}=\frac{1}{2}$,	$L^{(3)}_{6123}=\frac{1}{2}$,	$L^{(3)}_{3133}=\frac{1}{2}$,	$L^{(3)}_{5443}=1$,
$L^{(3)}_{6543}=\frac{1}{2}$,	$L^{(3)}_{3643}=\frac{1}{2}$,	$L^{(3)}_{6453}=\frac{1}{2}$,	$L^{(3)}_{3463}=\frac{1}{2}$,	$L^{(3)}_{5773}=1$,	$L^{(3)}_{6873}=\frac{1}{2}$,	$L^{(3)}_{3973}=\frac{1}{2}$,	$L^{(3)}_{6783}=\frac{1}{2}$,	$L^{(3)}_{3793}=\frac{1}{2}$,
$L^{(3)}_{1214}=\frac{1}{2}$,	$L^{(3)}_{1124}=\frac{1}{2}$,	$L^{(3)}_{4224}=1$,	$L^{(3)}_{5324}=\frac{1}{2}$,	$L^{(3)}_{5234}=\frac{1}{2}$,	$L^{(3)}_{1544}=\frac{1}{2}$,	$L^{(3)}_{1454}=\frac{1}{2}$,	$L^{(3)}_{4554}=1$,	$L^{(3)}_{5654}=\frac{1}{2}$,
$L^{(3)}_{5564}=\frac{1}{2}$,	$L^{(3)}_{1874}=\frac{1}{2}$,	$L^{(3)}_{1784}=\frac{1}{2}$,	$L^{(3)}_{4884}=1$,	$L^{(3)}_{5984}=\frac{1}{2}$,	$L^{(3)}_{5894}=\frac{1}{2}$,	$L^{(3)}_{4215}=\frac{1}{2}$,	$L^{(3)}_{4125}=\frac{1}{2}$,	$L^{(3)}_{2225}=1$,
$L^{(3)}_{6325}=\frac{1}{2}$,	$L^{(3)}_{6235}=\frac{1}{2}$,	$L^{(3)}_{4545}=\frac{1}{2}$,	$L^{(3)}_{4455}=\frac{1}{2}$,	$L^{(3)}_{2555}=1$,	$L^{(3)}_{6655}=\frac{1}{2}$,	$L^{(3)}_{6565}=\frac{1}{2}$,	$L^{(3)}_{4875}=\frac{1}{2}$,	$L^{(3)}_{4785}=\frac{1}{2}$,
$L^{(3)}_{2885}=1$,	$L^{(3)}_{6985}=\frac{1}{2}$,	$L^{(3)}_{6895}=\frac{1}{2}$,	$L^{(3)}_{5216}=\frac{1}{2}$,	$L^{(3)}_{5126}=\frac{1}{2}$,	$L^{(3)}_{6226}=1$,	$L^{(3)}_{3326}=\frac{1}{2}$,	$L^{(3)}_{3236}=\frac{1}{2}$,	$L^{(3)}_{5546}=\frac{1}{2}$,
$L^{(3)}_{5456}=\frac{1}{2}$,	$L^{(3)}_{6556}=1$,	$L^{(3)}_{3656}=\frac{1}{2}$,	$L^{(3)}_{3566}=\frac{1}{2}$,	$L^{(3)}_{5876}=\frac{1}{2}$,	$L^{(3)}_{5786}=\frac{1}{2}$,	$L^{(3)}_{6886}=1$,	$L^{(3)}_{3986}=\frac{1}{2}$,	$L^{(3)}_{3896}=\frac{1}{2}$,
$L^{(3)}_{1317}=\frac{1}{2}$,	$L^{(3)}_{4327}=\frac{1}{2}$,	$L^{(3)}_{1137}=\frac{1}{2}$,	$L^{(3)}_{4237}=\frac{1}{2}$,	$L^{(3)}_{5337}=1$,	$L^{(3)}_{1647}=\frac{1}{2}$,	$L^{(3)}_{4657}=\frac{1}{2}$,	$L^{(3)}_{1467}=\frac{1}{2}$,	$L^{(3)}_{4567}=\frac{1}{2}$,
$L^{(3)}_{5667}=1$,	$L^{(3)}_{1977}=\frac{1}{2}$,	$L^{(3)}_{4987}=\frac{1}{2}$,	$L^{(3)}_{1797}=\frac{1}{2}$,	$L^{(3)}_{4897}=\frac{1}{2}$,	$L^{(3)}_{5997}=1$,	$L^{(3)}_{4318}=\frac{1}{2}$,	$L^{(3)}_{2328}=\frac{1}{2}$,	$L^{(3)}_{4138}=\frac{1}{2}$,
$L^{(3)}_{2238}=\frac{1}{2}$,	$L^{(3)}_{6338}=1$,	$L^{(3)}_{4648}=\frac{1}{2}$,	$L^{(3)}_{2658}=\frac{1}{2}$,	$L^{(3)}_{4468}=\frac{1}{2}$,	$L^{(3)}_{2568}=\frac{1}{2}$,	$L^{(3)}_{6668}=1$,	$L^{(3)}_{4978}=\frac{1}{2}$,	$L^{(3)}_{2988}=\frac{1}{2}$,
$L^{(3)}_{4798}=\frac{1}{2}$,	$L^{(3)}_{2898}=\frac{1}{2}$,	$L^{(3)}_{6998}=1$,	$L^{(3)}_{5319}=\frac{1}{2}$,	$L^{(3)}_{6329}=\frac{1}{2}$,	$L^{(3)}_{5139}=\frac{1}{2}$,	$L^{(3)}_{6239}=\frac{1}{2}$,	$L^{(3)}_{3339}=1$,	$L^{(3)}_{5649}=\frac{1}{2}$,
$L^{(3)}_{6659}=\frac{1}{2}$,	$L^{(3)}_{5469}=\frac{1}{2}$,	$L^{(3)}_{6569}=\frac{1}{2}$,	$L^{(3)}_{3669}=1$,	$L^{(3)}_{5979}=\frac{1}{2}$,	$L^{(3)}_{6989}=\frac{1}{2}$,	$L^{(3)}_{5799}=\frac{1}{2}$,	$L^{(3)}_{6899}=\frac{1}{2}$,	$L^{(3)}_{3999}=1$.

For the sake of completeness, we also report the expressions for the $\mathbf{A}_2$ and $\mathbf{A}_3$ in the 2D case:

$$\mathbf{A}_2^{(2D)} = (-1)\begin{bmatrix} u_{d,x} & v_{d,x} & 0 & \\ 0 & 0 & u_{d,y} & v_{d,y} \\ u_{d,y} & v_{d,y} & u_{d,x} & v_{d,x} \end{bmatrix}, \tag{4.47a}$$

$$\mathbf{A}_3^{(2D)} = (-1/2)\begin{bmatrix} 2u_{d,x} & 0 & v_{d,x} \\ 0 & 2v_{d,y} & u_{d,y} \\ 2u_{d,y} & 2v_{d,x} & u_{d,x}+v_{d,y} \end{bmatrix} \tag{4.47b}$$

4.11 APPENDIX – STIFFNESS MATRIX DERIVATIVES

The virtual variation wrt $\mathbf{u}$ of the internal elastic forces as defined in Eq. (4.20) writes

$$\begin{aligned}\delta\mathbf{f}_{int} = \int_{V_o} \Big[&\mathbf{G}^T \left(\mathbf{H}+\mathbf{A}+\mathbf{A}_2+2\mathbf{A}_3\mathbf{A}\right)^T \mathbf{C} \left(\mathbf{H}+\frac{1}{2}\mathbf{A}+\mathbf{A}_2+\mathbf{A}_3\mathbf{A}\right)\mathbf{G}\delta\mathbf{u} \\ &+\mathbf{G}^T \left(\mathbf{H}+\mathbf{A}+\mathbf{A}_2+2\mathbf{A}_3\mathbf{A}\right)^T \mathbf{C} \left(\frac{1}{2}\delta\mathbf{A}+\mathbf{A}_3\delta\mathbf{A}\right)\mathbf{G}\mathbf{u}+ \\ &+\mathbf{G}^T \left(\delta\mathbf{A}+2\mathbf{A}_3\delta\mathbf{A}\right)^T \mathbf{C} \left(\mathbf{H}+\frac{1}{2}\mathbf{A}+\mathbf{A}_2+\mathbf{A}_3\mathbf{A}\right)\mathbf{G}\mathbf{u}\Big]\, dV_o.\end{aligned} \tag{4.48}$$

Recalling that $\mathbf{A}\delta\theta = \delta\mathbf{A}\theta$, we can write

$$\begin{aligned}\delta\mathbf{f}_{int} = \int_{V_o} \Big[&\mathbf{G}^T \left(\mathbf{H}+\mathbf{A}+\mathbf{A}_2+2\mathbf{A}_3\mathbf{A}\right)^T \mathbf{C} \left(\mathbf{H}+\mathbf{A}+\mathbf{A}_2+2\mathbf{A}_3\mathbf{A}\right)\mathbf{G}\delta\mathbf{u} \\ &+\mathbf{G}^T\delta\mathbf{A}^T\mathbf{N}\Big]\, dV_o,\end{aligned} \tag{4.49}$$

being

$$\mathbf{N} = \left(\mathbf{I}+2\mathbf{A}_3^T\right)\mathbf{C}\left(\mathbf{H}+\frac{1}{2}\mathbf{A}+\mathbf{A}_2+\mathbf{A}_3\mathbf{A}\right)\mathbf{G}\mathbf{u}. \tag{4.50}$$

The second term on the right-hand side of Eq. (4.49) can be rewritten to put in evidence the displacement virtual variation $\delta\mathbf{u}$ as

$$\delta f_I'' = \int_{V_o} G_{iI} L_{1jik} G_{kl} \delta u_l N_j \, dV_o, \tag{4.51}$$

where Einstein notation was used for convenience. The tangent stiffness matrix therefore writes:

$$\mathbf{K}_t = \mathbf{K}' + \mathbf{K}'' \tag{4.52}$$

where

$$\mathbf{K}' = \int_{V_o} \mathbf{G}^T \left(\mathbf{H}+\mathbf{A}+\mathbf{A}_2+2\mathbf{A}_3\mathbf{A}\right)^T \mathbf{C} \left(\mathbf{H}+\mathbf{A}+\mathbf{A}_2+2\mathbf{A}_3\mathbf{A}\right)\mathbf{G}\, dV_o, \tag{4.53}$$

$$K_{IJ}'' = \int_{V_o} G_{iI} L_{1jik} G_{kJ} N_j \, dV_o. \tag{4.54}$$

Substituting $\mathbf{u} = \mathbf{\Phi}_i\eta_i$ and $\mathbf{u}_d = \mathbf{U}_j\xi_j$ in Eq. (4.52), taking the derivative wrt either η_i and/or ξ_j and evaluating the resulting expressions at equilibrium and with zero defect amplitudes, as required by Eqs. (4.38)–(4.41), we can write the derivatives of $\mathbf{K}_t$ as:

$$\left.\frac{\partial\mathbf{K}_t}{\partial\eta_j}\right|_0 = \int_{V_o} \left[\mathbf{G}^T\left(\mathbf{H}^T\mathbf{C}\mathbf{A}_j + \mathbf{A}_j^T\mathbf{C}\mathbf{H}\right)\mathbf{G} + \mathbf{G}^T\left[(\mathbf{L}_1\cdot\mathbf{G})\cdot_{11}(\mathbf{C}\mathbf{H}\mathbf{G}\mathbf{\Phi}_i)\right]\right] dV_o, \tag{4.55a}$$

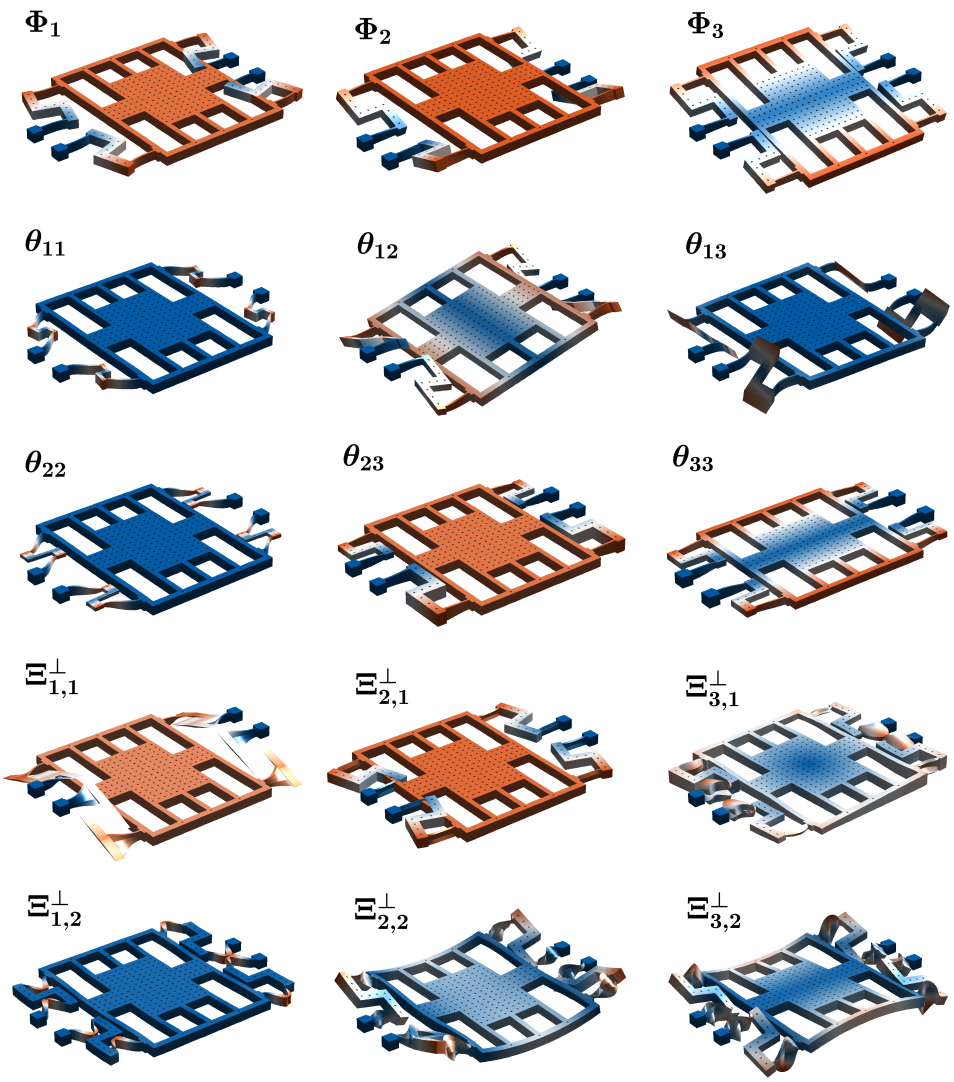

Figure 31: RB modes for Model-II, normalized in order to have a maximum displacement of 1 µm and with a scale factor of 50×. The colormap indicates the displacement magnitude (blue is zero, red is 1).

$$\left.\frac{\partial \mathbf{K}_t}{\partial \xi_j}\right|_0 = \int_{V_o} \mathbf{G}^T \left(\mathbf{H}^T \mathbf{C} \mathbf{A}_{2j} + \mathbf{A}_{2j}^T \mathbf{C} \mathbf{H}\right) \mathbf{G} \, dV_o, \tag{4.55b}$$

$$\begin{aligned}\left.\frac{\partial^2 \mathbf{K}_t}{\partial \eta_j \partial \xi_k}\right|_0 = \int_{V_o} \Big[&\mathbf{G}^T \left(\mathbf{A}_{2k}^T \mathbf{C} \mathbf{A}_j + \mathbf{A}_j^T \mathbf{C} \mathbf{A}_{2k} + 2\mathbf{A}_j^T \mathbf{A}_{3k}^T \mathbf{C} \mathbf{H} + 2\mathbf{H}^T \mathbf{C} \mathbf{A}_{3k} \mathbf{A}_j\right) \mathbf{G} \\ &+ \mathbf{G}^T \left[(\mathbf{L}_1 \cdot \mathbf{G}) \cdot_{11} (\mathbf{C}\mathbf{A}_2 + 2\mathbf{A}_3^T \mathbf{C}\mathbf{H}) \mathbf{G} \boldsymbol{\Phi}_i \right] \Big] \, dV_o,\end{aligned} \tag{4.55c}$$

$$\left.\frac{\partial^2 \mathbf{K}_t}{\partial \xi_j \partial \xi_k}\right|_0 = \int_{V_o} \mathbf{G}^T \left(\mathbf{A}_{2j}^T \mathbf{C} \mathbf{A}_{2k} + \mathbf{A}_{2k}^T \mathbf{C} \mathbf{A}_{2j}\right) \mathbf{G} dV_o, \tag{4.55d}$$

where, recalling that η_i and ξ_j are scalars, we used

$$\mathbf{A}(\mathbf{G}\boldsymbol{\Phi}_i \eta_i) = \mathbf{A}_i \eta_i,$$

$$\mathbf{A}_2(\mathbf{G}\mathbf{U}_j \xi_j) = \mathbf{A}_{2j} \xi_j,$$

(same for $\mathbf{A}_3$) to avoid a cumbersome notation, and where $\cdot_{ij}$ denotes the contraction of the i-th dimension of the first term with the j-th dimension of the second term.

4.12 APPENDIX – RB FOR MODEL–II

Also for Model–II, the RB selection criterion described in Remark 6 is adopted and eigenmodes up to 3 times the first eigenfrequency are retained. The reduction basis is thus formed as:

$$\mathbf{V} = [\boldsymbol{\Phi}_1, \boldsymbol{\Phi}_2, \boldsymbol{\Phi}_3, \theta_{11}, \theta_{12}, \theta_{13}, \theta_{22}, \theta_{23}, \theta_{33}, \boldsymbol{\Xi}_{1,1}, \boldsymbol{\Xi}_{2,1}, \boldsymbol{\Xi}_{3,1}, \boldsymbol{\Xi}_{1,2}, \boldsymbol{\Xi}_{2,2}, \boldsymbol{\Xi}_{3,2}], \quad (4.56)$$

that is, 3 VMs and all their corresponding MDs and DSs are included. Figure 31 shows the mode shapes. Apart from VMs, the interpretation of these vectors is in general not trivial. One can for instance recognize in θ_{33} a necessary element to correctly represent the rotation happening in mode $\boldsymbol{\Phi}_3$ and in θ_{11} the stretching of the suspension beams required to capture their nonlinear behavior. To better inspect the contribution of DSs, we plotted $\boldsymbol{\Xi}^{\perp}_{i,k}$, i.e. $\boldsymbol{\Xi}_{i,k}$ orthogonalized with respect to $\boldsymbol{\Phi}_i$ (via Gram-Schmidt). $\boldsymbol{\Xi}^{\perp}_{1,1}$ is particularly significant as it represent the out-of-plane motion of the structure induced on the first VM (x-polarized) by the presence of the wall-angle defect, which is responsible for the gyroscope quadrature error. Similarly, it can be observed how $\boldsymbol{\Xi}^{\perp}_{2,1}$ represent an in-plane motion associated to the second VM (z-polarized) due to the wall-angle defect. The contributions of $\boldsymbol{\Xi}^{\perp}_{i,2}$ are instead local and restricted to the suspension beams, as it can be expected given the local nature of the tapering.

4.13 APPENDIX – ADDITIONAL CASES

In this section we showcase some FRs for defects which affect the boundary conditions. We consider again the same beam studied in Sec. 4.7 (same mesh and NLvib settings); however, we limit the comparison to the only ROM_d and $\text{DpROM}-1_\text{d}$ models.

As it can be observed in Figs. 32a–33b, although the clamped ends of the beam are moved by the imposed defect, the response of the defected structure is well captured by the DpROM. In Fig. 33b, due to the large amplitude of the imposed defect, the value of the linear eigenfrequency is a little bit off, but the overall response (with the first two resonances tending to coincide) is well represented.

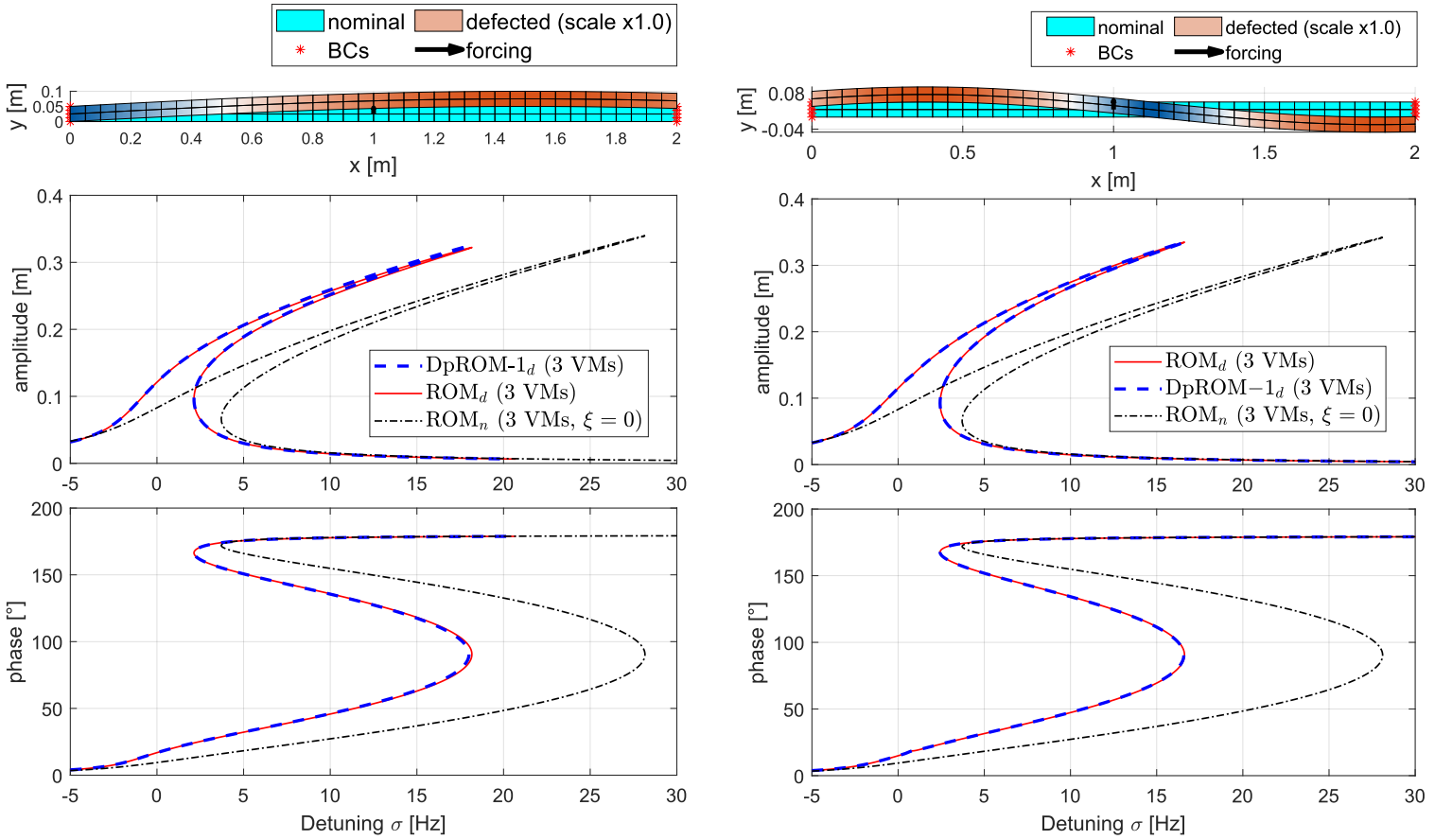

(a) Case 1: one clamp is moved out of position due to the presence of the defect. The defect is given by a sinusoidal with a spatial period of $2l_x$. FRs of DpROM-1_d and ROM$_d$ are shown in blue (dashed) and red (solid), respectively. ROM$_n$ (i.e. ROM$_d$ computed for $\xi = 0$) is also shown (black, dash-dotted) for reference. All the ROMs were computed using 3 VMs and the corresponding 6 MDs (+3 DSs for the DpROM). The defected mesh (top plot) is in scale.

(b) Case 2: both clamped ends are moved out of position due to the presence of the defect. The defect is given by a sinusoidal with a spatial period of $3l_x/2$ and a phase of $\phi/6$. FRs of DpROM-1_d and ROM$_d$ are shown in blue (dashed) and red (solid), respectively. ROM$_n$ (i.e. ROM$_d$ computed for $\xi = 0$) is also shown (black, dash-dotted) for reference. All the ROMs were computed using 3 VMs and the corresponding 6 MDs (+3 DSs for the DpROM). The defected mesh (top plot) is in scale.

Figure 32

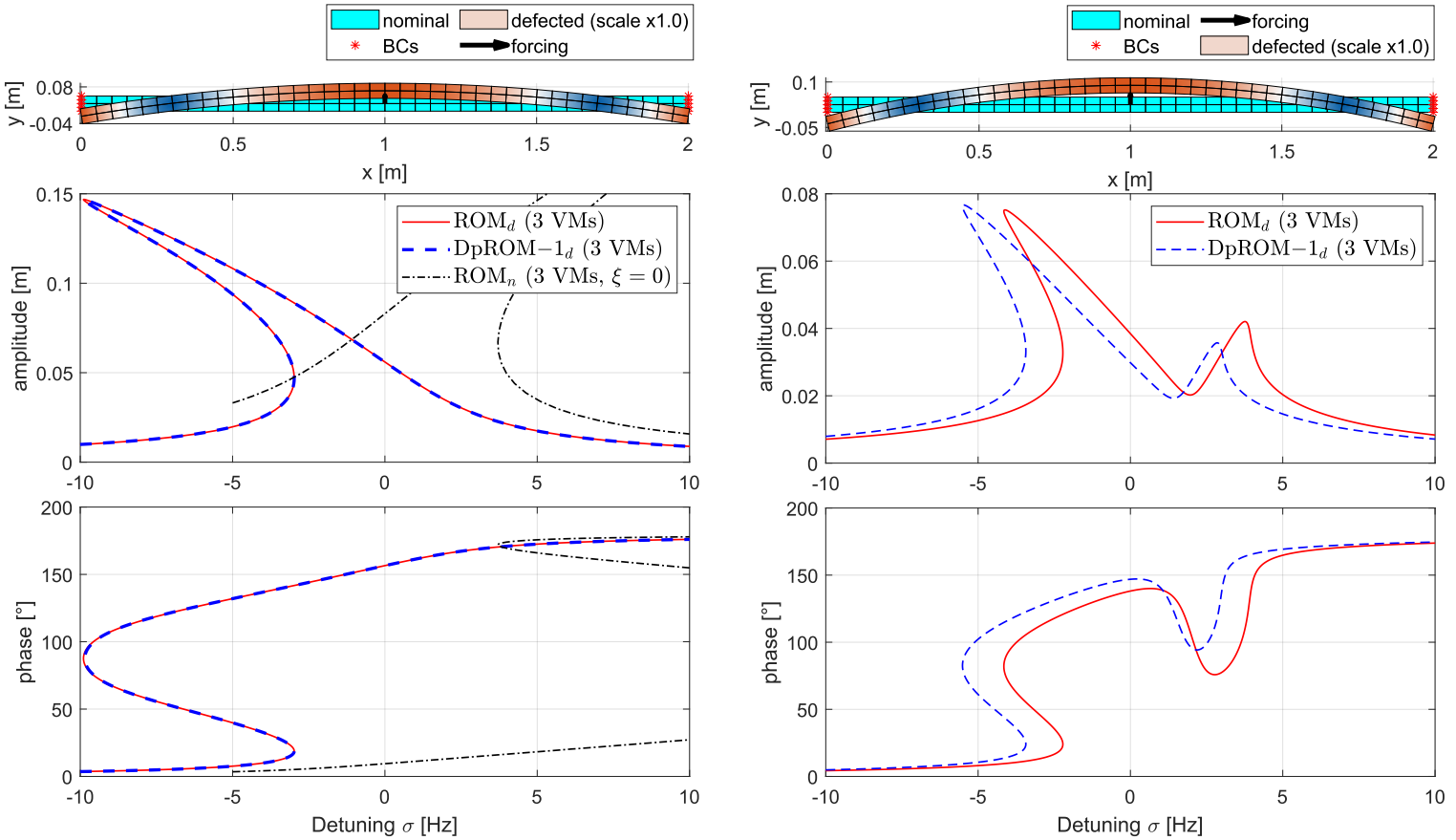

(a) Case 3a: both clamped ends moved out of position due to the presence of the defect. The defect is constructed as an arc of a circumference, with a given curvature. FRs of DpROM−1$_d$ and ROM$_d$ are shown in blue (dashed) and red (solid), respectively. ROM$_n$ (i.e. ROM$_d$ computed for $\xi = 0$) is also shown (black, dash-dotted) for reference. All the ROMs were computed using 3 VMs and the corresponding 6 MDs (+3 DSs for the DpROM). The defected mesh (top plot) is in scale.

(b) Case 3b: both clamped ends moved out of position due to the presence of the defect. The defect is constructed as an arc of a circumference, with a given curvature (higher than that in Fig. 33a, case 3b). FRs of DpROM−1$_d$ and ROM$_d$ are shown in blue (dashed) and red (solid), respectively. All the ROMs were computed using 3 VMs and the corresponding 6 MDs (+3 DSs for the DpROM). The defected mesh (top plot) is in scale.

Figure 33

5 DPROM FOR SUBSTRUCTURING

It's a trap!

—Admiral Ackbar, Star Wars Episode VI

Substructuring techniques, loosely speaking, consist into dividing the total domain of a structure into sub-domains which, to some extent, can be handled independently during a FE simulation run. If each substructure model is then reduced, we talk of Component Mode Synthesis (CMS) techniques. The most popular CMS strategies date back to the late sixties (Craig and Bampton, 1968; Rubin, 1975) and apply to linear dynamics. Recently, these approaches have been extended to nonlinear dynamics (Wu, Tiso, Tatsis, et al., 2019; Wu, Tiso, and van Keulen, 2018) using, again, a modal-based approach (with VMs, MDs, among other vectors).

In this chapter, we study the feasibility of applying the DpROM in a substructuring framework. Three main paths are possible: in the first, defect shapes for each substructure are chosen so that they *do not alter the interfaces* between adjacent substructures; in the second, defects *and* defect amplitudes (ξ) of each substructure are chosen so that interfaces are always compatible; in the third, *arbitrary defect shapes* are allowed. While the first and the second approach would translate into the (almost) straightforward application of known MOR strategies, the third one is more general and poses an interesting problem, as *interfaces are not a priori compatible*. In the following, we study how this problem can be addressed.

5.1 SUBSTRUCTURING AND CMS

In this section we briefly review Substructuring and Component Mode Synthesis. For more details, the reader is referred to Allen et al., 2020; Klerk et al., 2008.

5.1.1 Substructuring: primal and dual assembly

Considering $s = 1, \dots, S$ substructures with n_s dofs each, we can write

$$\mathbf{M}_s \ddot{\mathbf{u}}_s + \mathbf{C}_s \dot{\mathbf{u}}_s + \mathbf{K}_s \mathbf{u}_s = \mathbf{f}_s + \mathbf{g}_s \,, \tag{5.1}$$

where $\mathbf{M}_s$, $\mathbf{C}_s$, $\mathbf{K}_s \in \mathbb{R}_{n_s \times n_s}$ are the FOM mass, damping and stiffness matrices of the s-th substructure (being n_s the number of dofs), and $\mathbf{u}_s$, $\mathbf{f}_s$, $\mathbf{g}_s \in \mathbb{R}^{n_s}$ are the displacement vector, the external forces and the interface forces, respectively. The system of equations for the global structure can be written in diagonal form as

$$\begin{cases} \mathbf{M}\ddot{\mathbf{u}} + \mathbf{C}\dot{\mathbf{u}} + \mathbf{K}\mathbf{u} = \mathbf{f} + \mathbf{g} & \text{(5.2a)} \\ \mathbf{B}\mathbf{u} = \mathbf{0} & \text{(5.2b)} \\ \mathbf{L}^{\mathsf{T}}\mathbf{g} = \mathbf{0} & \text{(5.2c)} \end{cases}$$

where

$$\mathbf{M} = \operatorname{diag}(\mathbf{M}_1, \dots, \mathbf{M}_S) = \begin{bmatrix} \mathbf{M}_1 & \dots & 0 \\ \vdots & \ddots & \vdots \\ 0 & \dots & \mathbf{M}_S \end{bmatrix} \in \mathbb{R}^{n_S \times n_S}, \tag{5.3a}$$

$$\mathbf{C} = \operatorname{diag}(\mathbf{C}_1, \dots, \mathbf{C}_S), \quad \mathbf{K} = \operatorname{diag}(\mathbf{K}_1, \dots, \mathbf{K}_S), \tag{5.3b}$$

$$\mathbf{u} = \begin{Bmatrix} \mathbf{u}_1 \\ \vdots \\ \mathbf{u}_S \end{Bmatrix} \in \mathbb{R}^{n_S}, \tag{5.3c}$$

$$\mathbf{f}^T = \{\mathbf{f}_1^T, \dots, \mathbf{f}_S^T\}, \quad \mathbf{g}^T = \{\mathbf{g}_1^T, \dots, \mathbf{g}_S^T\}, \tag{5.3d}$$

being $n_S = \sum_{s=1}^{S} n_s$. $\mathbf{B}$ is the *compatibility matrix* (for conforming meshes, a signed Boolean matrix), and $\mathbf{L}$ is the *localization matrix*. Equations (5.2b) and (5.2c) state the compatibility and equilibrium conditions, respectively. Often it is convenient to define these conditions at the substructure level as

$$\begin{cases} \sum_{s=1}^{S} \mathbf{B}_s \mathbf{u}_s = \mathbf{0} & \text{(5.4a)} \\ \sum_{s=1}^{S} \mathbf{L}_s^T \mathbf{g}_s = \mathbf{0} & \text{(5.4b)} \end{cases}$$

where $\mathbf{B}_s$ and $\mathbf{L}_s$ are the $n_\lambda \times n_s$ compatibility and the $n_s \times n_u$ localization matrices pertaining to the s-th substructure, being n_λ the total number of interface compatibility constraints that need to be imposed and n_u the number of global *unique* dofs (i.e. without repetition of interface dofs, so that $n_u < n_S$). The following relationships hold

$$\mathbf{L} = \begin{bmatrix} \mathbf{L}_1 \\ \vdots \\ \mathbf{L}_S \end{bmatrix}, \quad \mathbf{B} = [\mathbf{B}_1, \dots, \mathbf{B}_S]\,. \tag{5.5}$$

From Eqs. (5.2) one can proceed using a primal or a dual formulation. In the *primal formulation* the unique set of n_u global unknowns $\mathbf{u}_u = \mathtt{unique}(\mathbf{u})$ is used and interface forces are eliminated using interface equilibrium. Using the localization matrix, we can write

$$\mathbf{u} = \mathbf{L}\mathbf{u}_u \quad \text{and/or} \quad \mathbf{u}_s = \mathbf{L}_s \mathbf{u}_u \quad \forall s, \tag{5.6}$$

which automatically satisfies compatibility, that is $\mathbf{B}\mathbf{u} = \mathbf{B}\mathbf{L}\mathbf{u}_u = \mathbf{o}$ (which also entails $\mathbf{L} = \mathrm{null}(\mathbf{B})$). The primal system therefore reduces to

$$(\mathbf{L}^T\mathbf{M}\mathbf{L})\ddot{\mathbf{u}}_u + (\mathbf{L}^T\mathbf{C}\mathbf{L})\dot{\mathbf{u}}_u + (\mathbf{L}^T\mathbf{K}\mathbf{L})\mathbf{u}_u = \mathbf{L}^T\mathbf{f} + \cancel{\mathbf{L}^T\mathbf{g}}\,. \tag{5.7}$$

In *dual formulation* the dofs vector $\mathbf{u}$ is retained instead, and the interface forces are constructed such that they act in opposite directions on the coupled substructures, that is

$$\mathbf{g} = -\mathbf{B}^T\boldsymbol{\lambda} \;\text{ and/or }\; \mathbf{g}_s = -\mathbf{B}_s^T\boldsymbol{\lambda} \tag{5.8}$$

where $\boldsymbol{\lambda}$ are Lagrange multipliers representing the interface forces intensities. Plugging Eq. (5.8) into Eqs. (5.2) we obtain the dual system as

$$\begin{cases} \mathbf{M}\ddot{\mathbf{u}} + \mathbf{C}\dot{\mathbf{u}} + \mathbf{K}\mathbf{u} + \mathbf{B}^T\boldsymbol{\lambda} = \mathbf{f} & \text{(5.9a)} \\ \mathbf{B}\mathbf{u} = \mathbf{0} & \text{(5.9b)} \end{cases}$$

or in matrix form

$$\begin{bmatrix} \mathbf{M} & \mathbf{0} \\ \mathbf{0} & \mathbf{0} \end{bmatrix} \begin{Bmatrix} \ddot{\mathbf{u}} \\ \ddot{\boldsymbol{\lambda}} \end{Bmatrix} + \begin{bmatrix} \mathbf{K} & \mathbf{B}^T \\ \mathbf{B} & \mathbf{0} \end{bmatrix} \begin{Bmatrix} \mathbf{u} \\ \boldsymbol{\lambda} \end{Bmatrix} = \begin{Bmatrix} \mathbf{f} \\ \mathbf{0} \end{Bmatrix} \tag{5.10}$$

where we considered the undamped system just for ease of notation. Being $\mathbf{B}^T$ the null space of $\mathbf{L}^T$, equilibrium condition (5.2c) is always satisfied. Dual formulation thus features more unknowns (repeated interface dofs, Lagrange multipliers) than its primal counterpart. Its success however is linked to its use in parallel solvers, such as the FETI method.

Example 1: Localization matrix

In this example, a 2D truss structure is divided into 4 substructures (a, b, c, d) with $n_a = 4$, $n_b = 2$, $n_c = 2$ and $n_d = 4$ dofs, for a total $n_S = 12$ dofs and $n_u = 6$ unique dofs.

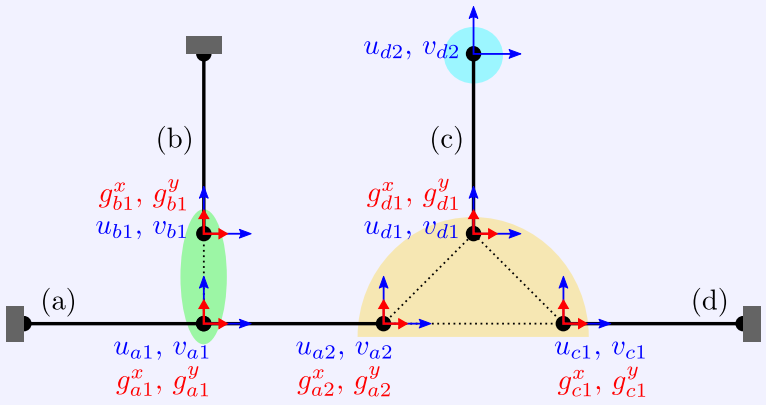

Equilibrium:

$$\mathbf{L}^T\mathbf{g} = \underbrace{\begin{bmatrix} 1&0&0&0\\ 0&1&0&0\\ 0&0&1&0\\ 0&0&0&1\\ 0&0&0&0\\ 0&0&0&0 \end{bmatrix}}_{\mathbf{L}_a^T} \underbrace{\begin{bmatrix} 1&0\\ 0&1\\ 0&0\\ 0&0\\ 0&0\\ 0&0 \end{bmatrix}}_{\mathbf{L}_b^T} \underbrace{\begin{bmatrix} 0&0\\ 0&0\\ 1&0\\ 0&1\\ 0&0\\ 0&0 \end{bmatrix}}_{\mathbf{L}_c^T} \underbrace{\begin{bmatrix} 0&0&0&0\\ 0&0&0&0\\ 1&0&0&0\\ 0&1&0&0\\ 0&0&1&0\\ 0&0&0&1 \end{bmatrix}}_{\mathbf{L}_d^T} \begin{Bmatrix} \mathbf{g}_a = \begin{bmatrix} g^x_{a1}\\ g^y_{a1}\\ g^x_{a2}\\ g^y_{a2} \end{bmatrix}\\ \mathbf{g}_b = \begin{bmatrix} g^x_{b1}\\ g^y_{b1} \end{bmatrix}\\ \mathbf{g}_c = \begin{bmatrix} g^x_{c1}\\ g^y_{c1} \end{bmatrix}\\ \mathbf{g}_d = \begin{bmatrix} g^x_{d1}\\ g^y_{d1}\\ g^x_{d2}\\ g^y_{d2} \end{bmatrix} \end{Bmatrix} = \mathbf{0}$$

Displacements in primal assembly:

$$\mathbf{u} = \begin{Bmatrix} \mathbf{u}_a = \begin{bmatrix} u_{a1}\\ v_{a1}\\ u_{a2}\\ v_{a2} \end{bmatrix}\\ \mathbf{u}_b = \begin{bmatrix} u_{b1}\\ v_{b1} \end{bmatrix}\\ \mathbf{u}_c = \begin{bmatrix} u_{c1}\\ v_{c1} \end{bmatrix}\\ \mathbf{u}_d = \begin{bmatrix} u_{d1}\\ v_{d1}\\ u_{d2}\\ v_{d2} \end{bmatrix} \end{Bmatrix} = \begin{bmatrix} \mathbf{L}_a = \begin{bmatrix} 1&0&0&0&0&0\\ 0&1&0&0&0&0\\ 0&0&1&0&0&0\\ 0&0&0&1&0&0 \end{bmatrix}\\ \mathbf{L}_b = \begin{bmatrix} 1&0&0&0&0&0\\ 0&1&0&0&0&0 \end{bmatrix}\\ \mathbf{L}_c = \begin{bmatrix} 0&0&1&0&0&0\\ 0&0&0&1&0&0 \end{bmatrix}\\ \mathbf{L}_d = \begin{bmatrix} 0&0&1&0&0&0\\ 0&0&0&1&0&0\\ 0&0&0&0&1&0\\ 0&0&0&0&0&1 \end{bmatrix} \end{bmatrix} \begin{Bmatrix} u_{a1}\\ v_{a1}\\ u_{a2}\\ v_{a2}\\ u_{d2}\\ v_{d2} \end{Bmatrix} = \mathbf{L}\mathbf{u}_u$$

Figure 34: Example of 4 substructures meshed with 2D truss elements. Interfaces between structures have been highlighted with different colors to ease the reading.

5.1.2 Component Mode Synthesis (CMS)

CMS refers to "the construction of substructures based on a reduced space" Klerk et al., 2008. In these methods, the response of the s-th subcomponent is assumed to be well represented in a subspace spanned by the m_s columns of the *reduced basis*

$\mathbf{V}_s$, being $m_s \ll n_s$. The displacement vector of the s-th substructure can therefore be approximated as

$$\mathbf{u}_s = \begin{Bmatrix} \mathbf{u}_s^B \\ \mathbf{u}_s^I \end{Bmatrix} \simeq \mathbf{V}_s \boldsymbol{\eta}_s = \begin{bmatrix} \mathbf{V}_s^{BB} & \mathbf{V}_s^{BI} \\ \mathbf{V}_s^{IB} & \mathbf{V}_s^{II} \end{bmatrix} \begin{Bmatrix} \boldsymbol{\eta}_s^B \\ \boldsymbol{\eta}_s^I \end{Bmatrix} \tag{5.11}$$

being $\boldsymbol{\eta}_s$ the vector of the reduced coordinates associated to $\mathbf{V}_s$ and where boundary[1] (superscript B) and interior dofs (superscript I) are put in evidence.

Example 2: Compatibility matrix

In this example, we show the use of the **B** matrix. Notice that at the interface between substructures a, c and d 6 constraint equations can be written, however only 4 are linearly independent. Usually this is not a problem; also, it easier to implement automatic procedures considering all possible constraint equations. Therefore, in this case $n_\lambda = 8$ equations were written, but this number could have been reduced to $n_\lambda = 6$.

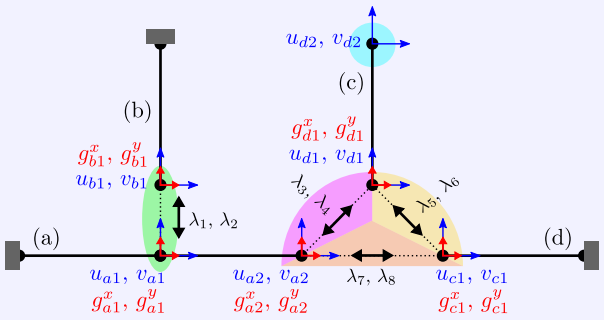

Compatibility:

$$\mathbf{Bu} = \underbrace{\begin{bmatrix} 1 & 0 & 0 & 0 \\ 0 & 1 & 0 & 0 \\ 0 & 0 & 1 & 0 \\ 0 & 0 & 0 & 1 \\ 0 & 0 & 0 & 0 \\ 0 & 0 & 0 & 0 \\ 0 & 0 & 1 & 0 \\ 0 & 0 & 0 & 1 \end{bmatrix}}_{\mathbf{B}_a} \underbrace{\begin{bmatrix} -1 & 0 \\ 0 & -1 \\ 0 & 0 \\ 0 & 0 \\ 0 & 0 \\ 0 & 0 \\ 0 & 0 \\ 0 & 0 \end{bmatrix}}_{\mathbf{B}_b} \underbrace{\begin{bmatrix} 0 & 0 \\ 0 & 0 \\ -1 & 0 \\ 0 & -1 \\ 1 & 0 \\ 0 & 1 \\ 0 & 0 \\ 0 & 0 \end{bmatrix}}_{\mathbf{B}_c} \underbrace{\begin{bmatrix} 0 & 0 & 0 & 0 \\ 0 & 0 & 0 & 0 \\ 0 & 0 & 0 & 0 \\ 0 & 0 & 0 & 0 \\ -1 & 0 & 0 & 0 \\ 0 & -1 & 0 & 0 \\ -1 & 0 & 0 & 0 \\ 0 & -1 & 0 & 0 \end{bmatrix}}_{\mathbf{B}_d} \begin{Bmatrix} \mathbf{u}_a = \begin{Bmatrix} u_{a1} \\ v_{a1} \\ u_{a2} \\ v_{a2} \end{Bmatrix} \\ \mathbf{u}_b = \begin{Bmatrix} u_{b1} \\ v_{b1} \end{Bmatrix} \\ \mathbf{u}_c = \begin{Bmatrix} u_{c1} \\ v_{c1} \end{Bmatrix} \\ \mathbf{u}_d = \begin{Bmatrix} u_{d1} \\ v_{d1} \\ u_{d2} \\ v_{d2} \end{Bmatrix} \end{Bmatrix} = \mathbf{0}$$

Interface forces in dual assembly:

$$\mathbf{B}^T\boldsymbol{\lambda} = \begin{bmatrix} \mathbf{B}_a^T = \begin{bmatrix} 1 & 0 & 0 & 0 & 0 & 0 & 0 & 0 \\ 0 & 1 & 0 & 0 & 0 & 0 & 0 & 0 \\ 0 & 0 & 1 & 0 & 0 & 0 & 1 & 0 \\ 0 & 0 & 0 & 1 & 0 & 0 & 0 & 1 \end{bmatrix} \\ \mathbf{B}_b^T = \begin{bmatrix} -1 & 0 & 0 & 0 & 0 & 0 & 0 & 0 \\ 0 & -1 & 0 & 0 & 0 & 0 & 0 & 0 \end{bmatrix} \\ \mathbf{B}_c^T = \begin{bmatrix} 0 & 0 & -1 & 0 & 1 & 0 & 0 & 0 \\ 0 & 0 & 0 & -1 & 0 & 1 & 0 & 0 \end{bmatrix} \\ \mathbf{B}_d^T = \begin{bmatrix} 0 & 0 & 0 & 0 & -1 & 0 & -1 & 0 \\ 0 & 0 & 0 & 0 & 0 & -1 & 0 & -1 \\ 0 & 0 & 0 & 0 & 0 & 0 & 0 & 0 \\ 0 & 0 & 0 & 0 & 0 & 0 & 0 & 0 \end{bmatrix} \end{bmatrix} \begin{Bmatrix} \lambda_1 \\ \lambda_2 \\ \lambda_3 \\ \lambda_4 \\ \lambda_5 \\ \lambda_6 \\ \lambda_7 \\ \lambda_8 \end{Bmatrix} = \begin{Bmatrix} \lambda_1 \\ \lambda_2 \\ \lambda_3 + \lambda_7 \\ \lambda_4 + \lambda_8 \\ -\lambda_1 \\ -\lambda_2 \\ -\lambda_3 + \lambda_5 \\ -\lambda_4 + \lambda_6 \\ -\lambda_5 - \lambda_7 \\ -\lambda_6 - \lambda_8 \\ 0 \\ 0 \end{Bmatrix} = \begin{Bmatrix} g^x_{a1} \\ g^y_{a1} \\ g^x_{a2} \\ g^y_{a2} \\ g^x_{b1} \\ g^y_{b1} \\ g^x_{c1} \\ g^y_{c1} \\ g^x_{d1} \\ g^y_{d1} \\ g^x_{d2} \\ g^y_{d2} \end{Bmatrix} = \mathbf{g}$$

Figure 35: Example of 4 substructures meshed with 2D truss elements. Interfaces between structures have been highlighted with different colors to ease the reading.

1 *caveat:* by "boundary" dofs we refer here to *interface* dofs between substructures. We assume that dofs associated to physical boundaries (e.g. clamp) are already removed through appropriate partitioning of matrices/vectors in the EoM.

Unless an interface-reduction strategy is adopted, usually boundary dofs are retained in physical coordinates, i.e.

$$\boldsymbol{\eta}_s^B = \mathbf{u}_s^B \in \mathbb{R}^{n_s^B}, \tag{5.12a}$$

$$\mathbf{V}_s^{BB} = \mathbf{I}_s \in \mathbb{R}^{n_s^B \times n_s^B} \tag{5.12b}$$

$$\mathbf{V}_s^{BI} = \mathbf{0} \in \mathbb{R}^{n_s^B \times n_s^I} \tag{5.12c}$$

with n_s^B and n_s^I the number of boundary and interior dofs, respectively, of substructure s, in which case we have

$$\mathbf{u}_s = \begin{Bmatrix} \mathbf{u}_s^B \\ \mathbf{u}_s^I \end{Bmatrix} \simeq \mathbf{V}_s \boldsymbol{\eta}_s = \begin{bmatrix} \mathbf{I}_s & \mathbf{0} \\ \mathbf{V}_s^{IB} & \mathbf{V}_s^{II} \end{bmatrix} \begin{Bmatrix} \mathbf{u}_s^B \\ \boldsymbol{\eta}_s^I \end{Bmatrix}. \tag{5.13}$$

The choice of the reduced basis depends on the method adopted, e.g. Ritz vectors, vibration and constraint modes in Craig-Bampton's method (Craig and Bampton, 1968), or rigid body modes and attachment modes in Rubin's method (Rubin, 1975). Regardless, the equations of motion of each substructure can be projected using the selected basis as

$$\underbrace{\mathbf{V}_s^T \mathbf{M}_s \mathbf{V}_s}_{\tilde{\mathbf{M}}_s} \ddot{\boldsymbol{\eta}}_s + \underbrace{\mathbf{V}_s^T \mathbf{K}_s \mathbf{V}_s}_{\tilde{\mathbf{K}}_s} \boldsymbol{\eta}_s = \underbrace{\mathbf{V}_s^T \mathbf{f}_s}_{\tilde{\mathbf{f}}_s} + \underbrace{\mathbf{V}_s^T \mathbf{g}_s}_{\tilde{\mathbf{g}}_s}. \tag{5.14}$$

where the notation $\tilde{\star}_s$ is used to denote a projected matrix/vector. One can then assemble the reduced substructures via primal or dual formulation into the global reduced system, in a similar manner to the one shown in the previous section for the full system.

5.2 PRELIMINARY CONSIDERATIONS

As stated at the beginning of the chapter, the aim here is to use DpROM with substructuring trying to accommodate *arbitrary* defects. As already mentioned, this means that we have to allow (initially) non-compatible interfaces. Primal assembly based methods, not allowing access to the interface dofs and forces, are then ruled out. As for dual assembly methods, to the best of the author's knowledge, the only ROM that can be found in literature is given by Gruber et al., 2019, where a strategy to stabilize the otherwise unstable Dual-Craig-Bampton[2] ROM is proposed. The price to pay for this stabilization, however, is a second reduction which, in our parametric setting, cannot be performed: for each new parameter realization a new ROM should be computed. A thorough dissertation on the pros and cons of different methods was performed by Bachmann, 2020. Upon these considerations, in the following the Finite-Element Tearing and Interconnecting (FETI) method, based on a dual assembly formulation, is presented.

5.3 FETI

The Finite-Element Tearing and Interconnecting was first presented in Farhat and Roux, 1991 as a subdomain method to minimize the cores intercommunication during parallel computing. In other words, the method tries to maximize each substructure's computational independence from each other. First introduced for static problems in structural mechanics, the method has become popular and many extensions have been proposed in literature (Farhat, Chen, et al., 1995; Farhat and Mandel, 1998).

2 Very similar to Rubin's method though.

5.3.1 Linear Static FETI

Let $\mathcal{I} = \{1, \ldots, N_I\}$ be the set numbering interfaces across all substructures, without repetition (i.e. shared interfaces are counted only once), being N_I the total number of interfaces. Let now $\mathcal{I}_s \subseteq \mathcal{I}$ be the subset containing only the number of the interfaces pertaining to substructure s.

Considering the linear elastic static problem, for each substructure s we can write

$$\begin{cases} \mathbf{K}_s \mathbf{u}_s = \mathbf{f}_s + \sum_{k \in \mathcal{I}_s} (\mathbf{B}_s^k)^T \boldsymbol{\lambda}_k & \text{for } s = 1, \ldots, S, \quad (5.15a) \\ \mathbf{B}_s^k \mathbf{u}_s + \mathbf{B}_r^k \mathbf{u}_r = 0 & \text{for } s = 1, \ldots, S \quad \text{and} \quad \forall k \in \mathcal{I}_s, \quad (5.15b) \end{cases}$$

being $\mathbf{B}_s^k$ the partition of $\mathbf{B}_s$ pertaining to interface k, $\boldsymbol{\lambda}_k$ the partition of $\boldsymbol{\lambda}$ pertaining to interface k and $r = r(s,k)$ the number of the substructure connected to substructure s through interface k.

In words, the S Eqs. (5.15a) state that elastic forces of each substructure must balance external loads applied to the structure and interface forces coming from all adjacent substructures. At the same time, compatibility between each pair of substructures is enforced by Eqs. (5.15b) (some equations can be redundant, see example in Fig. 35).

For the sake of illustration, let us consider only two substructures connected by one interface. Since $\mathcal{I} = \{1\}$, we can also ease notation noticing that $\mathbf{B}_s^k = \mathbf{B}_s$ and $\boldsymbol{\lambda}_k = \boldsymbol{\lambda}$. The problem then can be written as

$$\begin{cases} \mathbf{K}_1 \mathbf{u}_1 = \mathbf{f}_1 + \mathbf{B}_1^T \boldsymbol{\lambda} & (5.16a) \\ \mathbf{K}_2 \mathbf{u}_2 = \mathbf{f}_2 + \mathbf{B}_2^T \boldsymbol{\lambda} & (5.16b) \\ \mathbf{B}_1 \mathbf{u}_1 + \mathbf{B}_2 \mathbf{u}_2 = 0 & (5.16c) \end{cases}$$

and

$$\begin{cases} \mathbf{u}_1 = \mathbf{K}_1^{-1} \left(\mathbf{f}_1 + \mathbf{B}_1^T \boldsymbol{\lambda} \right) & (5.17a) \\ \mathbf{u}_2 = \mathbf{K}_2^{-1} \left(\mathbf{f}_2 + \mathbf{B}_2^T \boldsymbol{\lambda} \right) & (5.17b) \\ \left(\mathbf{B}_1 \mathbf{K}_1^{-1} \mathbf{B}_1^T + \mathbf{B}_2 \mathbf{K}_2^{-1} \mathbf{B}_2^T \right) \boldsymbol{\lambda} = -\mathbf{B}_1 \mathbf{K}_1^{-1} \mathbf{f}_1 - \mathbf{B}_2 \mathbf{K}_2^{-1} \mathbf{f}_2 \,. & (5.17c) \end{cases}$$

The last set of equations can be cheaply solved for $\boldsymbol{\lambda} \in \mathbb{R}^{n_\lambda}$ first using compatibility, then the equilibrium equation for each substructure can be solved independently, in parallel on different processors.

The case of unconstrained substructures can also be treated by adding rigid body modes to the displacement solution, by substituting the stiffness matrix inverse with its pseudoinverse and then by introducing an orthogonality condition: all details can be found in Farhat and Roux, 1991. In the same work, it is also offered a way to avoid the explicit computation of the interface operator

$$\mathbf{F}_I = \left(\mathbf{B}_1 \mathbf{K}_1^{-1} \mathbf{B}_1^T + \mathbf{B}_2 \mathbf{K}_2^{-1} \mathbf{B}_2^T \right), \quad (5.18)$$

via a preconditioned conjugate projected gradient (PCPG) algorithm.

Example 3: Compatibility in FETI

In this example, we have 4 interfaces, so that $\mathcal{I} = \{\alpha, \beta, \gamma, \delta\}$, $\mathcal{I}_a = \{\alpha, \beta, \delta\}$, $\mathcal{I}_b = \{\alpha\}$, $\mathcal{I}_c = \{\gamma, \delta\}$ and $\mathcal{I}_d = \{\beta, \gamma\}$. In the figure, the partitions of $\mathbf{B}$ representing the $\mathbf{B}_s^k$ compatibility matrices to be used in FETI are indicated.

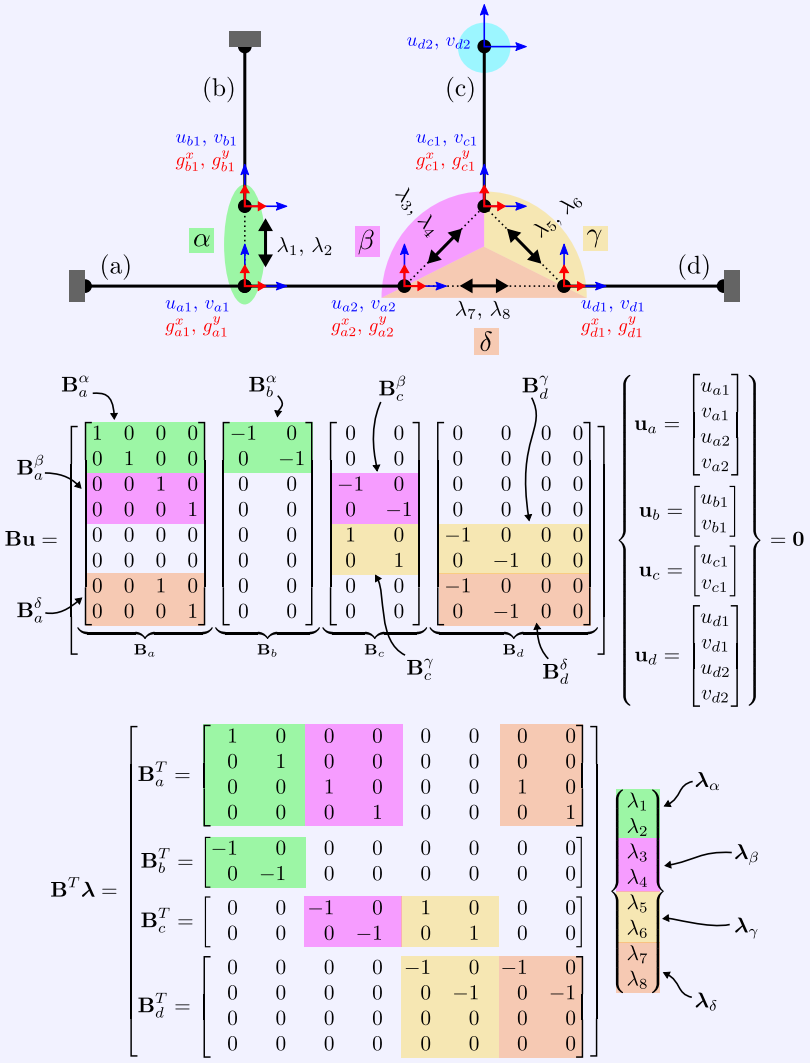

Figure 36: Example of 4 substructures meshed with 2D truss elements. Interfaces between structures have been highlighted with different colors to ease the reading.

5.3.2 Nonlinear Dynamic FETI

In Farhat, Chen, et al., 1995 the method was extended to nonlinear dynamics. For each substructure, the equilibrium equations write

$$\mathbf{M}_s\ddot{\mathbf{u}}_s + \mathbf{f}_{int,s}(\mathbf{u}_s) = \mathbf{f}_s + \sum_{k\in\mathcal{I}_s} (\mathbf{B}_s^k)^T\boldsymbol{\lambda}_k, \tag{5.19}$$

which can then be discretized in time and linearized as

$$\begin{aligned} \mathbf{S}_s(\mathbf{u}_{s,n}^j)\Delta\mathbf{u}_{s,n}^{j+1} &= \mathbf{r}_{s,n}^j + \sum_{k\in\mathcal{I}_s} (\mathbf{B}_s^k)^T\boldsymbol{\lambda}_{k,n}^{j+1}, \\ \Delta\mathbf{u}_{s,n}^{j+1} &= \mathbf{u}_{s,n}^{j+1} - \mathbf{u}_{s,n}^j, \end{aligned} \tag{5.20}$$

where n and j denote the time and the iteration steps, respectively, $\mathbf{S}_s$ is the tangent dynamic stiffness matrix (whose expression depends on the chosen algorithm and which comprises mass, damping and elastic terms), and $\mathbf{r}_s$ is the out-of-balance force vector (residual).

Following later works by Combescure and Gravouil, 2002; Gravouil and Combescure, 2001; Mahjoubi et al., 2009; A. Prakash and Hjelmstad, 2004, we adopt a velocity-based Newmark integration scheme with parameters γ and β and time step h; compatibility is imposed on *velocities*, i.e.

$$\mathbf{B}_s^k \dot{\mathbf{u}}_s + \mathbf{B}_r^k \dot{\mathbf{u}}_r = \mathbf{0} \qquad \text{for } s = 1, \dots, S \quad \text{and} \quad \forall k \in \mathcal{I}_s. \tag{5.21}$$

Going back to the simple example of two domains with one interface, we can write

$$\begin{cases} \mathbf{M}_1 \ddot{\mathbf{u}}_1 + \mathbf{C}_1 \dot{\mathbf{u}}_1 + \mathbf{f}_{int}(\mathbf{u}_1) = \mathbf{f}_1 + \mathbf{B}_1^T \boldsymbol{\lambda} & (5.22a) \\ \mathbf{M}_2 \ddot{\mathbf{u}}_2 + \mathbf{C}_2 \dot{\mathbf{u}}_2 + \mathbf{f}_{int}(\mathbf{u}_2) = \mathbf{f}_2 + \mathbf{B}_2^T \boldsymbol{\lambda} & (5.22b) \\ \mathbf{B}_1 \dot{\mathbf{u}}_1 + \mathbf{B}_2 \dot{\mathbf{u}}_2 = \mathbf{0} & (5.22c) \end{cases}$$

and use the Newark formulas for the discretized displacement and velocities

$$\mathbf{u}_{s,n+1} = \underbrace{\mathbf{u}_{s,n} + \left(\frac{\gamma-\beta}{\gamma} h\right) \dot{\mathbf{u}}_{s,n} + \left(\frac{\gamma-2\beta}{2\gamma} h^2\right) \ddot{\mathbf{u}}_{s,n}}_{\text{prediction}} + \underbrace{\frac{\beta h}{\gamma} \dot{\mathbf{u}}_{s,n+1}}_{\text{correction}}, \tag{5.23a}$$

$$\ddot{\mathbf{u}}_{s,n+1} = \overbrace{\frac{\gamma-1}{\gamma} \ddot{\mathbf{u}}_{s,n} - \frac{1}{\gamma h} \dot{\mathbf{u}}_{s,n}}^{\text{prediction}} + \overbrace{\frac{1}{\gamma h} \dot{\mathbf{u}}_{s,n+1}}^{\text{correction}}, \tag{5.23b}$$

where we marked the prediction/correction components to be used in the numerical scheme. As usual, Newton-Rapson iteration algorithm can be used to solve the nonlinear system. The residuals write

$$\mathbf{r}_s = \mathbf{M}_s \ddot{\mathbf{u}}_s + \mathbf{C}_s \dot{\mathbf{u}}_s + \mathbf{f}_{int}(\mathbf{u}_s) - \mathbf{f}_s - \mathbf{B}_s^T \boldsymbol{\lambda} = 0 \tag{5.24}$$

and, at time step n, we can expand it in Taylor series to the first order and set up an iteration scheme (index j) equalling to zero:

$$\mathbf{r}_{s,n}^{j+1} \approx \mathbf{r}_{s,n}^j + \left.\frac{\partial \mathbf{r}_s}{\partial \mathbf{u}_s}\right|_n^j \Delta \mathbf{u}_s + \left.\frac{\partial \mathbf{r}_s}{\partial \dot{\mathbf{u}}_s}\right|_n^j \Delta \dot{\mathbf{u}}_s + \left.\frac{\partial \mathbf{r}_s}{\partial \ddot{\mathbf{u}}_s}\right|_n^j \Delta \ddot{\mathbf{u}}_s + \left.\frac{\partial \mathbf{r}_s}{\partial \boldsymbol{\lambda}}\right|_n^j \Delta \boldsymbol{\lambda} = 0 \tag{5.25}$$

which in our scheme becomes

$$\begin{aligned} &\mathbf{r}_{s,n}^j + \mathbf{K}_s^t(\mathbf{u}_{s,n}^j) \Delta \mathbf{u}_s + \mathbf{C}_s \Delta \dot{\mathbf{u}}_s + \mathbf{M}_s \Delta \ddot{\mathbf{u}}_s + \mathbf{B}_s^T \Delta \boldsymbol{\lambda} = 0 \\ &\mathbf{r}_{s,n}^j + \left(\frac{1}{\gamma h} \mathbf{M}_s + \mathbf{C}_s + \frac{\beta h}{\gamma} \mathbf{K}_s^t(\mathbf{u}_{s,n}^j)\right) \Delta \dot{\mathbf{u}}_s + \mathbf{B}_s^T \Delta \boldsymbol{\lambda} = 0 \\ &\mathbf{S}(\mathbf{u}_n^j) \Delta \dot{\mathbf{u}}_s + \mathbf{B}_s^T \Delta \boldsymbol{\lambda} = -\mathbf{r}_{s,n}^j \end{aligned} \tag{5.26}$$

with $\Delta(\bullet) = (\bullet)_n^{j+1} - (\bullet)_n^j$.

In our example, we have

$$\begin{cases} \Delta \dot{\mathbf{u}}_1 = -\mathbf{S}(\mathbf{u}_{1,n}^j)^{-1} \left(\mathbf{r}_{1,n}^j + \mathbf{B}_1^T \Delta \boldsymbol{\lambda}\right) & (5.27a) \\ \Delta \dot{\mathbf{u}}_2 = -\mathbf{S}(\mathbf{u}_{2,n}^j)^{-1} \left(\mathbf{r}_{2,n}^j + \mathbf{B}_2^T \Delta \boldsymbol{\lambda}\right) & (5.27b) \\ \mathbf{B}_1(\dot{\mathbf{u}}_{1,n}^j + \Delta \dot{\mathbf{u}}_1) + \mathbf{B}_2(\dot{\mathbf{u}}_{2,n}^j + \Delta \dot{\mathbf{u}}_2) = \mathbf{0} & (5.27c) \end{cases}$$

and, after manipulation, the interface equation writes

$$\begin{aligned} &\left(\mathbf{B}_1(\mathbf{S}_{1,n}^j)^{-1} \mathbf{B}_1^T + \mathbf{B}_2(\mathbf{S}_{2,n}^j)^{-1} \mathbf{B}_2^T\right) \Delta \boldsymbol{\lambda} \\ &\qquad = \mathbf{B}_1 \left(\dot{\mathbf{u}}_{1,n}^j - (\mathbf{S}_{1,n}^j)^{-1} \mathbf{r}_{1,n}^j\right) + \mathbf{B}_2 \left(\dot{\mathbf{u}}_{2,n}^j - (\mathbf{S}_{2,n}^j)^{-1} \mathbf{r}_{2,n}^j\right). \end{aligned} \tag{5.28}$$

Solving the latter, Lagrange multipliers can be updated, then equilibrium equations can be solved to retrieve velocity increments, so that finally all the kinematic variables can be determined.

5.4 REDUCTION IN FETI

Due to the high level of independence between substructures in FETI, the application of reduction techniques to the substructures is fairly straightforward. Assuming that the response can be approximated as

$$\mathbf{u}_s \approx \mathbf{V}_s \eta_s, \tag{5.29}$$

the FETI system can be written simply as

$$\begin{cases} \mathbf{V}_1^T \mathbf{M}_1 \mathbf{V}_1 \ddot{\eta}_1 + \mathbf{V}_1^T \mathbf{C}_1 \mathbf{V}_1 \dot{\eta}_1 + \mathbf{V}_1^T \mathbf{f}_{int}(\mathbf{V}_1 \eta_1) = \mathbf{V}_1^T \mathbf{f}_1 + \mathbf{V}_1^T \mathbf{B}_1^T \lambda & (5.30a) \\ \mathbf{V}_2^T \mathbf{M}_2 \mathbf{V}_2 \ddot{\eta}_2 + \mathbf{V}_2^T \mathbf{C}_2 \mathbf{V}_2 \dot{\eta}_2 + \mathbf{V}_2^T \mathbf{f}_{int}(\mathbf{V}_2 \eta_2) = \mathbf{V}_2^T \mathbf{f}_2 + \mathbf{V}_2^T \mathbf{B}_2^T \lambda & (5.30b) \\ \mathbf{B}_1 \mathbf{V}_1 \dot{\eta}_1 + \mathbf{B}_2 \mathbf{V}_2 \dot{\eta}_2 = \mathbf{0} & (5.30c) \end{cases}$$

and the iterative solution described in the previous section can again be employed to solve the nonlinear system. For the sake of illustration, in the case two substructures, one interface and linear system, we write

$$\begin{cases} \left(\tilde{\mathbf{B}}_1 \tilde{\mathbf{S}}_1^{-1} \tilde{\mathbf{B}}_1^T + \tilde{\mathbf{B}}_2 \tilde{\mathbf{S}}_2^{-1} \tilde{\mathbf{B}}_2^T \right) \lambda = -\tilde{\mathbf{B}}_1 \tilde{\mathbf{S}}_1^{-1} \tilde{\mathbf{f}}_1 - \tilde{\mathbf{B}}_2 \tilde{\mathbf{S}}_2^{-1} \tilde{\mathbf{f}}_2 & (5.31a) \\ \eta_1 = \tilde{\mathbf{S}}_1^{-1} \left(\tilde{\mathbf{f}}_1 + \tilde{\mathbf{B}}_1^T \lambda \right) & (5.31b) \\ \eta_2 = \tilde{\mathbf{S}}_2^{-1} \left(\tilde{\mathbf{f}}_2 + \tilde{\mathbf{B}}_2^T \lambda \right) & (5.31c) \end{cases}$$

where $\tilde{\mathbf{B}}_s = \mathbf{B}_s \mathbf{V}_s$ and

$$\tilde{\mathbf{S}}_s = \mathbf{V}_s^T \mathbf{S} \mathbf{V}_s = \mathbf{V}_s^T \left(\frac{1}{\gamma h} \mathbf{M}_s + \mathbf{C}_s + \frac{\beta h}{\gamma} \mathbf{K}_s \right) \mathbf{V}_s \tag{5.32}$$

is the reduced (linear) dynamic stiffness matrix.

5.4.1 Nonlinear Craig-Bampton (in a nutshell)

We select the reduction basis $\mathbf{V}$ according to CB method (Craig and Bampton, 1968), extended to nonlinear systems through MDs (Wenneker and Tiso, 2014). The displacement of the structure can be approximated as (we drop the subscript s to ease notation):

$$\mathbf{u} = \begin{Bmatrix} \mathbf{u}^B \\ \mathbf{u}^I \end{Bmatrix} \simeq \mathbf{V}\eta = \begin{bmatrix} \mathbf{I} & 0 & 0 & 0 \\ \Psi^I & \Psi_\theta^I & \phi^I & \theta^I \end{bmatrix} \begin{Bmatrix} \mathbf{u}^B \\ \mathbf{u}_\theta^B \\ \eta_\varphi \\ \eta_\theta \end{Bmatrix}. \tag{5.33}$$

where the displacement vector was partitioned in order to have the interface ($\bullet^B$) dofs before the internal ones ($\bullet^I$). The vector in the basis are the Constraint Modes Ψ (CM), the Constraint Mode Derivatives Ψ_θ (CMDs), and the *internal* VMs ϕ^I and MDs θ^I. Notice that interface dofs $\mathbf{u}^B$ have not been reduced and that the size of coordinates associated to DCMs is proportional to the size of $\mathbf{u}^B$, reason why, although not physical, they are here named $\mathbf{u}_\theta^B$. In the following, we define the introduced vectors.

Constraint Modes (CM)

The i-th CMs can be loosely described as "the deformed shape the structure assumes when the i-th interface dof undergoes an unitary displacement, being the other interface dofs fixed". Considering the linear static problem with imposed boundary motion and opportunely partitioning vector and matrices between interface (B) and internal (I) dofs, we have

$$\mathbf{K}\mathbf{u} = \begin{bmatrix} \mathbf{K}^{BB} & \mathbf{K}^{BI} \\ \mathbf{K}^{IB} & \mathbf{K}^{II} \end{bmatrix} \begin{Bmatrix} \mathbf{u}^{B} \\ \mathbf{u}^{I} \end{Bmatrix} = \begin{Bmatrix} \mathbf{f}_u \\ 0 \end{Bmatrix} = \mathbf{F}_u, \tag{5.34}$$

where

$$\mathbf{f}_u = \left(\mathbf{K}^{BB} - \mathbf{K}^{BI}(\mathbf{K}^{II})^{-1}\mathbf{K}^{IB}\right)\mathbf{u}^{B}, \tag{5.35}$$

and

$$\boldsymbol{\Psi}_i^{I} = -(\mathbf{K}^{II})^{-1}\mathbf{K}^{IB}\mathbf{u}_i^{B}. \tag{5.36}$$

Choosing $\mathbf{u}_i^B$ with the i-th dof equal to 1 and zero elsewhere, we can collect all $\mathbf{u}_i^B$ in an identity matrix $\mathbf{I}$ so that, applying Eq. (5.36) to all interface dofs, we can compute all the (internal) CMs as

$$\boldsymbol{\Psi}^{I} = -(\mathbf{K}^{II})^{-1}\mathbf{K}^{IB}. \tag{5.37}$$

Finally, considering interface dofs, CMs write

$$\text{CM}: \quad \boldsymbol{\Psi} \triangleq \begin{bmatrix} \boldsymbol{\Psi}^{B} \\ \boldsymbol{\Psi}^{I} \end{bmatrix} = \begin{bmatrix} \mathbf{I} \\ -(\mathbf{K}^{II})^{-1}\mathbf{K}^{IB} \end{bmatrix}. \tag{5.38}$$

CMs then account for the static response of the substructure to a displacement of the interface.

Constraint Mode Derivatives (CMD).

In the case of large deformations, CMs alone cannot describe the static deformation of the structure. Although MDs may partially span the solution space of the nonlinear static response, typically a high number of VMs and MDs is required to retrieve accurate results. Although not canonical, in past works (see van den Broek, 2019) the author found that the derivative of CMs with respect to their amplitude sensibly improves the response.

The procedure is similar to the one presented to compute static MDs. Considering the i-th CM, we have

$$\mathbf{K}^{t}\boldsymbol{\Psi}_i = \mathbf{F}_u, \tag{5.39}$$

and taking the derivative with respect to the amplitude u_j^B, we obtain

$$\frac{\partial \mathbf{K}^{t}}{\partial u_j^{B}}\boldsymbol{\Psi}_i + \mathbf{K}^{t}\frac{\partial \boldsymbol{\Psi}_i}{\partial u_j^{B}} = 0, \tag{5.40}$$

where the linear stiffness matrix was substituted with the tangent stiffness matrix and the load vector was assumed displacement-independent. Finally, evaluating at equilibrium

$$\text{CMD}: \quad (\boldsymbol{\Psi}_\theta)_{ij} \triangleq \left.\frac{\partial \boldsymbol{\Psi}_i}{\partial u_j^{B}}\right|_{eq} = -(\mathbf{K}_{eq}^{t})^{-1}\left.\frac{\partial \mathbf{K}^{t}}{\partial u_j^{B}}\right|_{eq}\boldsymbol{\Psi}_i|_{eq}. \tag{5.41}$$

Notice that the full set of CMDs computed in this way is not full rank, therefore an orthogonalization step is always required. Moreover, it is often unfeasible to take all the available $n_s^B(n_s^B+1)/2$ CMDs (although the linearly independent vectors are less than this limit). One could then sensibly take only the subset of $(\boldsymbol{\Psi}_\theta)_{ii}$, or apply other selection strategies (e.g. singular value decomposition).

Internal VMs and MDs.

The dynamics of the interior dofs of the structure is trusted to a set of VMs and MDs (in the nonlinear case). The definition of these vectors is just the same as described in the previous chapters, however, they are computed using the internal dofs only, assuming the interfaces to be fixed. For instance, the eigenvalue problem writes

$$\left(\mathbf{K}^{II} - \omega_i^2 \mathbf{M}^{II}\right) \boldsymbol{\phi}_i^I = \mathbf{0}. \tag{5.42}$$

Having considered fixed interface dofs, we have that $\boldsymbol{\phi}_i^B = \mathbf{0}$. A similar procedure can be followed to compute θ_{ij}^I (and, again, we will have $\theta_{ij}^B = 0$).

5.4.2 Interface Reduction: Local level Characteristic Constraints (LCCs)

We introduce here a further step of reduction, involving the interface dofs. The main motivation is that even after reduction, the ROM in each substructure may still count a high number of coordinates. In the present context, where a tensorial approach has been adopted to evaluate internal forces, the number of dofs in each substructure cannot be too high in order not to spoil the benefits of the ROM itself. Several works have been presented in literature on this topic (see for instance Krattiger et al., 2019; Wu, Tiso, and van Keulen, 2018). To preserve independence between substructures, we resort here to the Local level Constraint modes (LCCs), which can be obtained as follows. Let us recall Eq. (5.13)

$$\mathbf{u}_s = \begin{Bmatrix} \mathbf{u}_s^B \\ \mathbf{u}_s^I \end{Bmatrix} \simeq \mathbf{V}_s \boldsymbol{\eta}_s = \begin{bmatrix} \mathbf{I}_s & \mathbf{0} \\ \mathbf{V}_s^{IB} & \mathbf{V}_s^{II} \end{bmatrix} \begin{Bmatrix} \mathbf{u}_s^B \\ \boldsymbol{\eta}_s^I \end{Bmatrix},$$

and let us partition the system matrices separating interface (non-reduced) dofs and interior (reduced) dofs:

$$\begin{bmatrix} \mathbf{I}_s & (\mathbf{V}_s^{IB})^T \\ \mathbf{0} & (\mathbf{V}_s^{II})^T \end{bmatrix} \begin{bmatrix} \mathbf{M}_s^{BB} & \mathbf{M}_s^{BI} \\ \mathbf{M}_s^{IB} & \mathbf{M}_s^{II} \end{bmatrix} \begin{bmatrix} \mathbf{I}_s & \mathbf{0} \\ \mathbf{V}_s^{IB} & \mathbf{V}_s^{II} \end{bmatrix} \triangleq \begin{bmatrix} \tilde{\mathbf{M}}_s^{BB} & \tilde{\mathbf{M}}_s^{BI} \\ \tilde{\mathbf{M}}_s^{IB} & \tilde{\mathbf{M}}_s^{II} \end{bmatrix}, \tag{5.43}$$

where we take the example of the mass matrix and where $\tilde{\bullet}$ denotes the reduced matrix. Notice that $\tilde{\mathbf{M}}_s^{BB} \neq \mathbf{M}_s^{BB}$. Selecting the partition pertaining the interface dofs, we can write the eigenvalue problem

$$\text{LCC}: \quad \left(\tilde{\mathbf{K}}_s^{BB} - \omega_i^2 \tilde{\mathbf{M}}_s^{BB}\right) \tilde{\boldsymbol{\phi}}_{s,i} = \mathbf{0} \tag{5.44}$$

which can be used to compute $\tilde{m}_s \ll n_s^B$ LCCs $\tilde{\boldsymbol{\phi}}_{s,i}$, collected in a matrix $\tilde{\boldsymbol{\phi}}_s$. Finally, we can write the reduction basis as

$$\begin{Bmatrix} \mathbf{u}_s^B \\ \mathbf{u}_s^I \end{Bmatrix} \approx \begin{bmatrix} \mathbf{I}_s & \mathbf{0} \\ \mathbf{V}_s^{IB} & \mathbf{V}_s^{II} \end{bmatrix} \begin{Bmatrix} \mathbf{u}_s^B \\ \boldsymbol{\eta}_s^I \end{Bmatrix} \approx \underbrace{\begin{bmatrix} \mathbf{I}_s & \mathbf{0} \\ \mathbf{V}_s^{IB} & \mathbf{V}_s^{II} \end{bmatrix} \begin{bmatrix} \tilde{\boldsymbol{\phi}}_s & \mathbf{0} \\ \mathbf{0} & \mathbf{I} \end{bmatrix}}_{\tilde{\mathbf{V}}_s} \begin{Bmatrix} \boldsymbol{\eta}_s^B \\ \boldsymbol{\eta}_s^I \end{Bmatrix}. \tag{5.45}$$

Notice that, even if LCCs can be computed independently for each substructure, their choice must be managed with care: since LCCs for the same interface and computed for different substructures are not a priori equal, interface compatibility

cannot be taken for granted anymore. Usually this is not a problem if the interface is "well behaved" (e.g. it responds in a rigid way) or if enough LCCs are included in the basis. A way around is to compute LCCs for the same interface on different substructures and then either select them all and orthogonalize the result or perform a singular value decomposition of the full set of vectors to select only the most relevant ones. In both cases, the same basis is then used for all substructures sharing that interface. However, if these strategies are used, should a substructure design be modified, all the reduced matrices/tensors of the substructures sharing an interface with the changed one would have to be recomputed.

Before concluding this section, we point out the recent contribution by Lee et al., 2020, where a reduced FETI using POD was proposed. In this work, master nodes coupled to the interfaces were used to link the domains; this strategy, however, is arguably not in the spirit of model order reduction.

5.4.3 Weak interface compatibility

When interface reduction is adopted, the compatibility condition Eq. (5.30c) might be too strong, resulting in *interface locking*. A way around this problem is to weaken the compatibility condition by defining a projection basis also for the Lagrange multipliers (Rixen, 1997).

$$\boldsymbol{\lambda} = \boldsymbol{\Lambda}\boldsymbol{\zeta}, \tag{5.46}$$

being $\boldsymbol{\Lambda}$ a reduction basis and $\boldsymbol{\zeta}$ the corresponding reduced Lagrange multipliers. Without loss of generality, a static component $\boldsymbol{\lambda}_0$ can be added separately to take into account the static response not spanned by the dynamic reduction. Premultiplying the interface equation (5.31a) by $\boldsymbol{\Lambda}^\mathsf{T}$, we can write

$$\boldsymbol{\Lambda}^\mathsf{T}\left(\tilde{\mathbf{B}}_1\tilde{\mathbf{S}}_1^{-1}\tilde{\mathbf{B}}_1^\mathsf{T} + \tilde{\mathbf{B}}_2\tilde{\mathbf{S}}_2^{-1}\tilde{\mathbf{B}}_2^\mathsf{T}\right)\boldsymbol{\Lambda}\boldsymbol{\zeta} = -\boldsymbol{\Lambda}^\mathsf{T}\tilde{\mathbf{B}}_1\tilde{\mathbf{S}}_1^{-1}\tilde{\mathbf{f}}_1 - \boldsymbol{\Lambda}^\mathsf{T}\tilde{\mathbf{B}}_2\tilde{\mathbf{S}}_2^{-1}\tilde{\mathbf{f}}_2, \tag{5.47}$$

which, indeed, corresponds to the compatibility restricted to a subset of constraints

$$\boldsymbol{\Lambda}^\mathsf{T}\left(\mathbf{B}_1\mathbf{u}_1 + \mathbf{B}_2\mathbf{u}_2\right) = \mathbf{0}. \tag{5.48}$$

A possible choice for $\boldsymbol{\Lambda}$ is to take the high end eigenspectrum of the interface operator $\mathbf{F}_\mathrm{I}$. However, a thorough discussion of this topic is out of the scopes of this work, and the interested reader is referred to Rixen, 1997. In the following, $\boldsymbol{\Lambda}$ is chosen as the orthogonalized set of LCCs coming from all the substructures sharing the interface, that is

$$\boldsymbol{\Lambda} = \mathrm{orth}\left(\left[\tilde{\boldsymbol{\Phi}}_1,\, \tilde{\boldsymbol{\Phi}}_2\right]\right). \tag{5.49}$$

Notice that this reduction is carried out independently and does not affect the substructure reduction bases, so the ROMs matrices/tensors do not change.

5.5 FETI WITH SHAPE DEFECTS

As mentioned in the previous sections, the addition of arbitrary defect shapes for each substructure poses the problem of interface compatibility: this led us to dual assembly approaches and, in particular, to FETI. Indeed, in the DpROM settings described in Chapters 3 and 4, we can write the final position of a material point as the sum of the nominal coordinates, a fictitious (small) displacement representing a defect, and the displacement, i.e.

$$\mathbf{x} = \mathbf{x}_0 + \mathbf{u} + \mathbf{u}_\mathrm{d},$$

so that we can rewrite the FETI linear static problem (for two substructures and one interfaces) as

$$\begin{cases} \mathbf{K}_1(\mathbf{u}_{d,1})\mathbf{u}_1 = \mathbf{f}_1 + \mathbf{B}_1^T\boldsymbol{\lambda} & (5.50a) \\ \mathbf{K}_2(\mathbf{u}_{d,2})\mathbf{u}_2 = \mathbf{f}_2 + \mathbf{B}_2^T\boldsymbol{\lambda} & (5.50b) \\ \mathbf{B}_1(\mathbf{u}_1 + \mathbf{u}_{d,1}) + \mathbf{B}_2(\mathbf{u}_2 + \mathbf{u}_{d,2}) = \mathbf{0}\,, & (5.50c) \end{cases}$$

where compatibility is now imposed on the sum $\mathbf{u} + \mathbf{u}_d$, and where the (linear) stiffness matrices depend on the defect as

$$\mathbf{K}_s(\mathbf{u}_d) = {}_{2n}\mathbf{K}_s + {}_{3d}\mathbf{K}_s \cdot \mathbf{u}_d + {}_{4dd}\mathbf{K}_s : (\mathbf{u}_d \otimes \mathbf{u}_d) \triangleq \mathbf{K}_{d,s}\,.$$

As a first step, we can solve the system in Eq. (5.50) to retrieve an *initial compatible* state. In other words, we enforce the interfaces of the two substructures to fit together *through the Lagrange multipliers*, being the structures otherwise at rest (no external loads. This can be expressed as

$$\begin{cases} \mathbf{u}_1 = \mathbf{K}_{d,1}^{-1}\mathbf{B}_1^T\boldsymbol{\lambda} & (5.51a) \\ \mathbf{u}_2 = \mathbf{K}_{d,2}^{-1}\mathbf{B}_2^T\boldsymbol{\lambda} & (5.51b) \\ \left(\mathbf{B}_1\mathbf{K}_{d,1}^{-1}\mathbf{B}_1^T + \mathbf{B}_2\mathbf{K}_{d,2}^{-1}\mathbf{B}_2^T\right)\boldsymbol{\lambda} = -\mathbf{B}_1\mathbf{u}_{d,1} - \mathbf{B}_2\mathbf{u}_{d,2}\,. & (5.51c) \end{cases}$$

Solving the system above, it is finally possible to compute the initial state of the structure, which can be used as initial conditions for a dynamic analysis.

Building on this new framework, it is possible to extend this strategy to (nonlinear) dynamics, and then to ROMs (or, rather, DpROM).

5.5.1 DpROM in FETI

The reduced parametric model can be built as described in Chapters 3 and 4, using (internal) VMs, MDs and Defect Sensitivities (DS, $\boldsymbol{\phi}_\xi^I$), with a few differences, as specified in Section 5.4. Namely, CMs (CMDs) have to be added for each boundary node and, if interface reduction is used, LCCs have to be computed to construct the final reduction basis.

As it will be shown in the numerical examples, in the same manner in which VMs and MDs only could not capture the correct behavior of the system and DSs had to be introduced, also in this case CMs and LCCs are not enough. In the same spirit of DS then, we can compute Defected CMs (DCMs) and Defected LCCs (DLCCs), differentiating with respect to the defect amplitudes ξ_j the static problem which defines the CM (similar procedure used for CMDs), obtaining

$$\text{DCM}: \quad (\boldsymbol{\Psi}_\xi)_{ij} \triangleq \left.\frac{\partial \boldsymbol{\Psi}_i}{\partial \xi_j}\right|_{eq} = -(\mathbf{K}_{eq}^t)^{-1}\left.\frac{\partial \mathbf{K}^t(\mathbf{U}_j)}{\partial \xi_j}\right|_{eq} \boldsymbol{\Psi}_i|_{eq}\,, \tag{5.52}$$

being $\mathbf{U}_j$ the j-th defect shape. Adding DCMs to the basis (after orthogonalization, to remove linearly dependent vectors), one obtains

$$\mathbf{u} = \begin{Bmatrix} \mathbf{u}^B \\ \mathbf{u}^I \end{Bmatrix} \simeq \mathbf{V}\boldsymbol{\eta} = \begin{bmatrix} \mathbf{I} & \boldsymbol{\Psi}_\xi^B & \mathbf{0} & \mathbf{0} & \mathbf{0} & \mathbf{0} \\ \boldsymbol{\Psi}^I & \boldsymbol{\Psi}_\xi^I & \boldsymbol{\Psi}_\theta^I & \boldsymbol{\phi}^I & \boldsymbol{\phi}_\xi^I & \boldsymbol{\theta}^I \end{bmatrix} \begin{Bmatrix} \mathbf{u}^B \\ \mathbf{u}_\xi^B \\ \mathbf{u}_\theta^B \\ \boldsymbol{\eta}_\varphi \\ \boldsymbol{\eta}_\xi \\ \boldsymbol{\eta}_\theta \end{Bmatrix}, \tag{5.53}$$

so that now there are m_d additional coordinates for each interface dof to take into account the presence of the defects, being m_d the number of defects. The set of

"interface coordinates" $\{\mathbf{u}^B, \mathbf{u}^B_\xi, \mathbf{u}^B_\theta\}$ can then be reduced using LCCs, taking care to partition $\tilde{\mathbf{M}}_s^{BB}$ and $\tilde{\mathbf{K}}_s^{BB}$ so that the whole set is included (that is, real interface dofs and additional interface dofs). This way, we have

$$\begin{Bmatrix} \mathbf{u}^B \\ \mathbf{u}^B_\xi \\ \mathbf{u}^B_\theta \end{Bmatrix} \approx \tilde{\boldsymbol{\phi}} \boldsymbol{\eta}^B \,. \tag{5.54}$$

Differentiating the eigenvalue problem defining these new LCCs, we obtain

$$\text{DLCC}: \quad (\tilde{\boldsymbol{\phi}}_\xi)_{ij} \triangleq \left.\frac{\partial \tilde{\boldsymbol{\phi}}_i}{\partial \xi_j}\right|_{eq} = -(\mathbf{K}^t_{eq})^{-1} \left.\frac{\partial \mathbf{K}^t(\mathbf{U}_j)}{\partial \xi_j}\right|_{eq} \tilde{\boldsymbol{\phi}}_i|_{eq}, \tag{5.55}$$

and the reduced interface dofs can be approximated as

$$\begin{Bmatrix} \mathbf{u}^B \\ \mathbf{u}^B_\xi \\ \mathbf{u}^B_\theta \end{Bmatrix} \approx \left[\tilde{\boldsymbol{\Phi}}, \tilde{\boldsymbol{\Phi}}_\xi\right] \begin{Bmatrix} \boldsymbol{\eta}^B \\ \boldsymbol{\eta}^B_\xi. \end{Bmatrix} \tag{5.56}$$

In synthesis, without interface reduction we have:

$$\begin{Bmatrix} \mathbf{u}^B \\ \mathbf{u}^I \end{Bmatrix} \approx \left[\begin{array}{ccc|ccc} \mathbf{I} & \boldsymbol{\Psi}^B_\xi & \mathbf{0} & \mathbf{0} & \mathbf{0} & \mathbf{0} \\ \boldsymbol{\Psi}^I & \boldsymbol{\Psi}^I_\xi & \boldsymbol{\Psi}^I_\theta & \boldsymbol{\Phi}^I & \boldsymbol{\Phi}^I_\xi & \boldsymbol{\Theta}^I \end{array}\right] \begin{Bmatrix} \mathbf{u}^B \\ \mathbf{u}^B_\xi \\ \mathbf{u}^B_\theta \\ \boldsymbol{\eta}_\varphi \\ \boldsymbol{\eta}_\xi \\ \boldsymbol{\eta}_\theta \end{Bmatrix}, \tag{5.57}$$

and, defining

$$\left[\begin{array}{ccc|ccc} \mathbf{I} & \boldsymbol{\Psi}^B_\xi & \mathbf{0} & \mathbf{0} & \mathbf{0} & \mathbf{0} \\ \boldsymbol{\Psi}^I & \boldsymbol{\Psi}^I_\xi & \boldsymbol{\Psi}^I_\theta & \boldsymbol{\Phi}^I & \boldsymbol{\Phi}^I_\xi & \boldsymbol{\Theta}^I \end{array}\right] \longleftrightarrow \begin{bmatrix} \mathbf{V}_s^{BB} & \mathbf{0} \\ \mathbf{V}_s^{IB} & \mathbf{V}_s^{II} \end{bmatrix}, \tag{5.58}$$

the basis for the DpROM with interface reduction writes

$$\begin{Bmatrix} \mathbf{u}^B \\ \mathbf{u}^I \end{Bmatrix} \approx \begin{bmatrix} \mathbf{V}_s^{BB} & \mathbf{0} \\ \mathbf{V}_s^{IB} & \mathbf{V}_s^{II} \end{bmatrix} \begin{bmatrix} \tilde{\boldsymbol{\Phi}}_s & \tilde{\boldsymbol{\Phi}}_\xi & \mathbf{0} \\ \mathbf{0} & \mathbf{0} & \mathbf{I} \end{bmatrix} \begin{Bmatrix} \boldsymbol{\eta}^B_s \\ \boldsymbol{\eta}^I_s \end{Bmatrix} \tag{5.59}$$

where LCCs and DLCCs were used.

Remarks

In the most general case, Constrain Modes (CM), CM Derivatives (CMD), Defected CMs (DCM), VMs, MDs, Local level Characteristic Constraint (LCC) and Defected LCCs (DLCC) are available to form the reduction basis. It is important to:

1) check for linearly independent vectors and remove linearly dependent ones;
2) check with care if interface reduction is necessary;
3) if the interface dynamics can be reasonably assumed to be linear, do not use CMDs;
4) for linear analysis, do not use CMDs and MDs;
5) if the defect does not change the interface, do not include DCMs and DLCCs associated to that defect;

6) remember that, although in substructuring (and parametric substructuring) more basis vectors are usually required with respect to standard ROMs,
    a) the size of each substructure is smaller;
    b) the basis of each substructure can be chosen independently, according to its expected dynamics (linear/nonlinear, frequency range, etc.) and present defects.

On the basis of these points, a more compact and efficient reduction basis can thus be constructed.

5.5.2 Interpretation

The Defected FETI (with DpROM) described so far, stirs a little bit away from traditional substructuring techniques. Indeed, with this method it is not only a matter of dividing the structure in subdomains and apply defects, that is a mere representation of the original geometry. Due to the static step to restore compatibility, the *starting equilibrium position is changed*. This fact, from a practical point of view, entails that the structure starts the dynamic analysis from a prestressed condition (which can be easily removed in linear analysis, but not in the nonlinear one). On the interpretation level, the physical phenomenon described by the method is an *assembling procedure*, where different components, each with independent defect, are forced to fit (e.g. in a pin-hole joint).

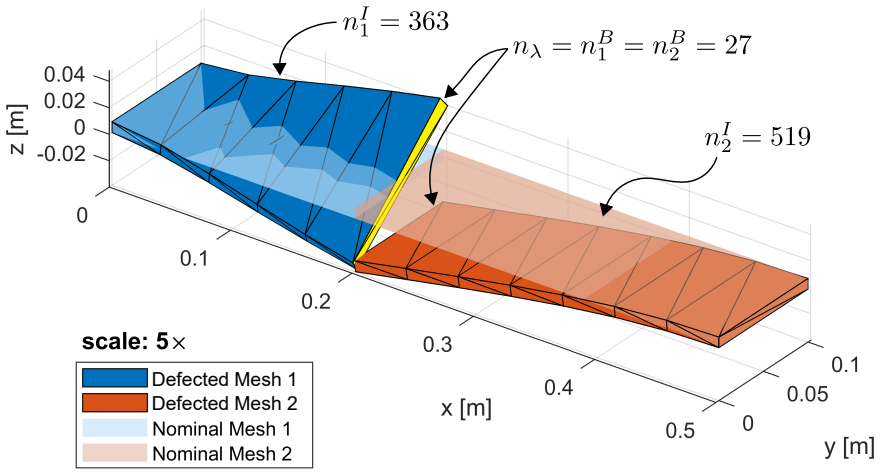

Figure 37: Substructure 1 ($200 \times 100 \times 8$ mm, blue) with torsional defect and substructure 2 ($300 \times 100 \times 8$ mm, red) with bending defect. Nominal meshes are also reported (shaded). Defect amplitudes are $\xi_1 = \xi_2 = 8$ mm (defects are plotted with a magnification factor $5\times$). The interface is highlighted in yellow.

5.6 NUMERICAL EXAMPLE

In this section, we study a simple example in linear dynamics to showcase the tools discussed in the previous sections, trying to give an overall idea of what are the benefits and the issues to be expected in different scenarios.

The model is shown in Fig. 37: a straight beam, clamped at both ends, is divided into two subdomains (blue and red). Each domain present one defect, torsion and bending of the beam, respectively. Material is aluminum and the domain is meshed using 10-noded tetrahedra. The number of interior dofs of each substructure and of interface dofs is also shown in the figure.

Before the start of the linear analysis, as described in the previous section, the FETI static problem given by Eqs. (5.51) is solved to restore compatibility. The results are shown in Fig. 38: this deformed shape represents the new equilibrium position with respect to which the dynamic analysis is performed.

5.6.1 Dynamic Simulation

Following, the details and settings for the simulation:

- A nodal load is placed at $(x, y, z) = (250, 50, 8)$ mm in z-direction, defined as

$$\mathbf{f}_{ext}(t) = \hat{\mathbf{f}}_{ext}\left(\cos\frac{\omega_{01}+\omega_{02}}{2}t + \cos\frac{\omega_{02}+\omega_{03}}{2}t\right), \tag{5.60}$$

  being $\hat{\mathbf{f}}$ a constant vector and ω_{0i} the i-th eigenfrequency of the nominal system;

- Defect amplitudes: $\xi = \xi_1 = \xi_2 = \{4, 8, 12\}$ mm (beam thickness is 8 mm);
- A time span of $T = (40\pi)/\omega_{01}$ is considered;
- The Generalized Relative Error computed over all the mesh displacements (GREt, Eq. (3.51)) is used to assess the performances, and is computed for
  - the nominal High Fidelity Model (HFM-n), that is the model without defects;

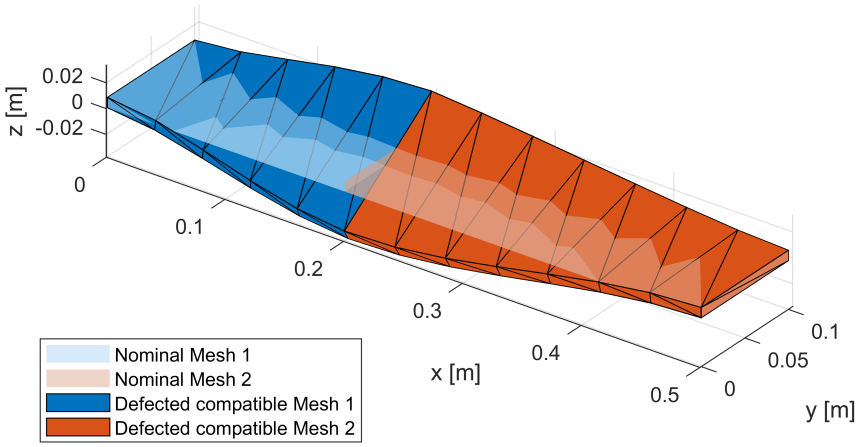

Figure 38: Substructures after compatibility is restored through the linear static FETI step. Defect amplitudes are $\xi_1 = \xi_2 = 8$ mm (defects are plotted with a magnification factor $5\times$).

- the defected High Fidelity Model (HFM-d), where the defects are included in the mesh and compatibility is restored using the static FETI step;
- the DpROMs, with and without Interface Reduction (IR). More precisely, we tested here the Budiansky-based version of the DpROM (see chapter 3), that is DpROM-N0$_n$ (see chapter 4);
- the full order model using the aforementioned Budiansky formulation (full-Bud), where defects are included in the strains rather than in the mesh. This is done to verify that the errors (GREt) are generated by the reduction basis, while the underlying formulation is correct.

5.6.2 Results

In Table 9 basis composition and corresponding GREt for different DpROMs are reported. First, DpROM with only VMs, DSs and CMs is tested: even when using 25 VMs (and DSs) wrong results were obtained. DCMs are then introduced, and GREt becomes very low even when using only 4 VMs. However, $n_\lambda = 27$ vectors for DCMs had to be added. Since in a real application case n_λ can be much higher, we also test DpROM with Interface Reduction (IR). Notice that without IR the total number of reduced coordinates is

$$n_{TOT} = n_{VM} + n_{DS} + n_{CM} + n_{DCM}, \tag{5.61}$$

while when IR is used we have

$$n_{TOT} = n_{VM} + n_{DS} + n_{LCC} + n_{DLCC}. \tag{5.62}$$

The final dimension of the basis then is determined after orthogonalization, so that the actual number of vectors is $n_{orth} \leqslant n_{TOT}$.

The DpROM with VMs, DSs, CMs, DCMs and LCCs is tested, leading to good results only when the number of LCCs approaches the number of the sum of CMs and DCMs, basically with no gain with respect to the case without IR. The same

Table 9: Test 1: bases composition and $GREt_i$ (with $i = 4, 8, 12$, corresponding to the defect amplitude ξ, in mm).

n_{VM}	n_{DS}	n_{CM}	n_{DCM}	n_{LCC}	n_{DLCC}	n_{TOT}	n_{orth}	$GREt_4$	$GREt_8$	$GREt_{12}$
15	15	27	0	0	0	57	57	87.49	102.26	175.13
20	20	27	0	0	0	67	67	82.81	98.41	141.94
25	25	27	0	0	0	77	77	46.61	84.53	91.49
2	2	27	27	0	0	58	58	1.19	3.64	7.07
3	3	27	27	0	0	60	60	1.13	3.57	6.95
4	4	27	27	0	0	62	62	0.96	3.45	6.83
4	4	27	27	25	0	33	33	81.99	92.78	107.37
4	4	27	27	27	0	35	35	71.03	90.34	98.41
4	4	27	27	35	0	43	43	31	64.64	75
4	4	27	27	40	0	48	48	7.7	25.28	43.31
4	4	27	27	45	0	53	53	5.48	16.03	28.74
4	4	27	27	50	0	58	58	3.67	9.19	16.25
4	4	27	27	54	0	62	62	0.96	3.45	6.83
4	4	27	27	10	10	28	28	79.16	81.5	86.01
4	4	27	27	15	15	38	38	24.37	34.44	43.89
4	4	27	27	20	20	48	48	15.83	19.91	25.44
4	4	27	27	22	22	52	52	9.41	11.34	13.48
4	4	27	27	24	24	56	56	6.05	8.3	10.93
4	4	27	27	27	27	62	62	0.96	3.45	6.83
4	4	27	27	35	35	78	62	0.96	3.45	6.83
4	4	27	27	54	54	116	62	0.96	3.45	6.83

Table 10: $GREt_i$ (with $i = 4, 8, 12$, corresponding to the defect amplitude ξ, in mm) for the full order models HFMn and full-Bud.

	$GREt_4$	$GREt_8$	$GREt_{12}$
HFM-n	38.7	87.73	97.32
full-Bud	0.06	0.19	0.35

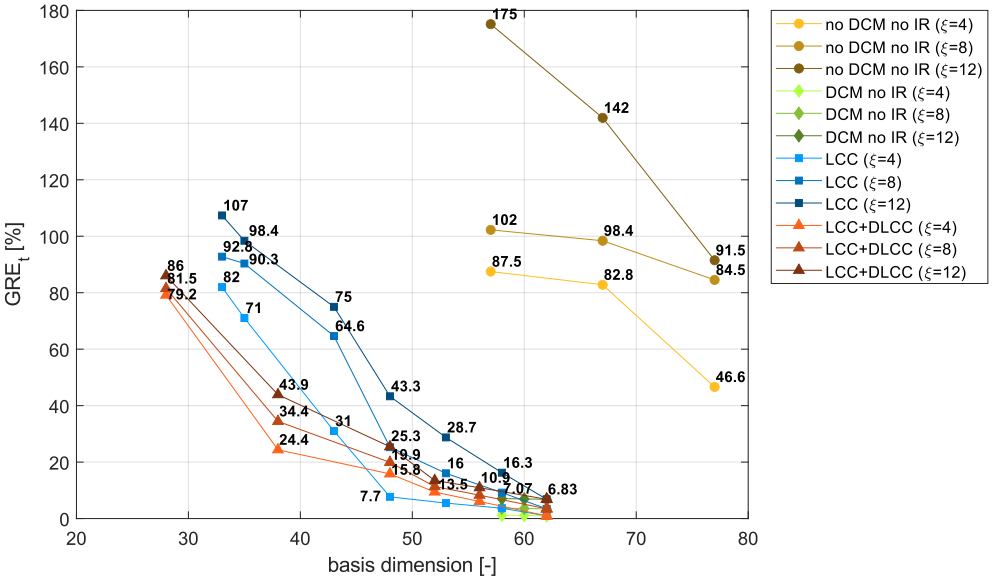

Figure 39: Test 1: synthetic results, ordered by basis dimension.

Table 11: Test 2: weak compatibility. The same basis is always used, only increasing the number of LCCs and DLCCs. For each case, the size of $\boldsymbol{\Lambda}$, n_Λ, is progressively decreased.

n_{VM}	n_{DS}	n_{CM}	n_{DCM}	n_{LCC}	n_{DLCC}	n_Λ	n_{TOT}	$GREt_4$	$GREt_8$	$GREt_{12}$
4	4	27	27	10	10	27	28	81.5	80.89	85.01
4	4	27	27	10	10	24	28	76.73	76.4	81.82
4	4	27	27	10	10	20	28	75.37	74.85	81.16
4	4	27	27	10	10	16	28	69.99	69.6	76.2
4	4	27	27	10	10	14	28	35.01	35.24	39.73
4	4	27	27	10	10	12	28	31.78	31.93	36.31
4	4	27	27	10	10	10	28	24.41	24.44	28.82
4	4	27	27	10	10	8	28	32.98	50.24	36.95
4	4	27	27	15	15	27	38	34.44	34.64	38.09
4	4	27	27	15	15	24	38	34.29	34.46	37.73
4	4	27	27	15	15	20	38	24.31	24.52	26.86
4	4	27	27	15	15	16	38	16.39	16.65	17.98
4	4	27	27	15	15	14	38	9.31	9.52	10.53
4	4	27	27	15	15	12	38	4.35	4.6	5.25
4	4	27	27	15	15	10	38	1.79	2.85	4.28
4	4	27	27	15	15	8	38	45.36	61.73	49.53
4	4	27	27	20	20	27	48	19.91	20.05	21.89
4	4	27	27	20	20	24	48	13.14	13.28	14.52
4	4	27	27	20	20	20	48	11.44	11.58	12.51
4	4	27	27	20	20	16	48	7.64	7.8	8.29
4	4	27	27	20	20	14	48	2.39	2.8	3.45
4	4	27	27	20	20	12	48	1.66	2.19	2.83
4	4	27	27	20	20	10	48	3.47	4.92	5.98
4	4	27	27	20	20	8	48	48.12	64.77	52.68
4	4	27	27	0	0	27	62	3.45	3.76	3.73
4	4	27	27	0	0	24	62	3.45	3.76	3.72
4	4	27	27	0	0	20	62	3	3.35	3.23
4	4	27	27	0	0	16	62	2.33	2.79	2.62
4	4	27	27	0	0	14	62	2.02	2.6	3.17
4	4	27	27	0	0	12	62	2.65	3.1	3.7
4	4	27	27	0	0	10	62	7.27	8.43	9.14
4	4	27	27	0	0	8	62	51.32	67.96	56.2

tests are repeated using both LCCs and DLCCs, obtaining similar results. Figure 39 summarizes the GRE values ordering for total basis size n_{TOT}.

In order to see if the results can be improved by weakening the compatibility condition when using IR, a second set of test are run. IR with LCC and DLCC is tested using a basis $\boldsymbol{\Lambda}$ as described in Sec 5.4.3. Results are collected in Table 11 and Fig. 40.

As it can be observed, results sensibly improve as compatibility is weakened, and the minimum error is obtained for $n_\Lambda = 10$ and $n_\Lambda = 12$. Remarkably, using a model with as low as 15 LCCs and 15 DLCCs, a $GREt = 1.79 - 4.28\%$ can be achieved if $n_\Lambda = 10$. Finally, we repeat the simulations for the IR-cases reported in Table 9, but using $n_\Lambda = 12$. The results are shown in Fig. 41. As it can be observed, now IR with LCCs and DLCCs outperforms all the other cases, both for accuracy and for basis dimension.

5.7 CONCLUSIONS

In this chapter we investigated the possibility to use DpROM in substructuring. First a strategy using FETI was devised in order to allow arbitrary defect shapes which, in general, might lead to non-compatible interfaces. The problem of reduction was discussed in detail, introducing an expanded Craig-Bampton basis including modal and defect derivatives to take into account nonlinearities and defects,

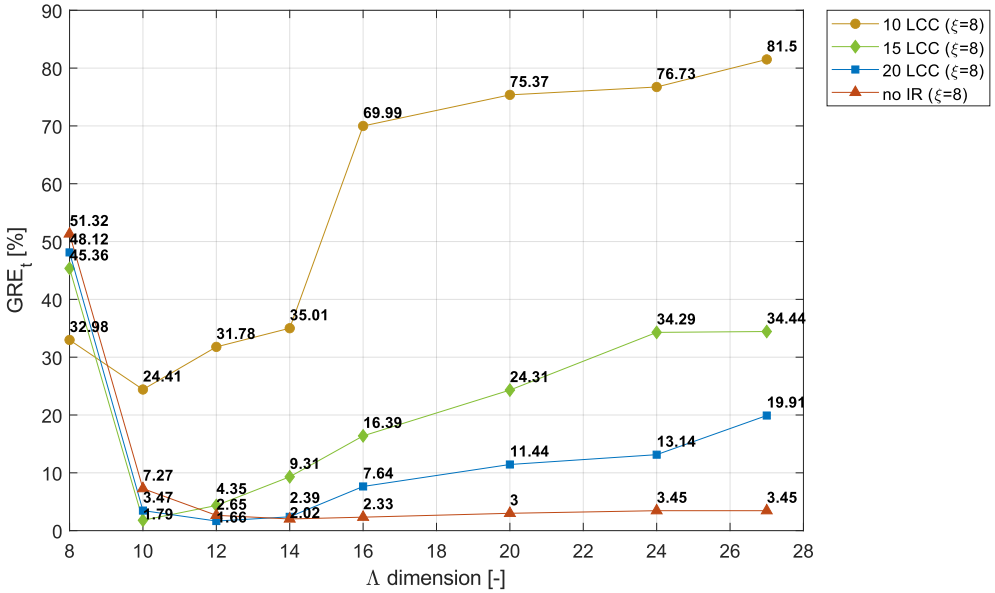

Figure 40: Test 2: synthetic results, ordered by Λ dimension. All the simulation are carried out for $\xi = 8\,mm$, with the number of LCCs (and DLCCs) shown in the legend. The case where compatibility is weakened and without IR is also shown for completeness.

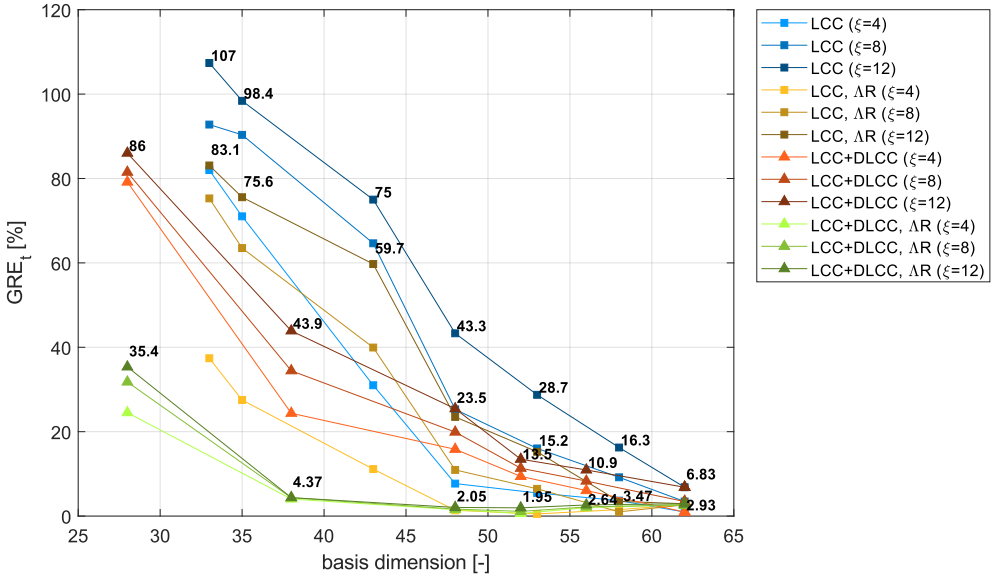

Figure 41: Test 3: synthetic results, ordered by basis dimension. The cases in shades of blue and red are the ones already shown in Fig. 39, reported for comparison. The remaining cases, labelled with "ΛR", correspond to the same cases, in terms of model, but imposing weak compatibility ($n_\Lambda = 12$).

respectively. In particular, interface reduction and weak compatibility were introduced. The proposed method can be used to describe structures whose parts are physically assembled, and whose interfaces do not initially fit for the presence of the defects. In the case in which the interfaces are not affected by the presence of the defects, the method instead greatly simplifies and can be used as a traditional CMS technique. Finally, an example for a test case in linear dynamics is thoroughly studied. The main conclusions that can be drawn from the numerical tests are that (i) DCMs are fundamental to capture the response of the defected structure, (ii) interface reduction without weak compatibility leads to poor results, (iii) comparatively, if using weak compatibility, DLCCs greatly improve the accuracy of the method.

Future work should focus on strategies, also available in literature, to select the optimal set of LCCs and weak compatibility modes ($\boldsymbol{\Lambda}$). The extension to the nonlinear dynamic domain, here presented on a theory level, should also be investigated with numerical examples.

6 CONCLUSIONS AND FUTURE WORK

All that is gold does not glitter,
Not all those who wander are lost
—J.R.R. Tolkien, The Fellowship of the Ring

In the present dissertation, projection-based reduced order models for nonlinear structural dynamics were discussed and extended. Being of particular interest for the MEMS industry, we focused on the modelling and analysis of structures with geometrical defects in their shape, which can usually be attributed to the manufacturing processes. The dynamic response of such structures can sensibly vary with respect to the nominal case, where the structure has no defects. In the case of MEMS sensors, this has a direct impact over the statistic distribution of the performances.

Elaborating on earlier deformation schemes, new ones have been developed to include the defect directly in the strain formulation. We showed that this way it is possible to refer most of the computations to the nominal mesh, build a reduced model, and parametrize it using some user-defined defect shapes. The Defect parametric Reduced Order Model, named DpROM, was presented, first following Budiansky deformation theory and then a two-steps deformation approach. Using Neumann expansion, it has been shown that higher order approximations can be obtained using the same formalism, achieving increased accuracy. Contextually, solutions to construct the projection basis were provided to adapt to the defect-parametric nature of the model. Finally, DpROM was tested in a substructuring environment. The challenging problem of accommodating arbitrary defects for each substructure, potentially leading to non-compatible interfaces, was addressed using the Finite Element Tearing and Interconnecting scheme. The latter is a dual substructuring strategy where the high level of independence featured by each substructure allowed us to set up a first static step to make non-compatible interfaces compatible, determining a new initial equilibrium position for the dynamic analysis. The benefits of DpROM was tested in several numerical examples, where both time and frequency domain analysis were performed.

Overall, DpROM offers a versatile tool to study defected structures in nonlinear regime, where the defects themselves can be easily constructed over the mesh and where the concepts needed to form the basis stem from traditional spectrum-based modal analysis. As discussed, however, while in time domain simulations very high speedups can be obtained, frequency domain responses speedups are heavily affected by the number of unknowns in the model. Moreover, the tensorial approach used to compute internal forces also suffers from large set of reduced coordinates, as the tensor construction time grows with the power of their size. These aspect call for strategies to either select a more compact projection basis and/or find an alternative way to evaluate the nonlinear forces vector and jacobian. Currently, some strategies are already under development.

As an alternative to tensors, a hyperreduction strategy have been adapted in Baghdadi, 2021 to the parametric setting of the DpROM. Using a *defected quadratic manifold lifting*, based on our strain formulation, to construct the training set for an Energy and Conserving Sampling and Weighting scheme (ECSW), it was possible to carry out the evaluation of the internal forces over the parameter domain over a limited set of elements, without the need to resort to tensors. The method was

tested on a MEMS frequency divider (Qalandar et al., 2014), showing how the approach can also correctly capture parametric resonances.

Following a different approach, it is also under development a strategy to use the DpROM without carrying out a frequency domain analysis for each new realization of the parameters. Indeed, always under the assumption of small defects, we can replace simulations with a sensitivity analysis. The system can then be simulated only *once*, using the nominal model, and then all the defected responses can be obtained using first and second order sensitivities from the nominal solution. Needless to say, this *update* procedure is extremely fast, and allows to test thousands of cases in the matter of seconds. Preliminary results, using Harmonic Balance, are promising and pave the way to the statistic analysis and uncertainty quantification.

BIBLIOGRAPHY

Acar, Cenk and Andrei Shkel

2008 *MEMS Vibratory Gyroscopes*, Springer, p. 256, ISBN: 9780387095356.

Allen, Matthew S., Daniel Rixen, Maarten van der Seijs, Paolo Tiso, Thomas Abrahamsson, and Randall L. Mayes

2020 *Substructuring in Engineering Dynamics*, CISM International Centre for Mechanical Sciences, Springer International Publishing, Cham, vol. 594, ISBN: 978-3-030-25531-2, DOI: 10.1007/978-3-030-25532-9, http://link.springer.com/10.1007/978-3-030-25532-9.

Amabili, Marco

2006 "Theory and experiments for large-amplitude vibrations of rectangular plates with geometric imperfections," *Journal of Sound and Vibration*, 291, 3-5, pp. 539-565, ISSN: 10958568, DOI: 10.1016/j.jsv.2005.06.007.

2013 "Reduced-order models for nonlinear vibrations, based on natural modes: the case of the circular cylindrical shell," *Philosophical Transactions of the Royal Society A: Mathematical, Physical and Engineering Sciences*, 371, 1993 [June 2013], p. 20120474, ISSN: 1364-503X, DOI: 10.1098/rsta.2012.0474, https://royalsocietypublishing.org/doi/10.1098/rsta.2012.0474.

Astolfi, Alessandro

2008 "Model reduction by moment matching for nonlinear systems," in *2008 47th IEEE Conference on Decision and Control*, February, IEEE, vol. 2015-Febru, pp. 4873-4878, ISBN: 978-1-4244-3123-6, DOI: 10.1109/CDC.2008.4738791, http://ieeexplore.ieee.org/document/7039956/%20http://ieeexplore.ieee.org/document/4738791/.

2010 "Model Reduction by Moment Matching for Linear and Nonlinear Systems," *IEEE Transactions on Automatic Control*, 55, 10 [Oct. 2010], pp. 2321-2336, ISSN: 0018-9286, DOI: 10.1109/TAC.2010.2046044, http://ieeexplore.ieee.org/document/5437314/.

Bachmann, Patrick

2020 *Substructuring and model order reduction for geometric nonlinearities with parameterized shape defects*, Master thesis (supervised by: Tiso P., Marconi J.), ETH Zürich.

Bader, Brett W. and Tamara G. Kolda

2006 "Algorithm 862: MATLAB tensor classes for fast algorithm prototyping," *ACM Transactions on Mathematical Software*, 32, 4 [Dec. 2006], pp. 635-653, DOI: 10.1145/1186785.1186794.

Bader, Brett W., Tamara G. Kolda, et al.

2015 *MATLAB Tensor Toolbox Version 2.6*, Available online, http://www.sandia.gov/~tgkolda/TensorToolbox/.

Baghdadi, Mostafa

2021 *SParametric Nonlinear Hyper-Reduction for Imperfect Structures using Quadratic Manifold Lifting : A Case Study on a Frequency Divider*, Master thesis (supervised by: Tiso P., Marconi J., Braghin F.), Politecnico di Milano.

Balajewicz, Maciej, David Amsallem, and Charbel Farhat
2015 "Projection-based model reduction for contact problems," *International Journal for Numerical Methods in Engineering*, 106 [Mar. 2015], pp. 644-663, ISSN: 0743-1619, DOI: 10.1002/nme, arXiv: 1503.01000, http://arxiv.org/abs/1503.01000.

Barrault, Maxime, Yvon Maday, Ngoc Cuong Nguyen, and Anthony T. Patera
2004 "An 'empirical interpolation' method: application to efficient reduced-basis discretization of partial differential equations," *Comptes Rendus Mathematique*, 339, 9 [Nov. 2004], pp. 667-672, ISSN: 1631073X, DOI: 10.1016/j.crma.2004.08.006, https://linkinghub.elsevier.com/retrieve/pii/S1631073X04004248.

Bathe, Klaus-Jurgen
2014 *Finite Element Procedures*, ISBN: 9780979004957.

Baur, Ulrike, Peter Benner, Bernard Haasdonk, Christian Himpe, and Immanuel Maier Mario Ohlberger
2017 *Comparison of methods for parametric model order reduction of instationary problems*, pp. 377-407, ISBN: 978-1-61197-481-2, http://www.mpi-magdeburg.mpg.de/preprints/.

Belytschko, Ted, Wing Kam Liu, Brian Moran, and Khalil I. Elkhodary
2014 *Nonlinear finite elements for continua and structures*, Second Edi, Wiley, p. 804, ISBN: 0471987735.

Benner, Peter, Serkan Gugercin, and Karen Willcox
2015 "A Survey of Projection-Based Model Reduction Methods for Parametric Dynamical Systems," *SIAM Review*, 57, 4 [Jan. 2015], pp. 483-531, ISSN: 0036-1445, DOI: 10.1137/130932715, http://epubs.siam.org/doi/10.1137/130932715.

Blockmans, B, T Tamarozzi, F Naets, and W Desmet
2015 "A nonlinear parametric model reduction method for efficient gear contact simulations," *International Journal for Numerical Methods in Engineering*, 102, 5 [May 2015], pp. 1162-1191, ISSN: 00295981, DOI: 10.1002/nme.4831, http://doi.wiley.com/10.1002/nme.4831.

Budiansky, Bernard
1967 "Dynamic Buckling of Elastic Structures: Criteria and Estimates," in *Proceedings of an International Conference Held at Northwestern University, Evanston, Illinois*, Pergamon Press Ltd, DOI: 10.1016/B978-1-4831-9821-7.50010-7, http://linkinghub.elsevier.com/retrieve/pii/B9781483198217500107.

Camier, C., C. Touzé, and O. Thomas
2009 "Non-linear vibrations of imperfect free-edge circular plates and shells," *European Journal of Mechanics, A/Solids*, 28, 3, pp. 500-515, ISSN: 09977538, DOI: 10.1016/j.euromechsol.2008.11.005, http://dx.doi.org/10.1016/j.euromechsol.2008.11.005.

Chang, Byung Su, Woon Tahk Sung, Jang Gyu Lee, Kang Yoon Lee, and Sangkyung Sung
2007 "Automatic mode matching control loop design and its application to the mode matched MEMS gyroscope," *2007 IEEE International Conference on Vehicular Electronics and Safety, ICVES*, DOI: 10.1109/ICVES.2007.4456398.

Chaturantabut, Saifon and Danny C Sorensen
2010 "Nonlinear Model Reduction via Discrete Empirical Interpolation," *SIAM Journal on Scientific Computing*, 32, 5 [Jan. 2010], pp. 2737-2764, ISSN: 1064-8275, DOI: 10.1137/090766498, http://epubs.siam.org/doi/10.1137/090766498.

Cho, Haeseong, Sang Joon Shin, Haedong Kim, and Maenghyo Cho

2020 "Enhanced model-order reduction approach via online adaptation for parametrized nonlinear structural problems," *Computational Mechanics*, 65, 2, pp. 331-353, ISSN: 14320924, DOI: 10.1007/s00466-019-01771-7, https://doi.org/10.1007/s00466-019-01771-7.

Combescure, Alain and Anthony Gravouil

2002 "A numerical scheme to couple subdomains with different time-steps for predominantly linear transient analysis," *Computer Methods in Applied Mechanics and Engineering*, 191, 11-12 [Jan. 2002], pp. 1129-1157, DOI: 10.1016/S0045-7825(01)00190-6, https://doi.org/10.1016/S0045-7825(01)00190-6%20https://linkinghub.elsevier.com/retrieve/pii/S0045782501001906.

Craig, Roy and Mervyn Bampton

1968 "Coupling of Substructures for Dynamic Analyses," 6, 7, pp. 1313-1319.

Crisfield, Michael Anthony

1991 *Non-linear Finite Element Analysis of Solids and Structures, Volume 1*, John Wiley I& Sons Ltd., ISBN: 0 471 92956 5, http://eu.wiley.com/WileyCDA/WileyTitle/productCd-0470666447.html.

Daniel, Luca, Ong Chin Siong, and LLow Sok Chay

2004 "A Multiparameter Moment Matching Model Reduction Approach for Generating Geometrically Parameterized Interconnect Performance Models," *Tcad*, 23, 5, pp. 1-15, ISSN: 0278-0070, DOI: 10.1109/TCAD.2004.826583, http://ieeexplore.ieee.org/xpls/abs%7B%5C_%7Dall.jsp?arnumber=1291580.

Dickens, J.M., J.M. Nakagawa, and M.J. Wittbrodt

1997 "A critique of mode acceleration and modal truncation augmentation methods for modal response analysis," *Computers and Structures*, 62, 6, pp. 985-998, ISSN: 0045-7949, DOI: https://doi.org/10.1016/S0045-7949(96)00315-X.

Farhat, Charbel, Po-shu Chen, and Jan Mandel

1995 "A scalable Lagrange multiplier based domain decomposition method for time-dependent problems," *International Journal for Numerical Methods in Engineering*, 38, 22 [Nov. 1995], pp. 3831-3853, DOI: 10.1002/nme.1620382207, https://onlinelibrary.wiley.com/doi/10.1002/nme.1620382207.

Farhat, Charbel, Michel Lesoinne, Patrick Letallec, Kendall Pierson, and Daniel Rixen

2001 "FETI-DP: A dual-primal unified FETI method part I: A faster alternative to the two-level FETI method," *International Journal for Numerical Methods in Engineering*, 50, 7, pp. 1523-1544, DOI: 10.1002/nme.76.

Farhat, Charbel and Jan Mandel

1998 "The two-level FETI method for static and dynamic plate problems part I: An optimal iterative solver for biharmonic systems," *Computer Methods in Applied Mechanics and Engineering*, 155, 1-2, pp. 129-151, ISSN: 00457825, DOI: 10.1016/S0045-7825(97)00146-1.

Farhat, Charbel and Francois-Xavier Roux

1991 "A method of finite element tearing and interconnecting and its parallel solution algorithm," *International Journal for Numerical Methods in Engineering*, 32, 6, pp. 1205-1227, DOI: 10.1002/nme.1620320604, http://onlinelibrary.wiley.com/doi/10.1002/nme.1620320604/abstract.

Farokhi, Hamed, Mergen H. Ghayesh, and Marco Amabili

2013 "Nonlinear dynamics of a geometrically imperfect microbeam based on the modified couple stress theory," *International Journal of Engineering Science*, 68 [July 2013], pp. 11-23, ISSN: 00207225, DOI: 10.1016/j.ijengsci.2013.03.001, http://dx.doi.org/10.1016/j.ijengsci.2013.03.001%20https://linkinghub.elsevier.com/retrieve/pii/S002072251300030X.

Fröhlich, Benjamin, Jan Gade, Florian Geiger, Manfred Bischoff, and Peter Eberhard

2018 "Geometric element parameterization and parametric model order reduction in finite element based shape optimization," *Computational Mechanics*, ISSN: 0178-7675, DOI: 10.1007/s00466-018-1626-1, http://link.springer.com/10.1007/s00466-018-1626-1.

Géradin, Michel and Daniel J Rixen

2014 *Mechanical vibrations: theory and application to structural dynamics*, John Wiley I& Sons.

2016 "A 'nodeless' dual superelement formulation for structural and multibody dynamics application to reduction of contact problems," *International Journal for Numerical Methods in Engineering*, 106, 10 [June 2016], pp. 773-798, ISSN: 00295981, DOI: 10.1002/nme.5136, http://doi.wiley.com/10.1002/nme.5136.

Ghavamian, F., P. Tiso, and A. Simone

2017 "POD–DEIM model order reduction for strain softening viscoplasticity," *Computer Methods in Applied Mechanics and Engineering*, 317, pp. 458-479, ISSN: 00457825, DOI: 10.1016/j.cma.2016.11.025, http://dx.doi.org/10.1016/j.cma.2016.11.025.

Gravouil, Anthony and Alain Combescure

2001 "Multi-time-step explicit - Implicit method for non-linear structural dynamics," *International Journal for Numerical Methods in Engineering*, 50, 1, pp. 199-225, ISSN: 00295981, DOI: 10.1002/1097-0207(20010110)50:1<199::AID-NME132>3.0.CO;2-A.

Gruber, Fabian M, Max Gille, and Daniel J Rixen

2019 "A strategy to stabilize the transient analysis and increase the approximation accuracy of dual Craig-Bampton reduced systems," *Finite Elements in Analysis I& Design*, 160, 2, pp. 32-45, DOI: 10.1016/j.finel.2019.03.003, https://doi.org/10.1016/j.finel.2019.03.003.

Guyan, R. J.

1965 "Reduction of stiffness and mass matrices," *AIAA Journal*, 3, 2 [Feb. 1965], pp. 380-380, ISSN: 0001-1452, DOI: 10.2514/3.2874, http://arc.aiaa.org/doi/10.2514/3.2874.

Hay, A., J. Borggaard, I. Akhtar, and D. Pelletier

2010 "Reduced-order models for parameter dependent geometries based on shape sensitivity analysis," *Journal of Computational Physics*, 229, 4, pp. 1327-1352, ISSN: 00219991, DOI: 10.1016/j.jcp.2009.10.033, http://dx.doi.org/10.1016/j.jcp.2009.10.033.

He, Jimin and Zhi-Fang Fu

2001 *Modal Analysis*, Elsevier, ISBN: 9780750650793, DOI: 10.1016/B978-0-7506-5079-3.X5000-1.

Hesthaven, J. S. and S. Ubbiali

2018 "Non-intrusive reduced order modeling of nonlinear problems using neural networks," *Journal of Computational Physics*, 363, pp. 55-78, ISSN: 10902716, DOI: 10.1016/j.jcp.2018.02.037, https://doi.org/10.1016/j.jcp.2018.02.037.

Hollkamp, Joseph J. and Robert W. Gordon

2008 "Reduced-order models for nonlinear response prediction: Implicit condensation and expansion," *Journal of Sound and Vibration*, 318, 4-5, pp. 1139-1153, ISSN: 10958568, DOI: 10.1016/j.jsv.2008.04.035.

Idelsohn, Sergio R and Alberto Cardona

1985 "A reduction method for nonlinear structural dynamic analysis," *Computer Methods in Applied Mechanics and Engineering*, 49, 3 [June 1985], pp. 253-279, ISSN: 00457825, DOI: 10.1016/0045-7825(85)90125-2, http://linkinghub.elsevier.com/retrieve/pii/0045782585901252.

Ionescu, Tudor C. and Alessandro Astolfi

2016 "Nonlinear moment matching-based model order reduction," *IEEE Transactions on Automatic Control*, 61, 10, pp. 2837-2847, ISSN: 00189286, DOI: 10.1109/TAC.2015.2502187.

Izadi, M., F. Braghin, D. Giannini, D. Milani, F. Resta, M. F. Brunetto, L. G. Falorni, G. Gattere, L. Guerinoni, and C. Valzasina

2018 "A comprehensive model of beams' anisoelasticity in MEMS gyroscopes, with focus on the effect of axial non-vertical etching," *5th IEEE International Symposium on Inertial Sensors and Systems, INERTIAL 2018 - Proceedings*, pp. 1-4, DOI: 10.1109/ISISS.2018.8358126.

Jain, Shobhit

2015 *Model Order Reduction for Non-linear Structural Dynamics*, TU Delft, DOI: uuid:cb1d7058-2cfa-439a-bb2f-22a6b0e5bb2a, https://repository.tudelft.nl/islandora/object/uuid%7B%5C%%7D3Acb1d7058-2cfa-439a-bb2f-22a6b0e5bb2a.

Jain, Shobhit and George Haller

2021 "How to Compute Invariant Manifolds and their Reduced Dynamics in High-Dimensional Finite-Element Models?" Pp. 1-40, arXiv: 2103.10264, http://arxiv.org/abs/2103.10264.

Jain, Shobhit and Paolo Tiso

2018 "Simulation-free hyper-reduction for geometrically nonlinear structural dynamics: A quadratic manifold lifting approach," *Journal of Computational and Nonlinear Dynamics*, 13, July 2018, pp. 1-12, ISSN: 15551423, DOI: 10.1115//1.4040021, http://computationalnonlinear.asmedigitalcollection.asme.org/article.aspx?articleid=2679584.

Jain, Shobhit, Paolo Tiso, and George Haller

2018 "Exact nonlinear model reduction for a von Kármán beam: Slow-fast decomposition and spectral submanifolds," *Journal of Sound and Vibration*, 423, pp. 195-211, ISSN: 10958568, DOI: 10.1016/j.jsv.2018.01.049, http://dx.doi.org/10.1016/j.jsv.2018.01.049.

Jain, Shobhit, Paolo Tiso, Johannes B. Rutzmoser, and Daniel J. Rixen

2017 "A quadratic manifold for model order reduction of nonlinear structural dynamics," *Computers and Structures*, 188, pp. 80-94, ISSN: 00457949, DOI: 10.1016/j.compstruc.2017.04.005, http://dx.doi.org/10.1016/j.compstruc.2017.04.005.

Jansen, E. L.

2008 "A perturbation method for nonlinear vibrations of imperfect structures: Application to cylindrical shell vibrations," *International Journal of Solids and Structures*, 45, 3-4, pp. 1124-1145, ISSN: 00207683, DOI: 10.1016/j.ijsolstr.2007.07.007.

Jutho, getzdan, Spencer Lyon, Mason Protter, Marcus P S, Leo, Jim Garrison, Frank Otto, Elliot Saba, Dmitri Iouchtchenko, Austin Privett, and Alexander Morley

2019 *Jutho/TensorOperations.jl: v1.1.0*, version v1.1.0, DOI: 10.5281/zenodo.3245497, https://doi.org/10.5281/zenodo.3245497.

Kast, Mariella, Mengwu Guo, and Jan S. Hesthaven

2020 "A non-intrusive multifidelity method for the reduced order modeling of nonlinear problems," *Computer Methods in Applied Mechanics and Engineering*, 364, p. 112947, ISSN: 00457825, DOI: 10.1016/j.cma.2020.112947, https://doi.org/10.1016/j.cma.2020.112947.

Kempe, Volker

2011 *Inertial MEMS*, Cambridge University Press, p. 475, ISBN: 9780521766586.

Kirsch, U.

2003 "A unified reanalysis approach for structural analysis, design, and optimization," *Structural and Multidisciplinary Optimization*, 25, 2, pp. 67-85, ISSN: 1615147X, DOI: 10.1007/s00158-002-0269-0.

Kirsch, U., M. Bogomolni, and I. Sheinman

2006 "Nonlinear dynamic reanalysis of structures by combined approximations," *Computer Methods in Applied Mechanics and Engineering*, 195, 33-36, pp. 4420-4432, ISSN: 00457825, DOI: 10.1016/j.cma.2005.09.013.

Klerk, D. De, D. J. Rixen, and S. N. Voormeeren

2008 "General Framework for Dynamic Substructuring: History, Review and Classification of Techniques," *AIAA Journal*, 46, 5, pp. 1169-1181, ISSN: 0001-1452, DOI: 10.2514/1.33274, http://arc.aiaa.org/doi/10.2514/1.33274.

Koiter, Warner Tjardus

1981 "Elastic Stability, Buckling and Post-Buckling Behaviour," in *Proceedings of the IUTAM Symposium on Finite Elasticity*, Springer Netherlands, pp. 13-24, DOI: 10.1007/978-94-009-7538-5_2, http://www.springerlink.com/index/10.1007/978-94-009-7538-5%7B%5C_%7D2.

Kołakowski, Przemysław, Marcin Wikło, and Jan Holnicki-Szulc

2008 "The virtual distortion method - A versatile reanalysis tool for structures and systems," *Structural and Multidisciplinary Optimization*, 36, 3, pp. 217-234, ISSN: 1615147X, DOI: 10.1007/s00158-007-0158-7.

Krack, Malte and Johann Gross

2019 *Harmonic Balance for Nonlinear Vibration Problems*, p. 159, ISBN: 9783030140229, DOI: 10.1007/978-3-030-14023-6.

Krattiger, Dimitri, Long Wu, Martin Zacharczuk, Martin Buck, Robert J. Kuether, Matthew S. Allen, Paolo Tiso, and Matthew R.W. Brake

2019 "Interface reduction for Hurty/Craig-Bampton substructured models: Review and improvements," *Mechanical Systems and Signal Processing*, 114, pp. 579-603, DOI: 10.1016/j.ymssp.2018.05.031.

Kuether, Robert J., Brandon J. Deaner, Joseph J. Hollkamp, and Matthew S. Allen

2015 "Evaluation of geometrically nonlinear reduced-order models with nonlinear normal modes," *AIAA Journal*, 52, 11, pp. 3273-3285, ISSN: 00011452, DOI: 10.2514/1.J053838.

Lassila, Toni and Gianluigi Rozza

2010 "Parametric free-form shape design with PDE models and reduced basis method," *Computer Methods in Applied Mechanics and Engineering*, 199, 23-24, pp. 1583-1592, ISSN: 00457825, DOI: 10.1016/j.cma.2010.01.007, http://dx.doi.org/10.1016/j.cma.2010.01.007.

Le Guennec, Y., J. P. Brunet, F. Z. Daim, M. Chau, and Y. Tourbier

2018 "A parametric and non-intrusive reduced order model of car crash simulation," *Computer Methods in Applied Mechanics and Engineering*, 338, pp. 186-207, ISSN: 00457825, DOI: 10.1016/j.cma.2018.03.005, https://doi.org/10.1016/j.cma.2018.03.005.

Lee, Si-Hun, Yongse Kim, DuHyun Gong, HyunShig Joo, Haeseong Cho, Haedong Kim, and SangJoon Shin

2020 "Fast and Novel Computational Methods for Multi-scale and Multi-physics: FETI and POD-ROM," *Multiscale Science and Engineering*, 2, 2-3, pp. 189-197, DOI: 10.1007/s42493-020-00048-z, https://doi.org/10.1007/s42493-020-00048-z.

Lu, Kuan, Yulin Jin, Yushu Chen, Yongfeng Yang, Lei Hou, Zhiyong Zhang, Zhonggang Li, and Chao Fu

2019 "Review for order reduction based on proper orthogonal decomposition and outlooks of applications in mechanical systems," *Mechanical Systems and Signal Processing*, 123, pp. 264-297, ISSN: 10961216, DOI: 10.1016/j.ymssp.2019.01.018, https://doi.org/10.1016/j.ymssp.2019.01.018.

Mahjoubi, Najib, Anthony Gravouil, and Alain Combescure

2009 "Coupling subdomains with heterogeneous time integrators and incompatible time steps," *Computational Mechanics*, 44, 6, pp. 825-843, DOI: 10.1007/s00466-009-0413-4.

Marconi, Jacopo, Giacomo Bonaccorsi, Daniele Giannini, Luca Falorni, and Francesco Braghin

2021 "Exploiting Nonlinearities for Frequency-Matched MEMS Gyroscopes Tuning," in *2021 IEEE International Symposium on Inertial Sensors and Systems (INERTIAL)*, IEEE, pp. 1-4, ISBN: 978-1-7281-5099-4, DOI: 10.1109/INERTIAL51137.2021.9430478, https://ieeexplore.ieee.org/document/9430478/.

Marconi, Jacopo, Paolo Tiso, and Francesco Braghin

2020 "A nonlinear reduced order model with parametrized shape defects," *Computer Methods in Applied Mechanics and Engineering*, 360 [Mar. 2020], p. 112785, ISSN: 00457825, DOI: 10.1016/j.cma.2019.112785, https://doi.org/10.1016/j.cma.2019.112785.

Marconi, Jacopo, Paolo Tiso, Davide E. Quadrelli, and Francesco Braghin

2021 "A higher-order parametric nonlinear reduced-order model for imperfect structures using Neumann expansion," *Nonlinear Dynamics* [May 2021], ISSN: 0924-090X, DOI: 10.1007/s11071-021-06496-y, eprint: 2102.01739.

Maulik, Romit, Bethany Lusch, and Prasanna Balaprakash

2020 "Reduced-order modeling of advection-dominated systems with recurrent neural networks and convolutional autoencoders," *arXiv*, arXiv: 2002.00470.

Mehrdad Pourkiaee, S. and Stefano Zucca

2019 "A Reduced Order Model for Nonlinear Dynamics of Mistuned Bladed Disks with Shroud Friction Contacts," *Journal of Engineering for Gas Turbines and Power*, 141, 1, pp. 1-13, ISSN: 15288919, DOI: 10.1115/1.4041653.

Mignolet, Marc P., Adam Przekop, Stephen A. Rizzi, and S. Michael Spottswood

2013 "A review of indirect/non-intrusive reduced order modeling of nonlinear geometric structures," *Journal of Sound and Vibration*, 332, 10, pp. 2437-2460, ISSN: 10958568, DOI: 10.1016/j.jsv.2012.10.017, http://dx.doi.org/10.1016/j.jsv.2012.10.017.

Nayfeh, Ali H and D. T. Mook

1985 *Nonlinear Oscillations*, p. 720, ISBN: 978-0471121428, DOI: 10.1002/9783527617586.

Nicolaidou, Evangelia, Thomas L Hill, and Simon A Neild

2021 "Detecting internal resonances during model reduction," *Proceedings of the Royal Society A: Mathematical, Physical and Engineering Sciences*, 477, 2250 [June 2021], p. 20210215, ISSN: 1364-5021, DOI: 10.1098/rspa.2021.0215, https://royalsocietypublishing.org/doi/10.1098/rspa.2021.0215.

Noor, Ahmed K and Jeanne M Peterst

1980 "Reduced Basis Technique for Nonlinear Analysis of Structures," *AIAA Journal*, 18, 4, pp. 455-462, ISSN: 0001-1452, DOI: 10.2514/3.50778, http://arc.aiaa.org/doi/abs/10.2514/3.50778.

Oulghelou, M and C Allery

2018 "Non intrusive method for parametric model order reduction using a bi-calibrated interpolation on the Grassmann manifold" [Dec. 2018], pp. 1-25, arXiv: 1901.03177, http://arxiv.org/abs/1901.03177.

Perez, R., G. Bartram, T. Beberniss, R. Wiebe, and S. M. Spottswood

2017 "Calibration of aero-structural reduced order models using full-field experimental measurements," *Mechanical Systems and Signal Processing*, 86, pp. 49-65, ISSN: 10961216, DOI: 10.1016/j.ymssp.2016.04.013, http://dx.doi.org/10.1016/j.ymssp.2016.04.013.

Perez, Ricardo, X. Q. Wang, and Marc P. Mignolet

2014 "Nonintrusive structural dynamic reduced order modeling for large deformations: Enhancements for complex structures," *Journal of Computational and Nonlinear Dynamics*, 9, 3, ISSN: 15551415, DOI: 10.1115/1.4026155.

Phalippou, P., S. Bouabdallah, P. Breitkopf, P. Villon, and M. Zarroug

2020 "'On-the-fly' snapshots selection for Proper Orthogonal Decomposition with application to nonlinear dynamics," *Computer Methods in Applied Mechanics and Engineering*, 367, p. 113120, ISSN: 00457825, DOI: 10.1016/j.cma.2020.113120, https://doi.org/10.1016/j.cma.2020.113120.

Pichler, Florian, Wolfgang Witteveen, and Peter Fischer

2017 "Reduced-Order Modeling of Preloaded Bolted Structures in Multibody Systems by the Use of Trial Vector Derivatives," *Journal of Computational and Nonlinear Dynamics*, 12, 5 [July 2017], p. 051032, ISSN: 1555-1415, DOI: 10.1115/1.4036989, http://computationalnonlinear.asmedigitalcollection.asme.org/article.aspx?doi=10.1115/1.4036989.

Pivovarov D Willner K, Steinmann P

2019 "Challenges of order reduction techniques for problems involving polymorphic uncertainty," *GAMM-Mitteilungen*, ISSN: 0936-7195, DOI: 10.1002/gamm.201900011, https://doi.org/10.1002/gamm.201900011.

Ponsioen, Sten, Shobhit Jain, and George Haller

2020 "Model reduction to spectral submanifolds and forced-response calculation in high-dimensional mechanical systems," *Journal of Sound and Vibration*, 488, p. 115640, ISSN: 10958568, DOI: 10.1016/j.jsv.2020.115640, https://doi.org/10.1016/j.jsv.2020.115640.

Prakash, A. and K. D. Hjelmstad

2004 "A FETI-based multi-time-step coupling method for Newmark schemes in structural dynamics," *International Journal for Numerical Methods in Engineering*, 61, 13, pp. 2183-2204, ISSN: 00295981, DOI: 10.1002/nme.1136.

Prakash, Arun

2007 *Multi-time-step domain decomposition and coupling methods for non-linear structural dynamics*, PhD thesis, University of Illinois at Urbana-Champaign.

Prikhodko, Igor P., Jeffrey A. Gregory, William A. Clark, John A. Geen, Michael W. Judy, Chae H. Ahn, and Thomas W. Kenny

2016 "Mode-matched MEMS Coriolis vibratory gyroscopes: Myth or reality?" *Proceedings of the IEEE/ION Position, Location and Navigation Symposium, PLANS 2016*, pp. 1-4, DOI: 10.1109/PLANS.2016.7479674.

Qalandar, K. R., B. S. Strachan, B. Gibson, M. Sharma, A. Ma, Steven W. Shaw, and K. L. Turner

2014 "Frequency division using a micromechanical resonance cascade," *Applied Physics Letters*, 105, 24, DOI: 10.1063/1.4904465.

Quarteroni, Alfio, Andrea Manzoni, and Federico Negri

2016 *Reduced Basis Methods for Partial Differential Equations*, UNITEXT, 3, Springer International Publishing, Cham, vol. 92, pp. 3-4, ISBN: 978-3-319-15430-5, DOI: 10.1007/978-3-319-15431-2, http://link.springer.com/10.1007/978-3-319-15431-2.

Rafiq, Danish and Mohammad Abid Bazaz

2020 "A framework for parametric reduction in large-scale nonlinear dynamical systems," *Nonlinear Dynamics*, 102, 3, pp. 1897-1908, ISSN: 1573269X, DOI: 10.1007/s11071-020-05970-3, https://doi.org/10.1007/s11071-020-05970-3.

Rao, Singiresu S and Fook Fah Yap

2011 *Mechanical vibrations*, Prentice hall Upper Saddle River, vol. 4.

Rixen, Daniel J

1997 *Substructuring and dual methods in structural analysis*, PhD thesis, Publications de la Faculté des Sciences appliquées.

Rubin, S.

1975 "Improved Component-Mode Representation for Structural Dynamic Analysis," *AIAA Journal*, 13, 8, pp. 995-1006, ISSN: 0001-1452, DOI: 10.2514/3.60497, http://arc.aiaa.org/doi/10.2514/3.60497.

Ryckelynck, D

2005 "A priori hyperreduction method: an adaptive approach," *Journal of Computational Physics*, 202, 1 [Jan. 2005], pp. 346-366, ISSN: 00219991, DOI: 10.1016/j.jcp.2004.07.015, https://linkinghub.elsevier.com/retrieve/pii/S002199910400289X.

Schwarzelbach, O., G. Fakas, and W. Nienkirchen

2001 "New approach for frequency matching of tuning fork gyroscopes by using a nonlinear driving concept," in *The 11th International Conference on Solid-State Sensorsand Actuators*, Springer, pp. 464-467, ISBN: 978-3-642-59497-7, DOI: https://doi.org/10.1007/978-3-642-59497-7_110, https://doi.org/10.1007/978-3-642-59497-7_110.

Shen, Yichang, Alessandra Vizzaccaro, Nassim Kesmia, Ting Yu, Loïc Salles, Olivier Thomas, and Cyril Touzé

2021 "Comparison of Reduction Methods for Finite Element Geometrically Nonlinear Beam Structures," *Vibration*, 4, 1, pp. 175-204, DOI: 10.3390/vibration4010014.

Sicklinger, Stefan Alfred

2014 *Stabilized co-simulation of coupled problems including fields and signals*, PhD thesis, Technische Universität München.

Sombroek, C. S.M., Paolo Tiso, L. Renson, and G. Kerschen

2018 "Numerical computation of nonlinear normal modes in a modal derivative subspace," *Computers and Structures*, 195, pp. 34-46, ISSN: 00457949, DOI: 10.1016/j.compstruc.2017.08.016, https://doi.org/10.1016/j.compstruc.2017.08.016.

Sung, Sangkyung, Woon Tahk Sung, Changjoo Kim, Sukchang Yun, and Young Jae Lee

2009 "On the mode-matched control of MEMS vibratory gyroscope via phase-domain analysis and design," *IEEE/ASME Transactions on Mechatronics*, 14, 4, pp. 446-455, ISSN: 10834435, DOI: 10.1109/TMECH.2009.2023985.

Tatar, E, C Guo, T Mukherjee, and G K Fedder

2013 "Interaction effects of temperature and stress on matched-mode gyroscope frequencies," in *2013 Transducers I& Eurosensors XXVII: The 17th International Conference on Solid-State Sensors, Actuators and Microsystems (TRANSDUCERS I& EUROSENSORS XXVII)*, June, IEEE, pp. 2527-2530, ISBN: 978-1-4673-5983-2, DOI: 10.1109/Transducers.2013.6627320, http://ieeexplore.ieee.org/document/6627320/.

Tiso, Paolo

2006 *Finite element based reduction methods for static and dynamic analysis of thin-walled structures*, PhD thesis, Technische Universiteit Delft.

2011 "Optimal second order reduction basis selection for nonlinear transient analysis," in *Proceedings of the 29th IMAC A Conference on Structural Dynamics 2011*, vol. 3, pp. 27-39, ISBN: 978-1-4419-9298-7, DOI: 10.1007/978-1-4419-9299-4_3, http://link.springer.com/10.1007/978-1-4419-9299-4%20http://link.springer.com/10.1007/978-1-4419-9299-4%7B%5C_%7D3.

Toselli, Andrea and Olof B. Widlund

2005 *Domain Decomposition Methods — Algorithms and Theory*, Springer Series in Computational Mathematics, Springer Berlin Heidelberg, Berlin, Heidelberg, vol. 34, pp. 35-53, ISBN: 978-3-540-20696-5, DOI: 10.1007/b137868.

Touzé, C., M. Vidrascu, and D. Chapelle

2014 "Direct finite element computation of non-linear modal coupling coefficients for reduced-order shell models," *Computational Mechanics*, 54, 2, pp. 567-580, ISSN: 01787675, DOI: 10.1007/s00466-014-1006-4.

Touzé, Cyril, Alessandra Vizzaccaro, and Olivier Thomas

2021 "Model order reduction methods for geometrically nonlinear structures: a review of nonlinear techniques," *Nonlinear Dynamics*, 105, 2, pp. 1141-1190, ISSN: 1573269X, DOI: 10.1007/s11071-021-06693-9, arXiv: 2107.05077.

Van den Broek, Jair

2019 *Modal derivatives based reduced-order modelling in parametrically driven structures and frequency dividers*, Master thesis (supervised by: Tiso P., Marconi J.), TU Delft, http://resolver.tudelft.nl/uuid:24ce9929-99ca-4a67-89b6-ffdfccd22345.

Van Ophem, S., E. Deckers, and W. Desmet

2019 "Parametric model order reduction without a priori sampling for low rank changes in vibro-acoustic systems," *Mechanical Systems and Signal Processing*, 130, pp. 597-609, ISSN: 08883270, DOI: 10.1016/j.ymssp.2019.05.035, https://linkinghub.elsevier.com/retrieve/pii/S0888327019303449.

Vizzaccaro, Alessandra, Loïc Salles, and Cyril Touzé
2020 "Comparison of nonlinear mappings for reduced-order modelling of vibrating structures: normal form theory and quadratic manifold method with modal derivatives," *Nonlinear Dynamics* [Sept. 2020], ISSN: 0924-090X, DOI: 10.1007/s11071-020-05813-1, https://doi.org/10.1007/s11071-020-05813-1%20http://link.springer.com/10.1007/s11071-020-05813-1.

Wang, X. Q., P. J. O'Hara, M. P. Mignolet, and J. J. Hollkamp
2018 "Reduced Order Modeling with Local Enrichment for the Nonlinear Geometric Response of a Cracked Panel," *AIAA Journal*, 57, 1, pp. 421-436, ISSN: 0001-1452, DOI: 10.2514/1.j057358.

Wang, X. Q., Gregory P. Phlipot, Ricardo A. Perez, and Marc P. Mignolet
2018 "Locally enhanced reduced order modeling for the nonlinear geometric response of structures with defects," *International Journal of Non-Linear Mechanics*, 101, August 2017, pp. 1-7, ISSN: 00207462, DOI: 10.1016/j.ijnonlinmec.2018.01.007, https://doi.org/10.1016/j.ijnonlinmec.2018.01.007.

Wang, Xiangyu, Song Cen, and Chenfeng Li
2013 "Generalized neumann expansion and its application in stochastic finite element methods," *Mathematical Problems in Engineering*, 2013, 1, ISSN: 1024123X, DOI: 10.1155/2013/325025.

Wedel-Heinen, Jakob
1991 "Vibration of geometrically imperfect beam and shell structures," *International Journal of Solids and Structures*, 27, 1, pp. 29-47, ISSN: 00207683, DOI: 10.1016/0020-7683(91)90143-4, http://dx.doi.org/10.1016/0020-7683(91)90143-4.

Weeger, Oliver, Utz Wever, and Bernd Simeon
2016 "On the use of modal derivatives for nonlinear model order reduction," *International Journal for Numerical Methods in Engineering*, 108, 13 [Dec. 2016], pp. 1579-1602, ISSN: 00295981, DOI: 10.1002/nme.5267, http://onlinelibrary.wiley.com/doi/10.1002/nme.3279/full%20http://doi.wiley.com/10.1002/nme.5267.

Weinberg, Marc S. and Anthony Kourepenis
2006 "Error sources in in-plane silicon tuning-fork MEMS gyroscopes," *Journal of Microelectromechanical Systems*, 15, 3, pp. 479-491, ISSN: 10577157, DOI: 10.1109/JMEMS.2006.876779.

Wenneker, Frits and Paolo Tiso
2014 "A substructuring method for geometrically nonlinear structures," *Conference Proceedings of the Society for Experimental Mechanics Series*, 1, 2, pp. 157-165, DOI: 10.1007/978-3-319-04501-6_14.

Woiwode, Lukas, Nidish Narayanaa Balaji, Jonas Kappauf, Fabia Tubita, Louis Guillot, Christophe Vergez, Bruno Cochelin, Aurélien Grolet, and Malte Krack
2020 "Comparison of two algorithms for Harmonic Balance and path continuation," *Mechanical Systems and Signal Processing*, 136 [Feb. 2020], p. 106503, DOI: 10.1016/j.ymssp.2019.106503, https://hal.archives-ouvertes.fr/hal-02424746.

Wu, Long and Paolo Tiso
2016 "Nonlinear model order reduction for flexible multibody dynamics: a modal derivatives approach," *Multibody System Dynamics*, 36, 4, pp. 405-425, ISSN: 1573272X, DOI: 10.1007/s11044-015-9476-5, http://dx.doi.org/10.1007/s11044-015-9476-5.

Wu, Long, Paolo Tiso, Konstantinos Tatsis, Eleni Chatzi, and Fred van Keulen

2019 "A modal derivatives enhanced Rubin substructuring method for geometrically nonlinear multibody systems," *Multibody System Dynamics*, 45, 1 [Jan. 2019], pp. 57-85, ISSN: 1384-5640, DOI: 10.1007/s11044-018-09644-2, http://dx.doi.org/10.1007/s11044-018-09644-2%20http://link.springer.com/10.1007/s11044-018-09644-2.

Wu, Long, Paolo Tiso, and Fred van Keulen

2018 "Interface Reduction with Multilevel Craig–Bampton Substructuring for Component Mode Synthesis," *AIAA Journal*, pp. 1-15, ISSN: 0001-1452, DOI: 10.2514/1.J056196, https://arc.aiaa.org/doi/10.2514/1.J056196.

Xiao, D.

2019 "Error estimation of the parametric non-intrusive reduced order model using machine learning," *Computer Methods in Applied Mechanics and Engineering*, 355, pp. 513-534, ISSN: 00457825, DOI: 10.1016/j.cma.2019.06.018, https://doi.org/10.1016/j.cma.2019.06.018.

Xiao, D., F. Fang, A. G. Buchan, C. C. Pain, I. M. Navon, and A. Muggeridge

2015 "Non-intrusive reduced order modelling of the Navier-Stokes equations," *Computer Methods in Applied Mechanics and Engineering*, 293, pp. 522-541, ISSN: 00457825, DOI: 10.1016/j.cma.2015.05.015, http://dx.doi.org/10.1016/j.cma.2015.05.015.

Xiao, D., F. Fang, C. C. Pain, and I. M. Navon

2017 "A parameterized non-intrusive reduced order model and error analysis for general time-dependent nonlinear partial differential equations and its applications," *Computer Methods in Applied Mechanics and Engineering*, 317, pp. 868-889, ISSN: 00457825, DOI: 10.1016/j.cma.2016.12.033, http://dx.doi.org/10.1016/j.cma.2016.12.033.

Zeoli, Mirko, Fred van Keulen, and Matthijs Langelaar

2005 "Fast reanalysis of geometrically nonlinear problems after shape modifications," in *6th World Congresses of Structural and Multidisciplinary Optimization*, June, Rio de Janeiro, pp. 1-11.

Zimmermann, Ralf

2019 "Manifold interpolation and model reduction," pp. 1-36, arXiv: 1902.06502, http://arxiv.org/abs/1902.06502.